MICROSCOPÍA DE FUERZAS ATÓMICAS AVANZADA APLICADA A SISTEMAS DE BAJA DIMENSIONALIDAD
ADVANCED ATOMIC FORCE MICROSCOPY FOR LOW-DIMENSIONAL SYSTEMS
PABLO ARES GARCÍA

UNIVERSIDAD AUTONOMA DE MADRID

MICROSCOPÍA DE FUERZAS ATÓMICAS AVANZADA APLICADA A SISTEMAS DE BAJA DIMENSIONALIDAD

ADVANCED ATOMIC FORCE MICROSCOPY FOR LOW-DIMENSIONAL SYSTEMS

Tesis doctoral

Pablo Ares García

Abril de 2017

Dirigida por: Prof. Julio Gómez-Herrero & Dra. Adriana Gil

Dpto. de Física de la Materia Condensada. Universidad Autónoma de Madrid

UNIVERSIDAD AUTÓNOMA DE MADRID

Departamento de Física de la Materia Condensada

MICROSCOPÍA DE FUERZAS ATÓMICAS AVANZADA APLICADA A SISTEMAS DE BAJA DIMENSIONALIDAD

Tesis presentada por

Pablo Ares García

Para optar al grado de Doctor en Ciencias Físicas

Directores de tesis

Dra. Adriana Gil Gil

Prof. Julio Gómez Herrero

Madrid, abril de 2017

A mis padres, Santiago y Ángela, que me dieron la vida.

A mi mujer, Cristina, que comparte la suya conmigo.

"Tenga cuidado con las cosas pequeñas. Su ausencia o presencia puede cambiarlo todo"

Han Shan, filósofo chino (finales del siglo VIII d.C. aproximadamente)

Index.

Motivación y resumen.

Esta tesis trata principalmente sobre el empleo y desarrollo de la microscopía de fuerzas atómicas -conocida habitualmente por sus siglas en inglés AFM (*Atomic Force Microscopy*)- y técnicas afines para el estudio de diversos sistemas de baja dimensionalidad, que son aquellos que tienen al menos una de sus dimensiones en la escala nanométrica.

Para entender el origen y motivación de este trabajo, conviene hacer un poco de historia. En 1981, Gerd Karl Binnig y Heinrich Rohrer inventaron el microscopio de efecto túnel, STM en sus siglas en inglés (*Scanning Tunneling Microscope*) en el IBM Research Center de Zúrich [1, 2], dando así origen a una nueva familia de microscopía conocida como de campo cercano o también de sonda local, SPM en sus siglas en inglés (*Scanning Probe Microscopy*). Esta nomenclatura viene del hecho de que estos microscopios funcionan acercando una punta muy afilada, la sonda local, a la superficie de la muestra que se quiere estudiar. El microscopio STM detecta la corriente túnel que aparece entre una punta metálica y la muestra, que puede ser semiconductora o metálica. La corriente túnel es una pequeña corriente que aparece por un efecto cuántico conocido como efecto túnel, y que cambia de forma muy abrupta con la distancia entre punta y muestra. Cuando se aplican unas pocas décimas de voltio y se acerca la punta a distancias de 2-3 radios atómicos esta corriente es del orden del nA. Si en estas condiciones se desplaza la punta sobre la muestra se pueden obtener imágenes de la superficie que se está estudiando, de manera similar a la que una persona ciega lee, detectando las diferentes rugosidades al desplazar sus dedos por un texto escrito en braille.

A principio de la década de los 80, el profesor Nicolás García comenzó una colaboración con los doctores Binnig y Rohrer para establecer los principios de funcionamiento del STM desde un punto de vista teórico. En 1983-84, el profesor Arturo Baró estuvo trabajando en el laboratorio dirigido por Binnig y Rohrer en Suiza, donde aprendió de primera mano todo sobre la construcción y funcionamiento de los STMs. Como resultado de esta colaboración, en 1984 Christoph Gerber y Heinrich Rohrer trajeron a España el primer STM que salía fuera de IBM y fue instalado por Gerber en la Universidad Autónoma de Madrid (UAM). Poco después, en 1986, Binnig y Rohrer ganaron el premio Nobel en Física por el invento del STM.

A partir de ese momento, el grupo del profesor Arturo Baró en Madrid comenzó a trabajar en el desarrollo del STM y rápidamente adquirió reputación en este nuevo campo. Como consecuencia, otros grupos del departamento de Física Fundamental (actual departamento de Física de la Materia Condensada) desarrollaron una actividad muy intensa en este campo, realizando sus propios desarrollos teóricos y experimentales. En 1986, Binnig,

Calvin F. Quate y Gerber inventaron el microscopio de fuerzas atómicas, AFM [3], cuyo principio de funcionamiento es similar al del STM, y el grupo del profesor Baró de inmediato se vio también interesado por esta invención. El laboratorio del profesor Baró decidió entonces continuar sus esfuerzos en ambas líneas desarrollando electrónica, software y mecánica para ambos tipos de microscopios. La llegada del Dr. Jaime Colchero al laboratorio dirigido por el profesor Baró, a principio de la década de los 90, contribuyó de manera decisiva al desarrollo de esta técnica, primero en el departamento y luego en España.

En 1998 los microscopios construidos en el laboratorio del profesor Baró eran muy avanzados. Debido al creciente interés de la comunidad científica en el campo de los SPMs surgieron varias compañías que fabricaban y comercializaban este tipo de microscopios. Por aquel entonces, el grupo del profesor Baró proporcionaba SPMs fabricados en su laboratorio a otros grupos de investigación en todo el mundo, a través de acuerdos de colaboración sin ánimo de lucro. Los precios de los SPMs comerciales eran muy elevados, por lo que la comunidad científica en España no lo tenía fácil para adquirir estos microscopios. En ese momento el profesor Baró junto con tres investigadores de la UAM, Jaime Colchero, José María Gómez Rodríguez y Julio Gómez Herrero, fundaron la empresa Nanotec Electrónica S.L. (de ahora en adelante Nanotec) para la fabricación, desarrollo y venta de SPMs. Debido a la larga experiencia en el campo acumulada por estos investigadores, desde el principio Nanotec fabricó AFMs y electrónicas de control para STMs muy competitivos. La alta calidad de esta instrumentación así como el esfuerzo para poner en el mercado los resultados de la investigación del grupo, se vieron reconocidos con el premio de investigación e innovación de la Comunidad de Madrid concedido al profesor Baró en 1998.

A partir de 1998, Nanotec comenzó proyectos ambiciosos con el objetivo de posicionarse en el mercado de los SPMs, combinando inversión en I+D con productos de alta calidad y con colaboraciones con muchos grupos investigadores por todo el mundo.

De esta forma llegamos a la primavera de 2003. Por aquel entonces Nanotec estaba en pleno crecimiento y buscaba ampliar su plantilla con, entre otros puestos, un licenciado en Física. Ese año me encontraba terminando la licenciatura de Física en la Universidad Complutense de Madrid y la opción de incorporarme a Nanotec me pareció muy atractiva. Me daba la oportunidad de trabajar en una empresa única en España, puntera en el desarrollo de instrumentación científica, manteniendo el contacto con la comunidad científica y estando al día de los avances del hoy ya establecido campo de la Nanotecnología. Tuve la enorme suerte de que la dirección de Nanotec apostase por mí y, de esta forma, entré a formar parte de la compañía.

Nada más entrar en Nanotec lo primero que tuve que hacer fue “empaparme” de la técnica, principalmente del AFM, ya que mis cometidos incluían el desarrollo de los microscopios,

enseñar a nuevos usuarios, escribir manuales de funcionamiento, instalar nuevos equipos, dar soporte técnico, realizar medidas de muestras de potenciales clientes y un sinfín de pequeñas tareas que son siempre necesarias en una empresa de base tecnológica. En todos estos aspectos el papel de la doctora Adriana Gil, primero como directora científica y más tarde como directora general de Nanotec, fue fundamental, no sólo por la formación que recibí de su parte, sino también por su ayuda y supervisión en la elaboración de informes, manuscritos y comunicaciones. A su vez, en mi primer año en Nanotec pasé largas temporadas en el Laboratorio de Nuevas Microscopías de la UAM, profundizando en los distintos aspectos de la técnica. Al cabo de un año, tras la marcha de un compañero ingeniero mecánico, se decidió que me encargase también de la parte más técnica del desarrollo mecánico, aprendiendo para ello el uso básico de programas CAD (siglas en inglés de *Computer-Aided Design*, diseño asistido por ordenador) para el diseño de sólidos y elaboración de planos y, bajo la supervisión de Adriana Gil, tuve la oportunidad de dirigir desarrollos instrumentales con el objetivo de mejorar y dar nuevas capacidades a los AFMs. Cabe mencionar aquí que Adriana Gil se había doctorado unos años antes bajo la dirección del Dr. Jaime Colchero, de quien aprendió sus amplios conocimientos sobre la microscopía de campo cercano.

A medida que fueron pasando los años, una activa política de colaboraciones de Nanotec con grupos investigadores me permitió, no sólo profundizar más en las distintas variantes de la técnica, sino también participar activamente en trabajos de investigación con grupos de todo el mundo. De nuevo cabe resaltar el papel de Adriana Gil en esta faceta, facilitando estas colaboraciones y siendo claves sus aportaciones a los avances que se iban consiguiendo. Los frutos de algunas de estas colaboraciones fueron varias publicaciones científicas.

Algunas de ellas, como "Cutting down the forest of peaks in acoustic dynamic atomic force microscopy in liquid" [4], "Variable-field magnetic force microscopy" [5], "Minimizing tip-sample forces in jumping mode atomic force microscopy in liquid" [6], y "Flatten plus: a recent implementation in WSxM for biological research" [7], se dieron con investigadores que habían formado parte del grupo del profesor Baró en la UAM (principalmente Julio Gómez Herrero de la UAM y Agustina Asenjo del Instituto de Ciencia de Materiales de Madrid ICMM-CSIC), grupos muy próximos a Nanotec. En estos trabajos, entre otras cosas, participé en el desarrollo de la técnica en campos a priori tan alejados como las medidas en medio líquido y las medidas de magnetismo (digo a priori porque, como veremos más adelante, uno de los trabajos realizados en esta tesis ha sido la combinación de ambos tipos de medida para permitir el estudio de sistemas "bio-nano magnéticos").

Otras publicaciones, como "Strain energy and lateral friction force distributions of carbon nanotubes manipulated into shapes by atomic force microscopy" [8], y "Neck-size distributions of through-pores in polymer membranes" [9], son el fruto de colaboraciones con investigadores de lugares tan dispares como son la Universidad de Purdue (los grupos

de los profesores Ron Reifenberger y Arvind Raman) en los Estados Unidos de América y el Bhabha Atomic Research Centre en la India. La experiencia obtenida en la colaboración con los investigadores de la Universidad de Purdue, participando en la nanomanipulación de nanotubos de carbono, fue fundamental para el trabajo correspondiente a la formación de contactos eléctricos mediante nanohilos de oro realizado en esta tesis.

Otra colaboración (por mediación de Adriana Gil y del profesor Julio Gómez Herrero), en este caso con el grupo de la profesora Rosa Menéndez del Instituto Nacional del Carbón INCAR-CSIC, dio como resultado dos publicaciones, "The effect of the parent graphite on the structure of graphene oxide" [10], y "Tailored graphene materials by chemical reduction of graphene oxides of different atomic structure" [11], que me permitieron una primera toma de contacto con el estudio de materiales bidimensionales, tema con un peso sustancial en esta tesis. Un resultado relevante de estos estudios es la prueba de la influencia de la estructura cristalina del grafito de partida, importante para la producción de láminas de óxido de grafeno y de grafeno reducido mediante métodos químicos.

Finalmente, de nuevo con investigadores de la UAM como Julio Gómez Herrero y Pedro J. de Pablo, así como con investigadores del grupo de Mark J. van Raaij del Centro Nacional de Biotecnología CNB-CSIC, otra publicación vio la luz, "Interplay between the mechanics of bacteriophage fibers and the strength of virus-host links" [12], que permitió, a la vez que la puesta a punto de un diseño nuevo de portapuntas para medidas en medio líquido (fundamental para trabajos posteriores desarrollados en esta tesis, como son las medidas de magnetismo en medio líquido y la alta resolución de la doble cadena de ARN), dar una explicación "mecánica" al hecho de que algunos virus necesiten enlazar al menos tres de sus seis "patas" para comenzar el proceso de infección.

Es importante mencionar que estos trabajos son previos a los presentados en esta memoria y no se darán más detalles de los mismos a lo largo de ella. Un listado completo de las publicaciones asociadas al trabajo aquí presentado se puede encontrar al final de esta memoria, en el apartado "*List of Publications*" ("Listado de Publicaciones").

En el transcurso de estas colaboraciones, el profesor Julio Gómez Herrero me ofreció la posibilidad de colaborar más con él de forma que, poco a poco a lo largo de varios años, pudiese dar lugar a la obtención de un doctorado. Tras acordar la codirección del profesor Julio Gómez Herrero y de la doctora Adriana Gil, en aquel momento directora científica de Nanotec, realicé el Máster en Física de la Materia Condensada y Nanotecnología de la UAM y di comienzo a una serie de experimentos en los laboratorios de la UAM. En octubre de 2014 desafortunadamente Nanotec Electrónica se vio obligada a cesar su actividad, acuciada por la baja demanda de instrumentación científica, hecho propiciado por las políticas de recortes en I+D tras el comienzo de la crisis económica mundial en 2008. Tras el cese de Nanotec, la dedicación a tiempo completo a las investigaciones y desarrollos ya iniciados surgió como una continuación lógica al trabajo de años anteriores.

Cabe destacar aquí el papel de mi director de tesis, facilitándome la posibilidad de incorporarme a su laboratorio y proporcionándome todo lo necesario para la realización, tanto de los estudios que teníamos en mente, como de otros nuevos que fueron surgiendo.

El resultado de dichos estudios se ve reflejado en esta memoria y comprende distintos aspectos de las ya bien establecidas Nanociencia y Nanotecnología. El origen de este campo de investigación se establece históricamente en diciembre de 1959 con la famosa conferencia de Richard Feynman titulada "*There is plenty of room at the bottom*" ("Hay mucho espacio al fondo"), donde Feynman trató sobre cómo manipular, controlar y fabricar objetos de muy pequeñas dimensiones, abordando la cuestión desde una perspectiva absolutamente distinta a como se había hecho hasta entonces, abriendo así un nuevo mundo de posibilidades a lo que más tarde se conocería como Nanotecnología.

Podemos definir la Nanotecnología como el diseño y manipulación de la materia en la escala nanométrica. El prefijo "nano" del Sistema Internacional de Unidades viene del griego νάνος que significa enano, y corresponde a un factor 10^{-9}. Aplicado a las unidades de longitud, corresponde a una mil millonésima parte de un metro (10^{-9} m). La Nanotecnología estudia la materia entre 0.1 y 100 nm aproximadamente (Figura 0.1). En esta escala, la materia ya no está gobernada por las leyes a las que estamos acostumbrados, si no que la mecánica cuántica juega un papel muy importante, lo que permite acceder a nuevas propiedades que sólo se manifiestan a esta escala. Al estar la Nanotecnología definida por el tamaño de los objetos a estudiar, es un área multidisciplinar que da cabida a muchos campos tan diversos como la ciencia de superficies, microfabricación, electrónica, química orgánica e inorgánica, biología molecular, física de semiconductores, ciencia de materiales, etc.

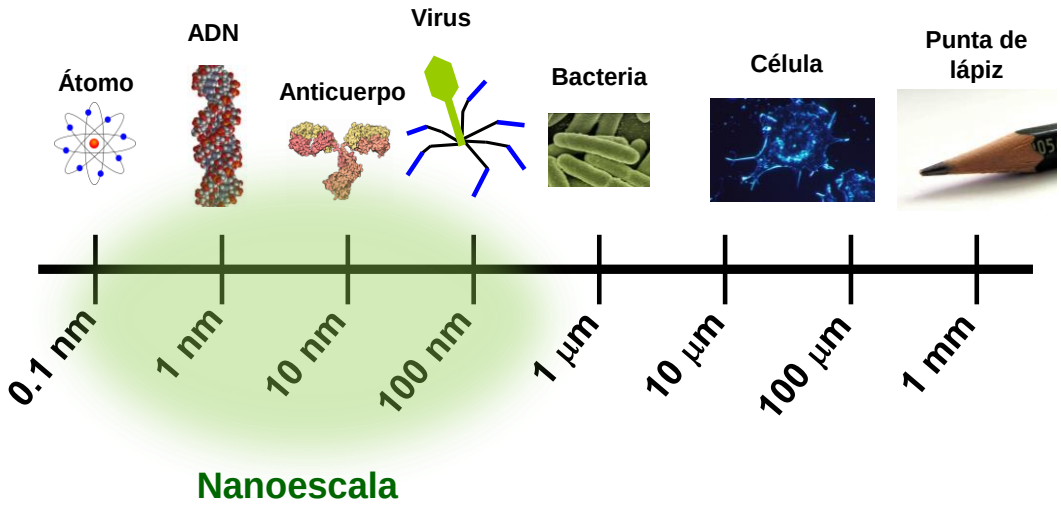

Figura 0.1 Esquema de escala de tamaños.

Tuvieron que pasar más de 30 años desde que Feynman expuso sus ideas hasta que éstas pudieron empezar a llevarse a cabo. Y el motivo no fue otro que la falta de herramientas para trabajar en la nanoescala. En ese sentido, la invención del microscopio de efecto túnel, STM, por Binnig y Rohrer en 1981 [1, 2] supuso toda una revolución. Si bien las técnicas de emisión de campo ya habían permitido visualizar átomos [13] aunque en unas condiciones muy restringidas, el STM permitió por primera vez visualizar y manipular átomos y moléculas de forma individual en condiciones mucho más generales. Como ya se ha mencionado antes, pocos años después, en 1986, Binnig, Quate y Gerber inventaron el microscopio de fuerzas atómicas, AFM, con un esquema de funcionamiento similar al STM, pero detectando fuerzas entre punta y muestra en lugar de corrientes [3]. Mientras que el STM necesita una muestra metálica o semiconductora para poder establecer una corriente túnel, el AFM puede aplicarse a cualquier tipo de muestra. Además, mientras que para sacarle el máximo partido al STM es conveniente trabajar en condiciones de ultra alto vacío, para mantener limpias las superficies a estudiar, el AFM permite un extraordinario rendimiento en diferentes ambientes (líquidos, aire y vacío). Esta versatilidad ha hecho del AFM una de las herramientas más utilizadas en el campo de la Nanotecnología.

La multidisciplinariedad de la Nanotecnología junto con la experiencia previa con el AFM, adquirida durante mi etapa en Nanotec, despertaron mi curiosidad y me proporcionaron un gran interés por la aplicación de esta técnica en diversos campos, así como por el desarrollo de la técnica en sí misma. Esto queda reflejado en la heterogeneidad de temas tocados en el transcurso de esta tesis, aunque con un marcado interés en el estudio de las propiedades electrónicas de sistemas uni- y bi- dimensionales. La adecuada combinación de estos sistemas, junto con la posibilidad de controlar y modificar en la nanoescala las propiedades de los mismos, serán la base de los dispositivos electrónicos del futuro. En ese sentido, en esta tesis por una parte se ha estudiado el comportamiento de distintos sistemas unidimensionales para su utilización como futuros cables en nanodispositivos, a la vez que se han estudiado materiales bidimensionales con posibles aplicaciones en la fabricación de dichos nanodispositivos.

El capítulo 1 de esta memoria es una introducción al microscopio de fuerzas atómicas, herramienta principal utilizada.

El capítulo 2 muestra una serie de desarrollos instrumentales realizados: por una parte el diseño, fabricación y puesta a punto de una mecánica nueva de AFM que permite su combinación con técnicas ópticas, como la fluorescencia por reflexión total interna. Y por otra parte el diseño, construcción y puesta en funcionamiento de una estación de puntas (*probe station* en inglés) con posibilidad de trabajar en alto vacío y con un rango de temperaturas comprendido entre 80 K y 400 K, para la caracterización eléctrica de materiales desde la micro- a la nanoescala. Si bien por limitaciones de tiempo no se han podido realizar experimentos extensos con estos sistemas, estoy seguro que serán muy utilizados en lo sucesivo.

El capítulo 3 presenta una serie de desarrollos metodológicos de la técnica del AFM, que incluyen, por una parte, la optimización de diferentes modos de medida en medio líquido para la obtención de alta resolución en muestras biológicas tipo ADN y ARN; y por otra parte, la implementación de medidas de fuerzas magnéticas en dichos medios, llevando el AFM a un punto que permite su aplicación al estudio de sistemas magnéticos nanométricos con aplicaciones biológicas. En segundo lugar, el desarrollo de dos métodos distintos y complementarios para la creación de nano- y micro- contactos, con especial utilidad a la hora de estudiar las propiedades eléctricas de nanobjetos, no sólo con el AFM, sino también como métodos alternativos a los tradicionales. Los resultados recogidos en los capítulos 2 y 3 reflejan la constante evolución de los instrumentos de medida, tanto para la mejora de las capacidades de los mismos, como para la implementación de nuevas funcionalidades, lo cual presenta en sí mismo un marcado interés para la comunidad científica, ya que posibilita el avance en muchos y muy variados campos.

El capítulo 4 versa sobre el estudio de nuevos sistemas de baja dimensionalidad: una primera parte dedicada a fibras unidimensionales de polímeros de coordinación, que presentan propiedades de conducción eléctrica extraordinarias, y una segunda parte dedicada a materiales bidimensionales, en particular al uso del AFM para modificar localmente las propiedades del grafeno a través de la aplicación de presiones ultra altas (> 10 GPa). El capítulo termina con la presentación de un nuevo material, hasta ahora solamente predicho teóricamente, aislado por primera vez en el transcurso de esta tesis, el antimoneno (una lámina de átomos de antimonio de espesor atómico) y la caracterización de varias de sus propiedades. El estudio de las propiedades y el comportamiento de materiales uni- y bidimensionales es esencial para el avance de la nanotecnología y de sus numerosas potenciales aplicaciones.

Finalmente, el capítulo 5 es un resumen de todo lo expuesto a lo largo de la memoria, así como nuevas perspectivas que se abren como resultado de este trabajo.

Referencias

[1] Binnig, G.; Rohrer, H. Scanning Tunneling Microscopy. *Helv. Phys. Acta* **1982,** *55*, 726-735.
[2] Binning, G.; Rohrer, H.; Gerber, C.; Weibel, E. Surface Studies by Scanning Tunneling Microscopy. *Phys. Rev. Lett.* **1982,** *49*, 57-61.
[3] Binnig, G.; Quate, C. F.; Gerber, C. Atomic Force Microscope. *Phys. Rev. Lett.* **1986,** *56*, 930-933.
[4] Carrasco, C.; Ares, P.; de Pablo, P. J.; Gomez-Herrero, J. Cutting down the forest of peaks in acoustic dynamic atomic force microscopy in liquid. *Rev. Sci. Instrum.* **2008,** *79*, 126106.
[5] Jaafar, M.; Gomez-Herrero, J.; Gil, A.; Ares, P.; Vazquez, M.; Asenjo, A. Variable-field magnetic force microscopy. *Ultramicroscopy* **2009,** *109*, 693-699.
[6] Ortega-Esteban, A.; Horcas, I.; Hernando-Perez, M.; Ares, P.; Perez-Berna, A. J.; San Martin, C.; Carrascosa, J. L.; de Pablo, P. J.; Gomez-Herrero, J. Minimizing tip-sample forces in jumping mode atomic force microscopy in liquid. *Ultramicroscopy* **2012,** *114*, 56-61.
[7] Gimeno, A.; Ares, P.; Horcas, I.; Gil, A.; Gomez-Rodriguez, J. M.; Colchero, J.; Gomez-Herrero, J. 'Flatten plus': a recent implementation in WSxM for biological research. *Bioinformatics* **2015,** *31*, 2918-2920.
[8] Strus, M. C.; Lahiji, R. R.; Ares, P.; Lopez, V.; Raman, A.; Reifenberger, R. Strain energy and lateral friction force distributions of carbon nanotubes manipulated into shapes by atomic force microscopy. *Nanotechnology* **2009,** *20*, 385709.
[9] Agarwal, C.; Pandey, A. K.; Das, S.; Sharma, M. K.; Pattyn, D.; Ares, P.; Goswami, A. Neck-size distributions of through-pores in polymer membranes. *J. Membr. Sci.* **2012,** *415*, 608-615.
[10] Botas, C.; Alvarez, P.; Blanco, C.; Santamaria, R.; Granda, M.; Ares, P.; Rodriguez-Reinoso, F.; Menendez, R. The effect of the parent graphite on the structure of graphene oxide. *Carbon* **2012,** *50*, 275-282.
[11] Botas, C.; Alvarez, P.; Blanco, C.; Dolores Gutierrez, M.; Ares, P.; Zamani, R.; Arbiol, J.; Morante, J. R.; Menendez, R. Tailored graphene materials by chemical reduction of graphene oxides of different atomic structure. *RSC Adv.* **2012,** *2*, 9643-9650.
[12] Ares, P.; Garcia-Doval, C.; Llauro, A.; Gomez-Herrero, J.; van Raaij, M. J.; de Pablo, P. J. Interplay between the mechanics of bacteriophage fibers and the strength of virus-host links. *Phys. Rev. E* **2014,** *89*, 052710.
[13] Muller, E. W. *Das Feldionenmikroskop. *Zeitschrift Fur Physik* **1951,** *131*, 136-142.

Abstract.

This PhD presents the use and development of Atomic Force Microscopy (AFM) and related techniques applied to the study of low-dimensional systems, which are those with at least one of its dimensions in the nanoscale.

Chapter 1 is an introduction to the atomic force microscope, the main tool employed along this PhD.

Chapter 2 presents two different instrumental developments performed during this PhD. First, the design, assembly and testing of an experimental setup to allow simultaneous AFM and Total Internal Reflection Fluorescence Microscopy (TIRFM). Second, the design, assembly and testing of a probe station setup, for the electrical characterization of micro- and nano- materials and devices at temperatures ranging from 80 to 400 K, in controlled atmospheres.

Chapter 3 deals with different methodological developments of the AFM technique. First, improvements of the AFM technique in liquids are presented. It includes the optimization of different high-sensitive force-detection methods for high resolution imaging of nucleic acids in liquids. High resolution of double-stranded RNA (dsRNA) under near-physiological conditions is obtained for the first time with AFM. Magnetic Force Microscopy (MFM) in liquid environments is also presented. A fine tuning of the experimental conditions allows imaging magnetic nanostructures in liquids with a resolution close to ambient conditions, opening the possibility of studying "bio-nano-magnetic" samples.

Second, two novel approaches for the fabrication of simple, clean and reliable electrodes for the electrical contact of nano-objects are presented. One is based on the use of exfoliated graphite flakes (EGF) as soft-electrodes. The other is named Probe-Assisted Nanowire (PAN) lithography. It is based on the adsorption of Au NWs on the sample of interest and subsequent manipulation with an AFM probe to create nanoelectrodes.

Chapter 4 presents studies on novel low-dimensional systems. There is a first part dealing with on surface isolation and characterization of highly conductive 1-dimensional chains of

coordination polymers, obtained from a wet chemistry approach, going down to the individual chain level.

The second part deals with the use of AFM to study 2-dimensional systems. It is first applied to locally tune the electronic properties of graphene upon ultrahigh pressure (> 10 GPa) modifications.
Finally, a new 2-dimensional material, antimonene, a single layer of antimony atoms, is introduced, isolated along this PhD for the very first time. Demonstration of its stability under ambient conditions, and characterization of its optical and electrical properties are shown.

Finally, chapter 5 is a summary of all the work presented in this manuscript, along with prospects derived from the results obtained here.

Chapter 1. Introduction to Atomic Force Microscopy.

1.1 Introduction

1.2 Basic concepts of Atomic Force Microscopy

1.2.1 AFM components

1.2.2 Standard operation modes

1.3 Advanced AFM measurements

1.3.1 Dynamic modes

1.3.2 Spectroscopy imaging (3D Modes)

1.3.3 Measurements in liquid environments

1.3.4 Magnetic Force Microscopy (MFM)

1.3.5 Conductive AFM (C-AFM)

1.3.6 Kelvin Probe Microscopy (KPM)

1.3.7 Lithography/nanomanipulation

1.4 References

1.1 Introduction

Microscopy is one of the major developments in the history of Science and Technology, being responsible of the advance of many different fields. According to the English Oxford Dictionary, a microscope is defined as "an optical instrument used for viewing very small objects, such as mineral samples or animal or plant cells, typically magnified several hundred times" [1]. The Cambridge Dictionary defines a microscope as "a device that uses lenses to make very small objects look larger, so that they can be scientifically examined and studied" [2]. These two definitions are clearly focused on optical microscopes (although the second one can include electron microscopes as well, since they also use lenses, electromagnetic lenses). The invention of the scanning tunneling and the atomic force microscopes represented a breakthrough in the concept of a microscope.

Although it is widely attributed to Galileo in the 1600's, the history of the microscope begins with Zacharias Jansen's invention of the first light microscope in the 1590's. Zacharias Jansen and his father Hans put several lenses in a tube and made a very important discovery. The object near the end of the tube appeared to be greatly enlarged, much larger than any simple magnifying glass could achieve by itself [3]. Figure 1.1 shows pictures of the first optical microscopes from Jansen and Galileo. Since these first compound microscopes, there has been a constant and outstanding evolution of microscopy. However, most optical microscopes resolution is dictated by the diffraction limit of the visible light photons, this is, by half the value of their wavelength, $\lambda/2 \sim 200$ nm.

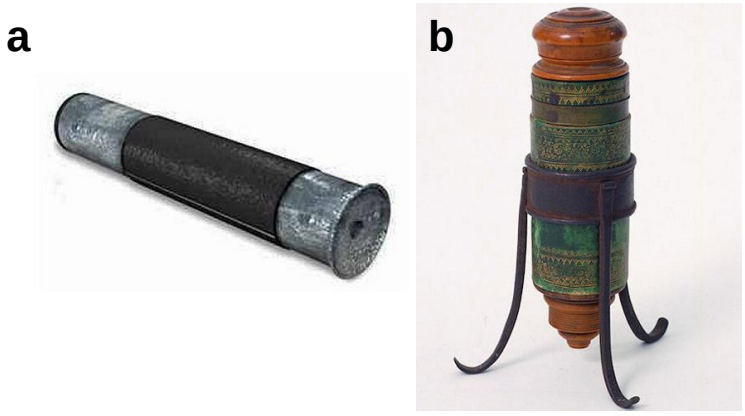

Figure 1.1 First optical microscopes. a) Optical microscope from Hans and Zacharias Jansen (1590's). b) Optical microscope from Galileo (1600's). Source: http://www.history-of-the-microscope.org

Ernst Ruska and Max Knoll developed the Transmission Electron Microscope (TEM) in 1931 and later Manfred von Ardenne in 1937 applied a scanning principle to develop the

Scanning Electron Microscope (SEM). These microscopes use a beam of accelerated electrons as a source of illumination. Electron microscopes use electromagnetic lenses to control and focus the electron beam. These electron lenses can be considered as analogous to the glass lenses of an optical light microscope. As the wavelength of an electron can be orders of magnitude shorter than that of visible light photons, resolution for electron microscopes is much better than for optical microscopes and in most cases is limited by spherical aberration of the electron lenses. In recent years, electron microscopies have benefited from subtle instrumentation advances, including improvements in the detectors combined with summing multiple subsequent frames (which dramatically improves the signal-to-noise ratio), reaching resolution values of ~ 0.05 nm, enabling the detection of even individual low-atomic-number atoms [4]. Figure 1.2 shows one of the first transmission electron microscopes built by Ernst Ruska.

Figure 1.2 Electron microscope built by Ernst Ruska in 1933. Source: https://commons.wikimedia.org

In the early 80's Gerd Binnig and Heinrich Rohrer developed the Scanning Tunneling Microscope (STM) [5, 6]. These microscopes, whose working principle is based on scanning a sharp tip very close to the surface of the sample under study, probing the tunneling current between tip and sample, meant a complete revolution to surface science. One of the main advantages of STMs compared to other microscopy techniques is the ability to measure heights. They allow not only the visualization of single atoms [5], but the manipulation of the matter at an atomic level [7]. Figure 1.3a shows one of the first STMs ever built and figure 1.3b the first atomic resolution image obtained with an STM.

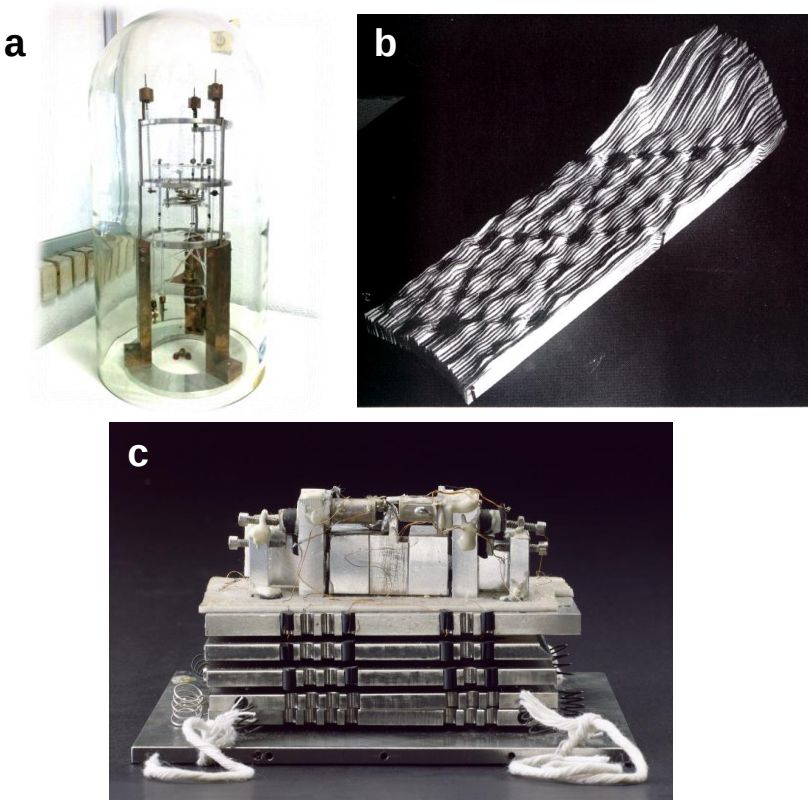

Figure 1.3 a) One of the first STMs ever made. The picture corresponds to the first STM that came to Spain, to Universidad Autónoma de Madrid. b) First atomic resolution image obtained with a STM, corresponding to the 7x7 reconstruction on Si (111) [5]. c) First AFM from Binnig, Quate and Gerber. Source: http://www.sciencemuseum.org.uk/

The later development of the Atomic Force Microscope (AFM, also known as Scanning Force Microscope, SFM) by Gerd Binnig again, together with Calvin Quate and Christoph Gerber [8] (figure 1.3c) and the Scanning Near-field Optical Microscope (SNOM) [9-11] gave rise to a whole new family of microscopes known as Scanning Probe Microscopes (SPM). The working principle of all them is the same, a sharp tip scanning very close to the sample under study probing a magnitude which depends strongly on the tip-sample distance. This dependency with the distance is the responsible of their very high sensitivity to topography changes and the origin of their high resolution. Figure 1.4 shows the working principle of SPMs, which can be easily compared with the way blind people use their white canes to walk.

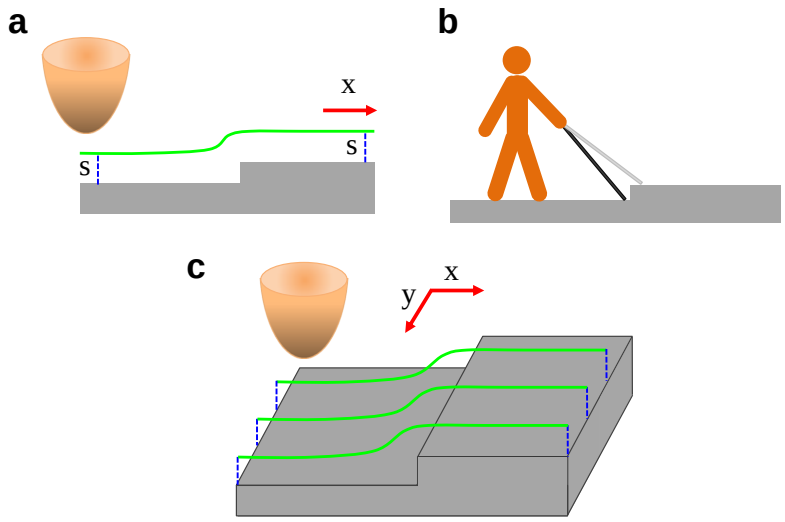

Figure. 1.4 a) Principle of operation of SPMs. b) Analogy with the way a blind person follows the floor topography. c) Line by line scanning to obtain an SPM image.

The different probed interactions define the kind of SPM. Figure 1.5 summarizes the different microscopes in the SPM family.

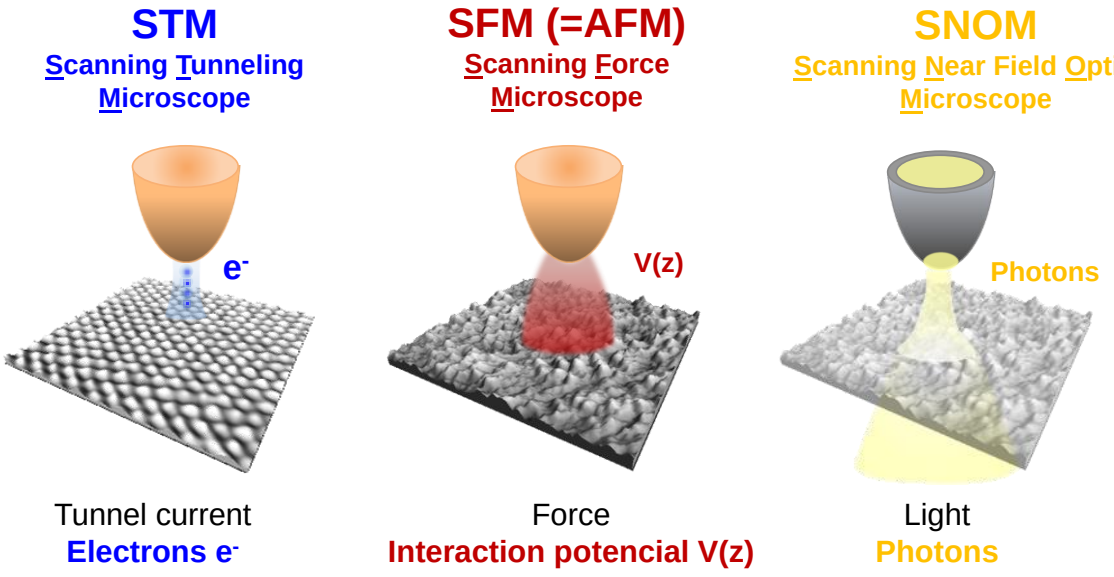

Figure 1.5 Family of SPMs.

It is interesting to think about optical and electron microscopes as instruments that deal with propagating waves controlled by lenses (far-field approach). On the contrary, scanning probe microscopes use the concept of non-propagating waves whose intensity decays exponentially with the distance (near-field approach). In this respect, both techniques can be considered as complementaries.

STM measures the tunneling current between tip and sample, hence conducting or semiconducting samples are required. AFM measures forces between the tip at the end of a cantilever and the sample, allowing the study of any kind of material: conductors, semiconductors, insulators, biological, etc. SNOM probes the evanescent waves of light by placing the tip very close (at a distance much smaller than the light wavelength), thus breaking the far field resolution limit. Probably because of its complex set up and the lack of reliable commercial tips, SNOM has experimented a moderate success when compared to their elder brothers AFM and STM. The ability of the AFM to study any kind of sample together with its versatility to work under different environmental conditions: liquids, air, controlled atmospheres, UltraHigh Vacuum (UHV), etc. has undoubtedly raised AFM as the most popular and widespread microscope among the SPM family.

The AFM was celebrating in 2016 its 30^{th} anniversary. Albeit it is a well stablished technique, used routinely in hundreds of laboratories throughout the world, it stays under continuous development. In the last years major advances have been addressed to improve its performance. A review of all the developments carried out on the AFM technique is completely out of the scope of this introduction, thus only some of the most relevant ones are presented. Apart from the standard static Contact and dynamic Amplitude Modulation (AM-AFM) [12] measuring modes, the use of other different modes allows relevant advances in many different fields. For instance, high sensitive force detection schemes such as Frequency Modulation (FM-AFM) [13], Force-distance based modes (Pulsed Force mode [14, 15], Jumping [16, 17], PeakForce [18], etc.) or Drive Amplitude Modulation (DAM-AFM) [19, 20] are allowing the study of many systems. In particular, they prove to be very powerful for measurements in liquid environments to study biological systems such as DNA [21], viral capsids [22] or antibodies [23] with unprecedented resolution, or to achieve true atomic resolution on surfaces [24]. High Speed AFM, pioneered in the early 2000's by T. Ando initially in liquid environments [25], and now commercially available from most of the manufacturers to work in different environments, has meant a breakthrough in AFM to study time-varying processes. Simultaneous excitation and detection of several eigenmodes of the cantilever [26, 27] has triggered a whole new branch of the AFM technique called Multifrequency AFM. It combines well stablished dynamic acquisition modes with simultaneous mapping of other properties [28, 29]. In the field of the so-called Non-Contact AFM (mostly related to AFM working in UHV conditions under the FM-AFM scheme), after the true atomic resolution achievement by F. Giessibl in 1995 [30], it is worth to mention the works of Y. Sugimoto and coworkers, where they

chemically identified surface atoms [31], and L. Gross and coworkers, who were able to resolve the chemical structure of molecules by using carbon monoxide terminated tips [32]. Another field in expansion is the combination of AFM with other techniques to simultaneously gain different information of the sample under study. Some examples of these combinations are SPMs + Electron Microscopy/Focused Ion Beam (FIB) [33], AFM + light optics (such as Raman spectroscopy, Fluorescence Microscopy) [34], Tip Enhanced Raman Spectroscopy (TERS) [35, 36] or AFM + Total Internal Reflection Fluorescence Microscopy (TIRFM) [37]. This last example, AFM + TIRFM is shown more in detail in Chapter 2.

This chapter is divided in two parts. The first one describes the basic components and operation modes of AFM, whereas the second part deals with some advanced modes that have been used in the experiments performed along this PhD.

1.2 Basic concepts of Atomic Force Microscopy

In general terms, as it has been mentioned in the introduction, the working principle of an AFM relies on the detection of the interaction between a sharp tip acting as a probe and the sample of interest. This interaction can be originated by different sources and it also depends on the system under study, as it is shown later. First, the different common elements to any AFM setup are described and then the standard measuring modes are presented.

1.2.1 AFM components

Any AFM setup can be divided into three main parts, as shown in figure 1.6: mechanics, software and electronics.

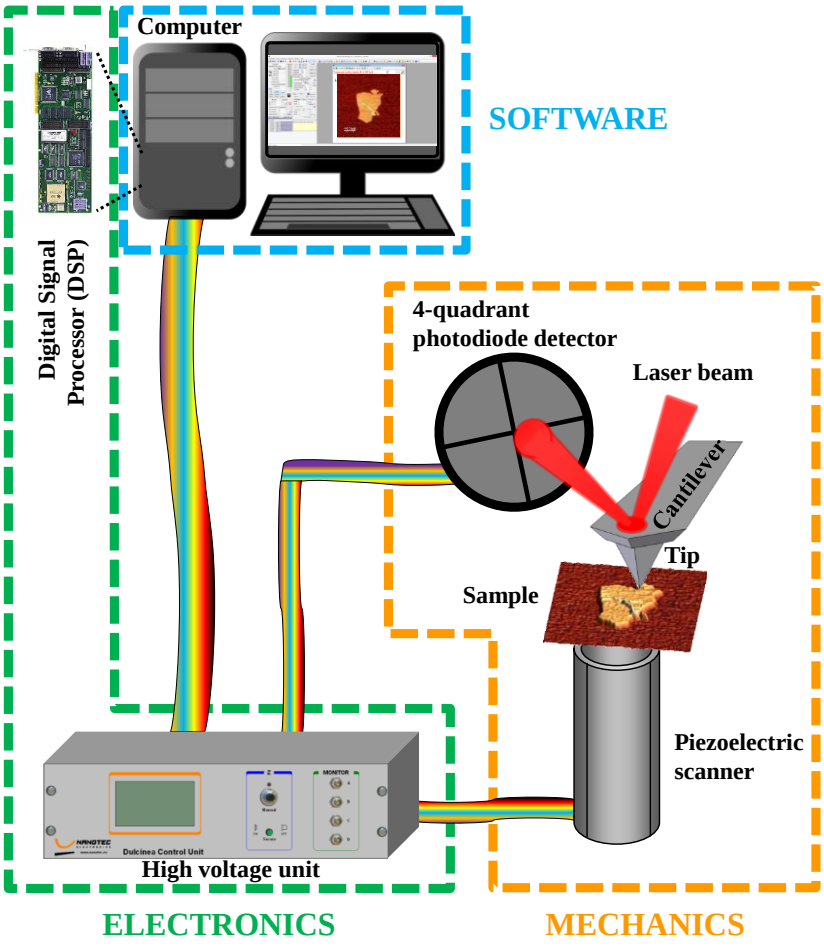

Figure 1.6 Main parts in an AFM setup.

Mechanics

It comprises all the opto-mechanical components responsible for the tip and sample movements as well as for the force detection.

- **Force sensor**

It is one of the critical parts of an AFM since its characteristics define the sensitivity of the measurements. The standard probes consist of a very sharp tip at the end of a microfabricated cantilever. Different probes can measure different properties of the sample so it is important to choose the right probe for each measurement. The probe also determines the force applied to the sample and the ultimate resolution of the system.

Most AFM probes are fabricated from silicon or silicon nitride using photolithographic techniques integrating tip and cantilever assemblies. The use of silicon fabrication techniques, commonly applied in microelectronics, is probable one of the most critical points for the success of atomic force microscopy. In this way, hundreds of tip and cantilever assemblies are produced on a single wafer, lowering their fabrication costs and allowing reliable and reproducible tips. AFM probes are consumables that need to be replaced when the tip wears out.

The fundamental reason to microfabricate cantilevers can be easily understood as follows: in order to avoid sample damage during scan, cantilevers with low stiffness are required. On the other hand, in order to achieve reasonable scan speeds, the cantilevers should also exhibit a high resonance frequency. The resonance frequency, ω, is given by equation:

$$\omega = \sqrt{\frac{k}{m}} \qquad (1.1)$$

where k is the stiffness and m the mass of the cantilever. Low k and high ω imply low m, that in turn implies low size and thus microfabrication.

For any cantilever, independently of its geometry, the working principle is the same, and for small deflections the force applied by the cantilever (F_N and F_L for normal and lateral (torsion) forces respectively) can be approximated by the Hooke's law. It can be summarized in equations (1.2) and (1.3).

$$F_N = k_N \Delta z \qquad (1.2) \qquad\qquad F_L = k_L \Delta x \qquad (1.3)$$

where the stiffness k_N and k_L are the normal and lateral spring constants of the cantilever ($k_N << k_L$). Normal forces act perpendicular to the cantilever plane producing a vertical deflection Δz. In a similar way, lateral forces act on the cantilever plane producing a Δx torsion. A precise determination of the spring constants values is necessary for quantitative force measurements as explained below.

Figure 1.7 shows some of the basic configurations of AFM probes. To facilitate its handling they come at the end of a millimeter sized chip (figure 1.7a). Apart from a sharp tip, AFM requires cantilevers with optimized spring constants. The spring constant of the cantilever depends on its shape, its dimensions and the material from which it is fabricated. In particular, the perpendicular stiffness of a rectangular cantilever can be readily estimated as:

$$k_N = \frac{E}{4} W \left(\frac{T}{L}\right)^3 \tag{1.4}$$

being E the elastic modulus, and W, T and L the Width, Thickness and Length of the cantilever. Most common shapes are rectangular (figure 1.7b) and triangular (figure 1.7c). There are as well more exotic geometries for advanced measurements. Cantilevers typically range from 40 to 200 μm in length, 15 to 40 μm in width, and 0.2 to 5 μm in thickness. New cantilevers to allow high speed imaging have appeared in the last years. They are characterized by their small dimensions (length and width typically an order of magnitude smaller than conventional cantilevers). AFM manufacturers offer microfabricated tips in different geometries where pyramidal (figure 1.7d) and conical are the most common ones.

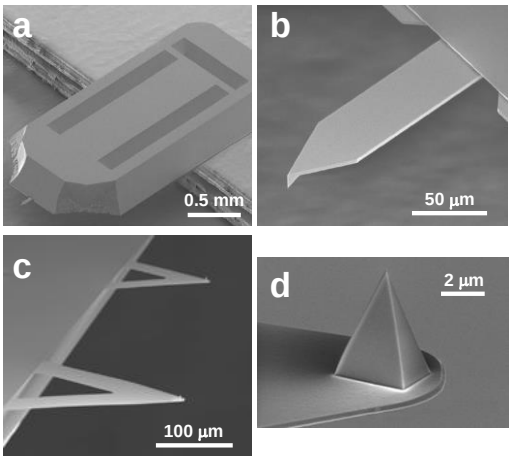

Figure 1.7 a) Typical cantilever chip. b) Rectangular cantilever. c) Triangular cantilevers. d) Pyramidal tip. Source: a) and b) www.nanoandmore.com c) and d) www.brukerafmprobes.com

The spring constants of the commonly used cantilevers range over several orders of magnitude, from ~ 10^{-2} to 10^{2} N/m. Their resonant frequency, an important parameter to consider when operating in dynamic modes, typically ranges from a few to hundreds of kHz. High resonant frequencies allow for non-contact AFM operation and faster responses. High speed cantilevers operate at MHz resonance frequencies, thus enabling very fast imaging.

A precise determination/calibration of the spring constants values is necessary for quantitative force measurements. Cantilevers manufacturers provide nominal values of k_N based on the geometry and the material of the cantilever, as explained above, but these values are typically very inaccurate. It is thus necessary to calibrate the spring constant value. There are different calibration techniques [38], though two of them are the most popular. The "thermal method" is based on the acquisition of the cantilever's thermal distribution spectrum (square of the fluctuations in amplitude as a function of frequency) and the use of the equipartition theorem [38-40]. In this way, the mean-square amplitude of the cantilever's thermal fluctuation in the vertical direction, $\langle z^2 \rangle$ follows equation (1.5):

$$\langle z^2 \rangle = \frac{k_B T}{k_N} \tag{1.5}$$

where k_B is Boltzmann's constant and T is the temperature of the cantilever. The other popular method, named "Sader method" after his inventor, John E. Sader, can be applied to rectangular cantilevers [41, 42]. It incorporates the viscosity and density of the medium in which the cantilever is immersed, along with experimentally determined values of the resonant frequency and quality factor, together with the cantilever length and width values. Thus it can be considered a "geometric" approach, although it does not need the cantilever thickness, which is the dimension more affected by uncertainty. The fundamental restrictions on the Sader method are that the amplitude of vibration must be small, the fluid must be incompressible, and the length of the beam must greatly exceed its nominal width [41]. Sader method leads to equation (1.6):

$$k_N = 0.1906 L Q (W 2\pi \nu_k)^2 \rho_f \Gamma_i(\nu_k) \tag{1.6}$$

where L and W are the cantilever length and width respectively, Q its quality factor, ν_k its resonant frequency, ρ_f the density of the fluid in which the cantilever is immersed and $\Gamma_i(\nu_k)$ the imaginary part of the hydrodynamic function. k_N value can be easily calculated online in the University of Melbourne webpage [43] or directly on some AFM softwares such as WSxM [44], just by entering the length and width (given by the manufacturer), the fundamental resonant frequency and the corresponding quality factor of the cantilever (determined by acquiring an amplitude *vs.* frequency curve for the cantilever). The Sader method has been used along this PhD to calibrate cantilever normal spring constants.

The lateral resolution of an AFM image is determined by several factors: the number of pixels during the acquisition of an image, piezo scanner specifications, quality of applied voltages, tip radius, etc. Tip radius of standard commercial probes ranges from ~ 2 to 15 nm. When imaging features smaller or with sizes similar to that of the tip radius, the most common artifact in AFM images arises from a phenomenon known as tip-sample dilation. As long as the tip is much sharper than the feature, the tip can follow its true edge profile. However, when the tip is wider than the feature, the image will be dominated by the shape of the tip. Figure 1.8 illustrates the tip-sample dilation artifact. Whereas in all the cases the

height of the feature will be properly measured, its apparent width will strongly depend on the tip radius.

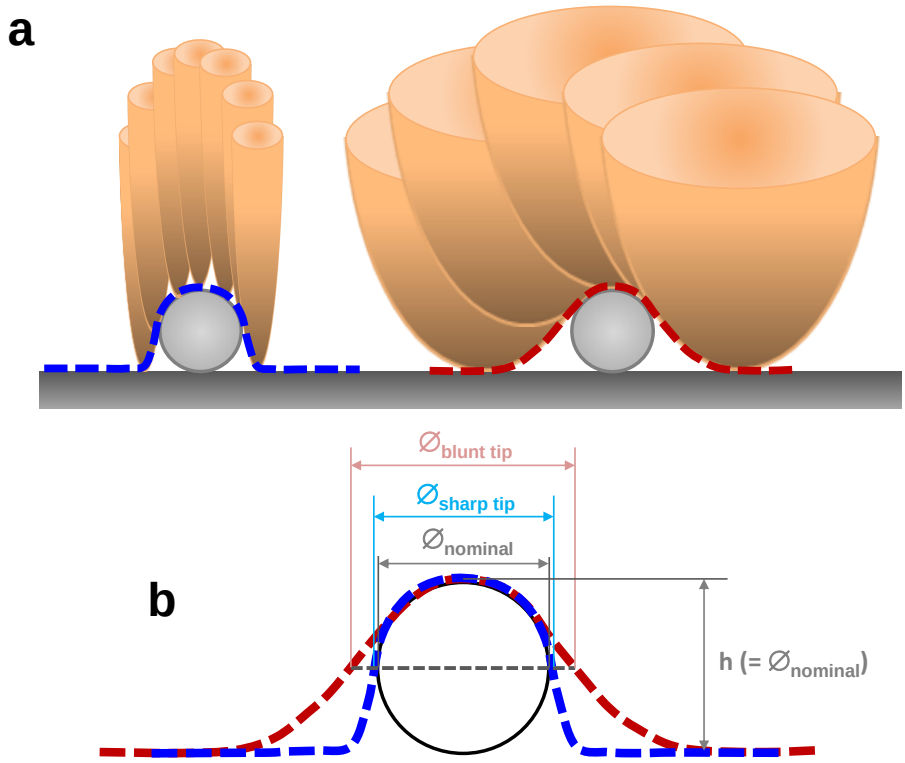

Figure 1.8 Tip-sample dilation. a) Representation of a nanoparticle visualized with a very sharp tip (left) and with a blunt tip (right). b) Comparison of the measured full width at half maximum.

Depending on the application, tips can present special coatings that enlarge their final tip radius, presenting nominal values of ~ 30 - 40 nm. For example, tips for magnetic force microscopy present a magnetic coating (typically from a hard magnetic alloy material) or tips for electrical applications present a metallized coating (typically gold or platinum).

Apart from the usual cantilever probes, there are other probes based on different geometries. Two relevant examples are tuning fork based probes and symmetrical length extension resonator based probes. Both of them are mainly used in ultrahigh vacuum AFM measurements.

Probes are consumables that represent an important market themselves. There is a lot of technical development behind probe fabrication, not only for improving their current performance but to open the AFM technique to new applications.

- **Deflection detection system: AFM head**

Once described the force detector, a way to detect the deflection of the cantilever is needed. Different techniques have been proposed: a scanning tunneling microscope tip placed on top of the cantilever [8], fiber-optic interferometers [45, 46], optical beam deflection [47], capacitive [48], piezoresistive [49] or piezoelectric [50] detection. Among all the different possibilities, the optical beam deflection (OBD) method is predominant, due to its simplicity, low noise, its reliability and its ability to be applied to a variety of cantilever sensors [51]. OBD readout uses a focused laser beam to measure the deflection of the cantilever tip. The laser beam is reflected from the cantilever towards a photodiode detector. When the cantilever is deflected due to tip-sample interactions, there is a change of the reflected laser beam angle, producing a shift in the laser spot position measured on the photodiode. The ratio of the path length between the cantilever and the detector to the length of the cantilever itself produces a mechanical amplification. As a result, the system can detect sub-Å vertical movement of the cantilever [51]. The AFM setup used in this PhD employs OBD. The assembly comprising the laser source, the cantilever and the photodiode detector, together with the positioning systems to align the laser beam on the cantilever and the reflected beam on the photodiode, is named the AFM head along this PhD. Figure 1.9 shows diagrams and pictures of the head mainly used in this PhD. In particular, figure 1.9c shows the laser beam path and the main components in the head. I carried out the design and assembly of this head, named *Lanza* head, during my period at Nanotec Electronica in collaboration with Julio Gomez-Herrero's lab. David Martinez-Martin performed tests and measurements optimizing its performance along his PhD thesis [52]. It was commercialized by Nanotec and several units were sold in such different places as Spain, Germany or the USA.

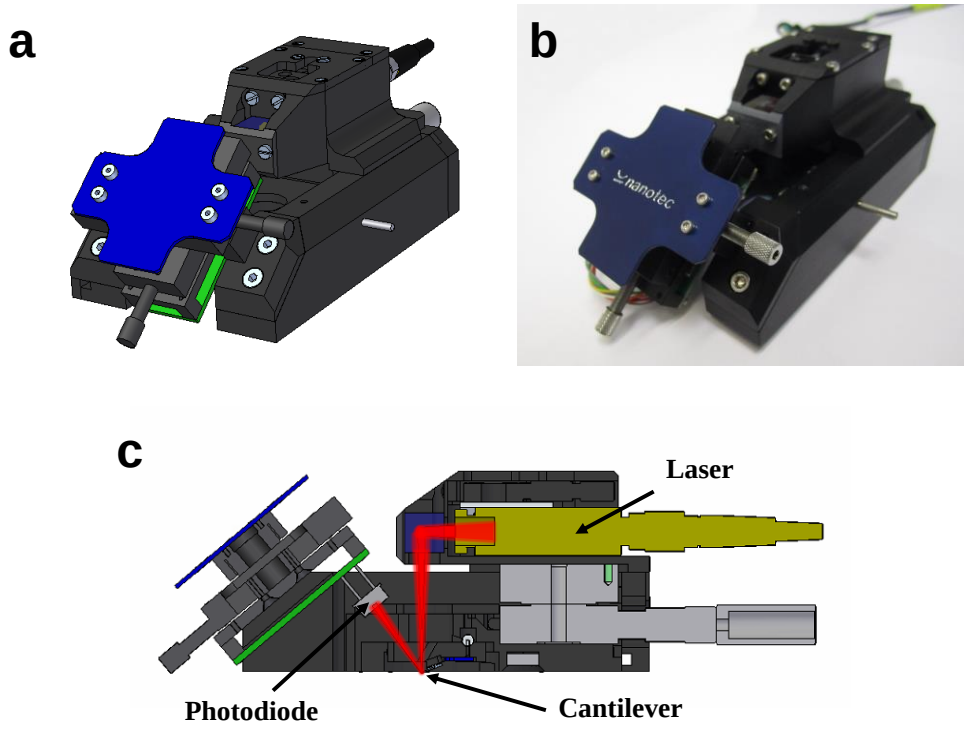

Figure 1.9 Force detection: AFM head. a) Computer-Aided Design (CAD) model of the *Lanza* AFM head mainly used in this PhD. b) Photograph of a real *Lanza* AFM head. c) Sectional view of the head showing its main parts and the laser beam path.

OBD allows for a simultaneous measurement of the vertical deflection (Normal force) and the torsion, i.e. lateral deflection (Lateral force) of the cantilever. The photodiode detector is divided into four quadrants; each of the quadrants generates a voltage proportional to the light intensity reaching it. By simple arithmetic both the Normal and Lateral forces can be measured as shown in figure 1.10.

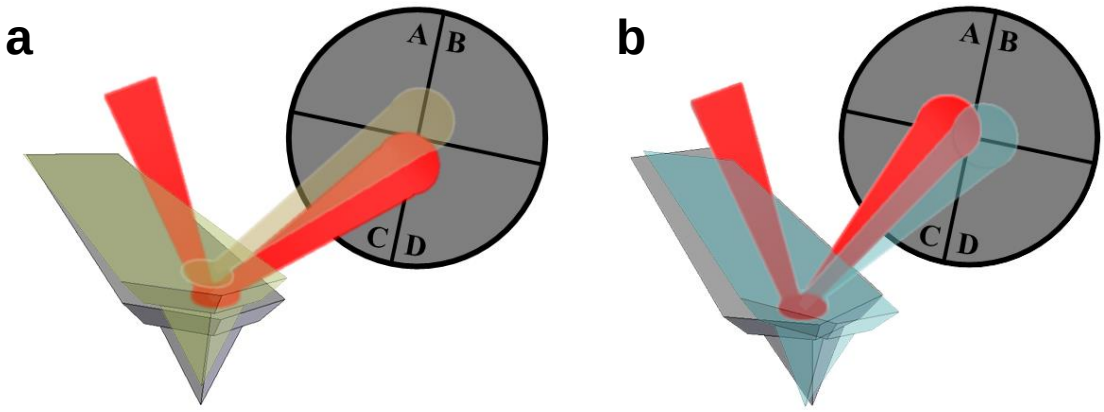

Figure 1.10 4-quadrant photodiode operation. a) Normal force detection. b) Lateral force detection.

OBD method main limitations include frequent laser and photodiode alignment and cantilevers with widths down to a few micrometers at least, to avoid the optical diffraction limit. The noise sources in OBD readout can be classified into three main groups: fundamental noise coming from the actual motion of the cantilever (Brownian thermal motion causes spontaneous oscillations in microcantilevers), noise coming from the measurement principle (laser and photodiode noise), and noise coming from the readout electronics (mainly voltage and current noise of the amplifier) [51]. The most relevant noise sources in the OBD method are the laser and the photodiode. Laser noise in OBD comes from both fluctuations in the laser beam intensity and its spatial distribution, and from laser mode hopping [53]. In our setup this has been minimized by using a low noise, low coherence and reduced speckle laser source coupled to a single-mode fiber cable. Photodiode shot noise comes from statistical fluctuations in the number of photons emitted by the laser. This is usually the dominant noise and it sets the lower limit for the deflection noise [53].

- **Positioning and scanning: piezoelectric scanners**

One of the key points that allowed the success of scanning probe microscopies was the use and development of piezoelectric scanners. Piezoelectricity was discovered by Jacques and Pierre Curie in 1880 and it is the standard way to transduce an electrical signal into a mechanical one. It is the electric charge that accumulates in certain solid materials in response to an applied mechanical stress. The direct piezoelectric effect can be seen as the internal generation of electrical charge resulting from an applied mechanical force [54]. It is

a reversible process; materials exhibiting the direct piezoelectric effect also exhibit the reverse piezoelectric effect, the internal generation of a mechanical strain resulting from an applied electrical field. This is the base of the scanners used in SPM. The core of a SPM scanner is a ceramic piezoelectric material that expands and contracts when voltages are applied. Controlled voltages lead to very precise movements, in the order of pm for a few mV and up to microns for voltages of the order of a hundred V. This behavior turns piezoelectric scanners into extremely fine positioning stages to move the probe over the sample (or the sample under the probe). Piezoelectric scanners are commonly known as *piezos*. Piezoelectric material used in piezos is usually of the $Pb(Zr_xTi_{1-x})O_3$ type, also known as PZT. One of the most important contributions of SPM was the introduction of a technology based on piezoelectrics to induce motion over millimeter range with sub-nanometer accuracy.

There are different geometries of piezos. Some of the most popular are: tripods, consisting in three orthogonal piezo bars, as in the first STM setup [5]; tubes, where the scanner is a hollow tube with different electrodes [55]; or flexure stages, which use separate piezos for each axis, and couples them through a flexure mechanism. This configuration has proven to be very suitable for high speed imaging [25]. Many SPMs use variations of the simple tube design. The basic configuration consists of electrodes attached to the outside of the tube, segmenting it electrically into vertical quarters, for +X, +Y, -X, and -Y travel. An electrode is also attached to the inner side of the tube to provide motion in the Z direction. When alternating voltages are applied to opposite electrodes, for example +X and –X, the induced strain of the tube causes it to bend back and forth in the X direction (in reality the end of the tube describes a circumference arc). Voltages applied to the Z electrode cause the scanner to extend or contract vertically. Figure 1.11 illustrates the basic piezo tube scanner movements.

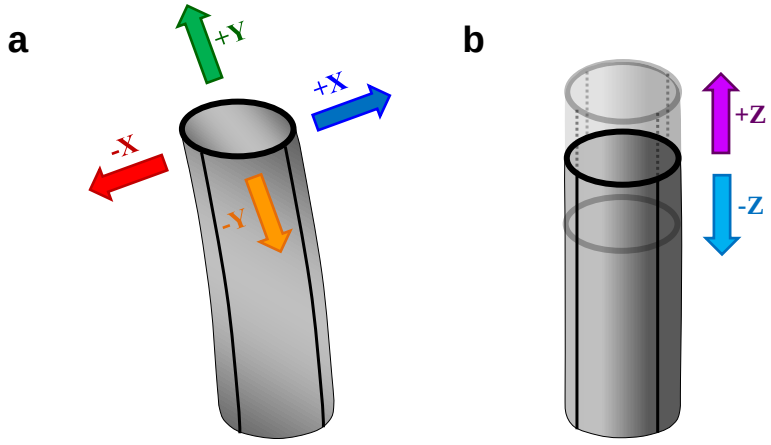

Figure 1.11 Piezoelectric scanners. a) XY motion for scanning and positioning. b) Z motion.

As a first approximation, the strain in a piezoelectric scanner varies linearly with the applied voltage. This allows for a direct conversion of the applied V into nm of displacement, after a calibration process using gratings with well-known distances. But in practice, the behavior of piezoelectric scanners is not so simple; the relationship between strain and electric field diverges from ideal linear behavior. There are different nonlinearities that need to be accounted for to have a reliable and precise calibration of the scanner. The most common ones are: intrinsic nonlinearity of the piezoelectric material, hysteresis (history memory that results in lagging in a line displacement when going back and forth that line), creep (two different timescales of the dimensional changes in a piezoelectrical material when an abrupt change in voltage is applied), aging (variation of the strain coefficient of a piezoelectric material with time and use) or cross coupling (tendency of X-axis or Y-axis scanner movement to have a spurious Z-axis component). There are two ways of compensating the nonlinearity effects: one is by performing a pre-calibration of the nonlinearities and using smart software signals managing. In this case, scanners work in the so called open-loop configuration. The other is by adding external position sensors to each of the scanner axes. The signal readout from the sensor of each axis is compared to a signal that represents the intended scanner position along that axis. A feedback system applies voltages to the scanner in real time to drive it to the desired position. This is the so-called closed-loop configuration. It can achieve very precise displacements, but it can introduce additional noise to the displacements due to the feedback actuation.

The piezoelectric systems used in most of the experiments here presented scan the sample under the probe. They are based on the combination of two piezo tubes: an inner tube acting as explained above plus an outer tube for extra Z displacements [56]. This design provides a high internal stiffness, thus minimizing the influence of external perturbations on the tip-sample stability, and low thermal drift. Two different scanners are used, one for large displacements (up to a maximum XY scanning range of ~ 70 x 70 μm^2 and 10 μm in the Z direction) and another for short displacements (10 x 10 μm^2 in XY and 4 μm in Z) enabling high resolution imaging. Although a system for the real-time correction of the piezo displacement could be integrated into the scanner design, both scanners were operated in an open loop configuration, with calibrations and software operation accounting for nonlinearities. Both scanners are designed as well as inertial positioners, allowing coarse tip-sample positioning by a slip-stick motion of the sample [57].

Piezoelectric scanners and AFM head are usually placed on a stage that includes a coarse tip-sample approach. In our case, the head is placed onto three micrometer screws, with the scanner below in the center of them. One of the micrometers is coupled to a motor for an automatic coarse approach.

Electronics

Electronics together with the control software running in a computer are the responsible for controlling and processing all the signals to drive a SPM. A low noise design for precise voltage and current measurement is required together with versatility to utilize various SPM techniques. There are multiple different architectures for SPM electronics. Among them, digital signal processor (DSP) control systems are widely used [58]. Here, the DSP-based electronics used in our setup is described. In this case, the term electronics refers to the control unit and the DSP. In our setup, the DSP is located inside the computer. Recent designs are based on Field Programmable Gate Array (FPGA) technology which either substitutes the DSP or combines with it.

- **High voltage unit**

The high voltage unit is the responsible for the high voltages (± 150 V in our setup) needed for the piezo movements. It houses power supplies and it also comprises lock-in amplifiers for the dynamic modes measurements. One of the main characteristics needed in a SPM high voltage unit is a low noise design, to enable the use of input/output very low voltage signals from/to the AFM head.

- **Digital Signal Processor (DSP)**

The DSP can be seen as the "brain" of a SPM. It is in charge of processing all the signals coming from the AFM hardware and to provide the low voltages (± 10 V in our setup) to be amplified by the high voltage unit. It comprises several Analog-to-Digital Converters (ADCs) as well as Digital-to-Analog Converters (DACs). Some of the main characteristics of a DSP for scanning probe microscopy are:

- Low noise design.

- Enough number of ADCs and DACs to provide flexibility enabling many configurations. ADCs are used for cantilever normal and lateral deflections, photodiode total intensity and outputs of the lock-in amplifiers (amplitude and phase of the cantilever oscillation in dynamic modes). There are usually as well some user-accessible (such as for a current input channel in conductivity measurements). DACs are employed for X, Y and Z low voltage signals (in this context low voltage means ± 10 V) and tip-sample Bias voltage. There are also user-configurable ones (such as for example to use as extra output voltage channels).

- Selectable gains and offsets.

- High sampling rate and optimized communication protocols to provide a fast response.

- Large onboard memory to allow complex operations and the storage of data when acquiring at high acquisition rates.

The DSP is also in charge of the feedback loop during scanning. The piezoelectric scanner provides sub-nanometric precision to allow the tip to be close enough to the sample to detect the tip-sample interactions. Then, in a standard scanning mode, the electronics drive the scanner in a type of raster pattern. In initial SPMs, the scanner moved across the first line of the scan, and back. It then stepped in the perpendicular direction to the second scan line, moved across it and back, then to the third line, and so forth. The direction of the lines is commonly called the fast-scan direction and the perpendicular direction, in which the scanner steps from line to line, is called the slow-scan direction. Nowadays more sophisticated scan patters based on this initial one are used, to improve the general scanner performance. While the scanner is moving across a scan line, the image data are sampled digitally at equally spaced intervals. The feedback loop is the responsible of keeping the tip-sample interaction constant during scanning by adjusting the piezo Z position, thus avoiding tip-sample crashes. The feedback loop uses the probed magnitude (that depends on the operation mode, typically cantilever deflection for contact modes and cantilever amplitude for dynamic modes) as an input; the output controls the distance along the Z axis between tip and sample. When the sample is scanned across the XY plane, sample topography variations change the magnitude used for feedback. The feedback loop then adjusts the Z height so that the probed magnitude is restored to a user-defined value (called Setpoint). The difference between the actual value of the probed magnitude and the Setpoint, called the error signal, is applied as feedback to the input of the system, thus adjusting the tip-sample distance continuously during scanning such that the probed magnitude remains approximately constant at the Setpoint value.

Many SPM systems use a Proportional-Integral (PI) feedback control [58] (a simplified version of the commonly used Proportional-Integral-Derivative (PID) control loop mechanism [59]). PI refers to the two terms operating on the error signal. If u(t) is the control signal sent to the system, y(t) is the measured output, SP is the desired output (Setpoint) and e(t) is the error signal e(t) = SP - y(t), then a PI controller has the form of equation (1.7)

$$u(t) = P\,e(t) + I \int e(t)dt \qquad (1.7)$$

The desired control loop dynamic is obtained by adjusting the two parameters P and I, commonly named feedback gains or feedback parameters.

In this PhD, a controller comprising a Dulcinea Control Unit with a M6701 Texas instruments DSP, from Nanotec Electronica, has been used. Figure 1.12 shows pictures of these two elements.

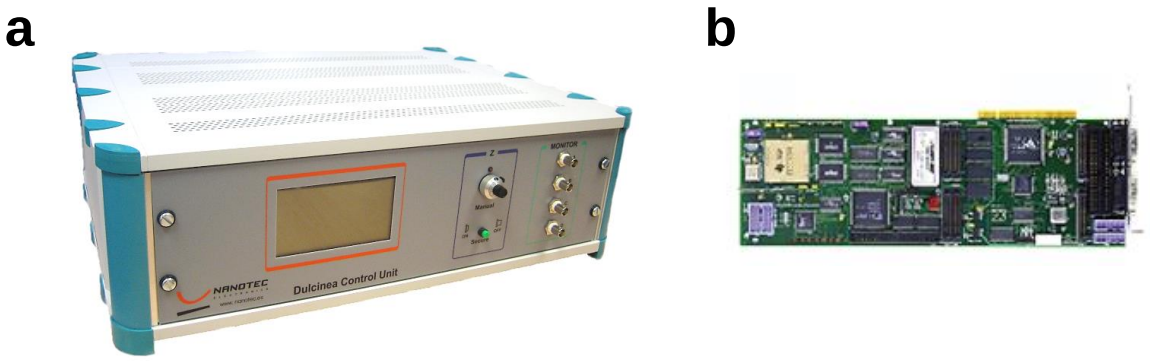

Figure 1.12 Electronics. a) Dulcinea control unit. b) Digital Signal Processor M6701.

Software

Control software is a key element in a SPM system. The combination of well-developed software with flexible electronics allows for multiple measuring modes and acquisition options. Each SPM manufacturer provides its own program.

SPM software can be typically divided into three different parts: Acquisition, Data process and Lithography.

- **Acquisition**

This is the most important part of the software. It is the responsible for the microscope control and new data acquisition, covering a wide range of measuring modes and different spectroscopy options.

- **Data process**

Once data are taken, within this part of the software extensive analysis can be performed. Typical SPM data are curves, images and movies. Apart from manufacturer's programs, there are multiple other programs (some of them freeware and other commercially available) devoted to SPM data visualization and analysis. Some of the most well-known are WSxM [44, 60, 61], Gwyddion [62] or SPIP^{TM} [63]. Any SPM program provides a number of data processing functions, including all the standard statistical characterization (surface roughness, peak-to-peak (valley-to-valley) distance, mean height…), levelling, data correction, line profiling, filtering of various kinds, 3D rendering or grain analysis functions. Some of them can contain as well a number of specific, uncommon or experimental data processing methods.

- **Lithography**

It allows performing modifications to the surface, using the tip as a *pen*. In a wider point of view, lithography allows designing an experiment by commanding the path for the tip and what actions to take at any moment along this path. Lithography methods can be designed and tested at any moment but at some point this part of the software interacts with the acquisition part. Lithography commands are generally written in a script language that is executed within the DSP in real time to perform the experiment.

In this PhD WSxM software has been used [44, 60, 61]. WSxM is a free software devoted to the control of SPM systems and processing of images and data acquired with such microscopes. It was initially created at the New Microscopies Lab, in the Universidad Autónoma de Madrid (UAM). Then it continued growing at Nanotec Electronica S.L. Now it is maintained and developed by WSxM solutions [61]. Figure 1.13 shows the cover of the WSxM software and a screen capture of the acquisition part.

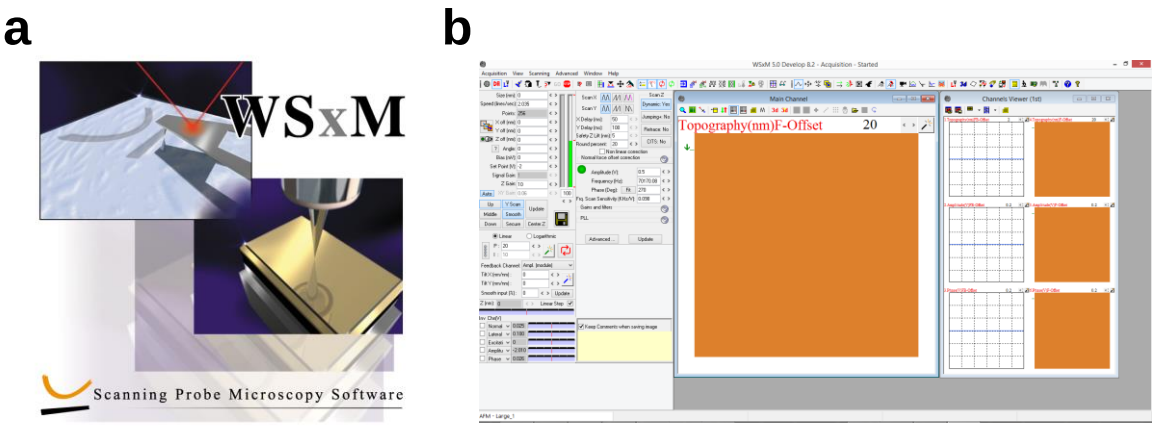

Figure 1.13 WSxM software. a) Cover. b) Main acquisition window.

1.2.2 Standard operation modes

As mentioned early, an atomic force microscope probes the interaction force between a tip and a sample. Several forces typically contribute to the deflection of an AFM cantilever [64]: long-range forces such as magnetic and electrostatic, interatomic and intermolecular van der Waals force and chemical, friction, deformations, meniscus… forces. Figure 1.14 shows the most relevant forces acting in an AFM according to the tip-sample distance.

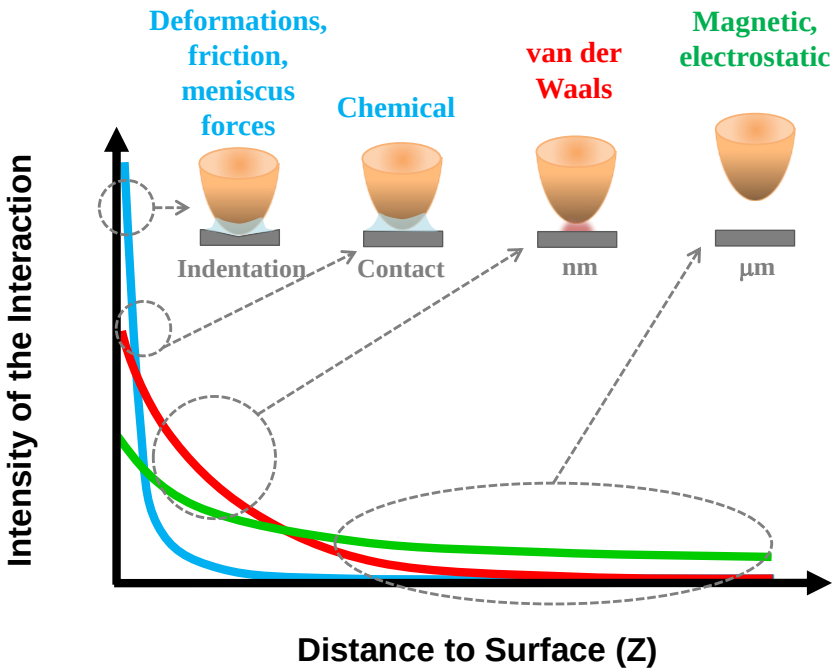

Figure 1.14 Diagram of the different tip-sample interactions.

By definition, a topography image in SPM is a z = f(x,y) where a given magnitude/s is/are kept constant by some kind of feedback/s. But as seen in figure 1.14, for the case of AFM there is a mix of interactions that affect the deflection of the cantilever. In many cases, there is one interaction that is much more relevant than the others, hence the topography can be then approximately considered as the result of a raster image where this interaction is kept constant. However, this is just and approximation and in general SPM topographies are ill-defined for most of the cases in the sense that several interactions contribute to the formation of the image. Consequently, different acquisition modes can yield different topography images and in some pathological cases the differences can be highly noticeable. In general, apart from the topography of the sample, an AFM allows measuring a variety of different properties such as friction [65], adhesion [66-68], electrostatic [69, 70], surface contact potential difference [71], conductivity [72], magnetic [73], dissipation [74, 75],

nanoindentations [66, 68, 76], etc. The dependence of the tip-sample interaction as a function of the distance can be seen in Figure 1.15.

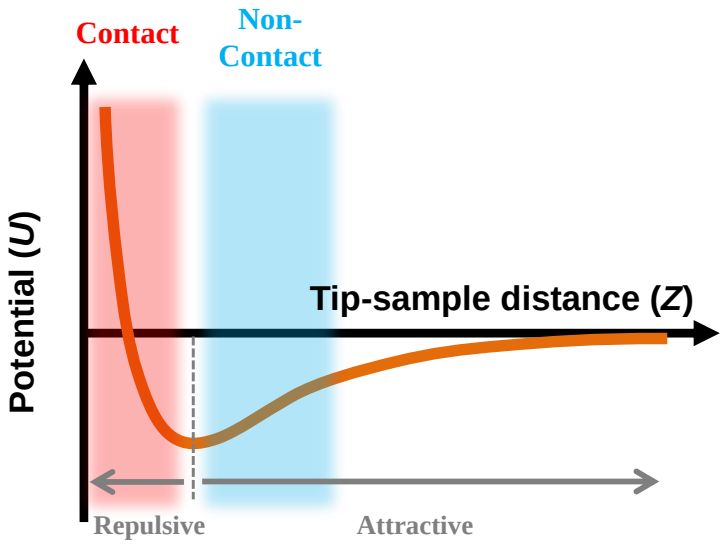

Figure 1.15 Diagram of the tip-sample interaction potential as a function of the distance.

For example, the type of curves as the one in figure 1.15 shows two different regimes: attractive and repulsive. These two regimes are defined by the sign of the force. The attractive regime corresponds to negative forces while the repulsive regime to positive forces. Since F = - dU/dZ, attractive and repulsive regimes correspond to the positions marked with arrows in figure 1.15. The force dominating the attractive regime is the most commonly associated with atomic force microscopy, the van der Waals force. Considering the tip-sample geometry, van der Waals force can be approximated by equation (1.8)

$$F_{vdW} = -\frac{AR}{6Z^2} \tag{1.8}$$

where R is the radius of the sphere that conforms the tip end, Z is the tip-sample distance and A is the Hamaker constant, with a value of the order of 10^{-19} J. The repulsive regime is dominated by Pauli repulsion due to overlapping of the electron orbitals of tip and sample.

Repulsive and attractive regimes basically define the most common AFM measuring modes: contact modes (including Jumping mode) and dynamic modes (non-contact and intermittent contact) respectively. Thus, the thumb rule is that and AFM topography represent a z = f(x,y) surface obtained by keeping constant the Pauli repulsion or the van der Waals forces.

- **Contact mode**

In Contact mode, as it name suggests, the tip is in mechanical contact with the sample surface. As the scanner traces the sample under the tip, the repulsive contact force causes the cantilever to bend. The AFM measures the cantilever deflection, which is proportional to the Normal force, thus following changes in topography. Friction maps can be obtained by measuring the Lateral force (see figure 1.10b). Figure 1.16 shows a schematic diagram of a line scan in Contact mode.

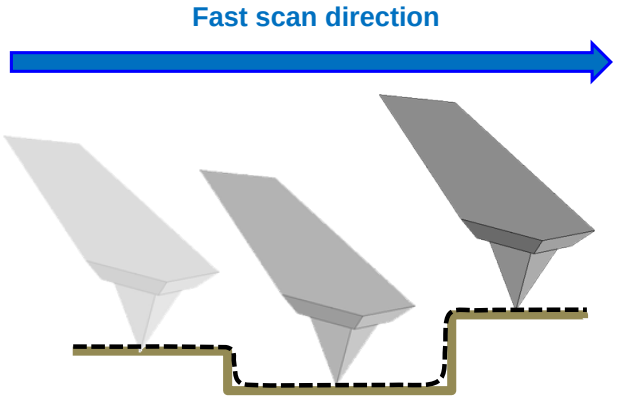

Figure 1.16 Schematic illustrating Contact mode.

Other forces are generally present during Contact mode operation: a capillary force exerted by the thin water layer often present in ambient conditions, adhesion forces which are a consequence of the attractive van der Waals interactions and the loading force exerted by the cantilever itself. The capillary force arises when water surrounds the tip, applying a strong attractive force (~ 10^{-8} N) that holds the tip in contact with the surface. The total force that the tip exerts on the sample is the sum of the capillary plus cantilever and tip interactions, and must be balanced by the repulsive force for Contact mode. To minimize the force exerted on the sample, low spring constant cantilevers are preferred. Depending on the cantilever, total forces on the sample can vary from hundreds of pN up to several μN.

There are two characteristics of Contact AFM in ambient conditions that have made it the option of choice for some particular measurements along this PhD. One is that Contact mode allows to avoid possible artifacts in height measurements compared to dynamic modes [77]. The other one is that Contact mode can achieve the “pseudo-atomic resolution” or “lattice resolution” topographic images, but it can as well achieve what it is called “true atomic resolution”. Although the mechanisms governing this high resolution are not completely understood, it is characterized by the possibility of distinguishing atomic

defects on the surface [78-80]. As an example, figure 1.17 shows atomic resolution on few-layer Boron Nitride. These two aspects have made Contact mode the best option to characterize layer height and structure of 2D materials.

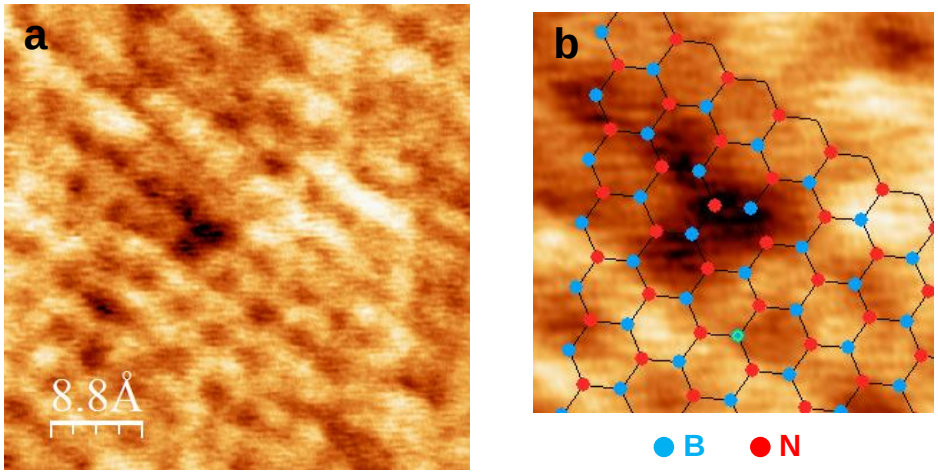

Figure 1.17 Contact mode atomic resolution on few-layer Boron Nitride (BN). a) 44x44 $Å^2$ topographic image showing a point defect. b) Zoom-in image of the point defect. The superimposed BN lattice reveals the defect as a 3B+N vacancy [81].

- **Dynamic modes**

Dynamic AFM methods are based on the changes observed in the dynamic properties of a vibrating tip that interacts with a surface. There exist two main branches for dynamic modes: *off resonance* and *in resonance* modes. While the former is used by a moderate number of researchers [82, 83] the second branch is the one commonly applied for the majority of AFM studies. In the forthcoming lines *in resonance* AFM modes are discussed in some detail.

Amplitude, Phase, Frequency and Dissipation of the oscillating cantilever are the main parameters used to probe tip-sample interactions. Dynamic modes offer the possibility of tuning the tip-sample interaction from hard intermittent contact, governed by repulsive forces, to soft non-contact in the attractive regime. Historically, they were developed to minimize tip-sample damage originated by friction forces present in Contact mode. Dynamic modes present different sensitive parameters and allow the possibility of measuring in different media (air, liquids or UHV), high resolution, etc. However, the interpretation of the images obtained in Dynamic modes often requires deep understanding of the dynamics of the cantilever introducing an additional level of complexity.

There are two major Dynamic AFM modes, Amplitude Modulation AFM (AM-AFM), typically also known as “tapping” mode [12] (although AM-AFM can be operated in a non-

contact regime, with no tapping the surface) and Frequency Modulation AFM (FM-AFM) [13]. In this PhD Drive Amplitude Modulation AFM (DAM-AFM) [19], a variation of FM-AFM, is also considered in some detail.

The most common dynamic operation mode in ambient conditions is AM-AFM. In AM-AFM the cantilever is excited at or near its resonance frequency. The oscillation amplitude is used as the feedback parameter to measure the topography of the sample surface. Additionally, material properties variations are mapped by recording the phase shift between the driving force and the tip oscillation, which is related to the effects of conservative (virial) and non-conservative (dissipation) forces within the tip-sample system. This section is focused on the main concepts of AM-AFM. Later in this chapter FM-AFM and DAM-AFM are also addressed. Dynamic modes operation has been profoundly studied; a precise and quantitative interpretation has been already performed elsewhere and is out of the scope of this chapter. Excellent reviews of dynamic modes were performed by Ricardo García and Rubén Pérez [84] and Franz Giessibl [85]. Figure 1.18 shows a schematic diagram of a line scan in a dynamic mode.

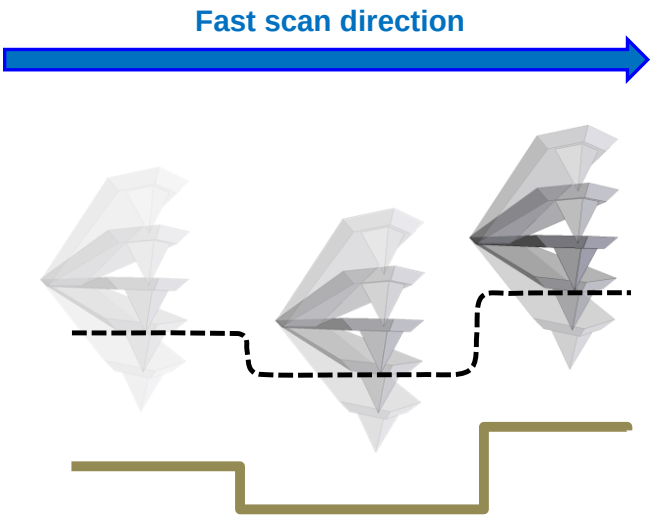

Figure 1.18 Schematic illustrating Dynamic modes (in particular a non-contact mode).

- Amplitude and Phase equations.

In a first approximation a cantilever-tip ensemble can be considered as a point-mass spring, then the tip motion can be approximately described by equation (1.9)

$$m\ddot{z} + \frac{m\omega_0}{Q}\dot{z} + kz = F_0 \cos(\omega t) + F_{ts} \qquad (1.9)$$

where F_0 and ω are the amplitude and angular frequency of the driving force, Q, ω_0 and k are the quality factor, angular resonance frequency and spring constant of the free cantilever. F_{ts} accounts for the tip-sample interaction.

The most relevant interaction forces in absence of external fields are the van der Waals force, short-range repulsive forces, adhesion and capillarity. Several approximations have to be done to take them into account in equation (1.9) (see [84] and references therein). In the absence of tip-sample interaction forces (F_{ts} = 0), the system can be described as a forced harmonic oscillator with damping. Its solution can be written as

$$z(t) = Be^{-\alpha t}\cos(\omega_r t + \beta) + A(\omega)\cos(\omega t - \phi) \tag{1.10}$$

This solution has a transient and a steady term. After a time $2Q/\omega_0$ the transient term will be reduced by a factor 1/e; from then on the motion of the cantilever will be dominated by the steady term. This steady term is a sinusoidal function with a phase lag with respect to the driving force. Thus, the Amplitude as a function of the frequency can be written as

$$A(\omega) = \frac{F_0/m}{\sqrt{(\omega_0^2-\omega^2)^2+\left(\frac{\omega\omega_0}{Q}\right)^2}} \tag{1.11}$$

and the Phase shift as

$$\phi = \arctan\left(\frac{\frac{\omega\omega_0}{Q}}{\omega_0^2-\omega^2}\right) \tag{1.12}$$

If there is no damping, the Amplitude takes the form:

$$A_0 = \frac{QF_0}{k} \tag{1.13}$$

The damping modifies the resonance frequency of the cantilever. Natural and free resonance frequencies follow the relation

$$\omega_r = \omega_0\sqrt{1-\frac{1}{2Q^2}} \tag{1.14}$$

From this it can be seen that if damping modifies the resonance frequency then it modifies the phase shift. Phase imaging is a common tool to map changes in material properties such as adhesion, viscoelasticity, Young's modulus, etc. [86, 87].

Assuming a parabolic tip-sample interaction potential, for small displacements with respect to the equilibrium position z_0 the tip-sample interaction can be treated as perturbation. An effective spring constant k_{ef} can be defined, which includes the tip-sample interaction.

$$k_{ef} = \left(k - \frac{dF_{ts}}{dz}\right)_{z_0} \tag{1.15}$$

The motion of the cantilever can then be expressed as a harmonic oscillator with an effective spring constant given by (1.15). In this way, equation (1.9) can be expressed in terms of a new frequency that, in a first approximation has the form

$$\omega = \omega_0 \left(1 - \frac{1}{2k}\frac{dF_{ts}}{dz}\right) \tag{1.16}$$

Equation (1.16) shows that the resonance frequency of a vibrating system is modified by the force gradient. The amplitude change in the oscillation can be as well referred to the force gradient through the expression

$$\Delta A \propto \frac{Q}{2k}\frac{dF_{ts}}{dz} \tag{1.17}$$

Equation (1.17) shows that the amplitude change is proportional to the Q factor and it is very sensitive to tip-sample distance changes. This is why it is used to track the surface topography. Figure 1.19 shows the typical cantilever dynamic response.

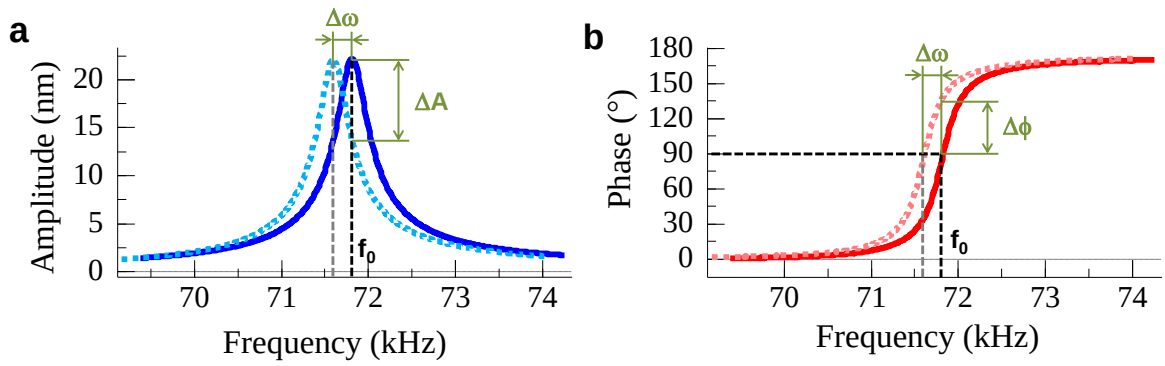

Figure 1.19 Cantilever dynamic response around the resonance without dissipation. a) Amplitude curve. b) Phase curve. In both a) and b) solid lines correspond to the free resonance curves while dotted lines correspond to the shift of the curves produced by an attractive force. Shifts in the relevant parameters are also indicated.

- **Jumping mode**

Jumping mode operation is based on measuring the cantilever deflection as in Contact mode, but in this case at each image point the feedback loop is first closed, to measure the topography of the sample, and then open, to evaluate the tip sample interaction by moving the tip away and towards the sample [16]. The sample is moved to the next image point being far from the tip. Since the tip literally jumps from one image point to another, this

mode is called Jumping mode (JM). In general, this acquisition scheme is known as Force-distance curve-based mode [88]. In JM the lateral displacement of tip and sample is done when they are not in contact, hence avoiding shear forces and the corresponding damage to tip and sample. From the data corresponding to the measured interaction, either a characteristic point is chosen, or some parameter is calculated by means of an appropriate algorithm. In this way, Adhesion and Stiffness maps can be acquired simultaneously to topography.

Initial JM was further improved by Ortega-Esteban *et al*. [17] by minimizing the maximum forces applied during scanning and conveniently identifying the tip-sample contact at each image point. While in the original version of JM the tip excursion for the forward and backward cycles was equal, in the improved version the cantilever deflection is monitored as the tip approaches the surface, stopping it if the deflection is greater than the Setpoint. Additionally, when working in liquids it uses a smart algorithm that removes the dragging force. After these improvements the mode was termed as Jumping mode plus (JM+). Figure 1.20 shows a schematic diagram on a line scan in Jumping mode plus.

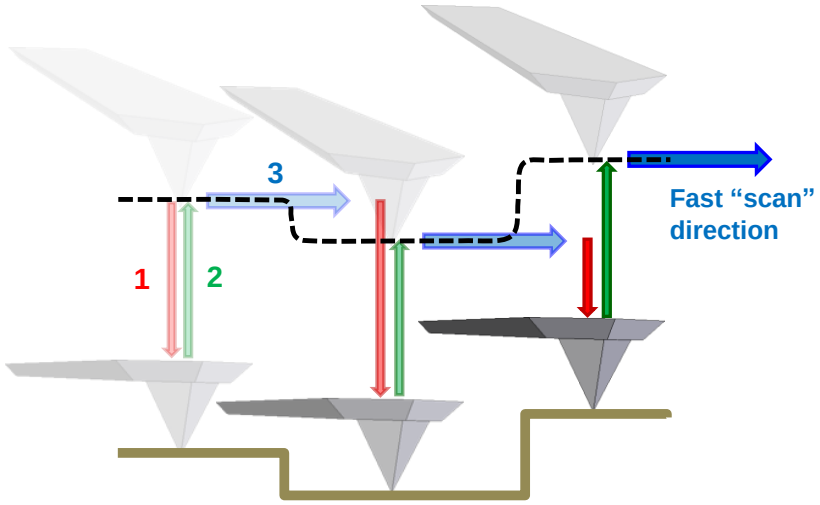

Figure 1.20 Schematic illustrating Jumping mode plus. 1: forward cycle, 2: backward cycle, 3: lateral displacement to the next point.

When comparing Jumping to Dynamic modes, JM offers low friction forces, a direct applied force control and a quite straightforward image interpretation. On the negative side, Jumping is slower than Dynamic modes. JM can also be combined with Dynamic modes, allowing measuring magnitudes such as phase or amplitude variation as a function of the tip-sample distance or to further reduce shear forces when imaging very weakly attached entities [89].

As a summary of the three basic modes already seen and to go deeper into the feedback schemes under each of them, figure 1.21 shows a cartoon with their operational configurations.

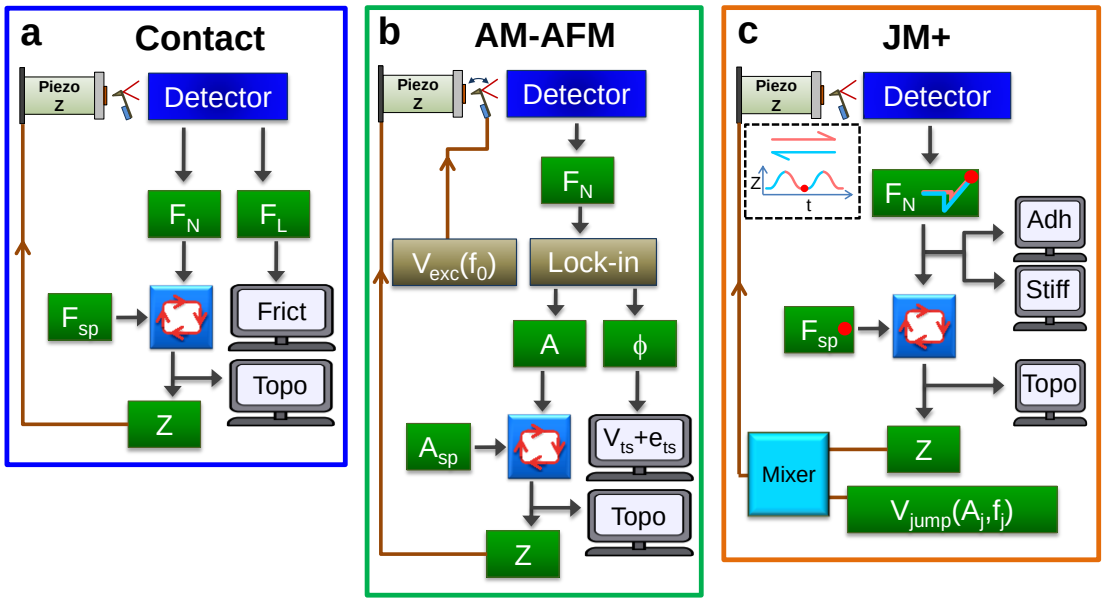

F_N	Normal force	V_{jump}	Z excursion
F_L	Lateral force	A_j	Amplitude of Z excursion
F_{sp}	Normal force set point	f_j	Frequency of Z excursion
A	Oscillation amplitude	**Frict**	Friction image
ϕ	Phase	V_{ts}	Conservative interactions image
A_{sp}	Oscillation amplitude set point	e_{ts}	Dissipation image
V_{exc}	Driving amplitude (to dither piezo)	**Adh**	Adhesion image
Lock-in	Lock-in amplifier	**Stiff**	Stiffness image
f_0	Cantilever resonance frequency	**Topo**	**Topography**

Figure 1.21 Operation diagrams of the three basic measuring modes. a) Contact mode: the tip is brought into mechanical contact with the surface and the cantilever deflection (Normal force) is directly used as the controlled input for the topography feedback. Friction maps are produced from the lateral force. b) AM-AFM: the cantilever is oscillated at its free resonance frequency (f_0) and the amplitude is used as the controlled input for the topography feedback. The phase produces a map of conservative (V_{ts}) + dissipative (e_{ts}) forces. (c) JM+: the cantilever is usually not oscillated, the system performs a quick Force *vs.* Distance curve (FZ) at each point of the scanned area, moving the tip laterally at the furthest tip sample distance minimizing lateral forces. The FZ is performed using a sinusoidal voltage wave (V_{jump}, with amplitude A_j and frequency f_j) that is applied to the piezoelectric scanner. Adhesion and Stiffness maps are produced from the FZ. The Normal force is directly used as the controlled input for the topography feedback.

- **Basic AFM spectroscopy: Force *versus* Distance curves**

A Force *versus* Distance (FZ) curve is a plot of the deflection of the cantilever as a function of the extension of the piezoelectric scanner [90]. When doing a FZ curve, the sample mounted on the piezoelectric scanner is moved up and down by applying voltages to the scanner, while the deflection of the cantilever is measured at the photodiode. These curves allow studying surface forces, but also provide valuable information on local material properties such us adhesion, stiffness, elasticity, Hamaker constant, charge densities, degrees of hydrophobicity… [91]. FZs can be employed as well with functionalized tips, i.e., tips covered with particular molecules that selectively adhere to other, in order to study specific forces [92]. FZs also allow performing single molecule force-clamp spectroscopy, a way to probe the dynamics of proteins by measuring their length and mechanical stability during each stage of folding [93].

FZs operation and applications have been profoundly studied. An excellent review of FZ curves by AFM was performed by H. J. Butt, B. Cappella and M. Kappl [94]. Figure 1.22 shows schematics on a FZ experiment and explains the behavior of the force along the approach and retract cycle.

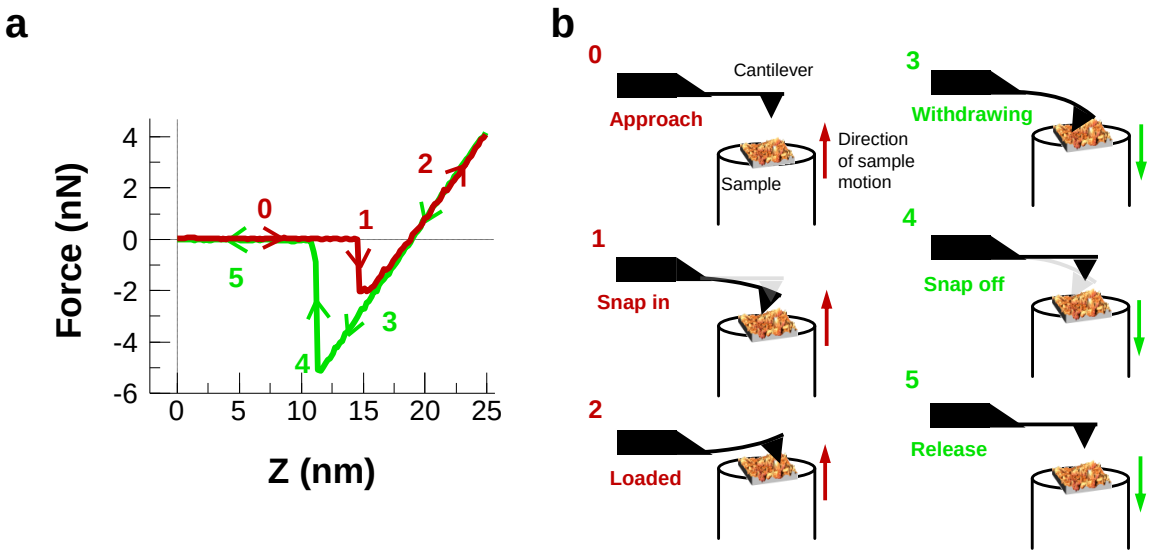

Figure 1.22 Experimental Force vs. distance (FZ) curves. a) Experimental FZ curve where the most relevant points are highlighted. b) Schematics illustrating a FZ approach/retract cycle: 0- Initially, the tip is assumed to be far enough from the sample so as not to be influenced by it. There is no change in the cantilever's deflection (Normal force). 1- When the tip is only a few nanometers from the sample, the gradient of the interaction becomes higher than the cantilever stiffness, an instability arises and the tip jumps into contact with the substrate (snap in point). 2, 3- After contact is made, a controlled loading and unloading of the tip against the sample is done. Since the maximum applied load can be controlled in a straightforward way, a quantitative determination of the importance of elastic and plastic processes can be performed. 4- When unloading, there is an extra force needed to separate tip and sample. This force is a consequence of the adhesive properties between the tip and the sample. Due to the adhesion forces, the tip does not detach the sample at the same Z position nor at the same force value at which it jumped into contact. The detaching point is called snap off point. The adhesion force can be calculated as the force difference between points 0 and 4 and the dissipated energy as the area of the FZ loop. 5- After the tip detaches the sample, there are no interactions, and the deflection keeps constant while retracting.

A simple extension of the applicability of FZ curves comes from the fact that different signals can be acquired simultaneously while moving the sample in the Z direction, to approach/retract it to/from the sample. In this way, when the cantilever is oscillating in a Dynamic mode, different spectroscopic curves can be acquired: along with the Normal force *vs.* distance curve Amplitude *vs.* distance or Phase *vs.* distance curves can be of interest. Figure 1.23 shows Normal force, Amplitude and Phase *vs.* Z curves.

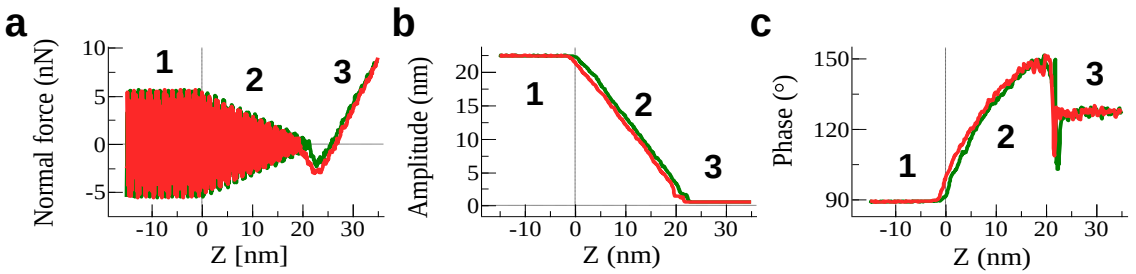

Figure 1.23 Simultaneous signals *vs.* distance of an oscillating cantilever. a) Force. b) Amplitude. c) Phase. Three different regimes can be observed: 1- Non interactive regime (slightly before the Z = 0). Normal force, Amplitude and Phase curves reflect a constant oscillation amplitude at resonance (Phase = 90°). 2- Tip-sample interaction starts and a linear decrease in the oscillation amplitude can be observed. This is known as the control regime: a Setpoint value can be placed on the Amplitude signal for Amplitude Modulation dynamic operation. 3- Tip jumps into contact and Normal force increases linearly with the distance. There is no Amplitude and the Phase keeps at a constant value.

1.3 Advanced AFM measurements

In this section, descriptions of the advanced modes used along this PhD are presented.

1.3.1 Dynamic modes

In the previous section Amplitude Modulation AFM mode is described. The common point among the different Dynamic modes is the oscillation excitation of the cantilever. The use of different signals as feedback channel to track the topography of a surface leads to the different Dynamic modes: AM-AFM uses the Amplitude. There is also a modified version of the AM-AFM mode in which, apart from the topography feedback on the Amplitude signal, there is an extra feedback loop on the Phase signal, by means of a Phase Lock Loop (PLL) [95]. A PLL varies the driving frequency of the cantilever so that it is always oscillating at resonance. The output of the PLL is the driving frequency shift. In this PhD this mode will be called Amplitude modulation + PLL mode (AM+PLL AFM). The advantage of using AM+PLL AFM compared to standard AM-AFM is that, whereas the Phase signal contains a mixture of information coming from conservative and non-conservative interactions, the driving frequency (output of the PLL) only contains conservative interactions [96]. In addition, since the cantilever is oscillating always at resonance, the system is very sensitive to amplitude changes from topography variations.

Frequency Modulation AFM (FM-AFM) uses the Frequency shift (directly related to the Force gradient) for the topography feedback and Drive Amplitude Modulation AFM (DAM-AFM) uses the amplitude of the oscillating driving force (related to the Dissipation). Both FM-AFM and DAM-AFM use three feedback loops; two nested loops for the topography and one additional loop working in parallel to obtain an extra channel of information. In the case of FM-AFM, tip-sample distance is adjusted to keep the Frequency shift constant generating a topography image. This topography image can be interpreted as a map of constant Force gradient. The amplitude of the driving force, which is controlled in the parallel feedback loop, represents the Dissipation. In the case of DAM-AFM, the first of the two nested feedback loops adjusts the driving force in order to maintain the oscillation amplitude constant. Now tip-sample distance is adjusted to keep the amplitude of the driving force constant. A PLL tracking the resonance frequency operates as parallel feedback loop. Topography images in DAM-AFM represent maps of constant Dissipation and the frequency shift controlled by the PLL provides a map of conservative interactions [19].

While AM-AFM is the most extended dynamic mode, it has limitations. For example, its application to the vacuum environment is difficult because of the long scanning times imposed by the high quality factor Q of the cantilevers in vacuum. FM-AFM and DAM-AFM overcome this drawback. FM-AFM is the most widespread mode for vacuum

environments and it has recently been extended to operate in liquids (where the Q factor is 4-5 orders of magnitude lower than in vacuum), with remarkable success [24, 97]. The main drawback of FM-AFM comes from the fact that the transition from noncontact to contact causes an instability in the feedback control [98]. This is particularly important for inhomogeneous surfaces in which, for example, the adhesion changes abruptly, or biological samples in liquid environments, which tend to contaminate the tip and introduce attractive interactions causing FM to become unstable [19]. Since the Dissipation generally grows monotonically as the tip approaches the sample surface [99], DAM-AFM overcomes in part the instability issue. Figure 1.24 shows Frequency shift and Dissipation *vs.* distance curves for a biological sample in liquid where the monotonic behavior of the Dissipation is observed independently of the tip state.

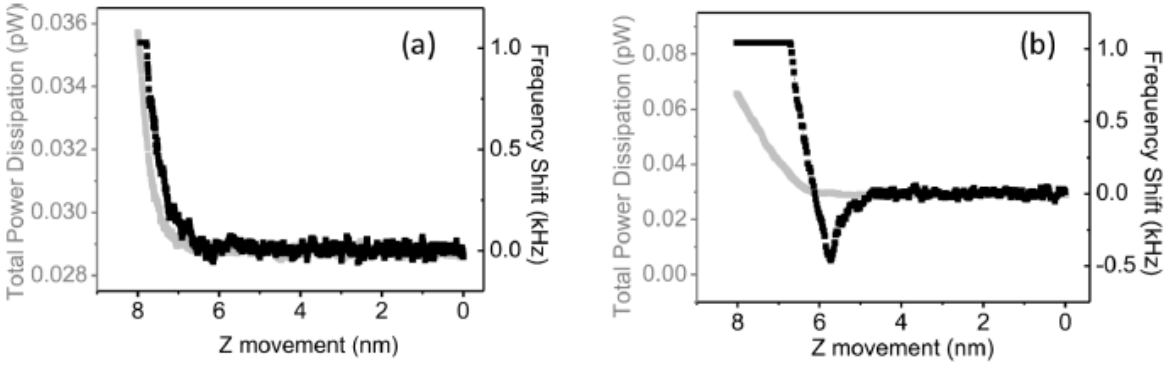

Figure 1.24 Frequency shift and Dissipation *vs.* distance with a biological sample in liquid for a) a fresh tip and b) a contaminated tip. Figure taken from reference [19].

The main disadvantage of both FM-AFM and DAM-AFM is the need of three different feedback loops (two nested loops for the topography and one additional loop working in parallel). This is why AM-AFM keeps being the preferential mode for the majority of the applications. To illustrate this, figure 1.25 shows a cartoon with the feedback schemes of the different Dynamic modes. Along this PhD, AM-AFM has been mainly used when working in air conditions, but when working in liquid environments both AM-AFM and DAM-AFM modes were employed (Chapter 3).

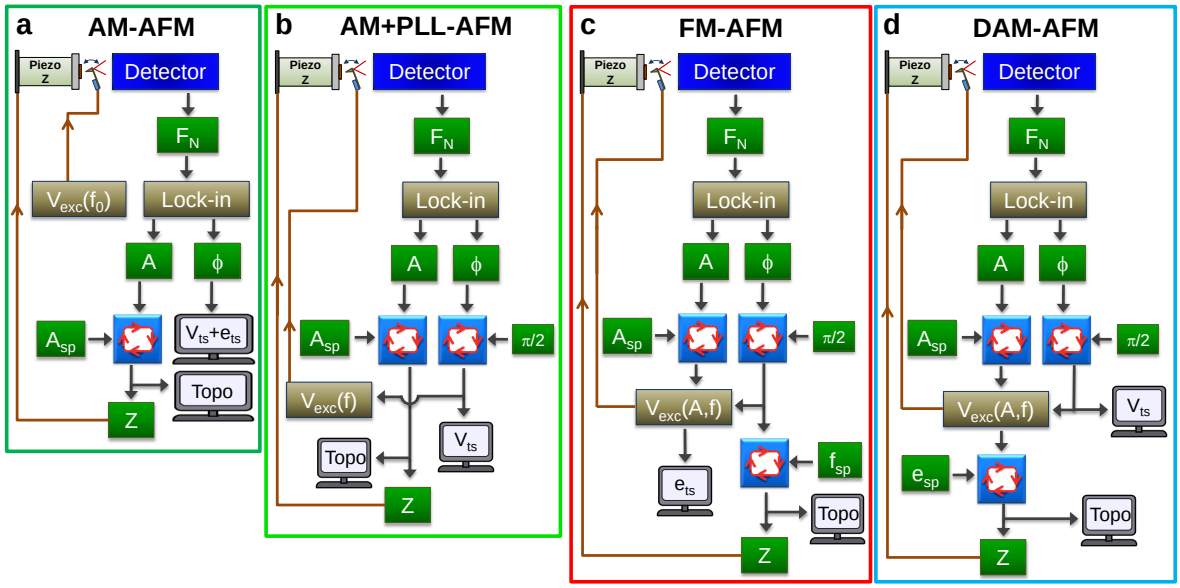

A	Oscillation amplitude	$\mathbf{A_{sp}}$	Oscillation amplitude set point
ϕ	Phase	$\mathbf{f_{SP}}$	Frequency set point
$\mathbf{V_{exc}}$	Driving amplitude (to dither piezo)	$\mathbf{e_{sp}}$	Dissipation set point
Lock-in	Lock-in amplifier	$\mathbf{V_{ts}}$	Conservative interactions image
$\mathbf{f_0}$	Cantilever resonance frequency	$\mathbf{e_{ts}}$	Dissipation image
f	Cantilever frequency	**Topo**	**Topography**

Figure 1.25 Dynamic modes operation diagrams (adapted from reference [19]).

1.3.2 Spectroscopy imaging (3D Modes)

Classical SPM images represent a magnitude G as a function of the geometrical position x, y: → G(x, y). 3D Modes images (also known as 2D plots) represent a magnitude G as a function of generalized variables λ_1, λ_2: → G(λ_1, λ_2), giving an "image" of the interaction [100, 101]. 3D Modes images are displayed in real time as any conventional image. 3D Modes can be acquired along one line of the surface, G = G(x, λ_1) or at one point on the surface, G = G(λ_1, λ_2). As in the case of usual geometric scan modes, several magnitudes can be simultaneously measured and displayed. Figure 1.26 depicts the 3D Modes operation principle and an example.

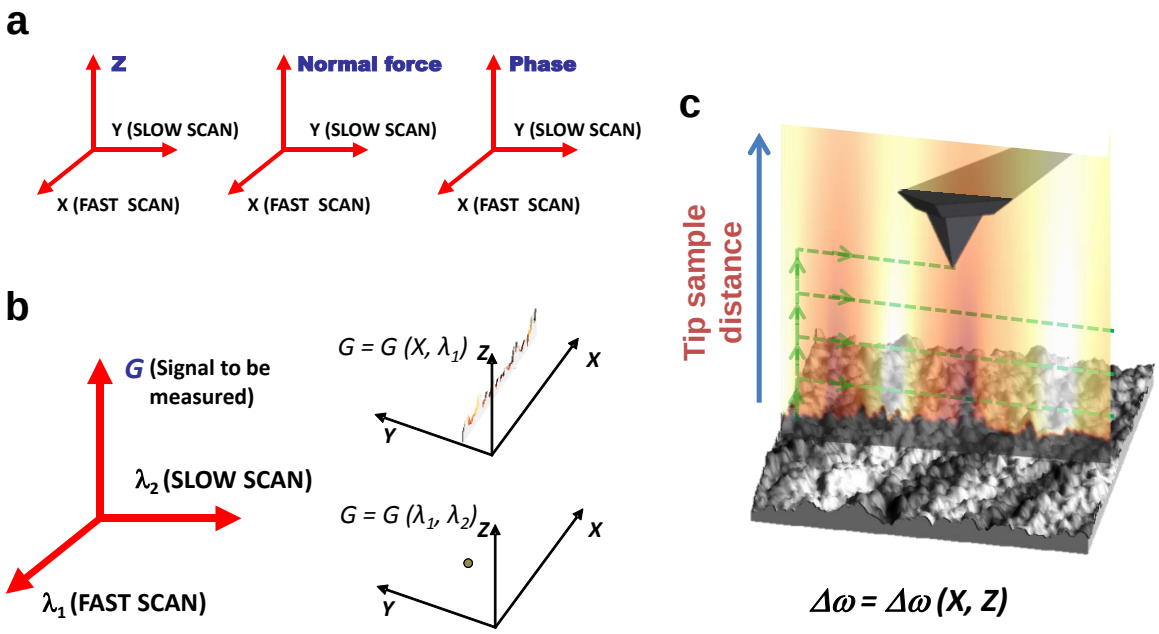

Figure 1.26 3D Modes operation. a) Some typical AFM images axes magnitudes. b) Left: generic 3D Modes images axes magnitudes. Right: generic representation of a 3D Modes acquisition along a line (top) and at a point (bottom). c) Scheme of a 3D Modes measurement of the magnetic interaction (through the frequency shift, Δω) along a line as a function of the tip-sample distance.

3D Modes have been employed in this PhD to study the magnetic interaction as a function of the tip-sample distance in different media (vacuum, air and liquid) while optimizing the acquisition of MFM data in liquids (Chapter 3).

1.3.3 Measurements in liquid environments

AFM is nowadays a powerful technique in biology [102], since it allows imaging and manipulating nanostructures in physiological conditions from cellular and membrane to single molecule level. This is an important feature, since biological specimens are normally fully functional only in liquid environments. Some of the most extended AFM applications in liquids are: 2-dimensional protein crystals and lipid membranes [103], molecular and cell biology [104-107], single proteins such as DNA [108], virus and protein nanocages [109], the study of molecular machines [110] or the mechanical properties of proteins by studying their folding and unfolding [93]. Depending on the application, different AFM measuring modes are typically used. Whereas for protein crystals and lipid membranes, that withstand lateral forces, Contact mode at the lowest force is usually applied, to study other biological systems which are prone to be detached from the substrate, Dynamic or Force-distance-based modes, such as Jumping, are preferred, since they minimize lateral forces and it is possible a better control on the applied load. A comparative study on the performance of the most common modes can be found in reference [111].

The main components of an AFM to be used in liquid environments comprise specific sample holder and cantilever holder. Sample holder has to ensure that no liquid will go to the piezoelectric scanner. This can be easily addressed by using sample holders in a pool fashion, although depending on the sample substrate this can even be skipped. The cantilever holder has to be adapted to allow a suitable operation in liquids under the different imaging modes. In particular, operation in Dynamic modes present some difficulties since the conventional setups used in air for oscillating the cantilever cannot be implemented in liquids. The most typical ways to oscillate the cantilever in liquid are the acoustic, the magnetic and the thermal methods [112]. The acoustic excitation consists of oscillating the cantilever by using a piezoelectric actuator attached to the cantilever holder. Although this method is very simple, the main drawback is the production of multiple peaks in the resonance curve, which unfortunately can hide the natural resonance frequency of the cantilever [113]. Still working at Nanotec, I participated in the development of a cantilever holder that removed the so-called *forest of peaks* by inserting a soft clay as damping material for the residual vibrations [114]. Later, we improved this design by introducing “acoustic barriers,” i.e., boundaries between two materials having significantly different acoustic impedances while cantilever vibration is excited [115]. This acoustic barriers combined with the soft clay damping allows to a good extend the suppression of spurious peaks. Figure 1.27 shows the main parts of the cantilever holder used along this PhD for measurements in liquid. This holder was named *Dolphin*. It was commercialized by Nanotec and several units were sold in such different places as Spain, Germany or the USA.

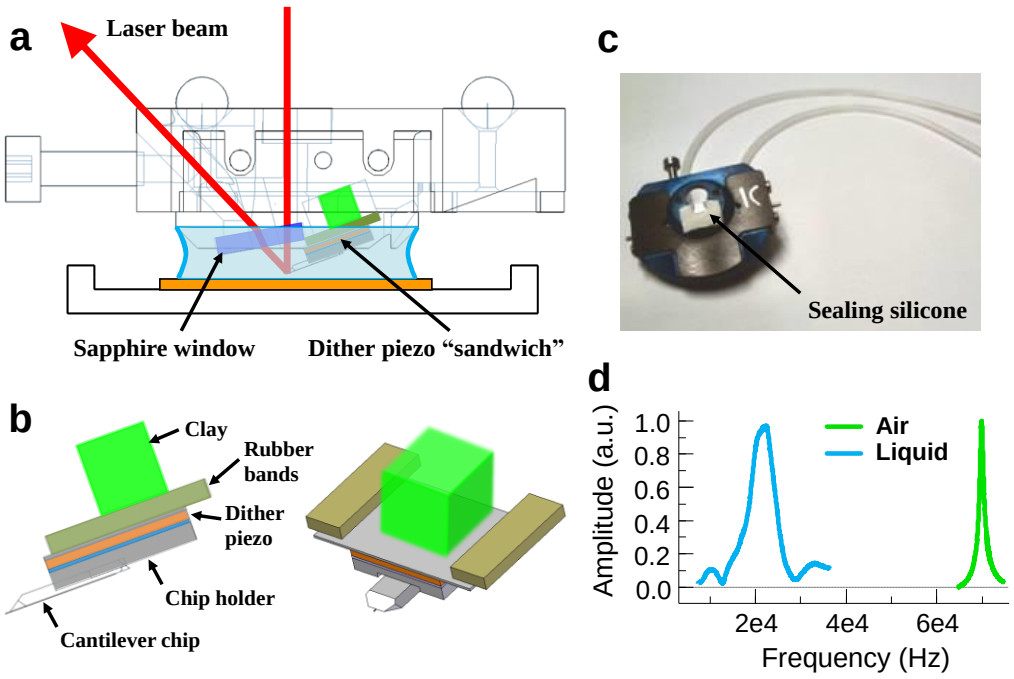

Figure 1.27 Measurements in liquid environments. a) Schematic diagram of the cantilever holder for liquids. b) Detail of the dither piezo "sandwich". Left: side view. Right: 3D view. As it can be seen in a), the top part of the "sandwich" is attached to the rest of the holder through the clay and the rubber bands, thus reducing residual vibrations. c) Photograph of a cantilever holder. d) Experimental cantilever resonance frequency curves in air (green) and liquid (blue).

As it can be seen in figure 1.27a, one of the main differences regarding a conventional cantilever holder for air measurements is the use of a window. This window avoids the instabilities characteristic of the surface of fluids and ensures a flat interface for the reflected laser beam, providing a stable spot on the photodiode. In figure 1.27b the different components of the oscillation generation in the holder can be seen, what is called "sandwich". Together with the damping clay, rubber bands are now placed in the interface with the holder body, creating in this way acoustic barriers that further suppress spurious peaks. Figure 1.27c shows a photograph of a *Dolphin* holder, were an elastic sealing silicone is placed over the whole "sandwich" to avoid liquid going into the dither piezo. Figure 1.27d shows resonance curves of an Olympus rectangular cantilever OMCL-RC800PSA (nominal parameters: length 100 μm, width 20 μm, spring constant 0.39 N/m and 69 kHz air resonance frequency). Both air and liquid environment curves present single resonances with no spurious peaks.

In this PhD different systems in liquid environments have been investigated in order to study their properties and to improve the performance of AFM in liquids. In this sense,

different high-sensitive force-detection methods have been employed to visualize the double helix of dsRNA under near-physiological conditions at high resolution (Chapter 3) and Magnetic Force Microscopy has been developed to allow magnetic measurements in liquid environments (Chapter 3).

1.3.4 Magnetic Force Microscopy (MFM)

Magnetic Force Microscopy (MFM) is a type of dynamic non-contact atomic force microscopy mode, where the magnetic interaction is probed using a magnetic tip [73]. If magnetic forces are the main contribution to the total interaction in an AFM setup, one generally speaks of Magnetic Force Microscopy.

Calling M_{tip} the tip magnetization and H_{sample} the magnetic field from the sample, the interaction energy between tip and sample, E(r), can be written as:

$$E(r) = -\mu_0 \int_{tip} \left[M_{tip}(r') H_{sample}(r + r') \right] d^3 r' \tag{1.18}$$

where μ_0 is the permeability constant. The force between tip and sample due to the magnetic interaction is given by

$$F(r) = -\mathrm{grad}[E(r)] \tag{1.19}$$

which can be measured directly through the changes in the cantilever deflection. These forces are very low (~ pN), therefore in order to increase measurement sensitivity, force gradient instead of force is measured by using Dynamic modes. From equation (1.16) it can be shown that the frequency shift on an oscillating cantilever due to an external force can be written as follows:

$$\Delta\omega = -\frac{\omega_0}{2k} \frac{dF_{ts}}{dz} \tag{1.20}$$

where $\Delta\omega$ is the frequency shift, ω_0 is the free resonance frequency, k is the cantilever spring constant, F_{ts} is the tip-sample interaction force and z is the direction of the interaction. Working in a Dynamic mode, this frequency shift can be directly measured using the PLL option, or indirectly, through the Phase channel. As it was shown in figure 1.14, where the different tip-sample interactions as a function of the distance where represented, in order to acquire only the magnetic interaction it is important to measure at an optimum tip-sample distance, one at which the other force contributions are negligible compared to the magnetic one. Although this distance will depend on the sample, the usual estimation is ~ 20 nm above the surface, where the magnetic contribution will be much stronger than the short range forces. The way to obtain magnetic images is to perform a first scan using a standard Dynamic mode obtaining the topography of the surface, and then a second scan, lifting the tip typically 30-60 nm above the surface to avoid the short range forces. Figure 1.28 shows the MFM operation principle. A much more detailed explanation of MFM can be found for example in Miriam Jaafar thesis [116].

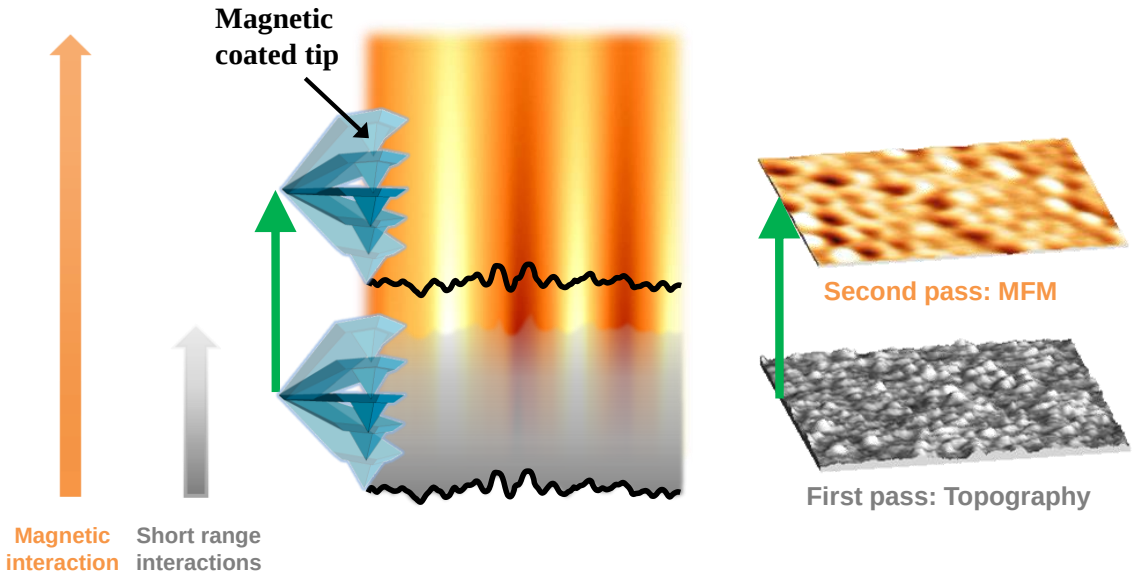

Figure 1.28 Magnetic Force Microscopy operation principle.

The most common tool to obtain the MFM images is called “Retrace mode”, also known as “Lift mode” in the particular case of raising the tip a given distance. This mode consists of making the tip scan twice above the same line. In this way, the magnetic images can be acquired “simultaneously” to the topography images. The first scan is made as usual, and the computer records the topography. Depending on the Retrace settings, there are different ways in which the tip will scan the sample in the retrace line. For MFM, the topography feedback is turned off and the second scan is done at constant height, using the topography recorded data. This way, the tip already knows how to scan the sample, it does not have to feel any strong interaction force from the topography and hence it can feel some other long-range forces, such as magnetic forces. However, in reality the piezo non- linearities prevent a perfect repetition of the topography resulting in small errors in the retrace image.

MFM has been widely used to study the magnetic properties at the nanoscale both in vacuum and ambient conditions [117], but not in liquid environments. In this PhD the acquisition of MFM data in liquids has been developed and optimized (Chapter 3). This technique will enable the study in liquid environments of magnetic properties of biological specimens that can dramatically change when studied far away from physiological conditions.

1.3.5 Conductive AFM (C-AFM)

The most basic way to perform electrical transport measurements is to place two electrodes on the material under study and apply a voltage ramp while measuring the current through the electrodes, obtaining a Current *versus* Voltage curve (IV curve). This is easy to carry out in the macroscale, but it becomes more difficult when the material under study is in the nanoscale, mainly due to the small dimensions of the objects under study and the difficulty in performing good electrical connections from nanometer-scale materials to the measuring devices from the macroworld. Conductive Atomic Force Microscopy (C-AFM) is used to probe the electrical properties of nano-objects at the nanoscale. It uses an AFM conductive tip as a second mobile electrode to locally measure the current when a Bias voltage is applied between tip and sample. Figure 1.29 shows a schematic view of the setup used for C-AFM applied to the study of the electrical properties of nano-objects located on an insulating substrate.

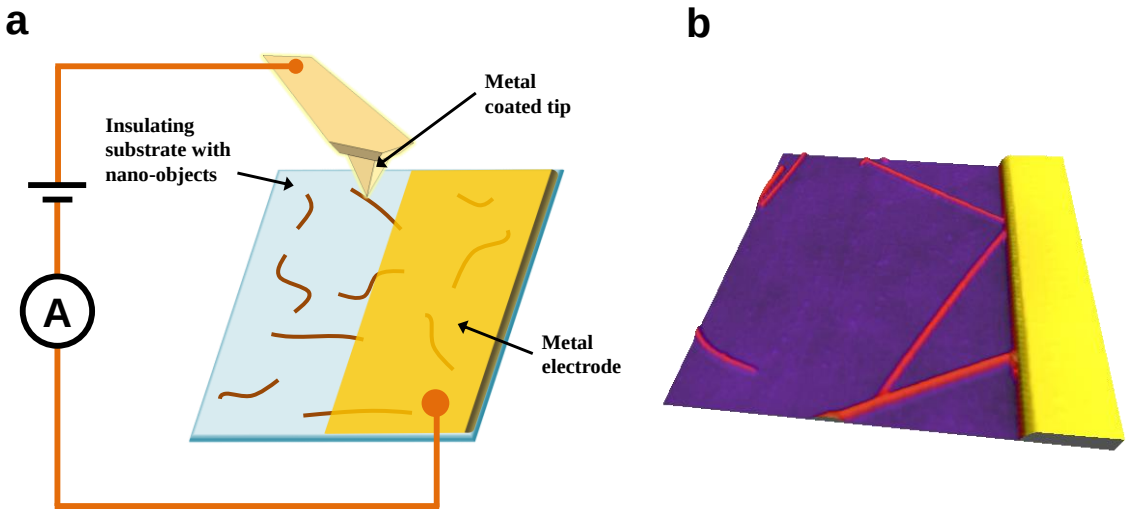

Figure 1.29 C-AFM setup. a) Sketch of a configuration where a metal electrode is placed on top of the nano-objects under study. Some of the nano-objects appear partially covered with the electrode. A Bias voltage is applied to a metallized AFM tip in order to study their electrical properties by measuring with an ammeter (A in the figure) the current flowing through the nano-objects. b) Experimental 3D rendered topographic image of a similar setup as explained in a). Three nano-objects can be seen coming out the metal electrode.

Depending on the nano-objects under study, different approaches are used to measure their electronic properties: the tip can be brought into Contact mode and, by applying a fixed Bias voltage between probe and sample, it maps the electronic properties of a surface [118]. Under this same imaging mode, a more sophisticated approach can be followed, performing

and IV curve on each pixel of the image [119], in a similar fashion as the STM does on Current Imaging Tunneling Spectroscopy (CITS) [120]. Although this approach in Contact mode can be also applied to study isolated molecules adsorbed on surfaces, as it was done by Dai *et al.* on multi-wall carbon nanotubes [72], in the cases of delicate samples that could not withstand continuous contact mode scanning, an approach in which samples are imaged in a Dynamic mode and IV measurements are performed in stable contact at selected points is preferred [121, 122]. In addition, scanning in contact with a metalized tip is very demanding, since the tip can be easily contaminated or peeled off, resulting in a high tip-sample contact resistance.

Along this PhD, the dynamic approach has been the common option of choice. C-AFM has been used to characterize the conducting properties of different systems: MMX chains obtained by drop casting, few-layer antimonene flakes obtained by micromechanical exfoliation and graphene areas modified by ultrahigh pressure (Chapter 4). Two new procedures to perform electrical contacts on nano-objects have been as well developed (Chapter 3). The first one is based on the deterministic transfer of exfoliated graphite flakes and the second one on the deposition and manipulation of gold nanowires. Both procedures are very useful combined with C-AFM. In addition, they are particularly relevant in the case of molecules with limited stability under standard lithographic conditions.

1.3.6 Kelvin Probe Microscopy (KPM)

Electrostatic Force Microscopy (EFM) is a type of dynamic non-contact atomic force microscopy where the electrostatic interaction is probed using a conductive tip [70, 123]. Some of the applications were EFM has been used comprise imaging charges [123], dopant properties of semiconductors [124], the adsorption of molecularly thin films of water on solid substrates [125], conducting properties of carbon nanotubes [126] or organic polymer solar cells [127]. In ultrahigh vacuum, extremely high resolution of the local charge distribution and surface potential has been obtained [128].

Kelvin Probe Force Microscopy (KPFM, or just Kelvin Probe Microscopy, KPM) measures the Contact Potential Difference (CPD) between the sample surface and the tip locally, from the force produced at the tip by an electrostatic interaction [71, 129]. KPM works by applying an adjustable bias voltage between a conducting tip and the sample. As in the case of EFM, KPM has been applied to the study of many different systems: electronic/electrical properties of metal/semiconductor surfaces [130] and semiconductor devices [131], electrical properties of organic materials/devices [127, 132, 133] or biological materials [134]. KPM has recently even been able to image the charge distribution within a single molecule by using carbon monoxide terminated tips in ultrahigh vacuum conditions [135]. Since the electrostatic interaction is quadratic in the voltage, the measured interaction has a static component and two other components varying with frequencies ω and 2ω. Using appropriate lock-in techniques and a feedback loop to adjust the tip-sample voltage, the local CPD can be determined with nanometer resolution.

In an AFM configuration, the force produced at the tip by an electrostatic potential U between tip and sample can be written as follows:

$$F = \frac{1}{2}\frac{\partial C}{\partial z}U^2 \tag{1.21}$$

where U is the potential difference between the tip and the sample surface and C is the capacitance of the probe-sample system. The derivative of the capacitance respect to distance, $\partial C/\partial z$, includes the geometrical and dielectric properties of the probe-sample system. This is important when interpreting the electrostatic images, since a local variation in the dielectric properties produces a change in the force. The force signal can also change due to a variation in the voltage difference U between tip and sample. This voltage is a DC voltage, but in the KPM method an AC voltage is added externally to be able to detect low force changes by using lock-in techniques. Considering this AC voltage, the potential between tip and sample can be written as $U=U_{dc}+U_{ac}\sin(\omega t)$. Then, the electrostatic force takes the form:

$$F = \frac{1}{2}\frac{\partial C}{\partial z}(U_{dc} + U_{ac}\sin(\omega t))^2 \tag{1.22}$$

Developing the squared term, the force can be separated into three different terms:

$$F = F_{dc} + F_{\omega}\sin(\omega t) + F_{2\omega}\sin(2\omega t) \quad (1.23)$$

where

$$F_{dc} = \frac{1}{2}\frac{\partial C}{\partial z}\left(U_{dc}^2 + \frac{1}{2}U_{ac}^2\right); \quad F_{\omega} = \frac{\partial C}{\partial z}U_{ac}U_{dc}; \quad F_{2\omega} = -\frac{1}{4}\frac{\partial C}{\partial z}U_{ac}^2 \quad (1.24)$$

The third term, $F_{2\omega}$, is proportional to the square of U_{ac} (which is fixed during the experiment) and to $\partial C/\partial z$, but does not depend on the constant potential U_{dc}. $\partial C/\partial z$ changes due to variations in the tip-sample distance owing to the sample topography and varies locally with the dielectric properties of the sample. Thus, the term $F_{2\omega}$ gives information on these dielectric properties. As in the case of $F_{2\omega}$, the term F_{ω} is proportional to $\partial C/\partial z$ and U_{ac}, but in this case it is also proportional to U_{dc}. As mentioned before, U_{ac} is fixed externally and it remains constant during the experiment. On the contrary, U_{dc} may vary locally due to different chemical potential values at the sample surface, making this voltage an interesting magnitude to be measured. F_{ω} and $F_{2\omega}$ can be measured separately by using lock-in techniques and different sample properties can be extracted.

To understand the KPM method, it can be assumed that the potential difference between tip and sample (U_{dc}) is composed by two terms, $U_{dc} = U_{extdc} - V_{CPD}$, where U_{extdc} is a constant potential applied externally, and V_{CPD} is the CPD between the sample surface and the tip. Then F_{ω} takes the form:

$$F_{\omega} = \frac{\partial C}{\partial z}U_{ac}U_{dc} = \frac{\partial C}{\partial z}U_{ac}(U_{extdc} - V_{CPD}) \quad (1.25)$$

The KPM method is based on an extra feedback loop that nullifies the term F_{ω}. To this end, it applies an adequate external potential, $U_{extdc} = V_{CDP}$, so $F_{\omega} = 0$. In this way, the output of the KPM feedback loop is a measurement of the CPD and, since it does not depend on $\partial C/\partial z$, it is independent of the dielectric properties of the sample and even of the tip-sample distance (however, if the tip is very far away, the gradient of the capacitance will be so small that F_{ω} will be almost zero independently of the value of the term in parenthesis). V_{CDP} is defined as [136]:

$$V_{CPD} = \frac{\phi_{tip} - \phi_{sample}}{-e} \quad (1.26)$$

where ϕ_{tip} and ϕ_{sample} are the work functions of the tip and the sample, and e is the elementary charge. Once the tip work function is calibrated (using a reference sample with a well-known work function value), by using KPM the sample work function can be mapped with nanometer resolution.

The conventional KPM method measures simultaneously the topography and the electrostatic signal. There are two main approaches to separate the electrostatic forces from

the van der Waals forces. Following Glatzel *et al*. nomenclature [137], whereas some authors use an Amplitude modulation (AM) scheme [131], others use a Frequency modulation (FM) one [128]. The main difference between the two methods is the sensitivity to the electrostatic force. In AM mode the electrostatic force is detected and in FM mode it is the force gradient. In the AM mode, topography and electrostatic signals are separated by using the first and second cantilever resonance frequencies. While the first resonance tracks the mechanical vibration, the second is used for the electric bias voltage, thus enhancing the sensitivity due to the amplification from the Q factor of this cantilever resonance. In the FM mode, crosstalk with topography is minimized by oscillating the bias voltage at low frequencies, in the range of 1-10 kHz. In this way, the resonance for the bias voltage is far away from the mechanical vibration of the cantilever.
The presence of the cantilever and the tip cone implies not only a loss of resolution but it may induce to incorrect values of the measured surface potential [138]. This can be minimized by using the FM mode [100], since by using the force gradient instead of the force, the effect of the tip cone is "differentiated away" for a certain range of tip-sample distances, where its dependence with the distance is not as strong as for the tip apex [100, 138], thus enhancing the resolution of the KPM data.

In this PhD, KPM has been used to study the work function variations of graphene modified under different ultrahigh pressures (Chapter 4), correlated with Raman spectroscopy data. An approach using AM+PLL AFM (see section 1.3.1) for the topography and FM mode with a bias voltage frequency of 7 kHz for the CPD has been employed. Figure 1.30 shows the operational configuration used for the KPM measurements in this PhD.

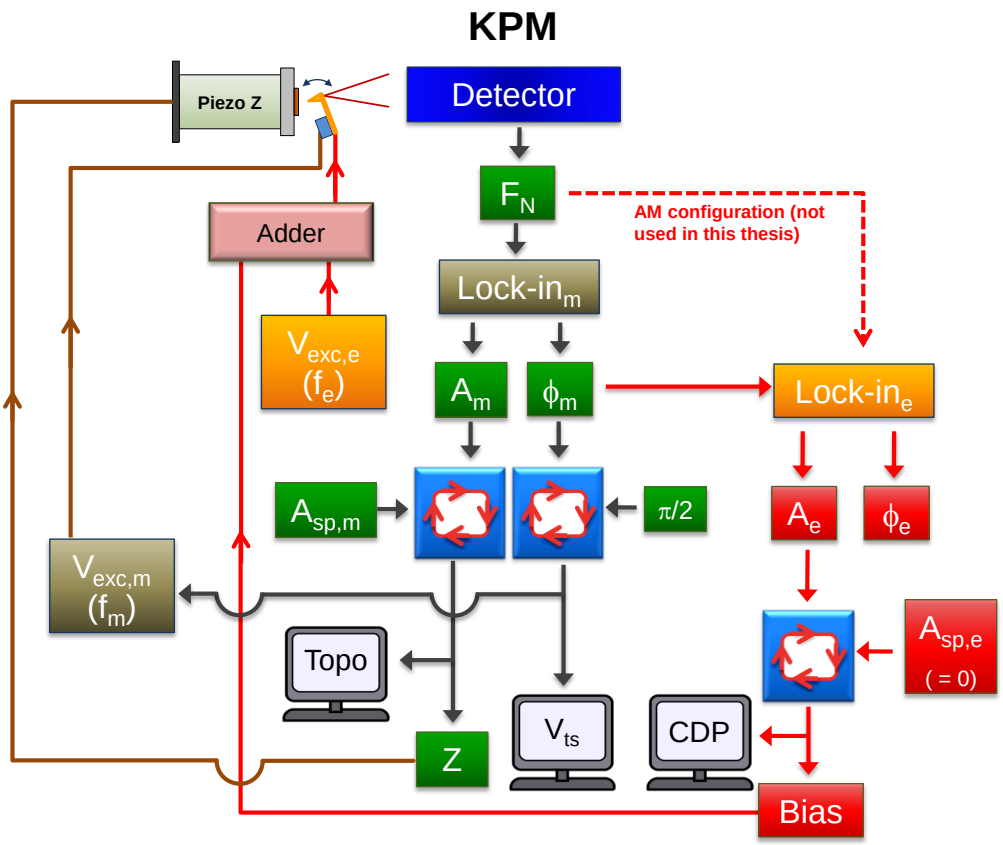

F_N	Normal force	**CPD**	Contact Potential Difference
A	Amplitude	**V_{ts}**	Conservative interactions image
ϕ	Phase	**Topo**	Topography
A_{sp}	Amplitude set point	***Subindex***	
V_{exc}	Driving amplitude	**m**	Mechanical
Lock-in	Lock-in amplifier	**e**	Electrical
f	Frequency		

Figure 1.30 KPM operation diagram.

1.3.7 Lithography/nanomanipulation

Scanning Probe Microscopies allow not only the visualization of surfaces and the study of the different tip-sample interactions, but the manipulation of the matter at the nanoscale, even at the atomic level. After the first manipulations performed with the STM, such as atomic modifications [139], molecular manipulation [140], or the positioning of single atoms [7], many different SPM nanomanipulation applications emerged. In SPM lithography the tip can be seen as a pen and the sample as a paper. In this way, the tip can be used to "draw" over the sample, where drawing usually consists on moving the tip over the sample performing specific actions different from the scanning ones. In a wider point of view, lithography allows designing experiments *à la carte*.

In the context of AFM there are many different nanolithography techniques: local oxidation [141, 142], nanoindentation and nanoscratching [143], magnetic field tip-induced nanolithography [144, 145], nanoparticle and nanotube manipulation [146, 147], local resistive switching [148], "Dip-pen" nanolithography [149], nanografting [150], atom manipulation in UHV conditions [151]… The possibility to control and modify surfaces at this level is driving us closer to the ultimate limit of two-dimensional nanoengineering.

In this PhD AFM nanolithography has been used to precisely move and assemble gold nanowires (Chapter 3). The cold welding ability of gold nanowires [152] has been exploited to create gold paths to precisely contact nanoobjects. Figure 1.31 shows an example of these gold nanowire manipulations.

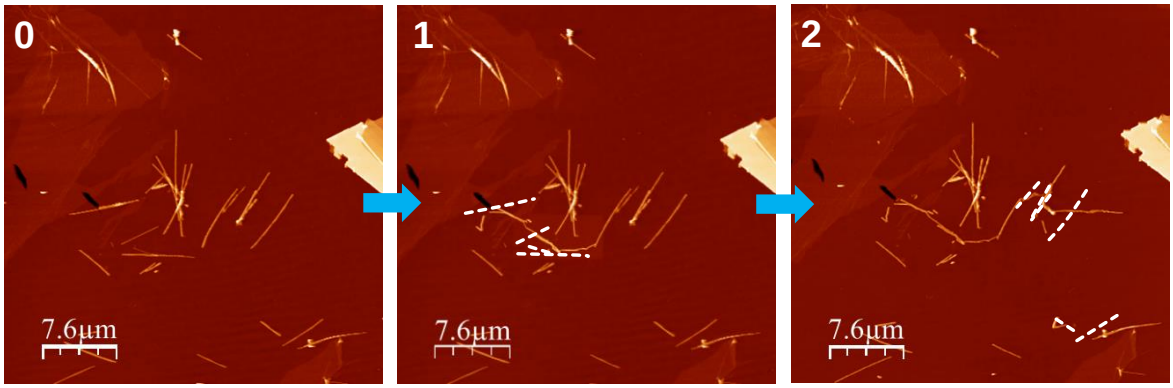

Figure 1.31 Gold nanowires manipulation. Series of nanomanipulations to create a gold path. Dashed lines represent the initial position of the manipulated nanowires in each of the panels.

1.4 References

[1] https://en.oxforddictionaries.com.
[2] http://dictionary.cambridge.org/.
[3] http://www.history-of-the-microscope.org.
[4] Meyer, J. C.; Girit, C. O.; Crommie, M. F.; Zettl, A. Imaging and dynamics of light atoms and molecules on graphene. *Nature* **2008,** *454*, 319-322.
[5] Binnig, G.; Rohrer, H. Scanning Tunneling Microscopy. *Helv. Phys. Acta* **1982,** *55*, 726-735.
[6] Binning, G.; Rohrer, H.; Gerber, C.; Weibel, E. Surface Studies by Scanning Tunneling Microscopy. *Phys. Rev. Lett.* **1982,** *49*, 57-61.
[7] Eigler, D. M.; Schweizer, E. K. Positioning single atoms with a scanning tunnelling microscope. *Nature* **1990,** *344*, 524-526.
[8] Binnig, G.; Quate, C. F.; Gerber, C. Atomic Force Microscope. *Phys. Rev. Lett.* **1986,** *56*, 930-933.
[9] Betzig, E.; Lewis, A.; Harootunian, A.; Isaacson, M.; Kratschmer, E. Near-Field Scanning Optical Microscopy (NSOM) - Development and Biophysical Applications. *Biophys. J.* **1986,** *49*, 269-279.
[10] Pohl, D. W. Optical near-field scanning microscope. EP112401-A; US4604520-A; EP112401-B; DE3276138-G; CA1243231-A, **1982**.
[11] Pohl, D. W.; Denk, W.; Lanz, M. Optical Stethoscopy - Image Recording with Resolution Lambda/20. *Appl. Phys. Lett.* **1984,** *44*, 651-653.
[12] Zhong, Q.; Inniss, D.; Kjoller, K.; Elings, V. B. Fractured Polymer/Silica Fiber Surface Studied by Tapping Mode Atomic-Force Microscopy. *Surf. Sci.* **1993,** *290*, L688-L692.
[13] Albrecht, T. R.; Grutter, P.; Horne, D.; Rugar, D. Frequency-Modulation Detection Using High-Q Cantilevers for Enhanced Force Microscope Sensitivity. *J. Appl. Phys.* **1991,** *69*, 668-673.
[14] RosaZeiser, A.; Weilandt, E.; Hild, S.; Marti, O. The simultaneous measurement of elastic, electrostatic and adhesive properties by scanning force microscopy: pulsed-force mode operation. *Meas. Sci. Technol.* **1997,** *8*, 1333-1338.
[15] Spizig, P.; Sanchen, D.; Förstner, F.; Koenen, J.; Marti, O.; Volswinkler, G. Scanning Probe in Pulsed-Force Mode, Digital and in Real Time. US7877816 B2, DE10062049A1, DE50107636D1, DE50113020D1, EP1342049A1, EP1342049B1, EP1640996A2, EP1640996A3, EP1640996B1, US7129486, US20040084618, US20100313311, WO2002048644A1, **2000**.
[16] de Pablo, P. J.; Colchero, J.; Gomez-Herrero, J.; Baro, A. M. Jumping mode scanning force microscopy. *Appl. Phys. Lett.* **1998,** *73*, 3300-3302.
[17] Ortega-Esteban, A.; Horcas, I.; Hernando-Perez, M.; Ares, P.; Perez-Berna, A. J.; San Martin, C.; Carrascosa, J. L.; de Pablo, P. J.; Gomez-Herrero, J. Minimizing tip-sample forces in jumping mode atomic force microscopy in liquid. *Ultramicroscopy* **2012,** *114*, 56-61.
[18] Pittenger, B. B.; Erina, N.; Su, C. Application Note #128. Quantitative Mechanical Property Mapping at the Nanoscale with PeakForce QNM. *Bruker* **2012**.
[19] Jaafar, M.; Martinez-Martin, D.; Cuenca, M.; Melcher, J.; Raman, A.; Gomez-Herrero, J. Drive-amplitude-modulation atomic force microscopy: From vacuum to liquids. *Beilstein J. Nanotechnol.* **2012,** *3*, 336-344.
[20] Martinez Martin, D.; Jaafar Ruiz-Castellanos, M.; Gomez Herrero, J. Method for controlling a scanning microscope. US9091704 B2, DE112012004221T5, US20140317789, WO2013053968A1, **2011**.
[21] Ido, S.; Kimura, K.; Oyabu, N.; Kobayashi, K.; Tsukada, M.; Matsushige, K.; Yamada, H. Beyond the Helix Pitch: Direct Visualization of Native DNA in Aqueous Solution. *ACS Nano* **2013,** *7*, 1817-1822.

[22] Ortega-Esteban, A.; Perez-Berna, A. J.; Menendez-Conejero, R.; Flint, S. J.; Martin, C. S.; de Pablo, P. J. Monitoring dynamics of human adenovirus disassembly induced by mechanical fatigue. *Sci. Rep.* **2013,** *3*.
[23] Perrino, A. P.; Garcia, R. How soft is a single protein? The stress-strain curve of antibody pentamers with 5 pN and 50 pm resolutions. *Nanoscale* **2016,** *8*, 9151-9158.
[24] Fukuma, T.; Kobayashi, K.; Matsushige, K.; Yamada, H. True atomic resolution in liquid by frequency-modulation atomic force microscopy. *Appl. Phys. Lett.* **2005,** *87*, 034101.
[25] Ando, T.; Kodera, N.; Takai, E.; Maruyama, D.; Saito, K.; Toda, A. A high-speed atomic force microscope for studying biological macromolecules. *Proc. Natl. Acad. Sci. U.S.A.* **2001,** *98*, 12468-12472.
[26] Garcia, R.; Rodriguez, T. R. Method of Using an Atomic Force Microscope and Microscope. WO2007036591 A1, CA2613515A1, EP1912055A1, EP1912055A4, US7921466, US20090229019, **2005**.
[27] Rodriguez, T. R.; Garcia, R. Compositional mapping of surfaces in atomic force microscopy by excitation of the second normal mode of the microcantilever. *Appl. Phys. Lett.* **2004,** *84*, 449-451.
[28] Garcia, R.; Herruzo, E. T. The emergence of multifrequency force microscopy. *Nat. Nanotechnol.* **2012,** *7*, 217-226.
[29] Herruzo, E. T.; Garcia, R. Bimodal Method for Quantifying Non-Topographical Properties in Force Field Microscopy. WO2014131925 A1, **2013**.
[30] Giessibl, F. J. Atomic-Resolution of the Silicon (111)-(7x7) Surface by Atomic-Force Microscopy. *Science* **1995,** *267*, 68-71.
[31] Sugimoto, Y.; Pou, P.; Abe, M.; Jelinek, P.; Perez, R.; Morita, S.; Custance, O. Chemical identification of individual surface atoms by atomic force microscopy. *Nature* **2007,** *446*, 64-67.
[32] Gross, L.; Mohn, F.; Moll, N.; Liljeroth, P.; Meyer, G. The Chemical Structure of a Molecule Resolved by Atomic Force Microscopy. *Science* **2009,** *325*, 1110-1114.
[33] Walters, D. A.; Hampton, D.; Drake, B.; Hansma, H. G.; Hansma, P. K. Atomic-Force Microscope Integrated with a Scanning Electron-Microscope for Tip Fabrication. *Appl. Phys. Lett.* **1994,** *65*, 787-789.
[34] Geisse, N. A. AFM and combined optical techniques. *Mater. Today* **2009,** *12*, 40-45.
[35] Anderson, M. S. Locally enhanced Raman spectroscopy with an atomic force microscope. *Appl. Phys. Lett.* **2000,** *76*, 3130-3132.
[36] Stockle, R. M.; Suh, Y. D.; Deckert, V.; Zenobi, R. Nanoscale chemical analysis by tip-enhanced Raman spectroscopy. *Chem. Phys. Lett.* **2000,** *318*, 131-136.
[37] Ortega-Esteban, A.; Bodensiek, K.; San Martin, C.; Suomalainen, M.; Greber, U. F.; de Pablo, P. J.; Schaap, I. A. T. Fluorescence Tracking of Genome Release during Mechanical Unpacking of Single Viruses. *ACS Nano* **2015,** *9*, 10571-10579.
[38] Burnham, N. A.; Chen, X.; Hodges, C. S.; Matei, G. A.; Thoreson, E. J.; Roberts, C. J.; Davies, M. C.; Tendler, S. J. B. Comparison of calibration methods for atomic-force microscopy cantilevers. *Nanotechnology* **2003,** *14*, 1-6.
[39] Butt, H. J.; Jaschke, M. Calculation of Thermal Noise in Atomic-Force Microscopy. *Nanotechnology* **1995,** *6*, 1-7.
[40] Hutter, J. L.; Bechhoefer, J. Calibration of Atomic-Force Microscope Tips. *Rev. Sci. Instrum.* **1993,** *64*, 1868-1873.
[41] Sader, J. E. Frequency response of cantilever beams immersed in viscous fluids with applications to the atomic force microscope. *J. Appl. Phys.* **1998,** *84*, 64-76.
[42] Sader, J. E.; Chon, J. W. M.; Mulvaney, P. Calibration of rectangular atomic force microscope cantilevers. *Rev. Sci. Instrum.* **1999,** *70*, 3967-3969.

[43] http://www.ampc.ms.unimelb.edu.au/afm/calibration.html.
[44] Horcas, I.; Fernandez, R.; Gomez-Rodriguez, J. M.; Colchero, J.; Gomez-Herrero, J.; Baro, A. M. WSXM: A software for scanning probe microscopy and a tool for nanotechnology. *Rev. Sci. Instrum.* **2007,** *78*, 013705.
[45] Martin, Y.; Williams, C. C.; Wickramasinghe, H. K. Atomic Force Microscope Force Mapping and Profiling on a Sub 100-A Scale. *J. Appl. Phys.* **1987,** *61*, 4723-4729.
[46] Rugar, D.; Mamin, H. J.; Erlandsson, R.; Stern, J. E.; Terris, B. D. Force Microscope Using a Fiber-Optic Displacement Sensor. *Rev. Sci. Instrum.* **1988,** *59*, 2337-2340.
[47] Meyer, G.; Amer, N. M. Novel Optical Approach to Atomic Force Microscopy. *Appl. Phys. Lett.* **1988,** *53*, 1045-1047.
[48] Brugger, J.; Buser, R. A.; Rooij, N. F. d. Micromachined atomic force microprobe with integrated capacitive read-out. *J. Micromech. Microeng.* **1992,** *2*, 218.
[49] Tortonese, M.; Barrett, R. C.; Quate, C. F. Atomic Resolution with an Atomic Force Microscope Using Piezoresistive Detection. *Appl. Phys. Lett.* **1993,** *62*, 834-836.
[50] Itoh, T.; Suga, T. Development of a force sensor for atomic force microscopy using piezoelectric thin films. *Nanotechnology* **1993,** *4*, 218.
[51] Dukic, M.; Adams, J. D.; Fantner, G. E. Piezoresistive AFM cantilevers surpassing standard optical beam deflection in low noise topography imaging. *Sci. Rep.* **2015,** *5*.
[52] Martinez-Martin, D., PhD thesis Nuevas técnicas basadas en microscopía de fuerza atómica: del vacío a los líquidos. *Departamento de Física de la Materia Condensada. Universidad Autónoma de Madrid.* **2011**.
[53] Fukuma, T.; Kimura, M.; Kobayashi, K.; Matsushige, K.; Yamada, H. Development of low noise cantilever deflection sensor for multienvironment frequency-modulation atomic force microscopy. *Rev. Sci. Instrum.* **2005,** *76*, 053704.
[54] Gautschi, G. Piezoelectric Sensorics: Force, Strain, Pressure, Acceleration and Acoustic Emission Sensors, Materials and Amplifiers. *Springer* **2002**.
[55] Binnig, G.; Smith, D. P. E. Single-Tube 3-Dimensional Scanner for Scanning Tunneling Microscopy. *Rev. Sci. Instrum.* **1986,** *57*, 1688-1689.
[56] Baro, A.; Gomez-Herrero, J.; Colchero, J.; Gomez-Rodriguez, J. M. Microscopio de fuerzas de bajo ruido, con amplio campo de visibilidad. ES2125165A1, ES2125165B1, **1996**.
[57] Pohl, D. W. Dynamic Piezoelectric Translation Devices. *Rev. Sci. Instrum.* **1987,** *58*, 54-57.
[58] Baselt, D. R.; Clark, S. M.; Youngquist, M. G.; Spence, C. F.; Baldeschwieler, J. D. Digital Signal Processor Control of Scanned Probe Microscopes. *Rev. Sci. Instrum.* **1993,** *64*, 1874-1882.
[59] Bennett, S. A brief history of automatic control. *IEEE Control Systems Magazine* **1996,** *16*, 17-25.
[60] Gimeno, A.; Ares, P.; Horcas, I.; Gil, A.; Gomez-Rodriguez, J. M.; Colchero, J.; Gomez-Herrero, J. 'Flatten plus': a recent implementation in WSxM for biological research. *Bioinformatics* **2015,** *31*, 2918-2920.
[61] http://wsxmsolutions.com/.
[62] http://gwyddion.net/.
[63] http://www.imagemet.com/.
[64] Isrraelachvili, J. Intermolecular and Surface Forces. *Academic Press, London* **1991**.
[65] Mate, C. M.; McClelland, G. M.; Erlandsson, R.; Chiang, S. Atomic-Scale Friction of a Tungsten Tip on a Graphite Surface. *Phys. Rev. Lett.* **1987,** *59*, 1942-1945.
[66] Burnham, N. A.; Colton, R. J. Measuring the Nanomechanical Properties and Surface Forces of Materials Using an Atomic Force Microscope. *J. Vac. Sci. Technol. A* **1989,** *7*, 2906-2913.

[67] De Pablo, P. J.; Colchero, J.; Gomez-Herrero, J.; Baro, A. M.; Schaefer, D. M.; Howell, S.; Walsh, B.; Reifenberger, R. Adhesion maps using scanning force microscopy techniques. *J. Adhes.* **1999,** *71*, 339-356.
[68] Landman, U.; Luedtke, W. D.; Burnham, N. A.; Colton, R. J. Atomistic Mechanisms and Dynamics of Adhesion, Nanoindentation, and Fracture. *Science* **1990,** *248*, 454-461.
[69] Hao, H. W.; Baro, A. M.; Saenz, J. J. Electrostatic and Contact Forces in Force Microscopy. *J. Vac. Sci. Technol. B* **1991,** *9*, 1323-1328.
[70] Martin, Y.; Abraham, D. W.; Wickramasinghe, H. K. High-Resolution Capacitance Measurement and Potentiometry by Force Microscopy. *Appl. Phys. Lett.* **1988,** *52*, 1103-1105.
[71] Nonnenmacher, M.; Oboyle, M. P.; Wickramasinghe, H. K. Kelvin Probe Force Microscopy. *Appl. Phys. Lett.* **1991,** *58*, 2921-2923.
[72] Dai, H. J.; Wong, E. W.; Lieber, C. M. Probing electrical transport in nanomaterials: Conductivity of individual carbon nanotubes. *Science* **1996,** *272*, 523-526.
[73] Martin, Y.; Wickramasinghe, H. K. Magnetic Imaging by Force Microscopy with 1000-A Resolution. *Appl. Phys. Lett.* **1987,** *50*, 1455-1457.
[74] Cleveland, J. P.; Anczykowski, B.; Schmid, A. E.; Elings, V. B. Energy dissipation in tapping-mode atomic force microscopy. *Appl. Phys. Lett.* **1998,** *72*, 2613-2615.
[75] Tamayo, J.; Garcia, R. Relationship between phase shift and energy dissipation in tapping-mode scanning force microscopy. *Appl. Phys. Lett.* **1998,** *73*, 2926-2928.
[76] Asenjo, A.; Jaafar, M.; Carrasco, E.; Rojo, J. M. Dislocation mechanisms in the first stage of plasticity of nanoindented Au(111) surfaces. *Phy. Rev. B* **2006,** *73*, 075431.
[77] Nemes-Incze, P.; Osvath, Z.; Kamaras, K.; Biro, L. P. Anomalies in thickness measurements of graphene and few layer graphite crystals by tapping mode atomic force microscopy. *Carbon* **2008,** *46*, 1435-1442.
[78] Gan, Y. Atomic and subnanometer resolution in ambient conditions by atomic force microscopy. *Surf. Sci. Rep.* **2009,** *64*, 99-121.
[79] Schimmel, T.; Koch, T.; Kuppers, J.; Lux-Steiner, M. True atomic resolution under ambient conditions obtained by atomic force microscopy in the contact mode. *Appl. Phys. A Mater. Sci. Process.* **1999,** *68*, 399-402.
[80] Sheiko, S. S.; Moller, M.; Reuvekamp, E.; Zandbergen, H. W. Calibration and Evaluation of Scanning-Force-Microscopy Probes. *Phy. Rev. B* **1993,** *48*, 5675-5678.
[81] Jin, C. H.; Lin, F.; Suenaga, K.; Iijima, S. Fabrication of a Freestanding Boron Nitride Single Layer and Its Defect Assignments. *Phys. Rev. Lett.* **2009,** *102*, 195505.
[82] Hoffmann, P. M.; Jeffery, S.; Pethica, J. B.; Ozer, H. O.; Oral, A. Energy dissipation in atomic force microscopy and atomic loss processes. *Phys. Rev. Lett.* **2001,** *87*, 265502.
[83] Patil, S.; Matei, G.; Dong, H.; Hoffmann, P. M.; Karakose, M.; Oral, A. A highly sensitive atomic force microscope for linear measurements of molecular forces in liquids. *Rev. Sci. Instrum.* **2005,** *76*, 103705.
[84] Garcia, R.; Perez, R. Dynamic atomic force microscopy methods. *Surf. Sci. Rep.* **2002,** *47*, 197-301.
[85] Giessibl, F. J. Advances in atomic force microscopy. *Rev. Mod. Phys.* **2003,** *75*, 949-983.
[86] Magonov, S. N.; Elings, V.; Whangbo, M. H. Phase imaging and stiffness in tapping-mode atomic force microscopy. *Surf. Sci.* **1997,** *375*, L385-L391.
[87] Schmitz, I.; Schreiner, M.; Friedbacher, G.; Grasserbauer, M. Phase imaging as an extension to tapping mode AFM for the identification of material properties on humidity-sensitive surfaces. *Appl. Surf. Sci.* **1997,** *115*, 190-198.

[88] Dufrene, Y. F.; Martinez-Martin, D.; Medalsy, I.; Alsteens, D.; Mueller, D. J. Multiparametric imaging of biological systems by force-distance curve-based AFM. *Nat. Methods* **2013,** *10*, 847-854.
[89] Van Der Hofstadt, M.; Huettener, M.; Juarez, A.; Gomila, G. Nanoscale imaging of the growth and division of bacterial cells on planar substrates with the atomic force microscope. *Ultramicroscopy* **2015,** *154*, 29-36.
[90] Heinzelmann, H.; Meyer, E.; Grutter, P.; Hidber, H. R.; Rosenthaler, L.; Guntherodt, H. J. Atomic Force Microscopy: General Aspects and Application to Insulators. *J. Vac. Sci. Technol. A* **1988,** *6*, 275-278.
[91] Cappella, B.; Dietler, G. Force-distance curves by atomic force microscopy. *Surf. Sci. Rep.* **1999,** *34*, 1, 5-3-104.
[92] Florin, E. L.; Moy, V. T.; Gaub, H. E. Adhesion Forces Between Individual Ligand-Receptor Pairs. *Science* **1994,** *264*, 415-417.
[93] Rief, M.; Gautel, M.; Oesterhelt, F.; Fernandez, J. M.; Gaub, H. E. Reversible unfolding of individual titin immunoglobulin domains by AFM. *Science* **1997,** *276*, 1109-1112.
[94] Butt, H. J.; Cappella, B.; Kappl, M. Force measurements with the atomic force microscope: Technique, interpretation and applications. *Surf. Sci. Rep.* **2005,** *59*, 1-152.
[95] Durig, U.; Zuger, O.; Stalder, A. Interaction Force Detection in Scanning Probe Microscopy - Methods and Applications. *J. Appl. Phys.* **1992,** *72*, 1778-1798.
[96] Palacios-Lidon, E.; Colchero, J. Quantitative analysis of tip-sample interaction in non-contact scanning force spectroscopy. *Nanotechnology* **2006,** *17*, 5491-5500.
[97] Fukuma, T.; Kobayashi, K.; Matsushige, K.; Yamada, H. True molecular resolution in liquid by frequency-modulation atomic force microscopy. *Appl. Phys. Lett.* **2005,** *86*, 193108.
[98] Gauthier, M.; Perez, R.; Arai, T.; Tomitori, M.; Tsukada, M. Interplay between nonlinearity, scan speed, damping, and electronics in frequency modulation atomic-force microscopy. *Phys. Rev. Lett.* **2002,** *89*, 146104.
[99] Kaggwa, G. B.; Kilpatrick, J. I.; Sader, J. E.; Jarvis, S. P. Artifact-free dynamic atomic force microscopy reveals monotonic dissipation for a simple confined liquid. *Appl. Phys. Lett.* **2008,** *93*, 011909.
[100] Gil, A., PhD thesis Study of the Tip-Sample Interaction at the Scanning Force Microscopy and its Application to the Visualization of Adsorption Processes on Surfaces. *Departamento de Física de la Materia Condensada. Universidad Autónoma de Madrid.* **2001**.
[101] Gomez-Navarro, C*., et al.* Scanning force microscopy three-dimensional modes applied to the study of the dielectric response of adsorbed DNA molecules. *Nanotechnology* **2002,** *13*, 314-317.
[102] Horber, J. K. H.; Miles, M. J. Scanning probe evolution in biology. *Science* **2003,** *302*, 1002-1005.
[103] Richter, R. P.; Brisson, A. Characterization of lipid bilayers and protein assemblies supported on rough surfaces by atomic force microscopy. *Langmuir* **2003,** *19*, 1632-1640.
[104] Hansma, H. G.; Pietrasanta, L. Atomic force microscopy and other scanning probe microscopies. *Curr. Opin. Chem. Biol.* **1998,** *2*, 579-584.
[105] Hinterdorfer, P.; Dufrene, Y. F. Detection and localization of single molecular recognition events using atomic force microscopy. *Nat. Methods* **2006,** *3*, 347-355.
[106] Kirmizis, D.; Logothetidis, S. Atomic force microscopy probing in the measurement of cell mechanics. *Int. J. Nanomedicine* **2010,** *5*, 137-145.
[107] Kurland, N. E.; Drira, Z.; Yadavalli, V. K. Measurement of nanomechanical properties of biomolecules using atomic force microscopy. *Micron* **2012,** *43*, 116-128.

[108] Hansma, P. K.*, et al.* Tapping Mode Atomic-Force Microscopy in Liquids. *Appl. Phys. Lett.* **1994,** *64*, 1738-1740.
[109] Ivanovska, I. L.; de Pablo, P. J.; Ibarra, B.; Sgalari, G.; MacKintosh, F. C.; Carrascosa, J. L.; Schmidt, C. F.; Wuite, G. J. L. Bacteriophage capsids: Tough nanoshells with complex elastic properties. *Proc. Natl. Acad. Sci. U.S.A.* **2004,** *101*, 7600-7605.
[110] Kodera, N.; Yamamoto, D.; Ishikawa, R.; Ando, T. Video imaging of walking myosin V by high-speed atomic force microscopy. *Nature* **2010,** *468*, 72–76.
[111] Moreno-Herrero, F.; Colchero, J.; Gomez-Herrero, J.; Baro, A. M. Atomic force microscopy contact, tapping, and jumping modes for imaging biological samples in liquids. *Phy. Rev. E* **2004,** *69*, 031915.
[112] Xu, X.; Raman, A. Comparative dynamics of magnetically, acoustically, and Brownian motion driven microcantilevers in liquids. *J. Appl. Phys.* **2007,** *102*, 034303.
[113] Putman, C. A. J.; Vanderwerf, K. O.; Degrooth, B. G.; Vanhulst, N. F.; Greve, J. Tapping Mode Atomic-Force Microscopy in Liquid. *Appl. Phys. Lett.* **1994,** *64*, 2454-2456.
[114] Carrasco, C.; Ares, P.; de Pablo, P. J.; Gomez-Herrero, J. Cutting down the forest of peaks in acoustic dynamic atomic force microscopy in liquid. *Rev. Sci. Instrum.* **2008,** *79*, 126106.
[115] Asakawa, H.; Fukuma, T. Spurious-free cantilever excitation in liquid by piezoactuator with flexure drive mechanism. *Rev. Sci. Instrum.* **2009,** *80*, 103703.
[116] Jaafar, M., PhD thesis Procesos de imanación en la Nanoescala mediante Microscopía de Fuerzas Magnéticas. *CSIC. Instituto de Ciencias Materiales de Madrid. UAM. Departamento de Física de la Materia Condensada.* **2009**.
[117] L. Yue; Liou, S.-H., Magnetic Force Microscopy Studies of Magnetic Features and Nanostructures. In *Scanning Probe Microscopy in Nanoscience and Nanotechnology 2*, Bhushan, B., Ed. Springer Berlin Heidelberg: 2011; pp 287-319.
[118] Shafai, C.; Thomson, D. J.; Simardnormandin, M.; Mattiussi, G.; Scanlon, P. J. Delineation of Semiconductor Doping by Scanning Resistance Microscopy. *Appl. Phys. Lett.* **1994,** *64*, 342-344.
[119] Oshea, S. J.; Atta, R. M.; Murrell, M. P.; Welland, M. E. Conducting Atomic-Force Microscopy Study of Silicon Dioxide Breakdown. *J. Vac. Sci. Technol. B* **1995,** *13*, 1945-1952.
[120] Hamers, R. J.; Tromp, R. M.; Demuth, J. E. Surface Electronic-Structure of Si(111)-(7 X 7) Resolved in Real Space. *Phys. Rev. Lett.* **1986,** *56*, 1972-1975.
[121] de Pablo, P. J.; Martinez, M. T.; Colchero, J.; Gomez-Herrero, J.; Maser, W. K.; Benito, A. M.; Munoz, E.; Baro, A. M. Mechanical and electrical properties of nanosized contacts on single-walled carbon nanotubes. *Adv. Mater.* **2000,** *12*, 573-576.
[122] Kelley, T. W.; Granstrom, E. L.; Frisbie, C. D. Conducting probe atomic force microscopy: A characterization tool for molecular electronics. *Adv. Mater.* **1999,** *11*, 261–264.
[123] Stern, J. E.; Terris, B. D.; Mamin, H. J.; Rugar, D. Deposition and Imaging of Localized Charge on Insulator Surfaces Using a Force Microscope. *Appl. Phys. Lett.* **1988,** *53*, 2717-2719.
[124] Abraham, D. W.; Williams, C.; Slinkman, J.; Wickramasinghe, H. K. Lateral Dopant Profiling in Semiconductors by Force Microscopy Using Capacitive Detection. *J. Vac. Sci. Technol. B* **1991,** *9*, 703-706.
[125] Hu, J.; Xiao, X. D.; Ogletree, D. F.; Salmeron, M. Imaging the Condensation and Evaporation of Molecularly Thin-Films of Water with Nanometer Resolution *Science* **1995,** *268*, 267-269.
[126] Bachtold, A.; Fuhrer, M. S.; Plyasunov, S.; Forero, M.; Anderson, E. H.; Zettl, A.; McEuen, P. L. Scanned probe microscopy of electronic transport in carbon nanotubes. *Phys. Rev. Lett.* **2000,** *84*, 6082-6085.
[127] Palacios-Lidon, E.; Perez-Garcia, B.; Abellan, J.; Miguel, C.; Urbina, A.; Colchero, J. Nanoscale characterization of the morphology and electrostatic properties of poly(3-octylthiophene)/graphite-nanoparticle blends. *Adv. Funct. Mater.* **2006,** *16*, 1975-1984.

[128] Kitamura, S.; Iwatsuki, M. High-resolution imaging of contact potential difference with ultrahigh vacuum noncontact atomic force microscope. *Appl. Phys. Lett.* **1998,** *72*, 3154-3156.
[129] Weaver, J. M. R.; Abraham, D. W. High-Resolution Atomic Force Microscopy Potentiometry *J. Vac. Sci. Technol. B* **1991,** *9*, 1559-1561.
[130] Sommerhalter, C.; Matthes, T. W.; Glatzel, T.; Jager-Waldau, A.; Lux-Steiner, M. C. High-sensitivity quantitative Kelvin probe microscopy by noncontact ultra-high-vacuum atomic force microscopy. *Appl. Phys. Lett.* **1999,** *75*, 286-288.
[131] Kikukawa, A.; Hosaka, S.; Imura, R. Silicon PN Junction Imaging and Characterizations Using Sensitivity Enhanced Kelvin Probe Force Microscopy *Appl. Phys. Lett.* **1995,** *66*, 3510-3512.
[132] Hoppe, H.; Glatzel, T.; Niggemann, M.; Hinsch, A.; Lux-Steiner, M. C.; Sariciftci, N. S. Kelvin probe force microscopy study on conjugated polymer/fullerene bulk heterojunction organic solar cells. *Nano Lett.* **2005,** *5*, 269-274.
[133] Luo, Y.; Gustavo, F.; Henry, J. Y.; Mathevet, F.; Lefloch, F.; Sanquer, M.; Rannou, P.; Grevin, B. Probing local electronic transport at the organic single-crystal/dielectric interface. *Adv. Mater.* **2007,** *19*, 2267-2273.
[134] Sinensky, A. K.; Belcher, A. M. Label-free and high-resolution protein/DNA nanoarray analysis using Kelvin probe force microscopy. *Nat. Nanotechnol.* **2007,** *2*, 653-659.
[135] Mohn, F.; Gross, L.; Moll, N.; Meyer, G. Imaging the charge distribution within a single molecule. *Nat. Nanotechnol.* **2012,** *7*, 227-231.
[136] Melitz, W.; Shen, J.; Kummel, A. C.; Lee, S. Kelvin probe force microscopy and its application. *Surf. Sci. Rep.* **2011,** *66*, 1-27.
[137] Glatzel, T.; Sadewasser, S.; Lux-Steiner, M. C. Amplitude or frequency modulation-detection in Kelvin probe force microscopy. *Appl. Surf. Sci.* **2003,** *210*, 84-89.
[138] Colchero, J.; Gil, A.; Baro, A. M. Resolution enhancement and improved data interpretation in electrostatic force microscopy. *Phy. Rev. B* **2001,** *64*, 245403.
[139] Becker, R. S.; Golovchenko, J. A.; Swartzentruber, B. S. Atomic-Scale Surface Modifications Using a Tunneling Microscope. *Nature* **1987,** *325*, 419-421.
[140] Foster, J. S.; Frommer, J. E.; Arnett, P. C. Molecular Manipulation Using a Tunnelling Microscope. *Nature* **1988,** *331*, 324-326.
[141] Dagata, J. A.; Schneir, J.; Harary, H. H.; Evans, C. J.; Postek, M. T.; Bennett, J. Modification of Hydrogen-Passivated Silicon by a Scanning Tunneling Microscope Operating in Air. *Appl. Phys. Lett.* **1990,** *56*, 2001-2003.
[142] Day, H. C.; Allee, D. R. Selective Area Oxidation of Silicon With a Scanning Force Microscope. *Appl. Phys. Lett.* **1993,** *62*, 2691-2693.
[143] Jung, T. A.; Moser, A.; Hug, H. J.; Brodbeck, D.; Hofer, R.; Hidber, H. R.; Schwarz, U. D. The Atomic Force Microscope Used as a Powerful Tool for Machining Surfaces. *Ultramicroscopy* **1992,** *42*, 1446-1451.
[144] Jaafar, M.; Gomez-Herrero, J.; Gil, A.; Ares, P.; Vazquez, M.; Asenjo, A. Variable-field magnetic force microscopy. *Ultramicroscopy* **2009,** *109*, 693-699.
[145] Onoue, T.; Siekman, M. H.; Abelmann, L.; Lodder, J. C. Probe recording on CoNi/Pt multilayered thin films by using an MFM tip. *J. Magn. Magn. Mater.* **2004,** *272*, 2317-2318.
[146] Falvo, M. R.; Clary, G. J.; Taylor, R. M.; Chi, V.; Brooks, F. P.; Washburn, S.; Superfine, R. Bending and buckling of carbon nanotubes under large strain. *Nature* **1997,** *389*, 582-584.
[147] Junno, T.; Deppert, K.; Montelius, L.; Samuelson, L. Controlled Manipulation of Nanoparticles with an Atomic-Force Microscope. *Appl. Phys. Lett.* **1995,** *66*, 3627-3629.
[148] Moreno, C.; Munuera, C.; Valencia, S.; Kronast, F.; Obradors, X.; Ocal, C. Reversible Resistive Switching and Multilevel Recording in La0.7Sr0.3MnO3 Thin Films for Low Cost Nonvolatile Memories. *Nano Lett.* **2010,** *10*, 3828-3835.

[149] Piner, R. D.; Zhu, J.; Xu, F.; Hong, S. H.; Mirkin, C. A. "Dip-pen" nanolithography. *Science* **1999,** *283*, 661-663.
[150] Xu, S.; Liu, G. Y. Nanometer-scale fabrication by simultaneous nanoshaving and molecular self-assembly. *Langmuir* **1997,** *13*, 127-129.
[151] Oyabu, N.; Custance, O.; Yi, I. S.; Sugawara, Y.; Morita, S. Mechanical vertical manipulation of selected single atoms by soft nanoindentation using near contact atomic force microscopy. *Phys. Rev. Lett.* **2003,** *90*, 176102.
[152] Lu, Y.; Huang, J. Y.; Wang, C.; Sun, S. H.; Lou, J. Cold welding of ultrathin gold nanowires. *Nat. Nanotechnol.* **2010,** *5*, 218-224.

Chapter 2. Instrumental developments.

2.1 Introduction

2.2 AFM setup for simultaneous inverted optical microscopy techniques

2.2.1 Design

2.2.2 Operation and Results

2.3 Variable-temperature ambient-controlled motorized Probe Station

2.3.1 Design

2.3.2 Operation and Results

2.4 Conclusions

2.5 References

2.6 Appendix

2.1 Introduction

In this chapter the two different instrumental developments performed during the PhD are presented.

First, a new AFM setup designed to allow simultaneous AFM and inverted optical microscopy techniques measurements, in particular, AFM and Total Internal Reflection Fluorescence (TIRF) microscopy [1, 2] is introduced. TIRF microscopy (TIRFM) uses an evanescent wave to selectively illuminate and excite fluorophores, in a region of the specimen immediately adjacent to the glass substrate-liquid interface. The AFM/TIRFM combination presented here is an original design performed in collaboration with Dr. Pedro J. de Pablo's group. The AFM setup includes fully motorized laser and photodiode alignments as well as tip-sample approach. The whole combination is based on the one assembled by Dr. Iwan Schaap at the University of Göttingen in Germany, that has already achieved initial results showing the potential of the technique [3]. In the frame of this collaboration, the AFM/TIRFM will enable the visualization of protein cages attached to a glass substrate, to study their genome release during mechanical unpacking. One of the main advantages of the design presented here, compared to other AFM configurations compatible with inverted optical microscopy, is an enhanced resolution thanks to improvements on the stiffness of the setup. This has been achieved by minimizing the mechanical loop [4] (the distance between the structural elements that are required to hold the probe at a fixed distance from the sample), which reduces the mechanical noise. As it is shown later, the achieved resolution has allowed distinguishing different adsorption geometries of protein cages on substrates and structural features. An extra advantage of this design is that it can be controlled with the WSxM software [5]. WSxM allows a variety of measuring modes and user configurable options that will enable studies which are now inaccessible or very difficult to other systems. For example, in the frame of the collaboration that gave rise to this development, Jumping Mode plus (JM+) [6] will enable to study the force-controlled disassembly of viral capsids induced by mechanical fatigue while TIRFM data are acquired.

Second, a probe station setup for the electrical characterization of micro- and nano-materials and devices at different temperatures, ranging from 80 to 400 K, in a controlled atmosphere is presented. In the laboratory there was already a two-terminal probe station installed by Dr. Cristina Gómez-Navarro. It used manual actuators to position the probes and was operated in ambient conditions. The new probe station substitutes the existing one in the laboratory. It allows performing conductivity measurements in a wide range of temperatures, opening the possibility of studying the variation of the electrical properties of micro- and nano-objects as a function of the temperature. For this purpose, the probe station system designed here is placed inside a high vacuum chamber, to avoid liquid condensation on the sample when decreasing the temperature. Thus, a perfect control of the X, Y and Z movements of the probes with submicron resolution compatible with the vacuum system is

needed. To this end, two sets of piezoelectric motors assembled in a XYZ configuration combined with an optical microscope have been employed. Nowadays there is not a commercially available probe station system with a similar setup, and hence we are considering the commercialization of our design. Minimization of the thermal expansion of the sample holder as the temperature changes is also required, to prevent the tips from moving out of the selected contact points as well as from damaging the sample. Most commercially available cryogenic probe stations (https://www.cascademicrotech.com/, http://www.arscryo.com or http://microxact.com, for example) use probe arms to manually control the positioning of the probes. Probe arms make the vacuum chamber designs complex, they are not user-friendly, their minimum step size is typically ~ 5 μm and also introduce stability issues due to their low natural resonance frequency. These probe stations are more focused on the characterization of 2" to 4" wafer size samples and require a high budget to be purchased (typically ~ 150 – 200 k€). More cost-effective commercial academic and laboratory research cryogenic probe stations (~ 45 k€ http://www.lakeshore.com, ~ 50 k€ http://www.janis.com/) use manually controlled probe arms as well. The original design presented in this PhD is a research-grade cryogenic probe station, with piezo actuated X, Y and Z movements with a minimum step size of ~ 2 nm, and a maximum travel range of 25 mm along the in-plane and 20 mm for the out-of-plane directions, whose final total production cost (including vacuum pumping system and all the necessary electronics for electrical characterization) is ~ 28 k€. There are as well commercial compact robots based on piezoelectric elements that could be used to motorize the probes positioning (http://imina.ch/). They provide a much lower step size than the probe arms (~ 50 nm), but the cost of these robots is very high (~ 52 k€ in comparison to ~ 5 k€ for the similar elements in the design presented here). In addition, in these robots the Z movement is not completely vertical; motion in the out-of-plane direction is performed by changing the tilt of the probe, which produces an undesired motion in the in-plane direction, which can lead to failure contacts when the probe is needed to touch micrometer sized elements.

These two instrumental developments could seem very far apart. Nevertheless, they are linked by the common feature of a fully motorized control of the X, Y and Z movements at submicron resolution. This achievement has been addressed by the use of piezoelectric actuators. Nowadays piezoelectric motors are an attractive alternative to conventional electromagnetic motors [7]. This is possible thanks to new acting materials, in combination with fast electronic control and an increased knowledge in the design of mechanical multimode-resonators. Piezoelectric motors are a cost-effective solution that can easily fulfill the requirements of both developments presented here. They can move tens of mm very fast (travelling speeds up to several mm/s) to coarse position the different moving elements within seconds. This fast motion is combined with resolutions down to a few nm for fine positioning. They can hold loads of several hundreds of grams, needed to precisely move and hold in position (power-off locking ability) the moving elements in the systems.

And they can be easily made to satisfy high vacuum and low temperature requirements (no need for several assembled parts such as rotor, stator, ball-bearings, etc.). In the developments presented here, Piezo LEGS® from PiezoMotor® [8] have been employed combined with miniature linear guides. Piezo LEGS® motors use piezo actuators co-sintered to a single body with four movable legs made out of ceramic "muscles". Figure 2.1 shows a diagram with the operation principle of the piezoelectric motors used in this PhD.

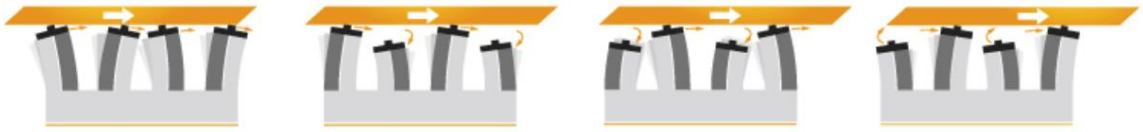

Figure 2.1 Principle of operation of the piezoelectric motors used in this PhD, Piezo LEGS® from PiezoMotor®. Source: http://www.piezomotor.com/

By applying controlled voltages to the piezoceramic "muscles", their movement is synchronized to move back and forth in a precise linear motion taking steps. By controlling these steps, piezomotors move in the nanometer range and reach travelling speeds of several millimeters per second. If needed, the company also offers small motion sensors compatible with the piezoelectric motors for a precise determination of the step length.

For the laser and photodiode alignment in the AFM head development, as well as for the X, Y and Z positioning of the tips in the probe station development, the Piezo LEGS® Linear 6N LL10 model has been used because of its compact design and power-off locking ability. For the tip-sample approach in the AFM head, the Piezo LEGS® Linear Twin-C 20N LTC20 version was selected because it can deliver up to 20 N force (the AFM head of ~ 1 kg (~ 10 N) is supported on three motors, that allow a total of 60 N of force, more than enough to operate the AFM head) with sub-micron/nanometer positioning and power-off locking. In addition, this motor model is compatible with previous head designs. Detailed specifications of these motors can be found in the Appendix, where the critical parameters have been highlighted. Figure 2.2 shows pictures of both piezoelectric motors.

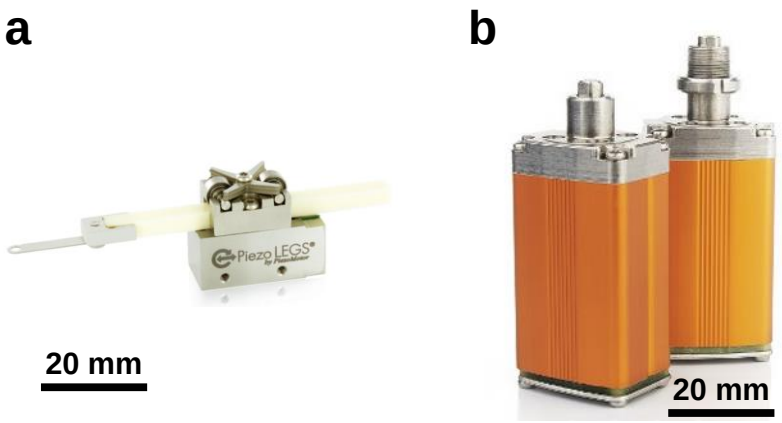

Figure 2.2 a) Piezo LEGS® Linear 6N LL10 motor. b) Piezo LEGS® Linear Twin-C 20N LTC20 motors. Source: http://www.piezomotor.com/

The design of all the mechanical parts and assemblies of the developments presented in this PhD has been performed with the Solid Edge software [9]. Solid Edge is a 3D CAD (computer-aided design) software. It provides solid and assembly modeling together with 2D orthographic view functionality. While these developments are original works, they are possible thanks to many different contributions. The coupling of the AFM stage with the TIRFM has counted with the collaboration of Dr. Iwan Schaap. The probe station system has been designed following the requirements of Dr. Cristina Gómez-Navarro. The machining of the mechanical parts has been carried out both by the "Servicios generales de apoyo a la investigación experimental" (SEGAINVEX) and by Santiago Márquez and José María Pérez from the technical staff of the Física de la Materia Condensada department (FMC). The electronics developed to control the piezoelectric motors have been designed and built also in SEGAINVEX. The software to control the motors, in the case of the AFM/TIRFM combination was already integrated on WSxM [5] by Nanotec software department, in a first motorized evolution from the Lanza head. In the probe station case, a first version of the control software was made by us and later revised and improved by Ignacio Horcas from the technical staff of FMC. Finally, in the probe station development, the temperature control electronics and software were provided by SEGAINVEX, and some extra electronics to automatize the IV acquisition were designed and built by Ignacio Horcas.

It is first presented the design of the systems followed by their operation and some results showing their capabilities.

2.2 AFM setup for simultaneous inverted optical microscopy techniques

2.2.1 Design

A ray of light passing from one medium to another of lower refractive index with a given incident angle will undergo reflection and refraction at the interface. When the incident angle is increased sufficiently, reaching the so-called critical angle, the ray is entirely reflected towards the first medium. This phenomenon is known as total internal reflection. In a TIRF microscope, the incident light coming from a high numerical aperture (NA) immersion objective is totally reflected at the glass surface-liquid interface and only an evanescent wave illuminates the sample. The evanescent electromagnetic field decays exponentially from the interface, penetrating to a depth typically in the range of 30 to 300 nm into the sample medium. This fact allows fluorescence studies of samples lying within this range, avoiding the background noise of the bulk solution. Figure 2.3a shows the operation principle of TIRFM. Figure 2.3b shows schematics of the assembly to combine it with AFM.

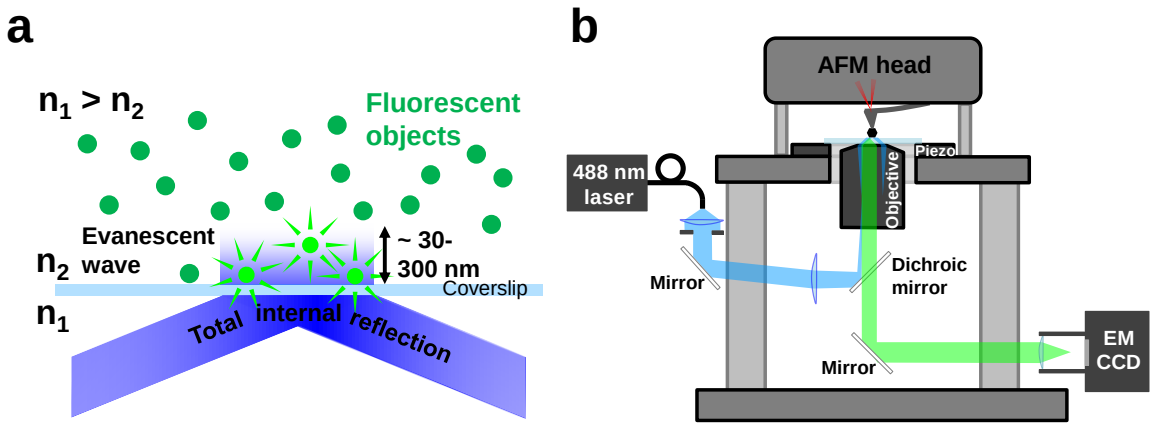

Figure 2.3 a) TIRFM operation principle. b) Schematics of the AFM/TIRFM combination.

A combined AFM/TIRFM system has to fulfill a few basic requirements. Fluorescence requires a high NA oil immersed objective. This kind of objectives allow total internal reflection (oil refractive index, n_1, similar to that of the glass coverslip, higher than water refractive index, n_2), and to capture as much light as possible. Thus, the objective is very close to the glass substrate (the distance from the lens to the glass substrate is ~ 0.12 mm) and a high resolution micrometer or a piezo actuator is needed for positioning. AFM requires an open optical axis for fitting the objective and the AFM tip has to be able to be aligned with this axis. For this purpose, there are two basic approaches: a tip-scanned or a sample-scanned configuration. A sample-scanned approach was chosen since it allows a

better alignment of the AFM tip with the optical axis. This configuration was achieved by using a scanner with a clear aperture for inverted optical microscopy access. As it is shown in Chapter 1, AFM piezoelectric scanners can have different geometries, but most of them are not compatible with inverted optical microscopy access. Nowadays, it is possible to find commercial piezo scanners with clear apertures that overcome this issue. However, these scanners typically have slower time response and lower stability and resolution than more conventional piezo scanner geometries. The challenge of this development was the design of a new AFM setup compatible with a piezo scanner of this family, while keeping as much as possible the high standards in stability, resolution and functionalities such as those by AFMs from the Nanotec kind. And at the same time, to ease the operation of the instrument.

The new AFM setup presented here is based on the Lanza head, which we designed during my period at Nanotec Electronica. Still there, I designed and took part in the assembly of an evolution of Lanza, motorizing laser and photodiode alignments and tip-sample approach to operate in the standard piezotubes Nanotec AFMs configuration. This design, namely Lanza-MT, also included an integrated variable-gain IV preamplifier for C-AFM measurements and the same type of piezomotors described above. For the AFM/TIRFM combination I took advantage of the Lanza-MT head design, making it compatible with a piezo scanner presenting a clear aperture in order to allow optical microscopy access from the bottom. Figure 2.4 presents 3D CAD views of Lanza and Lanza-MT heads. Lanza head presents an open architecture to allow manual adjustment of laser and photodiode (figure 2.4a). As Lanza-MT does not require manual operation for optical tuning/alignment, we designed an enclosure to isolate the head from external noises (figure 2.4b). The use of this enclosure is possible thanks to the motorization of the laser and photodiode adjustment elements. This can be seen in figures 2.4c and d, where schematics of the head interiors are presented. Laser and photodiode adjustment elements are highlighted in blue. Whereas Lanza head uses manual stages, Lanza-MT head uses Piezo LEGS® Linear 6N LL10 motors (figure 2.2a) instead. The motion of these motors is controlled either by a software interface or a remote control, preventing the need of manual access, which is indeed an extra when working with controlled environments. Another advantage of the motorization is that the use of an enclosure, hiding the inside of the head, enabled the simplification of its different mechanical parts, easing their machining.

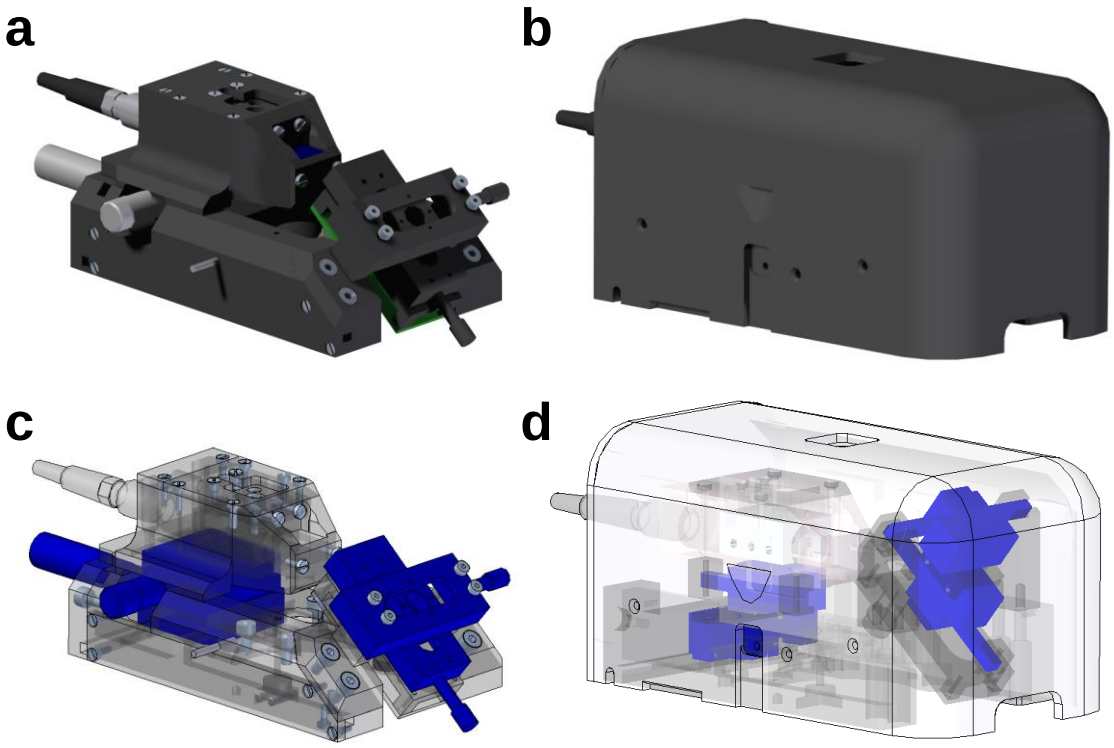

Figure 2.4 3D CAD models of Lanza head and its motorized evolution. a) and b) Rendered views. c) and d) Schematic views showing in blue the laser and photodiode moving elements.

Figure 2.5 shows CAD renders and photographs of both heads on their respective stages. Figures 2.5a and b show the conventional Lanza head, which is supported on three micrometer screws. The two screws at the front are moved by hand, while the third one is motorized through a DC motor. Figures 2.5c and d show Lanza-MT stage, where the head is supported on three Piezo LEGS® Linear Twin-C 20N LTC20 motors allowing a complete motorized tip-sample approach.

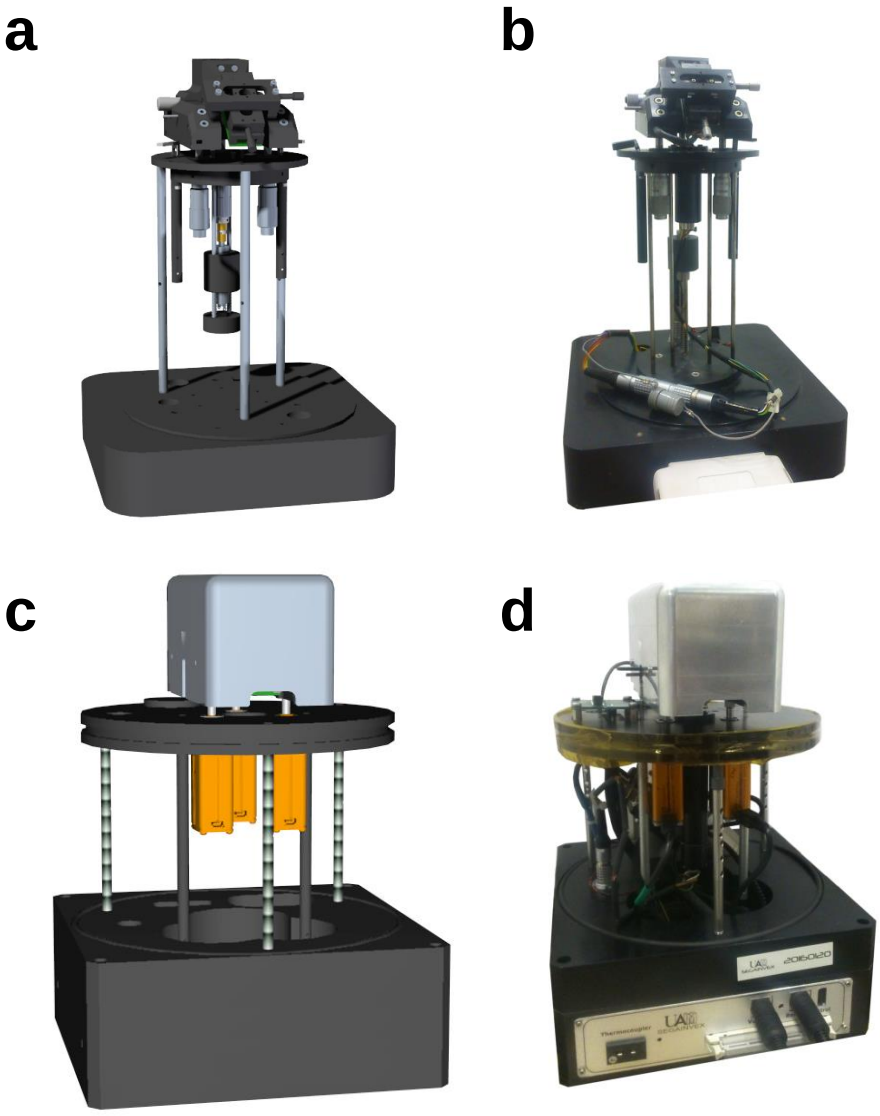

Figure 2.5 Lanza and Lanza-MT AFM setups. a) and b) Lanza rendered view and photograph respectively. c) and d) Lanza-MT rendered view and photograph respectively.

As already mentioned, for the AFM/TIRFM combination a piezo scanner presenting a clear aperture was used to gain inverted optical microscopy access. A P-733.3DD scanner from Physik Instrumente (PI) [10] was employed. This scanner (figure 2.6) provided an open-loop travel range of 33 μm in X and Y and 14 μm in Z with a typical resolution of 0.1 nm (a detailed list of specifications can be found on the Appendix, where the most critical ones are highlighted).

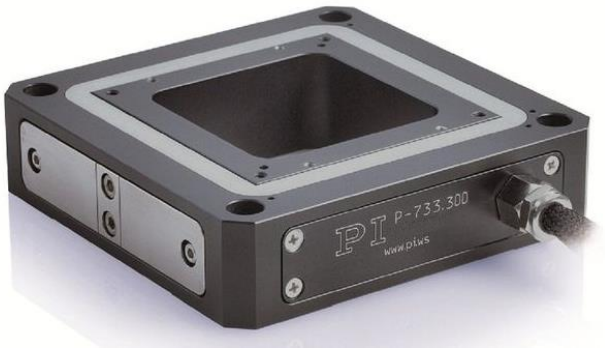

Figure 2.6 P-733.3DD piezo scanner. Source: https://www.physikinstrumente.com/

P-733.3DD scanner integrates capacitive sensors to compensate its nonlinearity effects (see section "Positioning and scanning: piezoelectric scanners" in Chapter 1). However, we did not use the signal readout from the sensors for an active feedback in order to minimize noises. It can be simultaneously recorded together with the X, Y, Z voltages applied to the scanner. This feature allows for a post-processing recalibration of the distances in the acquired data if needed.

This kind of scanner and the need to leave room under the sample stage for the optical elements of TIRFM impaired the usual configuration for the tip-sample approach system, placed below the head (as in figure 2.5). To overcome this issue, a new AFM head (figure 2.7), based on Lanza-MT, was designed, incorporating the three Piezo LEGS® Linear Twin-C 20N LTC20 motors for the approach in an inverted configuration.

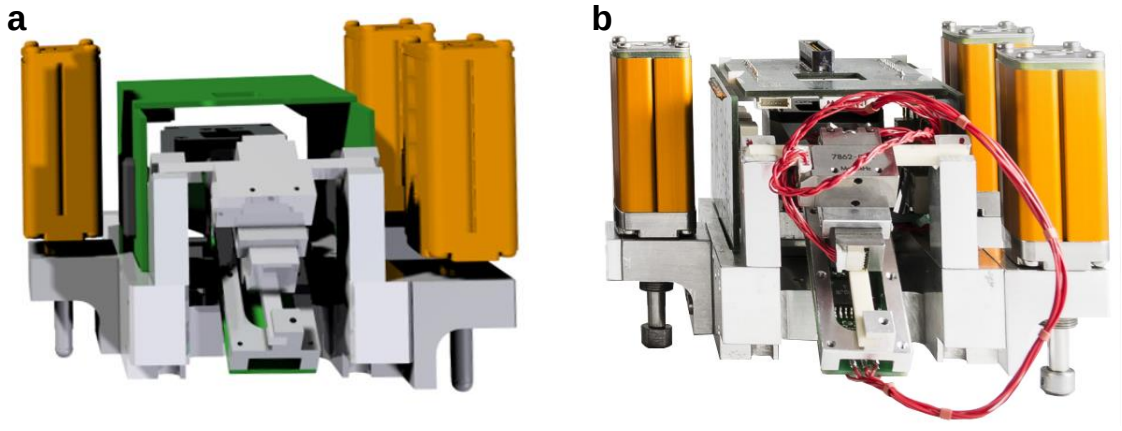

Figure 2.7 Head for the AFM/TIRFM combination, where the approach motors were incorporated on the head itself. a) 3D rendered view. b) Photograph of the assembled head.

The influence of external perturbations on the tip-sample stability can be reduced by damping mechanisms and/or enough stiffness of the SPM structure. Large-amplitude low-frequency noise, which is relatively unaffected by conventional damping systems, can threaten proper SPM operation unless the SPM internal structure has enough stiffness. This can be nicely seen in Figure 2.8 by D. Pohl [4]. It can be inferred that for effective isolation of external perturbations, frequency characteristics of damping and stiffness of the system have to be as far apart as possible.

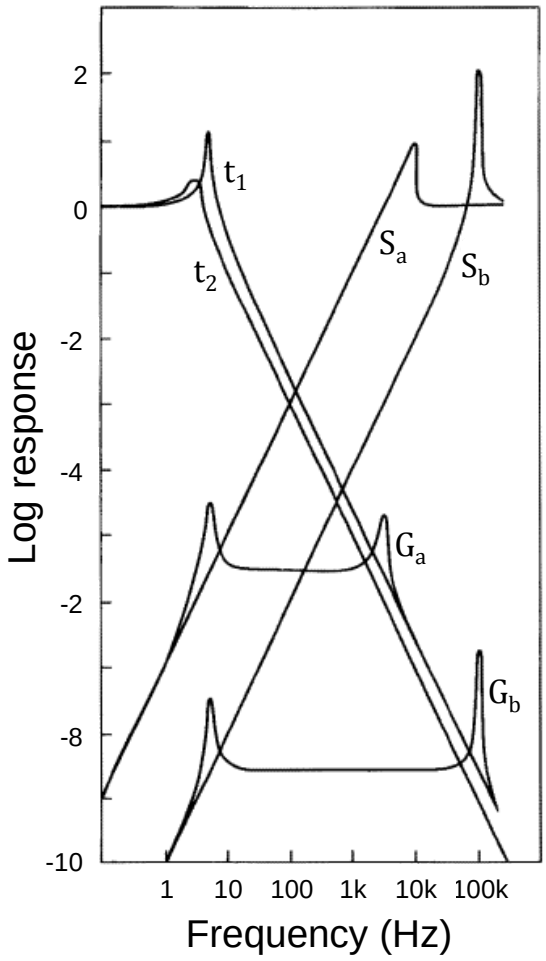

Figure 2.8 Frequency characteristics of damping (t_1, typical for damping systems with metallic springs and eddy-current attenuation, and t_2, typical for commercial antivibration pads made from rubber) and stiffness (S_a, typical for SPMs consisting of several-cm-size structures made of piezoelectric ceramics and steel, and S_b, which represents about the best stiffness one can expect for SPMs with piezoelectric ceramic scanners). G_a, G_b correspond to the combination of t_1 with S_a, S_b respectively. Figure adapted from reference [4].

Thus, the stiffness frequency characteristic of the structure has to be maximized. This was achieved by maximizing the stiffness of the SPM, which implied minimizing the mechanical loop. In order to minimize the mechanical loop of the system, a specific platform was designed to be placed onto the P-733.3DD piezo scanner frame. In this way, the AFM head rested on this platform instead of on the stage (see figure 2.9), implying a decrease of the mechanical loop worth of consideration. The sample holder was designed as well to minimize the total mass on the piezo to provide a higher resonance frequency of the scanner. It consists on an aluminum part attached to the piezo where the glass coverslips for the samples are fixed. Figure 2.9 presents schematics showing the mechanical loop reduction and a 3D render view of the piezo scanner assembly.

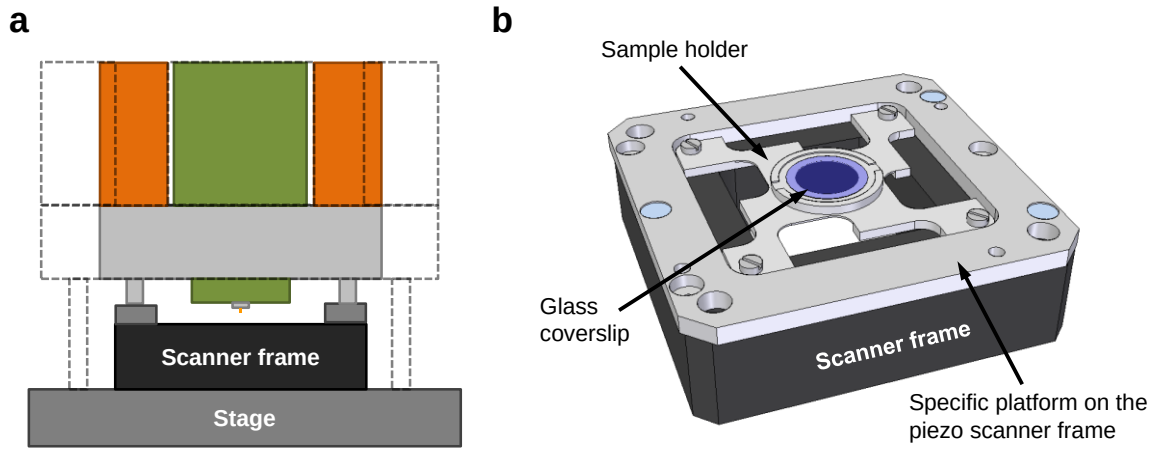

Figure 2.9 a) Minimization of the mechanical loop. Dashed lines: design if the head was to be placed on the stage. Solid: design to minimize the mechanical loop. b) 3D render of the piezo scanner assembly showing its different parts.

The AFM head and scanner assembly had to be accommodated on a stage allowing enough space for the optical elements of TIRFM. Figure 2.10 shows the AFM assembly of the AFM/TIRFM combination. The stage provided access for the TIRFM assembly and allowed coupling all the needed optical elements.

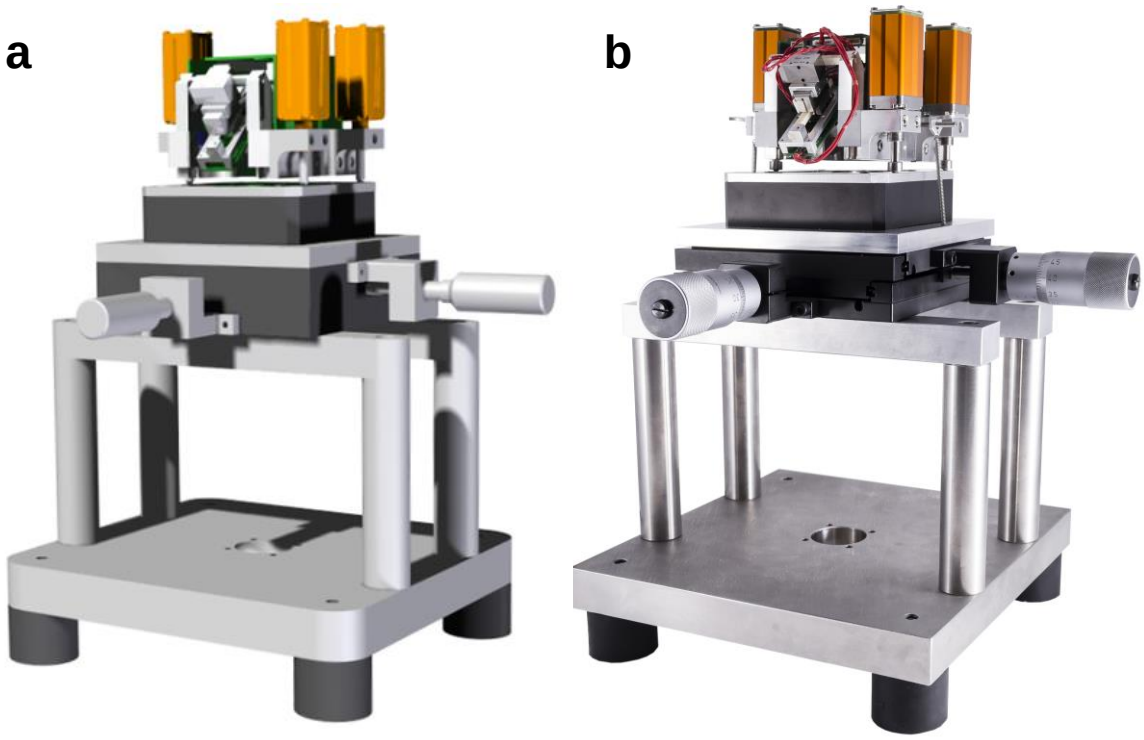

Figure 2.10 AFM assembly. a) 3D rendered view. b) Photograph.

The optical assembly was carried out by Francisco Moreno-Madrid, under the supervision of Dr. Pedro J. de Pablo and Dr. Iwaan Schaap. The whole setup was placed into an acoustic-isolated temperature-controlled enclosure with a passive antivibration system (air damping), built by the technical staff of the FMC department. Since the AFM head developed here is fully motorized, once tip and sample are in place there is no need for opening the enclosure. Figure 2.11 shows photographs of the final AFM/TIRFM setup.

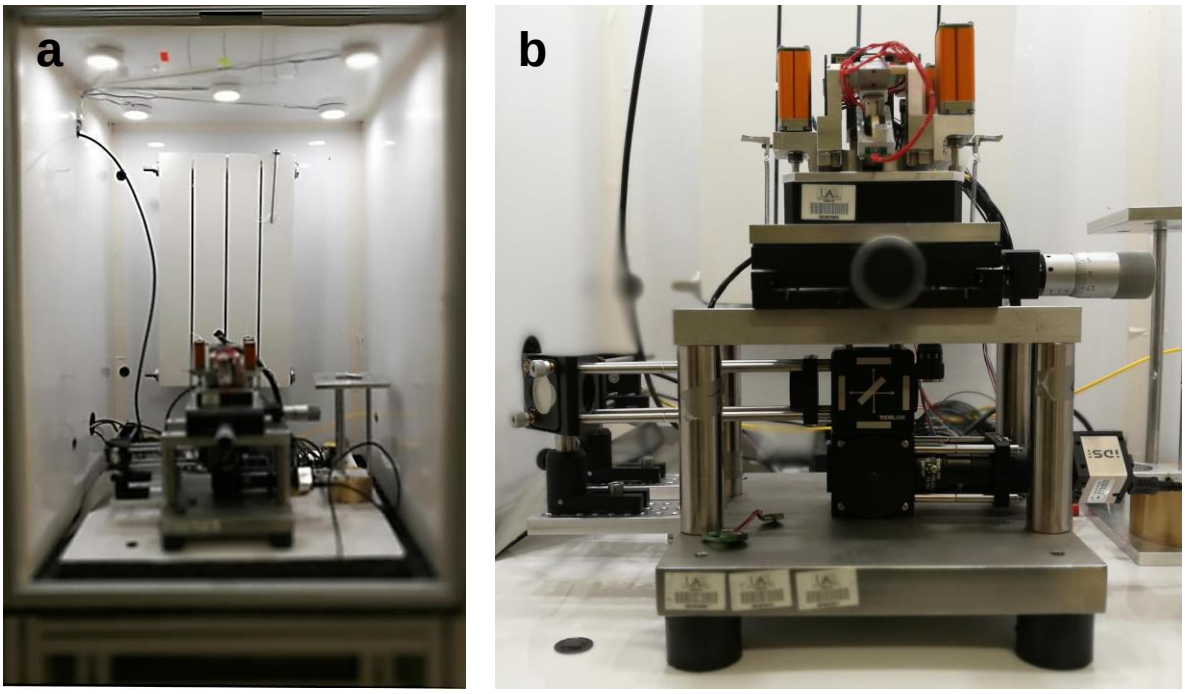

Figure 2.11 a) Final AFM/TIRFM combination setup, including the isolation enclosure. b) Detail of the final assembly.

2.2.2 Operation and Results

First AFM measurements were carried out using reference samples such as highly oriented pyrolytic graphite (HOPG) and DNA molecules adsorbed on a mica substrate (sample courtesy of Alejandro Martín from Dr. Fernando Moreno-Herrero's group). Both were demanding samples in the sense that high sensitivity and stability of the system were required for their proper visualization. Figure 2.12 shows images of HOPG and DNA molecules acquired in ambient conditions using Nanosensor PointProbePlus probes [11] (spring constant k ~ 30 N m^{-1} and resonance frequency f_0 = 325 kHz) under the AM-AFM mode.

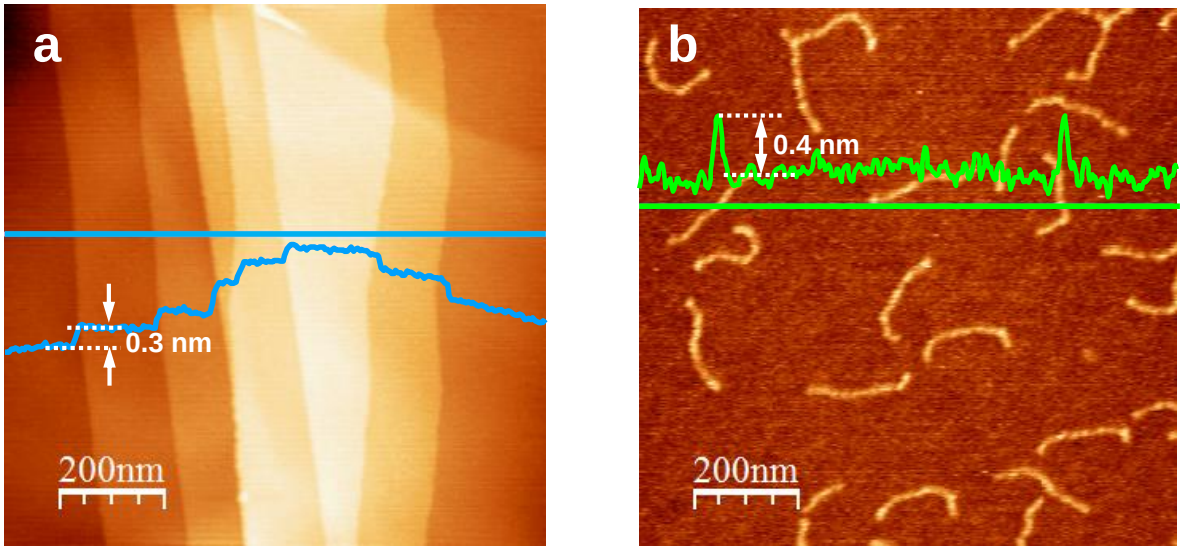

Figure 2.12 Reference samples images acquired with the AFM/TIRFM setup in ambient conditions using AM-AFM. a) HOPG. Oscillation amplitude A = 25 nm. b) DNA molecules adsorbed on mica. A = 10 nm.

Figure 2.12a reveals monoatomic steps on the HOPG surface, whereas figure 2.12b presents several DNA molecules. As expected, DNA molecules measured height is less than their theoretical diameter, due to the salt layer used to adsorb them on the mica and to some sample deformation (produced by either elastic deformation induced by the tip or the interaction with the substrate) [12]. Much more measurements in air conditions with different samples were performed (with the help of Dr. Eloy Pérez Enciso) ensuring proper functioning and stability of the system.

Measurements in buffer conditions were then performed on the kind of samples of interest that triggered this development, virus-like particles (VLPs). VLPS are protein cages resembling viruses that are not infectious. They can be used as nanoscale platforms for the self-assembly of internally and/or externally functionalized particles [13]. In particular,

VLPs derived from the bacteriophage P22 were used because they are promising candidates for the design of nanomaterial systems with biotechnological applications [13]. VLPs in their expanded form with a polymer cargo were produced by Prof. Trevor Douglas' group and prepared for AFM scanning by Francisco Moreno-Madrid. Figure 2.13 shows P22 VLPs in buffer conditions (PBS 100 mM phospathe, 50 mM NaCl, pH = 7). A 20 µL drop of diluted stock solution was incubated on a freshly cleaved HOPG surface. After 20 min, sample was washed with buffer solution until a volume of 90 µL was reached. Olympus Biolever-mini probes [14] (BL-AC40TS-C2, spring constant k ~ 0.07 N m^{-1} and resonance frequency in liquid ~ 25 kHz) in the AM-AFM mode were employed.

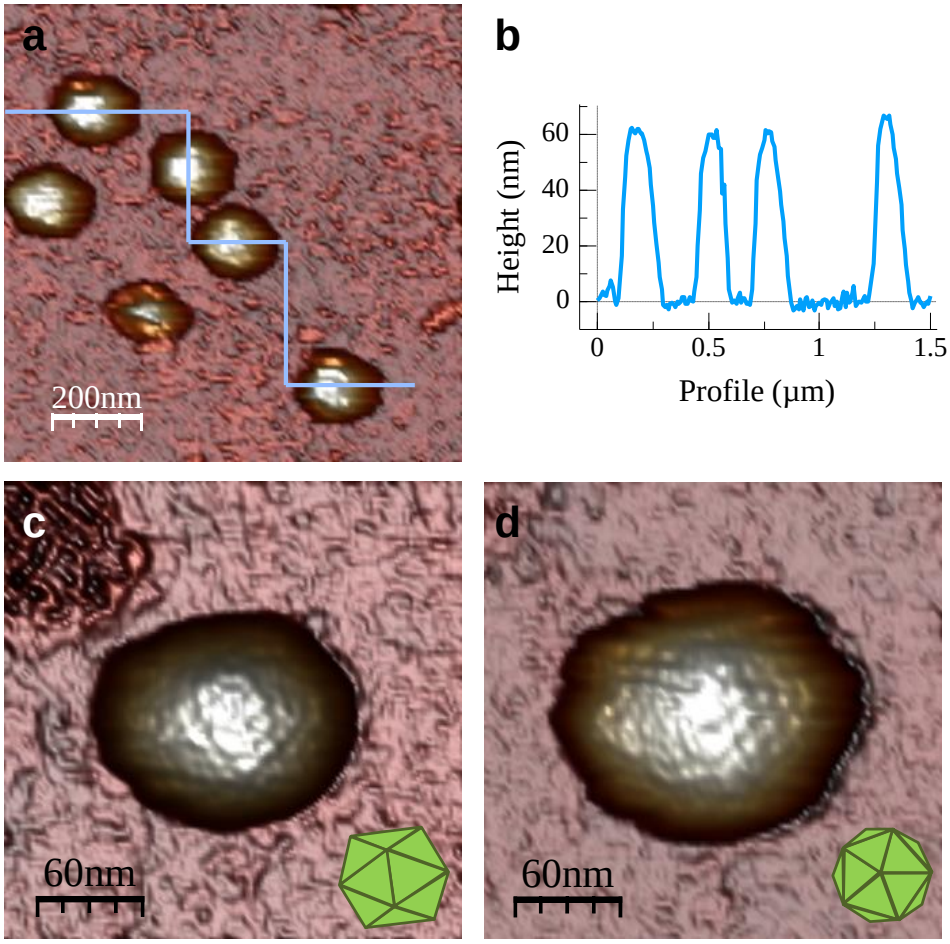

Figure 2.13 a) P22 VLPs adsorbed on HOPG. b) Height profile along the blue line in a). c) and d) High resolution images of two different P22 VLPs showing different adsorption geometries, 2-fold (S2) in c) and 5-fold (S5) symmetry in d). Insets show schematic views of the corresponding symmetries. Oscillation amplitude A = 4 nm in all the cases.

P22 VLPs in figure 2.13 present heights in good agreement with reported values [13]. High resolution images allow to discriminate adsorption geometries and even to visualize

different subunits within the nanocages. These images are comparable to the state-of-the-art high resolution images of VLPs found in the literature [13].

Figure 2.14 shows an individual nanoindentation assay, consisting of deforming a capsid with the AFM tip until mechanical failure is observed. The ability to perform this kind of experiments together with the high resolution imaging in figure 2.13 shows the potential of the developed system for the study of cargo diffusion from fractured single VLPs. The higher resolution imaging ability of the AFM/TIRFM setup designed here compared with previous setups [3] will allow performing studies on smaller VLPs. Moreover, the variety of measuring modes and user configurable options in WSxM software will enable to perform very precise force-controlled experiments.

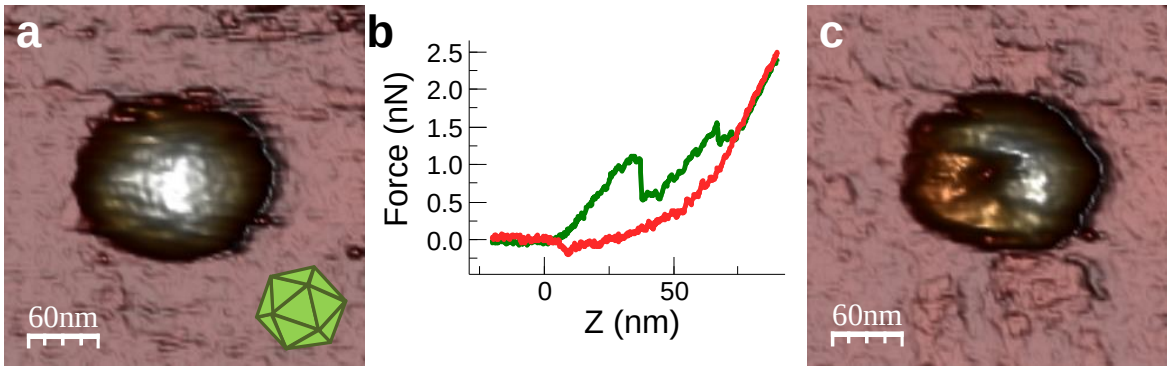

Figure 2.14 Individual AFM nanoindentation assay. a) P22 VLP in a 3-fold symmetry (S3) orientation before the indentation. The inset shows a schematic view of this symmetry. b) FZ curve performed on the VLP in a). c) P22 VLP after the nanoindentation. The breakage of the capsid can be clearly seen.

From the FZ curve in figure 2.14b both the rigidity (k, elastic constant) and the strength of the particle (F_{break}, breaking force) can be obtained, resulting in k ~ 0.25 N m^{-1} and F_{break} ~ 1.2 nN respectively. These values are compatible with the previous work by Llauró *et al.* [13] assessing the operational capabilities of the system.

Finally, simultaneous AFM and TIRFM measurements were performed to ensure the proper functioning of the combined system. To this end, 100 nm diameter commercial fluorescent beads from TetraSpeck™, in a PBS 100 mM phosphate, 50 mM NaCl buffer solution, were drop-casted on a silanized glass coverslip [15] and left to adsorb for 5 minutes. Then buffer was replaced with clean buffer to remove as much as possible beads that were not adsorbed. Sample preparation and optical adjustments were carried out by Francisco Moreno-Madrid. Figure 2.15 shows a TIRFM image of the glass coverslip with adsorbed beads.

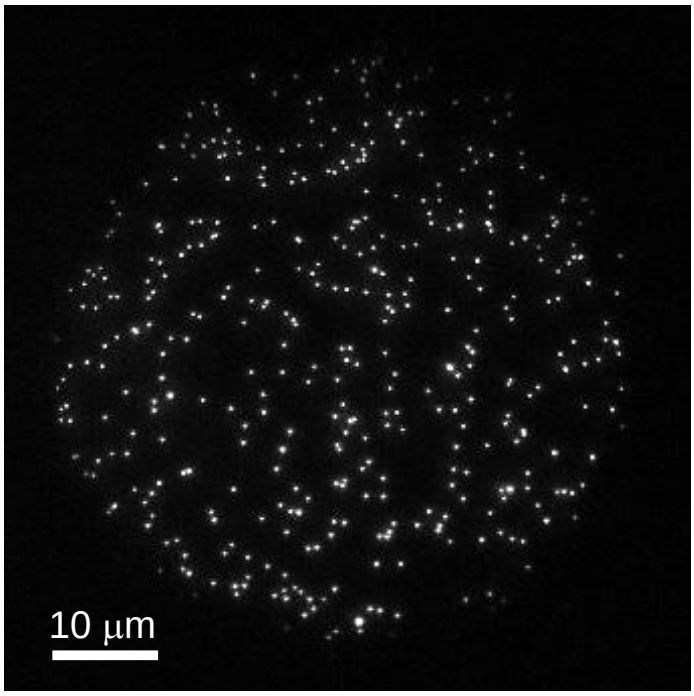

Figure 2.15 TIRFM image of 100 nm diameter commercial fluorescent beads adsorbed on a silanized glass coverslip.

To demonstrate the simultaneous AFM/TIRFM capabilities, imaging and nanomanipulation of beads with the AFM tip was performed (figure 2.16).

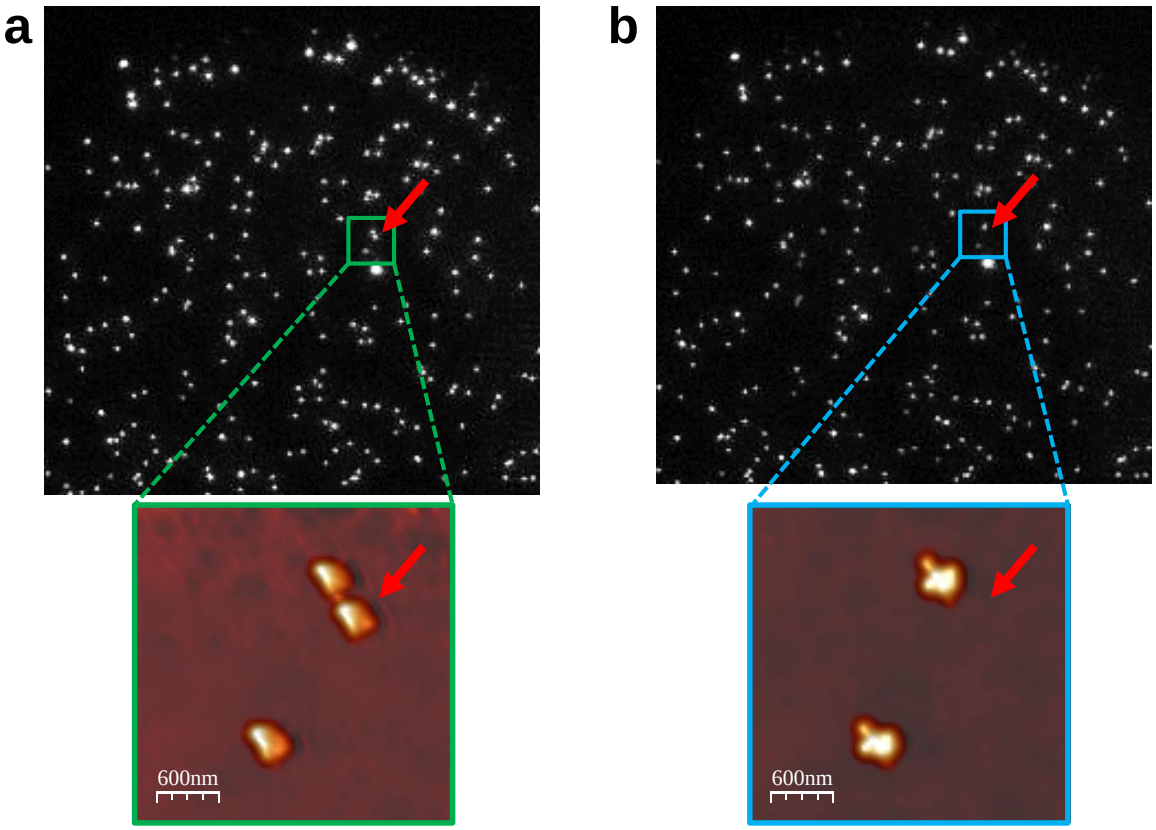

Figure 2.16 Simultaneous AFM/TIRFM. a) Top panel: TIRFM image of 100 nm diameter fluorescent beads. Bottom panel: Simultaneous AFM topographic image of the region enclosed by the green square. b) Same as a) after performing a nanomanipulation with the AFM tip. The bead marked with the red arrow was deliberately picked up with the AFM tip.

Beads in figure 2.16 were scanned in AM-AFM mode with an Olympus Biolever-mini probe (BL-AC40TS-C2). Some remaining beads in the buffer attached to the tip, thus producing a final asymmetric tip apex (this can be noticed in the AFM image of figure 2.16a, where the beads present a different shape from the expected spherical). After acquiring the AFM image in figure 2.16a, the scan was stopped and the tip was moved in Contact mode, along a horizontal line passing through the bead marked with a red arrow in figure 2.16. In this way, the bead was picked up by the AFM tip. A video acquired with the TIRFM showing the AFM nanomanipulation is available in the following link (link to a powerpoint file, to see the video please download it an open it with powerpoint):

https://www.dropbox.com/s/22o6b5ej9eosfne/AFM-TIRFM_nanomanipulation.pptx?dl=0

Figure 2.16b shows the TIRFM and AFM images after the nanomanipulation. The bead marked with the red arrow was picked up by the AFM tip, thus disappearing from the images. Please notice the change in the shape of the beads in the AFM image in figure 2.16b due to a change in the tip apex when picking up the bead. These measurements demonstrate the simultaneous AFM/TIRFM capabilities and give an idea of the kind of experiments that will be accessible with the developed system.

2.3 Variable-temperature ambient-controlled motorized Probe Station

2.3.1 Design

As mentioned in the introduction, this original developed probe station system allows measuring the electrical properties of micro- and nano-objects as a function of the temperature, from 80 to 400 K, and in different environments and/or conditions (high vacuum, low temperature, air ambient or controlled gas atmospheres). The main novelty of the probe station presented here consists in the design and construction of X, Y, Z motorized compact stages, compatible with these temperature and atmosphere conditions, to position the probes with nanometer resolution. Piezo LEGS® Linear 6N LL10 motors combined with linear translation guides (figure 2.2a) were used. Figure 2.17 shows the design of the stage.

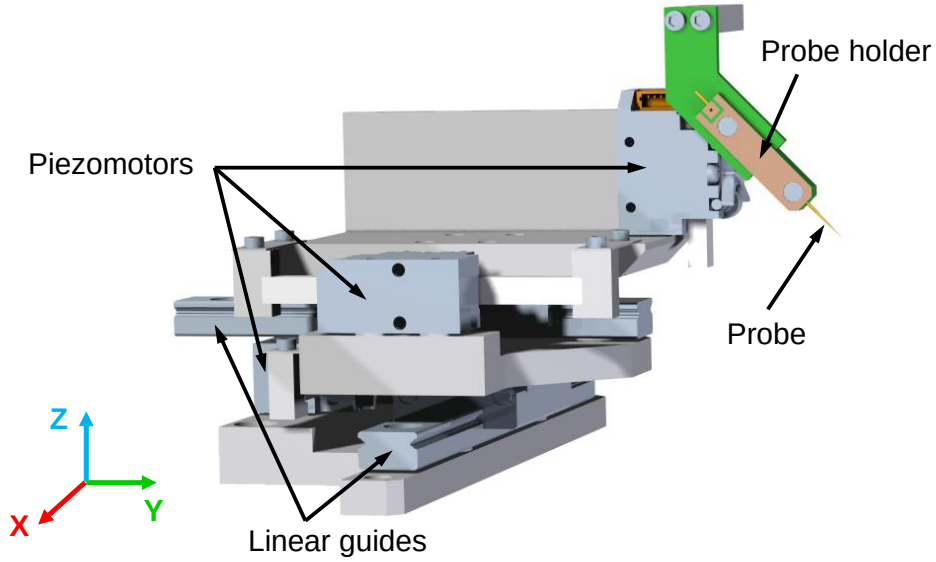

Figure 2.17 3D rendered view of the XYZ motorized stage designed showing its different parts.

Coupling parts to assembly the stage were made on aluminum. The size of the whole X, Y, Z assembly is ~ 110 x 100 x 70 (mm), although it could be easily reduced to ~ 70 x 70 x 70 (mm) if necessary by using shorter linear guides. The probe holder was made directly on printed circuit boards, providing the necessary electrical connections for the probe. Commercial probe holders could be used by simply replacing the corresponding coupling part to the piezomotor into a suitable one. The total motion range in X, Y and Z directions is 25 x 25 x 20 (mm) respectively with a minimum step size of ~ 2 nm.

An existing vacuum chamber in the laboratory was chosen for the probe station; therefore all the necessary parts were designed to fit the whole system into this chamber. Figure 2.18 shows a schematic view of the different components in the system.

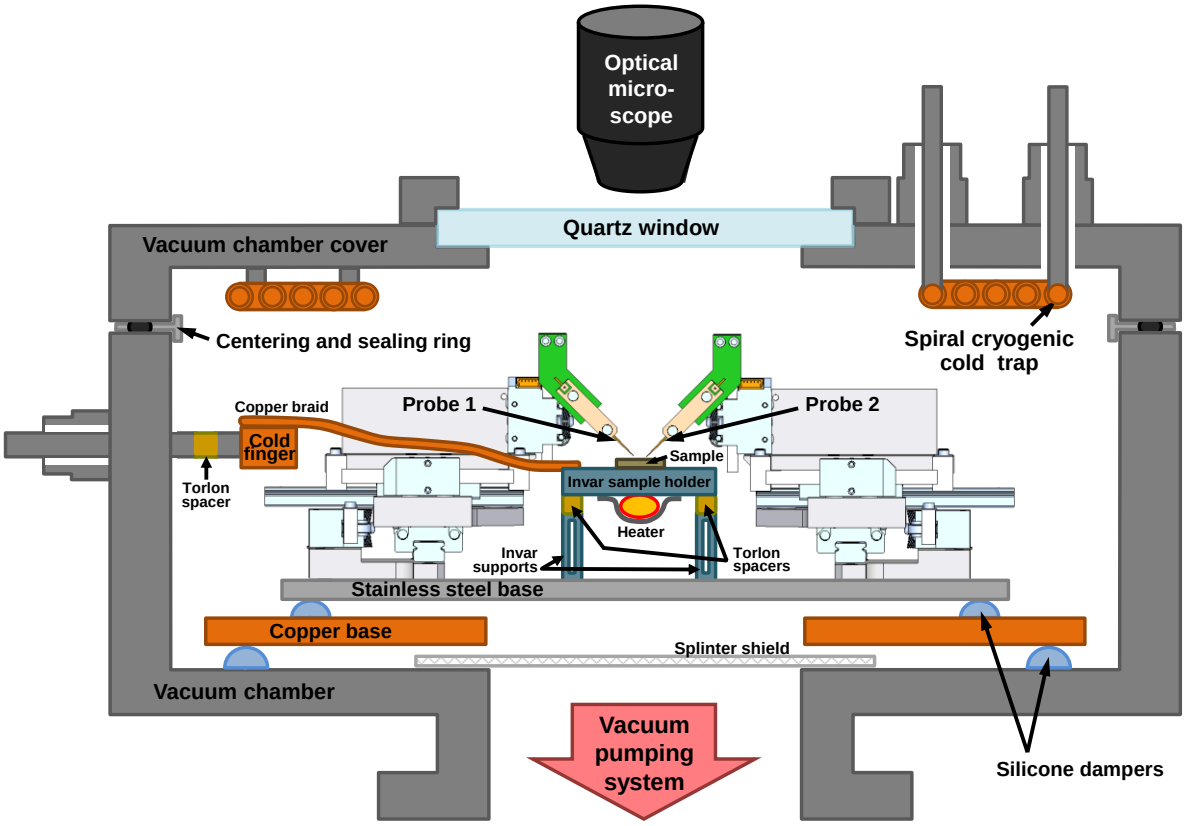

Figure 2.18 Schematic representation of the different elements in the system.

The design presented here was assembled in a two-terminal probe plus a gate electrode configuration, but it considers as well a four-terminal probe [16] arrangement for a future upgrade.

The system comprises a vacuum chamber where the vacuum pumping system was placed at the bottom (it could be placed on one side of the chamber to allow optical access from the bottom if necessary). A splinter shield was added to avoid damaging the pumping system. A turbo pumping station (HiCube Eco 80 from Pfeiffer Vacuum [17]) composed of a diaphragm pump and a turbopump was selected, reaching a pressure of ~ 10^{-4} hPa in 15 minutes and a base pressure of 1.10^{-6} hPa.
A special cover was designed for the top part of the chamber, allowing optical access through a quartz window. Quartz was selected because of its wide transparency range,

which extends from the UV to the near IR, allowing the use of different illuminations, in case of photoinduced electrical transport measurements or the study of luminescent materials. The cover includes a spiral cryogenic cold trap, consisting of a copper tube circuit with spiral geometry which is filled with liquid nitrogen (LN_2). This trap is cooled down before cooling the sample when at least a pressure of ~ 10^{-4} hPa is reached, to condense the remaining water vapor on the chamber. In this way, water condensation on the sample is prevented and at the same time the vacuum is improved.

The stage where the probe station is placed is composed of two different bases with separating silicon dampers for better vibration isolation: a first copper base, initially intended as well to work as a cryogenic cold trap (but this function was later discarded due to its low cool efficiency) and a stainless steel base, where the motorized stages and the sample holder are fixed.

The sample holder initially consisted on a copper element directly attached to a LN_2 cold finger, but preliminary tests showed some thermal drift when changing the temperature. Thermal drift represents a major inconvenience because the thermal expansion/contraction of the sample holder as the temperature changes results in tips-substrate displacements that can damage the tips and/or the sample [18]. The normal procedure to overcome thermal drift is to lift the probe tips as the temperature changes, but this is tedious and time-consuming. To minimize thermal drift, the sample holder was modified to be an invar plate attached to the stainless steel base through invar supports. Invar, also known generically as FeNi36, is a nickel-iron alloy notable for its uniquely low coefficient of thermal expansion, thus minimizing thermal drift when changing the temperature. In addition, the sample holder was not directly attached to the cold finger, but coupled to it through a flexible copper braid, thus minimizing the mechanical strain induced by thermal expansion. Moreover, each probe holder consists of two specific printed circuit boards that hold the tip in between by magnetic actuation. This fixing mechanism allows the tips to slightly accommodate their position to partly counteract thermal drift displacements. More sophisticated flexible probe tips [18] could be adapted to this design.

A halogen lamp placed on the sample holder bottom acts as a heater. Cold finger and heater actuations allow sample temperatures from 80 to 400 K. Pt100 platinum resistance thermometer elements were used in both the cold trap and the sample holder to measure their temperatures.

Maximum sample size is 30 x 26 x 15 (mm), thus allowing 1” diameter wafers. Figure 2.19 shows photographs of the probe station system assembly and its different parts.

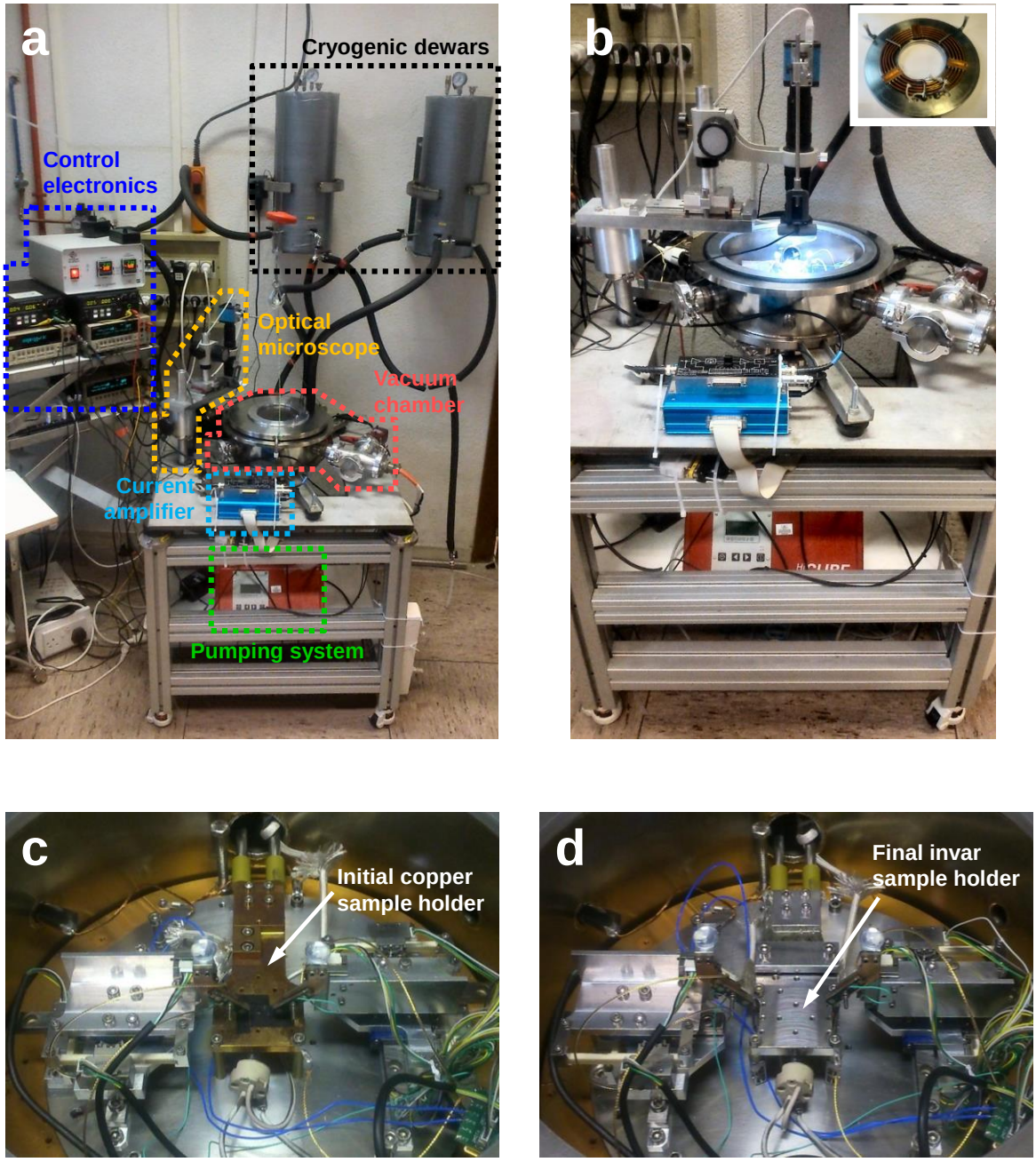

Figure 2.19 Probe station system. a) Total assembly. The different parts of the system are highlighted. b) Detail of the vacuum chamber without the cover and with the optical microscope at its measuring position. Inset in the top right corner corresponds to the inside part of the cover, showing the spiral cryogenic cold trap. c) Initial design of the probe station with a copper sample holder directly attached to the cold finger. d) Final design with an invar sample holder coupled to the cold finger through a copper braid.

The final setup replaced the previous probe station in the laboratory (operated in ambient conditions through manual actuators), taking advantage of all its electronic equipment for electrical measurements (Keithley 2400 sourcemeter, Keithley 2000 multimeter and variable-gain low noise current amplifier DLPCA-200). The high vacuum chamber was grounded to provide electromagnetic shielding to the probe station, preventing noise pick-up. The sample holder of the new probe station was electrically isolated from the rest of the chamber through Torlon® spacers (Torlon® is an easy-to-machine polyamide-imide which presents strength comparable with metal in a wide temperature range and high vacuum compatibility). These spacers isolate the sample holder both from the stainless steel base and the cold finger, thus enabling to apply a gate voltage to the sample holder for field-effect transistor (FET) configuration measurements. When using a gate voltage, it imposes an electric field into the device, which in turn attracts or repels charge carriers to or from the region between a source terminal and a drain terminal. The density of charge carriers in turn influences the conductivity between the source and drain. Figure 2.20 shows a schematic representation of the electrical circuit on the designed two-terminal probe station.

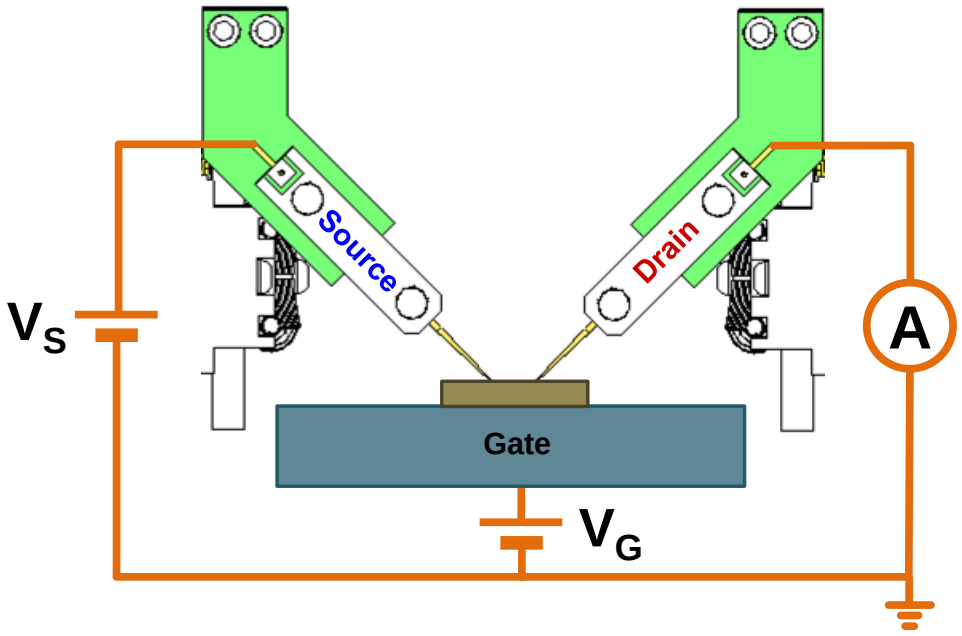

Figure 2.20 Schematic representation of the electrical circuit. **A** represents a variable gain low noise current amplifier. V_S and V_G are the voltages applied to source and gate respectively.

2.3.2 Operation and Results

First measurements were carried out in ambient conditions at room temperature with test resistors to check the proper functioning of the whole system. Resistors with nominal resistances of 0.1, 1, 10 and 100 MΩ were contacted with standard probe station tips. Figure 2.21 shows the IV curves acquired for each resistor, where the most suitable current amplifier gain was selected for each of the cases.

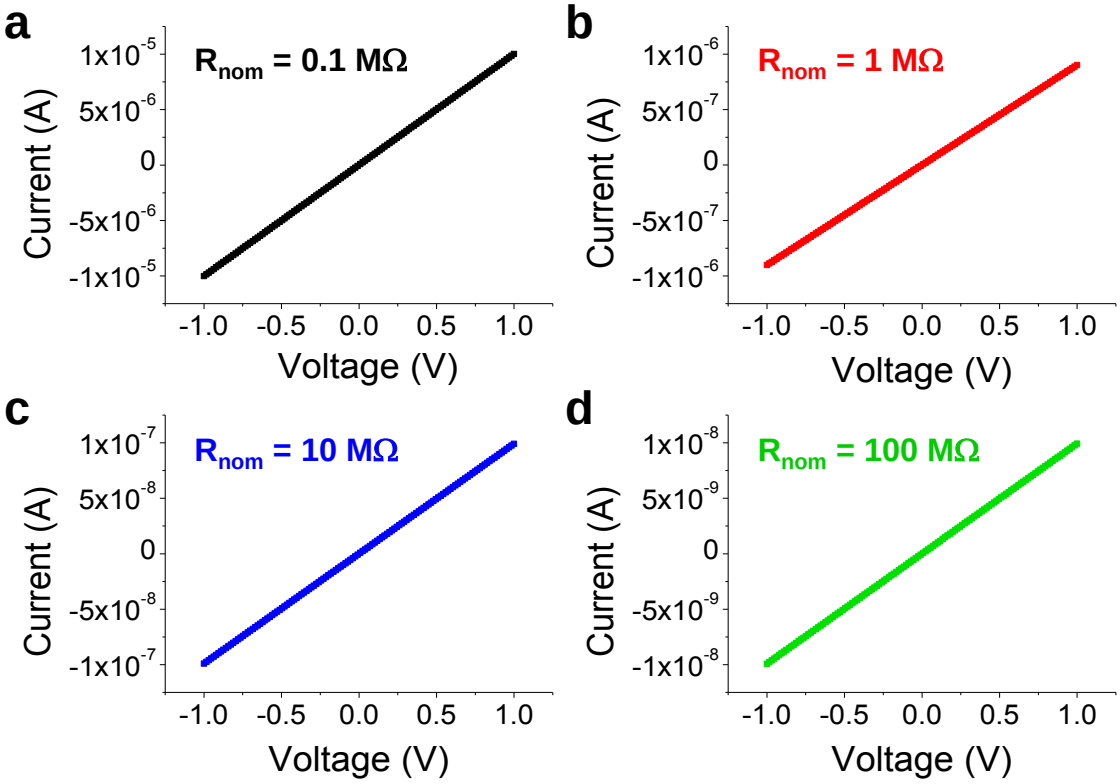

Figure 2.21 Initial probe station tests with different commercial resistors. IV curves for resistors of nominal resistances (R_{nom}) a) 0.1, b) 1, c) 10 and d) 100 MΩ respectively.

As it can be seen, the IV curves exhibit very low noise without traces of 50 Hz noise pick-up components, not even for the lowest currents measured, in the order of nA, in figure 2.21d. From the slopes of the IV curves the resistance values for each resistor can be calculated. Table 2.1 summarizes the obtained results.

Table 2.1 Resistance values of the commercial resistors used to test the probe station. R_{nom} refers to the nominal resistance values. R_{mult} and R_{ps} refer to the values measured with a multimeter and with the probe station respectively.

R_{nom} (MΩ)	R_{mult} (MΩ)	R_{ps} (MΩ)
0.1	0.099	0.100
1	1.100	1.108
10	10.100	10.090
100	100.351	100.300

The number of decimals of the resistance values corresponds to the precision given by the multimeter (the electronic equipment of the probe station, mentioned above, allows for better data precision).

Resistance values obtained with the probe station show a very good agreement with the values measured using a multimeter, confirming the proper functioning of the probe station.

After the resistors measurements, a "real" well-known sample was loaded into the probe station to further check the proper system operation. Single-wall carbon nanotubes grown by Chemical Vapor Deposition (CVD) on a 300 nm SiO_2/Si substrate were employed (sample courtesy of Dr. Cristina Gómez-Navarro). Figure 2.22 shows an optical microscopy image of the sample, were Au/Pd microelectrodes terminated in square pads for the probes positioning were fabricated by e-beam lithography. Some of these microelectrodes were connected through a carbon nanotube (not visible in the optical image).

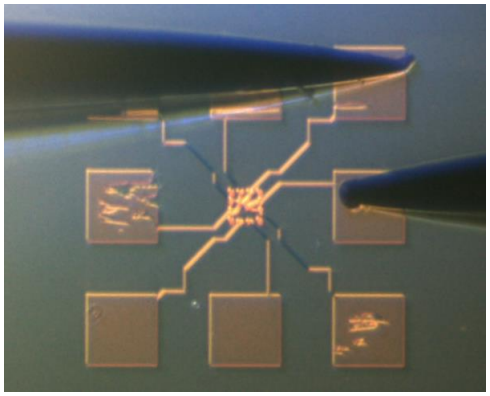

Figure 2.22 Optical micrograph of the single-wall carbon nanotubes sample with gold microelectrodes. The probes were positioned in contact with the square pads to perform electrical characterization.

Measurements on a FET-like configuration were performed. Voltage ramps from -1.4 to +1.4 V were applied to the source terminal (V_S) while the gate voltage (V_G) was varied from -5 to +5 V in 1 V steps. Current was then measured at the drain terminal (I_D). Figure 2.23 shows the results of these measurements.

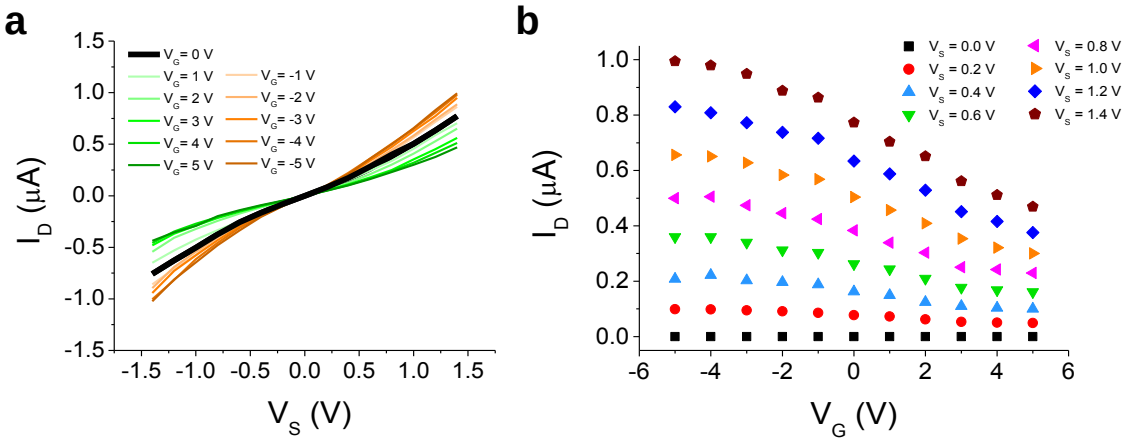

Figure 2.23 Electrical characterization of a single-wall carbon nanotube in ambient conditions in a FET-like configuration. a) I_D–V_S curves for various values of V_G. b) I_D–V_G for various values of V_S.

The electric field of the gate electrode couples to the nanotubes. As it can be seen in figure 2.23, for negative V_G this leads to an accumulation of holes and an increasing conductance, whereas for a positive V_G the holes are depleted, yielding a lower conductance, in good agreement with the literature [19, 20].

The probe station is currently a central element for the electrical characterization of $[Cu_{2.6}I_{2.6}(TAA)]_n$ (TAA = Thioacetamide) nano-films, a new 2D coordination polymer synthesized by Dr. Félix Zamora's group. Measurements performed at variable temperature (85 - 373 K) are being carried out by Miriam Moreno-Moreno and Dr. Cristina Gómez-Navarro. These nano-films are a very promising new 2D material because of their cheap production in high quantities, easy preparation, high transparency (transmittance higher than 80% in the visible spectrum) and high conductivity. Figure 2.24 presents electrical characterization at different temperatures of a ~ 10 nm thick $[Cu_{2.6}I_{2.6}(TAA)]_n$ film deposited on a 300 nm SiO_2/Si substrate.

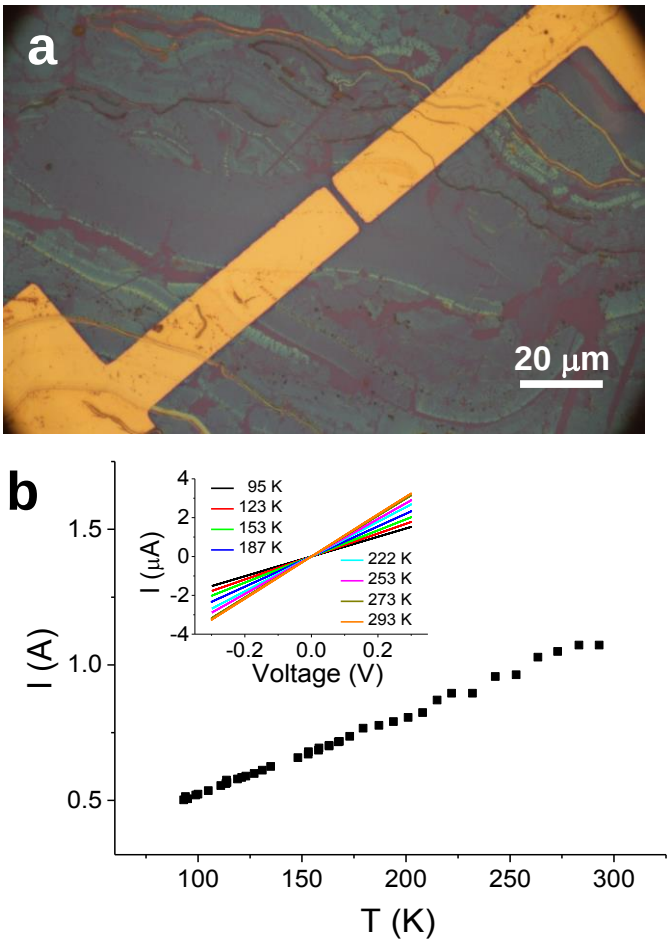

Figure 2.24 Electrical characterization of a $[Cu_{2.6}I_{2.6}(TAA)]_n$ nano-film at different temperatures. a) Optical microscopy image. Blueish areas correspond to the nano-film, where the different colors reflect different film thicknesses. The thinner part of the film, corresponding to the central part of the image, is ~ 10 nm thick. Gold electrodes for probe station measurements are also visible. b) Current at a fixed voltage of 0.1 V as a function of the temperature for the nano-film. Inset shows IV characteristics at selected temperatures.

Figure 2.24a shows an optical microscopy image of the nano-film under study. The different colors reflect different film thicknesses: purple color corresponds to the SiO_2 substrate, faint blue areas correspond to the thinner film areas (thickness ~ 10 nm) whereas brighter blue/green/yellow colors reflect areas of the film with higher thicknesses. The nano-film was in contact with ~ 100 nm thick gold electrodes evaporated on it using stencil masks. The gap between electrodes is ~ 2 - 3 μm. Figure 2.24b presents the electrical characterization of the nano-film at different temperatures, ranging from 93 K to room temperature. For this purpose, once the sample was loaded into the developed probe station, it was first cooled down to 93 K and then slowly heated up, taking IV characteristics at different temperatures up to room temperature. The inset in figure 2.24b presents some of these IV characteristics.

These films present an electrical conductivity up to 30 S cm^{-1}. They show linear IVs and a decreasing conductivity with decreasing temperature. This observation can be ascribed to a highly p-doped conductor with weak disorder. Nevertheless, the complexity of this kind of materials does not allow for a straightforward interpretation of the underlying mechanisms responsible for the observed behaviour. Further experiments on these nano-films are being carried out during the writing of this manuscript to better understand their properties.

It is important to remark that the developed probe station proved crucial for the study of the electrical properties of such kind of nano-films, otherwise inaccessible with a room temperature probe station. The electrical characterization performed on these nano-films at different temperatures demonstrates that the probe station is ready and give an idea of the kind of experiments that will be accessible with it.

Electrical transport in coordination polymers is studied within the framework of several consecutive National projects and it is a long standing tradition in our group. The study on the $[Cu_{2.6}I_{2.6}(TAA)]_n$ nano-film can be considered as a natural extension of the work that will be later described in Chapters 3 and 4, on the electrical conductance of 1D MMX coordination polymers, that revealed the necessity of this new experimental setup in the laboratory.

2.4 Conclusions

The original design, construction and first measurements of two different instrumental developments have been presented: a new AFM setup designed to allow measurements simultaneously with TIRFM and a probe station setup for the electrical characterization of micro- and nano- materials and devices at temperatures ranging from 80 K to 400 K in a controlled atmosphere.

Both developments are linked by the need of fully motorized control of the X, Y and Z movements of the different elements with submicron resolution. This has been successfully addressed by using piezoelectric actuators, allowing travelling speeds of several centimeters per second, precise sub-micron/nanometer positioning and no need for gears or mechanical transmission with power-off locking. Acquired experience from my previous position at Nanotec Electrónica S.L. with this type of linear actuators has been fundamental for the efficient developments of both setups.

On the course of this PhD, several ideas about new experiments in 2D materials and biophysics came up originated by investigations related to the results reported here. These ideas required the implementation of the instrumental developments described in this chapter. As frequently happens, this instrumentation is inherited by new members of the research group that carry out these experiments. This is certainly the case along this PhD. The goal of this chapter has been to describe the proper functioning and capabilities of the developed systems. In addition, the two instruments presented here not only will allow experiments that were inaccessible in the group, but they will open new lines of research and collaborations with other groups, enabling the advance of different research fields.
In the case of the AFM/TIRFM combination, a collaboration with Prof. Trevor Douglas (Indiana University) will study the disassembly of P22 VLPs internally functionalized with green fluorescence protein (GFP). The plan consists on monitoring GFP diffusion upon mechanical unpacking of single nano-cages with different GFP functionalization. While in immature P22 particles, GFP is bound to the inner wall, it detaches during maturation and GFP becomes free within mature P22 particles [21]. The different structure of both particles would result in different diffusion rates after the particle is broken. Simultaneous AFM/TIRFM measurement of this system will shed light on the mechanisms governing the behavior of VLPs loaded with a foreign cargo. This knowledge will help to improve the design of nano-containers for their use in biotechnological applications.
In the case of the probe station setup, collaboration with Dr. Félix Zamora group (Universidad Autónoma de Madrid) is ongoing to study the electrical properties of coordination polymers, based on Cu(I)-X (X are halides: Cl^-, Br^-, I^-) with general formula $[CuX(L)]_n$, where L is an organic ligand, as pyrazine, pyridines or other ligands with molecular recognition capabilities. These compounds are clear examples of the so-called smart materials (designed materials with one or more properties that can be significantly modified in a controlled way by external changes in their environment). Their

characterization at low temperatures is relevant to gain insight on their intrinsic conductivity character, possible phase transitions or luminescent behaviors, among others [22]. Their study in different atmospheres is also interesting due to their possible application as gas sensors [23].

2.5 References

[1] Ambrose, E. J. Surface Contact Microscope for the Study of Cell Movements. *Nature* **1956,** *178*, 1194-1194.

[2] Axelrod, D. Cell-Substrate Contacts Illuminated by Total Internal-Reflection Fluorescence. *J. Cell Biol.* **1981,** *89*, 141-145.

[3] Ortega-Esteban, A.; Bodensiek, K.; San Martin, C.; Suomalainen, M.; Greber, U. F.; de Pablo, P. J.; Schaap, I. A. T. Fluorescence Tracking of Genome Release during Mechanical Unpacking of Single Viruses. *ACS Nano* **2015,** *9*, 10571-10579.

[4] Pohl, D. W. Some Design Criteria in Scanning Tunneling Microscopy. *IBM J. Res. Dev.* **1986,** *30*, 417-427.

[5] Horcas, I.; Fernandez, R.; Gomez-Rodriguez, J. M.; Colchero, J.; Gomez-Herrero, J.; Baro, A. M. WSXM: A software for scanning probe microscopy and a tool for nanotechnology. *Rev. Sci. Instrum.* **2007,** *78*, 013705.

[6] Ortega-Esteban, A.; Horcas, I.; Hernando-Perez, M.; Ares, P.; Perez-Berna, A. J.; San Martin, C.; Carrascosa, J. L.; de Pablo, P. J.; Gomez-Herrero, J. Minimizing tip-sample forces in jumping mode atomic force microscopy in liquid. *Ultramicroscopy* **2012,** *114*, 56-61.

[7] Schoner, H. P. Piezoelectric Motors and their Applications. *Eur. T. Electr. Pow.* **1992,** *2*, 367-371.

[8] http://www.piezomotor.com/.

[9] https://www.plm.automation.siemens.com/es_es/products/solid-edge/.

[10] https://www.physikinstrumente.com/en/.

[11] http://www.nanosensors.com/.

[12] Moreno-Herrero, F.; Colchero, J.; Baro, A. M. DNA height in scanning force microscopy. *Ultramicroscopy* **2003,** *96*, 167-174.

[13] Llauro, A.; Schwarz, B.; Koliyatt, R.; de Pablo, P. J.; Douglas, T. Tuning Viral Capsid Nanoparticle Stability with Symmetrical Morphogenesis. *ACS Nano* **2016,** *10*, 8465-8473.

[14] http://probe.olympus-global.com/en/.

[15] Michel, J. P.; Ivanovska, I. L.; Gibbons, M. M.; Klug, W. S.; Knobler, C. M.; Wuite, G. J. L.; Schmidt, C. F. Nanoindentation studies of full and empty viral capsids and the effects of capsid protein mutations on elasticity and strength. *Proc. Natl. Acad. Sci. U.S.A.* **2006,** *103*, 6184-6189.

[16] Valdes, L. B. Resistivity Measurements on Germanium for Transistors. *Proc. IRE* **1954,** *42*, 420-427.

[17] https://www.pfeiffer-vacuum.com/en/.

[18] Lindemuth, J., Variable Temperature Measurements in Cryogenic Probe Stations. In *Frontiers of Characterization and Metrology for Nanoelectronics*, Seiler, D. G.; Diebold, A. C.; McDonald, R.; Garner, C. M.; Herr, D.; Khosla, R. P.; Secula, E. M., Eds. 2009; Vol. 1173, pp 343-345.

[19] Martel, R.; Schmidt, T.; Shea, H. R.; Hertel, T.; Avouris, P. Single- and multi-wall carbon nanotube field-effect transistors. *Appl. Phys. Lett.* **1998,** *73*, 2447-2449.

[20] Tans, S. J.; Verschueren, A. R. M.; Dekker, C. Room-temperature transistor based on a single carbon nanotube. *Nature* **1998,** *393*, 49-52.

[21] Llauro, A.; Luque, D.; Edwards, E.; Trus, B. L.; Avera, J.; Reguera, D.; Douglas, T.; de Pablo, P. J.; Caston, J. R. Cargo-shell and cargo-cargo couplings govern the mechanics of artificially loaded virus-derived cages. *Nanoscale* **2016,** *8*, 9328-9336.

[22] Amo-Ochoa, P.; Hassanein, K.; Gomez-Garcia, C. J.; Benmansour, S.; Perles, J.; Castillo, O.; Martinez, J. I.; Ocon, P.; Zamora, F. Reversible stimulus-responsive Cu(I) iodide pyridine coordination polymer. *Chem. Commun.* **2015,** *51*, 14306-14309.

[23] Hassanein, K.; Amo-Ochoa, P.; Gomez-Garcia, C. J.; Delgado, S.; Castillo, O.; Ocon, P.; Martinez, J. I.; Perles, J.; Zamora, F. Halo and Pseudohalo Cu(I)-Pyridinato Double Chains with Tunable Physical Properties. *Inorg. Chem.* **2015,** *54*, 10738-10747.

2.6 Appendix

Piezo LEGS® Linear 6N LL10 motor specifications

Type	Stainless Steel LL1011A	Unit	Note
Maximum Stroke	80 (L-20.8)	mm	100.8 mm rod, no mechanical adapter
Speed Range (a)	0-15	mm/s	recommended, no load
Step Length (b)	4 0.0005 (c)	µm µm	one wfm-step one microstep (c)
Resolution	< 1	nm	driver dependent
Recommended Operating Range	0-3	N	for best microstepping performance and life time
Stall Force	6.5	N	
Holding Force	7	N	
Vaccum	–	torr	
Maximum Voltage	48	V	
Power Consumption (d)	5	mW/Hz	=0.5 W at 100 Hz wfm-step frequency
Connector	JST BM05B-SRSS-TB		
Mechanical Size	22 x 19 x 10.8	mm	see drawing for details
Material in Motor Housing	Stainless Steel		
Weight	23	gram	approximate
Operating Temp.	-20 to +70	ºC	

(a) Max value is typical for waveform Rhomb at 2 kHz, no load, temperature 20ºC.

(b) Typical values for waveform Delta, 3 N load, temperature 20ºC.

(c) Driver dependent; 8192 microsteps per wfm-step for driver in the PMD200-series.

(d) At temperature 20ºC, intermittent runs.

Note: All specifications are subject to change without notice.

Critical parameters appear highlighted.

Piezo LEGS® Linear Twin-C 20N LTC20 motors specifications

Type	**LTC2014-013 Nut Mount**	**Unit**	**Note**
Maximum Stroke	12.8	mm	
Speed Range (a)	0-10	mm/s	recommended, no load
Step Length (b)	2.5 0.0003 (c)	µm	one wfm-step one microstep (c)
Resolution	< 1	nm	driver dependent
Recommended Operating Range	0-10	N	for best microstepping performance and life time
Stall Force	20	N	
Holding Force	22	N	
Maximum Voltage	48	V	
Power Consumption (d)	10	mW/Hz	=1 W at 100 Hz wfm-step frequency
Connector	USB mini-B		
Mechanical Size	51.2 x 27 x 21	mm	see drawing for details
Material in Motor Housing	Stainless Steel, Aluminium		
Weight	95	gram	approximate
Operating Temp.	0 to +50	ºC	

(a) Max value is typical for waveform Rhomb at 2 kHz, no load, temperature 20ºC.

(b) Typical values for waveform Delta, 10 N load, temperature 20ºC.

(c) Driver dependent; 8192 microsteps per wfm-step for driver in the PMD200-series.

(d) At temperature 20ºC, intermittent runs.

Note: All specifications are subject to change without notice

Critical parameters appear highlighted.

P-733.3DD piezo scanner specifications

	P-733.3DD	Unit	Tolerance
Active axes	X, Y, Z		
Motion and positioning			
Integrated sensor *	Capacitive		
Open-loop travel, -20 to 120 V	33 µm × 33 µm × 14 µm		min. (20 % / -0 %)
Closed-loop travel	30 µm × 30 µm × 10 µm		
Open-loop resolution	0.1	nm	typ.
Closed-loop resolution	0.1	nm	typ.
Linearity error (X, Y)	0.03*	%	typ.
Linearity error (Z)	0.03*	%	typ.
Repeatability (X, Y)	<2	nm	typ.
Repeatability (Z)	<1	nm	typ.
Pitch (X,Y)	<±5	µrad	typ.
Yaw (X, Y)	<±10	µrad	typ.
Runout θZ (motion in Z)	<±5	µrad	typ.
Mechanical properties			
Stiffness	4 (10 in Z)	N/µm	±20 %
Unloaded resonant frequency	1200 (1100 in Z)	Hz	±20 %
Resonant frequency @ 120 g	–	Hz	±20 %
Resonant frequency @ 200 g	530 (635 in Z)	Hz	±20 %
Push / pull force capacity in motion direction	50 / 20	N	max.
Drive properties			
Piezo ceramic	PICMA® P-885		
Electrical capacitance	6.2 (3.3 in Z)	µF	±20 %
Dynamic operating current coefficient	25 (41 in Z)	µA / (Hz × µm)	±20 %
Miscellaneous			
Operating temperature range	-20 to 80	°C	
Material	Aluminum		
Mass	0.675	kg	±5 %
Cable length	1.5	m	±10 mm
Sensor / voltage connection	Sub-D Special		

Critical parameters appear highlighted.

* A commercial PI E-509 Signal Conditioner/Piezo Servo Module unit is used to transduce the readout of the position sensors into voltages which are then simultaneously acquired with the X, Y, Z applied voltages.

Chapter 3. Methodological developments.

3.1 Introduction

3.2 AFM improvements in liquids

3.2.1 High resolution Atomic Force Microscopy of double-stranded RNA in liquid by different high-sensitive force-detection methods

3.2.1.1 Introduction

3.2.1.2 Results and discussion

3.2.2 Magnetic Force Microscopy in liquids

3.2.2.1 Introduction

3.2.2.2 Results and discussion

3.3 New approaches to nano-object electrical contacts

3.3.1 Exfoliated graphite flakes as soft-electrodes

3.3.1.1 Introduction

3.3.1.2 Results and discussion

3.3.2 Probe-Assisted Nanowire (PAN) lithography: a new paradigm for nanoelectrode fabrication

3.3.2.1 Introduction

3.3.2.2 Results and discussion

3.4 Conclusions

3.5 References

3.1 Introduction

In this chapter four different methodological developments carried out during this PhD are presented. They can be classified in two different groups: the first two developments are related to the improvement of the AFM technique in liquid environments. The other two developments deal with the fabrication of simple, clean and reliable electrodes for the electrical contact of nano-objects.

In the group related to AFM measurements in liquids, the first development consists on the optimization of the high resolution acquisition conditions to image nucleic acids in liquids, using different high-sensitive force-detection methods. It is commonly accepted that FM-AFM in liquids can provide higher resolution than other imaging modes. Images of double-stranded RNA with similar spatial resolution are obtained independently of the mode, pointing towards that the limiting factors for high resolution AFM imaging of soft material in liquid media are, rather than the imaging mode, the force between tip and sample and the sharpness of the tip apex.
The second development presents Magnetic Force Microscopy (MFM) to acquire images of magnetic nanostructures in liquid environments. There is an increasing role of magnetic nanostructures in fields such as medicine, biotechnology or catalysis. Nevertheless, a suitable technique to study their individual magnetic properties in physiological conditions (where soft biological samples are not subjected to changes in their structure), with the resolution and sensitivity needed was still lacking. The ability for detecting magnetic nanostructures, along with the well-known capabilities of AFM in liquids to study biological material, suggests it as a potential technique to perform these studies. Optimization of the MFM signal acquisition in liquid media is performed and it is applied to characterize the magnetic signal of magnetite nanoparticles.

In the group related to the fabrication of electrical contacts again we follow a long standing tradition in the laboratory. The first development is based on the deterministic transfer of exfoliated graphite flakes by all-dry viscoelastic stamping to create soft-electrodes. The second development consists on the creation of gold nanoelectrodes by drop-casting deposition and subsequent AFM manipulation of gold nanowires. Conventional methods to fabricate micro- and nanoelectrodes require much more time, resources and/or conditions that some samples cannot withstand. The two approaches presented here provide easy, clean, good quality and cost-effective solutions as alternatives to standard techniques. These methods are particularly useful in the case of molecules with limited stability under standard lithographic conditions. Both procedures are particularly relevant for conductive atomic force microscopy (C-AFM) studies. Moreover, they are much more general techniques and, in the gold nanowires case, due to its ability to easily create nanoelectrodes that could even contact nano-objects with dimensions down to tens of nm, we think it could replace standard lithographic techniques used in nanotechnology such as e-beam lithography.

3.2 AFM improvements in liquids

3.2.1 High resolution Atomic Force Microscopy of double-stranded RNA in liquid by different high-sensitive force-detection methods

3.2.1.1 Introduction

Since the determination of the double helix structure of dexoyribonucleic acid (DNA) in 1953 by James Watson and Francis Crick [1], nucleic acids attract a lot of attention and resources. These molecules, which include both DNA and RNA (ribonucleic acid) and other synthetic derivatives recently discovered (see for instance peptide nucleic acid, PNA [2]) are the cornerstone of biology, since they code the genetic information of living beings including animals, plants, microorganisms, viruses, etc... Many techniques, such as scanning probe microscopies are employed to study their properties. For many years, RNA was considered only as the molecule involved in the readout of information stored in DNA. Nowadays, it is known that RNA plays also critical roles not only in transmission but also in gene regulation, and that it can even be catalytic, carrying out biochemical reactions like proteins do. RNA in its double-stranded form (dsRNA) has been discovered to play as well important roles, as for instance gene silencing, activating the immune response against viral attacks or storing the genetic material of a variety of viruses, adding an additional dimension to a molecule that was primarily considered to be single-stranded, opening the door to potential biotechnological applications. Hence, the recent interest for the characterization of its mechanical properties, including single-molecule techniques such as atomic force microscopy, magnetic tweezers, and optical tweezers [3-5].

While extensive work has been already performed with dsDNA, a high resolution atomic force microscopy imaging study of dsRNA was still lacking. This was very likely because of the higher complexity of imaging the dsRNA structure, where both major and minor grooves have similar dimensions and because methods to equilibrate dsRNA molecules on flat surfaces have only been recently reported [4]. DNA helical regularity was first observed in Contact mode AFM in a seminal work by Mou *et al.* [6]. However, contact imaging proved not to be the best option for imaging biological materials, and Dynamic modes, which minimize shear forces, are usually preferred [7]. Amplitude Modulation AM-AFM is the one commonly used for both air [8, 9] and liquid environments [10, 11], and has proven to achieve high resolution on different biological samples [12-15], including dsDNA [16-19]. Other Dynamic modes such as Frequency Modulation (FM-AFM) [20-23] or Drive Amplitude Modulation (DAM-AFM) [24], have been also used to obtain high resolution in liquid medium. This degree of resolution is possible

because oscillation amplitudes are adjusted to a value in the same order as the decay length of the interaction force between tip and sample [25, 26]. Indeed, the minor and major grooves of dsDNA have been resolved in FM-AFM [27] at an unprecedented resolution. Other intermittent contact imaging modes such as PeakForce Tapping [28] or Jumping Mode plus (JM+) [29] allow detecting tip-sample interactions at angstrom precision with piconewton sensitivity and high spatial resolution. In the case of nucleic acids, Pyne and coworkers reported high resolution images of dsDNA using PeakForce AFM [19].

It is commonly accepted that the force sensitivity in FM-AFM is enhanced compared with that of other conventional AFM methods. But as mention in Chapter 1, tip contamination, which is very common when measuring biological samples under physiological conditions, results in instabilities in the FM-AFM feedback, making it difficult to operate in these conditions. In the work presented here, dsRNA has been imaged for the first time with a lateral resolution enough to resolve a ~ 1.5 nm periodicity (half a full helical turn) compatible with the A-form of dsRNA. High resolution images of dsRNA have been obtained using AM-AFM, DAM-AFM, and JM+. Simulations of AFM images of dsDNA and dsRNA with different tip radius and comparison with experimental images have been performed, to get insights of the tip radius required for high resolution imaging of these structures. As discussed below, provided a sharp tip and the best possible working conditions for each mode, high resolution on soft biological samples can be achieved in liquid environment nearly independently of the imaging mode [7, 26].

This work has been performed in collaboration with Dr. Fernando Moreno-Herrero and Prof. José M. Valpuesta groups from the Centro Nacional de Biotecnología (CNB) of the Consejo Superior de Investigaciones Científicas (CSIC). Dr. Elías Herrero-Galán has fabricated the dsRNA samples and Dr. María Eugenia Fuentes-Pérez has been in charge of sample preparations for AFM imaging. The content of this section is based on reference **Ares, P**.; Fuentes-Perez, M. E.; Herrero-Galan, E.; Valpuesta, J. M.; Gil, A.; Gomez-Herrero, J.; Moreno-Herrero, F. High resolution atomic force microscopy of double-stranded RNA. *Nanoscale* 2016, *8*, 11818-11826 (see also List of Publications).

3.2.1.2 Results and discussion

As a starting point, dsDNA was first used as a molecular standard for high resolution in AFM. dsDNA is a good benchmark to adjust the experimental and operational conditions to image nucleic acids in liquid, reproducing recently published results [18, 19, 27]. Experimental conditions compatible with different imaging modes for high resolution AFM imaging of dsDNA were set up so these could be later applied to dsRNA. Standard methods to adsorb dsDNA on mica use Mg^{2+} as divalent cation, but this methodology failed to equilibrate dsRNA on mica [3]. Therefore, Ni^{2+} was employed as a divalent cation to equilibrate both dsDNA and dsRNA molecules on mica, following published protocols [4]. As dsDNA sample, plasmid pGEM3Z (2743 bp, promega) linearized with *BamHI* and purified with a QIAquick PCR purification kit (Qiagen, Hilden, Germany) was used. dsRNA molecules were fabricated as described in [4]. Freshly-cleaved mica sheets were first treated with 10 μl of buffer A (10 mM $NiCl_2$ and 10 mM Tris-HCl pH 8.0). Then, 1 μl (0.6 ng) of dsRNA or dsDNA was added to the droplet and incubated for 15 minutes at room temperature. After incubation, 40 μl of buffer A was added to the sample and then completed with 50 μl of buffer B (10 mM Tris-HCl pH 8.0) to reach a final volume of 100 μl.

In order to compare the high resolution capability of Dynamic and Force-distance imaging modes, a cantilever suitable for both kinds of working modes was chosen. Commercial Biolever mini BL-AC40TS-C2 cantilevers from Olympus [30] were used for all the measurements. Nominal parameters of these cantilevers are: resonance frequency in air 110 kHz, resonance frequency in liquid 25 kHz, spring constant 0.09 N m^{-1} and tip radius 8 nm. Each of the cantilever spring constants were calibrated following Sader's method [31] yielding values of 0.07 ± 0.01 N m^{-1}. The combination of a relatively high resonance frequency in liquids (appropriate for Dynamic modes) and their low spring constant (required to minimize the applied load in Force-distance based imaging modes) make them ideal to compare different acquisition modes. The deflection sensitivity of the optical detection system was calibrated from force curves, resulting in ~ 9 nm/V. This very low value proved to be crucial to control the low amplitudes and forces required for high resolution imaging. Figure 3.1 shows images of dsDNA molecules adsorbed on a mica surface in liquid environment, using AM-AFM with a cantilever oscillation amplitude of 0.7 nm.

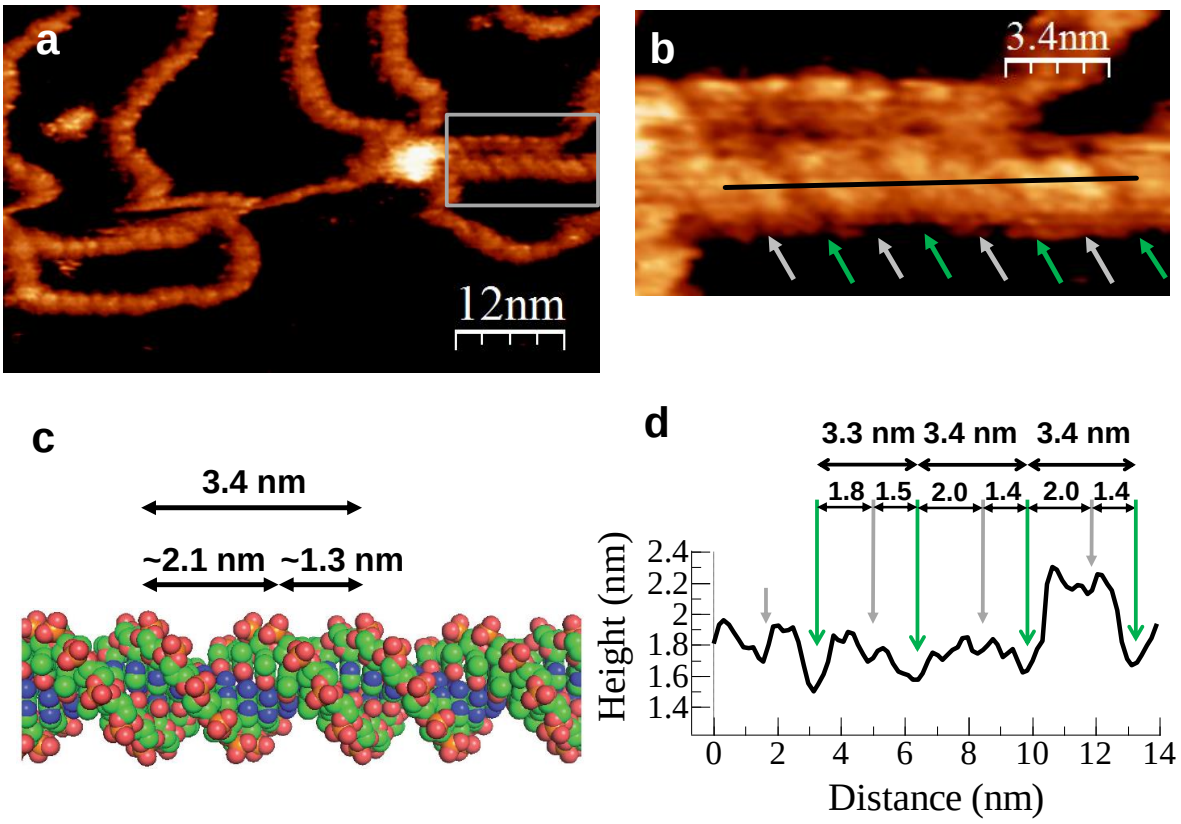

Figure 3.1 High resolution imaging of dsDNA using AM-AFM. a) Low magnification image where a periodic corrugation and a helical structure along the molecules can be seen. b) Detail at higher magnification of a) highlighting the double-band corrugation that corresponds to the major (green arrows) and minor (gray arrows) grooves. c) Model of dsDNA showing relevant dimensions. Each color represents different chemical species, red: oxygen, green: carbon, blue: nitrogen and orange: phosphorus. d) Height profile along the line in b). Color scale (from dark to bright) in a) and b) was adjusted to enhance the corrugation observed along the dsDNA (2.9 nm total range in a) and 1.7 nm in b)).

Scan rates and feedback parameters were adjusted for optimum contrast and stability. A periodic corrugation can be clearly observed within the molecules despite an obvious tip-sample dilation effect, which made dsDNA strands look wider than the expected 2 nm crystallographic width. Figure 3.1b shows this corrugation in detail. A very good agreement between the B-form model for dsDNA structure (figure 3.1c) and the profile dimensions (figure 3.1d) can be observed. The periodicity is ascribed to the major and minor grooves of the dsDNA structure with a helical pitch of 3.4 ± 0.3 nm. The resolution achieved is comparable to that reported in previous AFM studies [17-19, 27, 32], proving that the used setup provided the required stability and resolution to image nucleic acids at the nanometer scale.

Next, a similar procedure was applied to image dsRNA molecules adsorbed on mica. The sample was prepared and imaged in liquid using AM-AFM with identical imaging conditions as previously used for dsDNA. Figure 3.2 shows images of dsRNA molecules on these conditions.

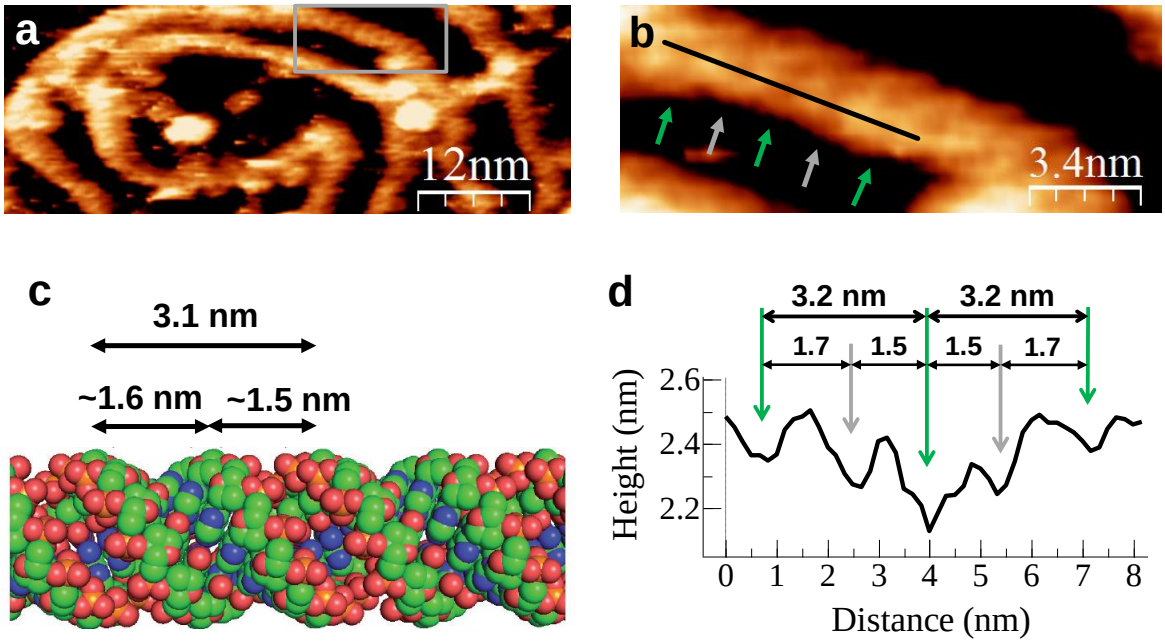

Figure 3.2. High resolution imaging of dsRNA using AM-AFM. a) Low magnification image where a narrower periodic corrugation compared to dsDNA is observed. b) Detail at higher magnification of a). Occasionally, a monotonic periodicity compatible with the presence of the major and minor grooves (marked in the figure with green and grey arrows) was observed, but this was not always achievable. c) Model of dsRNA showing relevant dimensions. Each color represents different chemical species, red: oxygen, green: carbon, blue: nitrogen and orange: phosphorus. d) Height profile along the line in b). Color scale (from dark to bright) in a) and b) was adjusted to enhance the corrugation observed along the dsRNA (1.4 nm total range in a) and 1.2 nm total range in b)).

Figure 3.2b shows in detail the corrugation observed. A distance between valleys of 1.5 - 1.7 nm is measured in the profile taken along the axis of the molecule. This distance can be ascribed, within error, to the corresponding dimensions of both the major and minor grooves of the A-form structure of dsRNA (see figures 3.2c and d). However, in most of the cases, a single periodicity of 3.2 ± 0.3 nm that coincides with the helical pitch of dsRNA could only be identified. This implies that, counter-intuitively, the minor groove of dsRNA (~ 1.5 nm) was in general more difficult to observe than the minor groove of dsDNA (~ 1.3 nm), even though the former is wider and identical working conditions were employed for imaging both samples (compare figures 3.1d and 3.2d). It could be explained by the particular orientation and distance of the phosphate groups (orange and red spheres

in models, figures 3.1c and 3.2c) of each strand of dsRNA. Whereas phosphate groups in dsDNA appear in the outer edges of the double helix pointing outwards, in dsRNA they are facing each other and leave a narrower minor groove. This particular orientation of phosphate groups in dsRNA is suggested as a possible reason for the inability to adsorb dsRNA on mica using Mg^{2+} [3], and may also explain why the AFM tip can hardly resolve the minor groove in RNA samples preventing its frequent visualization. Alternatively, if the mechanism for dsRNA adsorption to the mica surface involves base complexation with Ni^{2+} and dislocation [4], it may affect the overall secondary structure of dsRNA, hampering the visualization of the minor groove.

In order to get further insight into the mechanisms for the high resolution imaging of soft biological samples in liquids, dsRNA molecules were imaged using other AFM imaging modes: AM-AFM, DAM-AFM and JM+. Regardless of the imaging mode employed, the tip-sample coarse approach was always performed in AM-AFM mode and, once in range, the proper feedback scheme for each measuring mode was adopted (see Chapter 1 for feedback scheme diagrams for each mode), adjusting the Setpoint and the feedback parameters to values that optimize image acquisition with no sample damage, judged from repetitive imaging of the same area. Following this procedure, forces during coarse approach were minimized. The cantilever free amplitude for the approach was set to a relatively high value of ~ 7 nm, with a Setpoint of about 75% of this value. With these settings, using the *Full Auto Approach* option in the WSxM software no false engagements were detected. Once engaged, in Dynamic modes the drive amplitude was changed to reduce the cantilever amplitude to imaging values. Accordingly, the amplitude Setpoint was also reduced (0.6 - 0.7 nm), to remain just below the threshold value at which the cantilever was lifted off the sample. For JM+, Setpoints in the range of 0.05 - 0.07 V, corresponding to forces of the order of 35-50 pN, and Z excursions in the range of 15 - 35 nm were used. Table 3.1 presents a detailed summary of imaging conditions (P,I feedback values may vary among different microscopes. The values shown here could be seen as a reference for Nanotec Electronica Cervantes AFM users).

Table 3.1 Measuring and imaging parameters employed in this study

AM-AFM	
Scan rate (lines s^{-1})	3-5
Main feedback channel	Amplitude
Setpoint main feedback	0.5-0.8 nm
P,I values main feedback*	20,10
DAM-AFM	
Scan rate (lines s^{-1})	4-8
Main feedback channel	Dissipation
Setpoint main feedback	0.2-0.5 fW
P,I values main feedback*	50,25
Setpoint Amplitude (nm)	0.6
P,I values Amplitude*	8000,80
P,I values Phase*	6,12
JM+	
Scan rate (lines s^{-1})	3-4
Main feedback channel	Force
Setpoint main feedback	30-40 pN
P,I values main feedback	40,20
Amplitude of Z excursion (nm)	15-35
Frequency of Z excursion (kHz)	0.5-1
Common parameters	
Image size (nm)	50-150
Number of points per line	512
Pixel resolution (nm pix^{-1})	0.1-0.3
Cantilevers	Biolever mini BL-AC40TS-C2 k = 0.09 N/m, f_0 (liquids) = 25 kHz, nominal tip radius = 8 nm
Cantilever free amplitude for approach (nm)	~ 7
Approach Setpoint (nm)	~ 5 (75% of free amplitude)
Optical sensitivity (nm/V)	9

Areas of 1 x 1 μm^2 were first scanned at low resolution to locate molecules with straight segments over several tens of nm. Higher resolution images were recorded at scan sizes of 50 x 50 – 150 x 150 nm^2, 512 x 512 pixels (pixel resolution between 0.1 and 0.3 nm pix^{-1}) and scanning frequencies of 3-8 lines s^{-1}. The fast scan direction was preferably set to be parallel to these segments to minimize low frequency noise and to facilitate the helical pitch visualization. Indeed, helical pitch visualization was easier along the fast scan axis but it was also possible to observe the periodicity of dsRNA and dsDNA along molecules not aligned to the fast scan axis. Initially, each scan line in the image was scanned from left to right (trace direction) and from right to left (retrace direction) to check for consistency of the observed topographic features. Then, images were only acquired in trace direction to increase the scan rate. Raw images were treated with the following standard processing functions implemented in WSxM software: flatten plus background subtraction [33], artifact lines removal produced by tip attachments, Gaussian filtering and both cross-sectional and longitudinal profiles along the molecules to measure distances along these profiles. The color scales of the images were adjusted to enhance the visualization of the corrugation at the upper region of the molecules. This is why all data below a certain threshold appear black. This last filtering procedure is commonly applied in high resolution dsDNA data [18, 19].

Figure 3.3 shows dsRNA molecules imaged in AM-AFM, DAM-AFM and JM+ under conditions of low invasiveness (small oscillating amplitudes, low dissipation power and small contact force, respectively). High resolution was obtained in all cases, allowing the observation of at least a single periodicity along the dsRNA molecules. Since AFM heights critically depend on the force that the tip applies to the nucleic acid [19, 27, 34], the level of invasiveness and damage of the different imaging modes was assessed by measuring the dsRNA height and its comparison with consecutive images. The height of several dsRNA molecules obtained with the three imaging modes employed (figure 3.3d) was almost the same and of about 2.5 ± 0.3 nm, in good agreement with the crystallographic dimensions of 2.6 nm for the dsRNA.

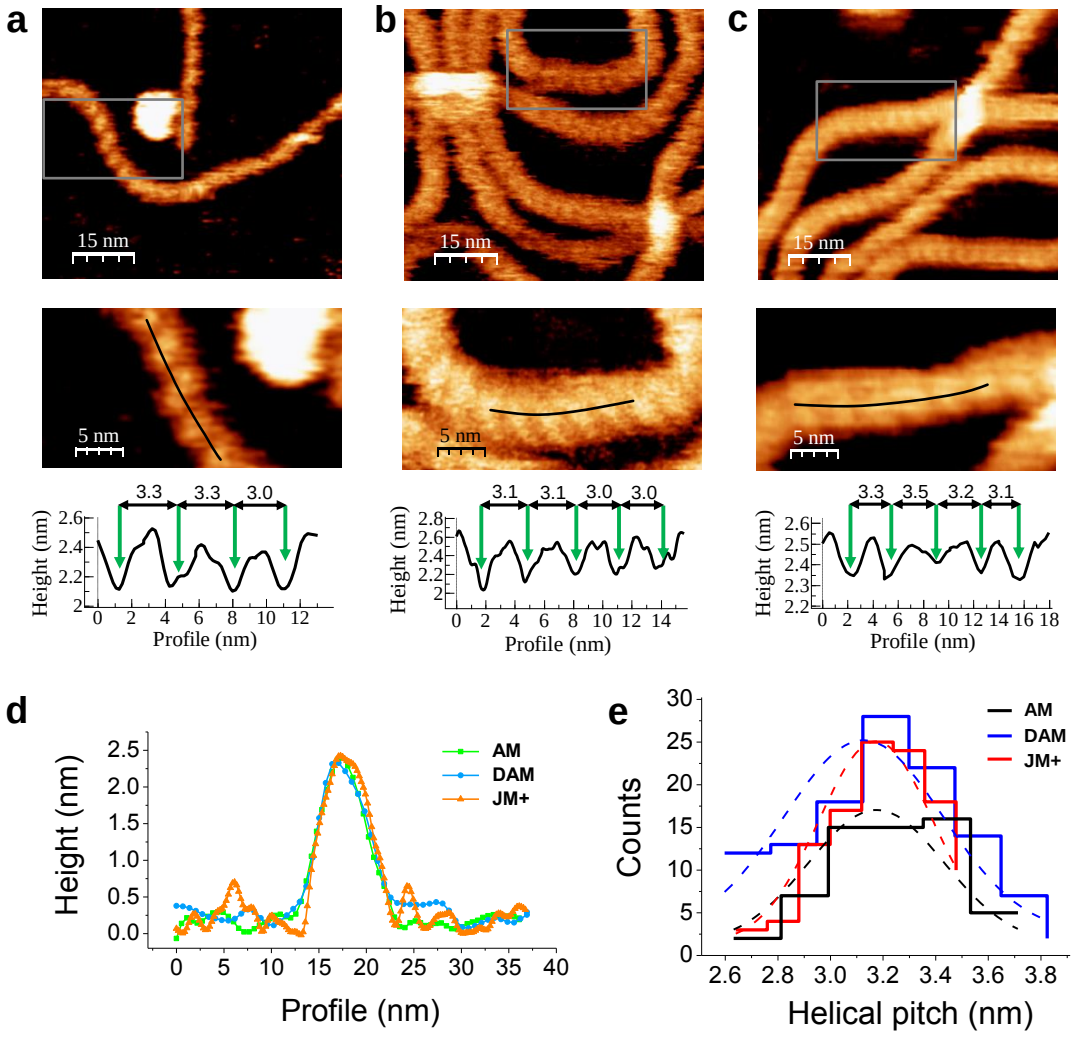

Figure 3.3 High resolution AFM images of dsRNA acquired in different imaging modes. a) AM-AFM. b) DAM-AFM. c) JM+. Top row: large field of view including several dsRNA molecules. Middle row: higher magnification details of the squared region shown in the top row. Bottom row: height profiles along the lines in the zoom-in images. Color scale was adjusted to enhance the corrugation observed along the dsRNA. d) Cross-sectional profiles of dsRNA molecules imaged with AM-AFM, DAM-AFM, and JM+. e) Histograms of the helical pitch for each of the three measuring modes employed in this work. Data were taken along different segments of the same molecule and on different molecules. Gaussian fits (dashed lines) provide mean ± standard deviation (SD) values of 3.2 ± 0.3, 3.1 ± 0.4, and 3.2 ± 0.3 nm, for AM-AFM, DAM, and JM+ imaging modes, respectively.

Figure 3.3 shows that the helical pitch is clearly resolved independently of the measuring mode. The helical pitch along different segments over the same molecule and also on different molecules was measured (figure 3.3e), overall along 8, 13, and 14 molecules that resulted in 64, 116 and 114 data values for AM-AFM, DAM-AFM, and JM+, respectively.

The distribution for each mode was fitted with a Gaussian function with similar mean values and standard deviations, independently of the imaging mode. The mean periodicity was 3.1 ± 0.3 nm (mean ± standard deviation (SD)), a value consistent with the A-form structure of dsRNA. In fact, a rise per base pair of 0.29 nm was directly measured with AFM for dsRNA [4], giving a distance of 3.19 nm for the 11 bases contained in a single turn of the A-form structure of dsRNA. The wide distributions described here (figure 3.3e) are consistent with the structural irregularities previously reported [19, 27]. This variability may be induced by the strong electrostatic interaction with the mica caused by Ni^{2+} cations. Together, these data show that a similar high resolution can be obtained, regardless of the imaging mode employed, when working at optimal operating conditions. Similar conclusions when working with different feedback architectures and/or applied to other biological samples are reported elsewhere [7, 26].

As mentioned before, commercial cantilevers specially chosen to image soft samples in liquid environments were employed for the measurements. These probes have a relatively high resonance frequency and low spring constant. They also have a nominal tip radius of 8 nm, which in principle is too large to expect sub-helical pitch resolution with them. It is interesting then to explore the role played by the dimensions of the tip in the achievement of the observed high resolution using a hard sphere model. For this purpose, AFM images of both dsDNA and dsRNA were simulated and dilated with tips of different radii and compared with experimental data. AFM images of dsDNA and dsRNA structures were simulated using a fragment of 48-mer poly A-T sequence for both structures, but represented as B-form, for dsDNA, or A-form, for dsRNA. The molecular structure in Protein Data Bank (PDB) format was produced using 3D-Dart software [35]. Graphical representations of the dsDNA and dsRNA crystal structures were generated using the UCSF Chimera package [36]. These graphics were represented in a grayscale chosen to represent the height of the structures. Top views were selected and then TIFF files generated, which were imported in WSxM, obtaining in this way AFM-like images of the crystal structures. Images were dilated using the tip-sample dilation option in WSxM. The dilation algorithm uses a parabolic tip of radius r, with $z = \frac{x^2+y^2}{2r}$, where xyz are the lateral and vertical coordinates of the image [37]. Dilation simulations treated both tip and molecule as hard undeformable bodies. Similar simulation procedures are also applied to dsDNA [23, 27] and, although it is just a qualitative model, it is enough to illustrate the importance of the tip apex size to image nucleic acid molecules. A model comprising realistic physical interactions between tip and sample is beyond the scope of this work. Figure 3.4 compares the dsRNA full width at half-maximum (fwhm) of the cross-sectional profile of a simulated image, using a tip of nominal radius (8 nm), with the experimental data for an image acquired with a tip radius close to this nominal value. As it can be observed, the radius of the tip used for the acquisition was slightly lower than the nominal value and yet not enough to provide high resolution.

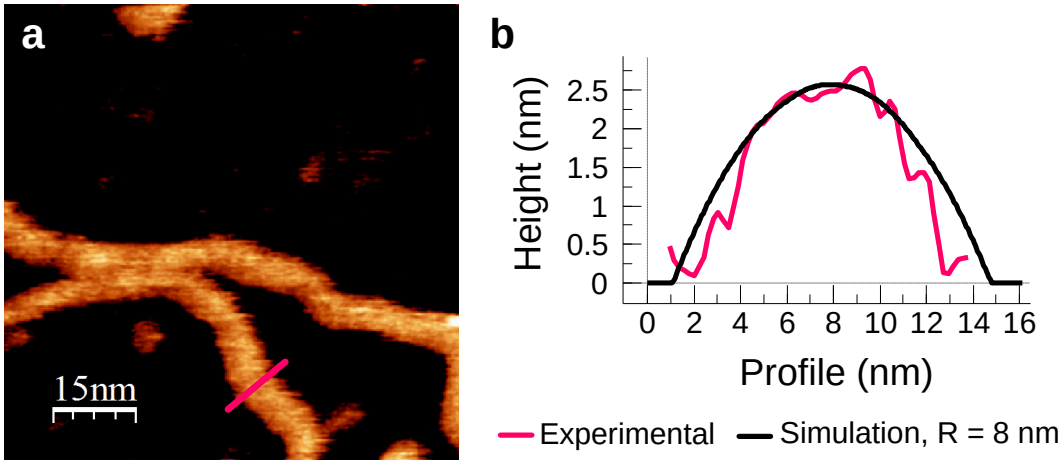

Figure 3.4 dsRNA molecules measured using a tip with radius close to the nominal value. a) AFM topographic image where no helical resolution can be seen along the molecules. Color scale (from dark to bright) was adjusted to enhance the corrugation (2.5 nm total range). b) Comparison of cross-sectional profiles corresponding to the line in a) and an 8 nm radius tip-dilated simulation. The radius of the tip used for the acquisition was close to the nominal 8 nm value and not enough to provide high resolution.

Figure 3.5 shows a further comparison of the fwhm of simulated images at different tip radii with the experimental data. As it can be seen, tips of radii 0.7 - 1.2 nm allowed enough resolution to make both major and minor grooves visible. Tips with larger radii (2.7 - 5.5 nm) led to images where only a single periodicity was detected.

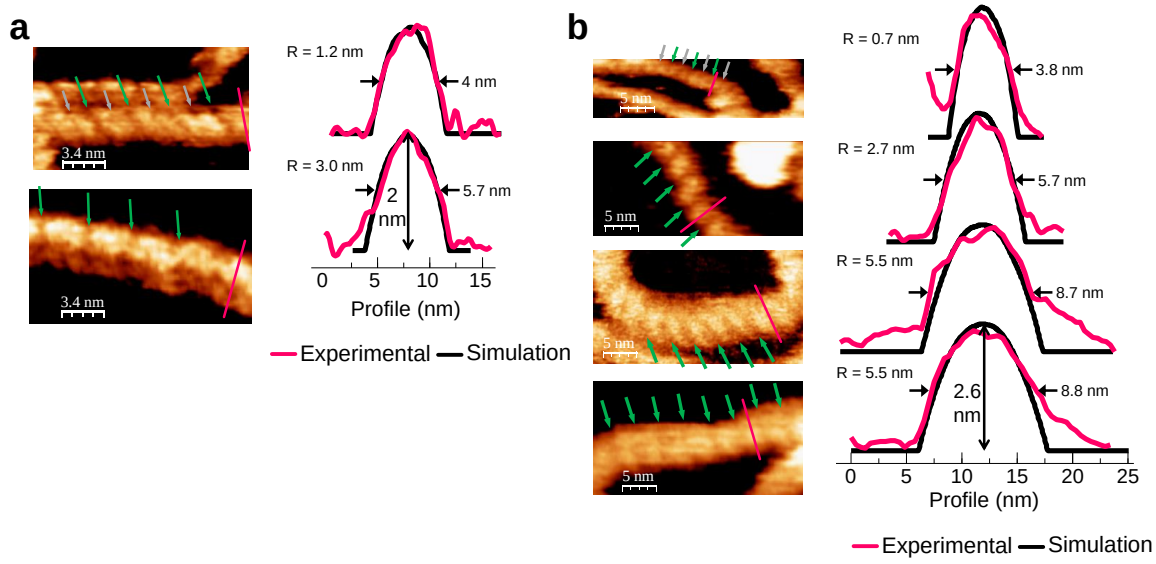

Figure 3.5 dsDNA and dsRNA high resolution imaging dependence with the tip radius. a) Data relative to dsDNA. Simulated AFM images with a tip radius of 1.2 nm provide a similar experimental cross-sectional profile in images where both major and minor grooves are visible. An estimated tip radius of 3.0 nm provide images where only the major groove is resolved. b) Data relative to dsRNA. Simulations with a tip radius of 0.7 nm provide images where both the major and minor grooves are visible. Images where single periodicity is observed provide an estimation for the tip radius of 2.7 and 5.5 nm. Lines across the molecules correspond to the experimental profiles. Full width at half-maximum is also shown.

Importantly, these simulation data indicate that the tips used to acquire the experimental images were much sharper than specified by the manufacturer. A higher resolution than expected from a commercial tip has been reported before with other biological samples. Some examples include the observation of single monomers at the surface of viral particles [38], the visualization of single antibody subunits [39] or the detection of conformational changes in two-dimensional crystals of membrane proteins [40]. A likely explanation could be that the high resolution arises from a single protrusion or an impurity attached to the AFM tip, as already suggested by other authors [18, 27]. In any case, simulation data presented here highlights the relevance of the tip apex size to image nucleic acids.

Finally, we intend to estimate the maximum tip radius that still allows high resolution imaging and to determine which of the two grooves is observed in the images. The longitudinal profile in simulated AFM images for different tip radius was calculated and from these profiles, the depth of the tip penetration in the groove was compared with the vertical noise of the instrument. In order to determine the instrumental noise level in the vertical direction (z), the tip was approached to a freshly-cleaved mica surface under AM-AFM experimental conditions for high resolution imaging. Once in range, with the

scan size set to zero, the height channel was recorded for two minutes at a data acquisition bandwidth of 4.5 Hz. Figure 3.6 shows the height values represented as a histogram.

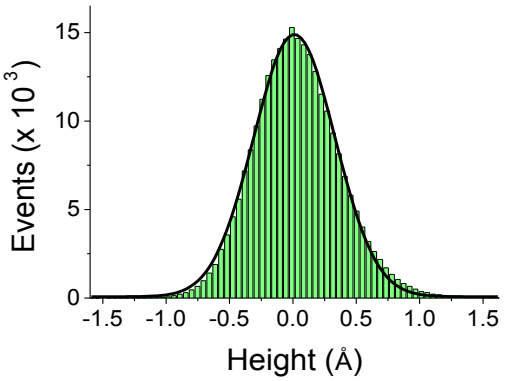

Figure 3.6 Noise in AFM height measurement.

The height distribution was fitted by a Gaussian function giving a RMS noise value of 0.3 Å. The Rose criterion was then used to estimate the minimum experimental depth that was able to be resolved. Signal-to-noise ratio (SNR) compares the level of a desired signal to the level of background noise. It can be defined as SNR = signal amplitude/RMS noise. According to the Rose criterion, for a signal to be distinguished from the noise, the ratio between the power of the signal and the noise should be larger than 5 [41, 42]. Since amplitudes follow a square root relationship with power, applying the Rose criterion to our data SNR $\gtrsim \sqrt{5}$. It can be concluded that the minimum depth to be resolved with the experimental height noise is ~ 0.7 Å. The implication is that only corrugations deeper than 0.7 Å would be visible. Figure 3.7 shows simulated AFM images of dsDNA and dsRNA structures dilated with tips of different radii.

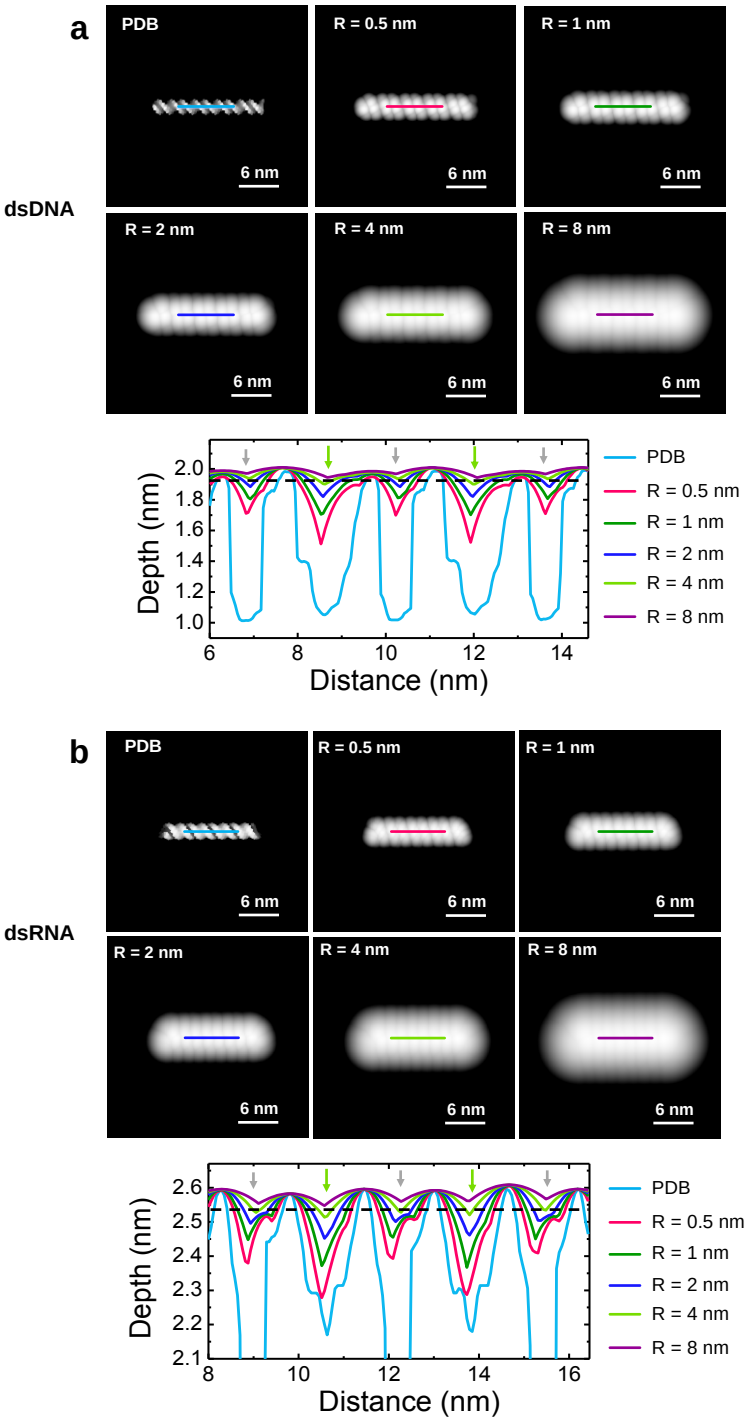

Figure 3.7 Simulations of AFM images of a) dsDNA and b) dsRNA. Top row: simulated AFM topographic images for different tip radius. Bottom row: height profiles taken in the central part of the molecule along the longitudinal axis of the simulated images. The height interval was adjusted for dsDNA and dsRNA to improve visualization of the penetration depths of profiles for the different tip radii. Dashed line represents the minimum depth experimentally observable according to the Rose criterion (see main text).

According to the 0.7 Å threshold rule from the Rose criterion (dashed lines in figure 3.7), both major and minor grooves could only be visible when the tip radius is $\lesssim$ 2.5 nm, in agreement with the previous comparison of experimental and simulated data. As expected, with increasing tip radius the simulations show a decrease of the apparent depth of both major and minor grooves (in a naive view, when the tip radius is large it cannot enter the grooves). In dsDNA simulations the major groove always looked deeper than the minor groove independently of the tip radius used. Hence, as the tip radius increases, the ability to resolve the minor groove gradually reduces, pointing to the fact that when a single periodicity is observed it corresponds to the major groove. However, in the case of dsRNA, this observation is not that obvious because as the tip radius increases both grooves present similar apparent depths (see for instance profiles for R = 4 nm and R = 8 nm). So, a clear answer regarding which of the two grooves was observed in the dsRNA images that show the single 3.1 nm periodicity (figure 3.3) cannot be given. Still, for very sharp tips the major groove was slightly favored with respect to the minor, as it occurred with dsDNA, suggesting that the single periodicity corresponds as well to the major groove.

In summary, the measurements and simulations that have been carried out in this section have shown that high resolution of nucleic acids in liquid is nearly independent of the imaging mode and that there are two aspects which are critical: minimization of the interacting force with the proper tuning of each measuring mode parameters; and the sharpness of the tip, which likely arises from a small feature or a protrusion located at the tip apex of the relatively blunt commercial cantilevers.

3.2.2 Magnetic Force Microscopy in liquids

3.2.2.1 Introduction

As explained in Chapter 1, Magnetic Force Microscopy (MFM) is an AFM-based technique where a nanometric magnetic probe is raster-scanned in close proximity to a surface detecting the local magnetic fields near the surface [43]. MFM has been applied to the study of a variety of magnetic systems [44], including magnetic nanoparticles (MNPs) [45-48], but always in vacuum or atmospheric conditions. AFM is a powerful technique in biophysiscs [49, 50], nanomedicine [51] or nanobiotechnology [52], since it allows imaging and manipulating nanostructures in physiological conditions on a single molecule level [53, 54]. Since biological specimens can dramatically change their properties when studied far away of physiological conditions, Schreiber *et al.* [48] commented on the importance of being able to develop MFM imaging in liquid media. But up to now there was not an MFM technique suitable to study "bio-nano-magnetic" samples in liquids.

Nowadays magnetic nanostructures play important roles in different fields such as medicine, biology or catalysis. For example, the use of MNPs is growing a lot of attention for its potential applications [55] that include therapeutic drug, gene and radionuclide delivery, contrast enhancement agents for magnetic resonance imaging, magnetic separation of labelled cells and other biological entities or methods for the catabolism of tumors via hyperthermia. Several pathologies such as Hepatitis B [56], Alzheimer's, Huntington's and Parkinson's diseases [57, 58] or atherosclerosis [59] are characterized for the presence of magnetic deposits in diseased tissue. There are animals, such as the rainbow trout, where a magnetic sense is related to the presence of magnetic nanocrystals for magnetoreception [60]. Many studies as well are focused on the encapsulation of magnetic particles in different biological entities: magnetic bacteria [61] to be used as magnetic markers for biosensing [62], or virus like particles, as seen in Chapter 2, which are promising templates for building up nanometric-sized magnetic clusters by taking advantage of their inner cavity as a nanoreactor [63, 64]. Nano-magnetic catalysts are also attracting a lot of attention because they generally avoid loss of catalyst increasing their reusability [65].

Despite the importance of measuring "bio-nano-magnetic" objects in physiological conditions, the applicability of MFM to biological systems was limited up to now because of the difficulty in developing MFM for detecting magnetic interactions in liquids [48]. This is as a consequence of the high damping forces on the cantilever, which are several times greater than in air. These damping forces are the origin of the low quality factor (Q) of the cantilever resonance characteristic of liquid measurements, which results in a significant loss of sensitivity in the MFM signal. More than 20 years ago, Giles *et al.* [66]

used MFM to record bits on a computer hard disk in air and in liquid. But in their study topography was acquired with the tip in Contact mode, which is unacceptable for the majority of biological applications, where the biological specimens under consideration are weakly immobilized to a flat surface [62] because the tip will destroy the sample [7]. Moreover, they used different pH values of the liquid, in order to change the adhesion and the attractive forces to measure as close as possible to the surface, to improve the magnetic contrast. This is as well unacceptable for many biological applications, where the biological specimens need to be under specific buffer conditions. More recently, Dietz *et al.* [67] reported the detection of superparamagnetic nanoparticles in liquid using bimodal AFM. But in this case the contrast obtained was a cross-talk of nanomechanical and magnetic interactions, preventing deeper studies on their magnetic properties. The work presented here introduces the development of MFM imaging in liquid media and discusses its potential for detecting and imaging nanoscale magnetic domains in biological samples.

The results presented in this section are published in reference **Ares, P**.; Jaafar, M.; Gil, A.; Gomez-Herrero, J.; Asenjo, A. Magnetic Force Microscopy in Liquids. *Small* 2015, *11*, 4731-4736 (see also List of Publications), and have been achieved in collaboration with Dr. Miriam Jaafar and Dr. Agustina Asenjo from the Instituto de Ciencia de Materiales de Madrid (ICMM) of the CSIC. The tip-sample magnetic interaction in different media (high vacuum, air and liquids) has been studied using magnetic hard disk drives as a benchmark and the acquisition conditions in liquid environment have been highly optimized. The final sensitivity of MFM in liquids has been explored by imaging Fe_3O_4 MNPs coated with dimercaptosuccinnic acid (DMSA), prepared by Dr. Maria del Puerto Morales from the ICMM, which are promising nanostructures for different nanomedicine applications due to their biocompatibility and low toxicity [68].

3.2.2.2 Results and discussion

First step consisted in imaging the magnetic domains of a piece of a high density disk drive (magnetic motives of ~ 60 nm). Commercial MFM probes were used in both air and liquid (distilled water) environments. PPP-MFMR from Nanosensors^{TM} [69] were employed. PPP-MFMR probes have a resonant frequency of 75 kHz in air and a typical force constant of 2.8 N m^{-1}. The tip has a hardmagnetic coating and a radius of curvature < 30 nm. The coating is characterized by a coercivity of ~ 300 Oe. Probes were magnetized by means of a strong permanent magnet prior to the measurements for signal strength enhancement. Figure 3.8 shows the topography and magnetic contrast obtained from the frequency shift (using a Phase Lock Loop, PLL) in both media, measuring in a double-pass configuration as explained in Chapter 1 for MFM studies.

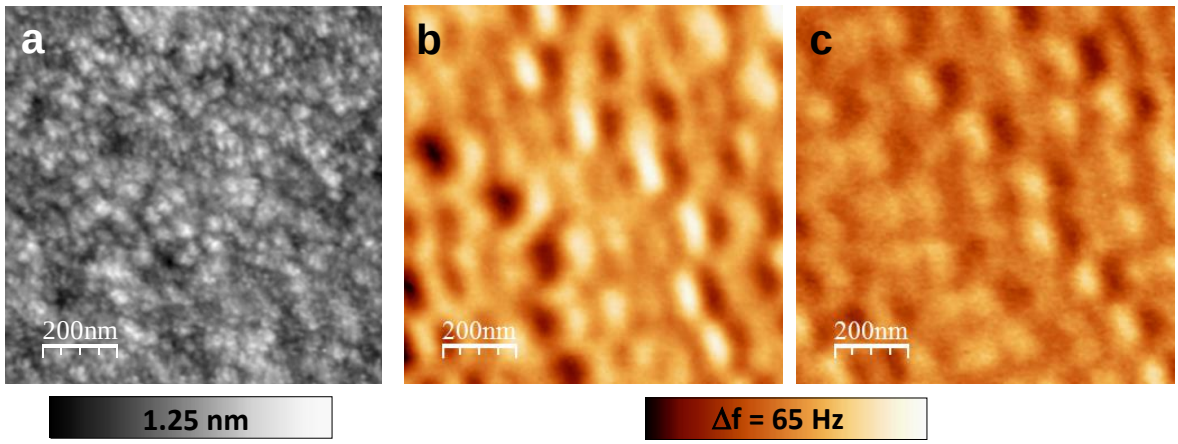

Figure 3.8 a) High density hard disk surface topography. Cantilever amplitude = 5 nm. b) MFM image of the hard disk magnetic bits taken in ambient air conditions. Z lift = 15 nm. c) MFM image taken in liquid. Z lift = 6 nm (the scanned area is not the same as in b)).

As expected, the MFM image acquired in air (figure 3.8b) presents a more marked contrast than the one in liquid (figure 3.8c), but still the sensitivity and lateral resolution of the image in liquid allow to easily resolve the ~ 60 nm domains. Notice that both magnetic images share the color scale for a readily comparison. Figure 3.9 shows topography and frequency shift images in 1^{st} and 2^{nd} passes in both air and liquid media, showing the absence of topography cross-talk along the MFM images.

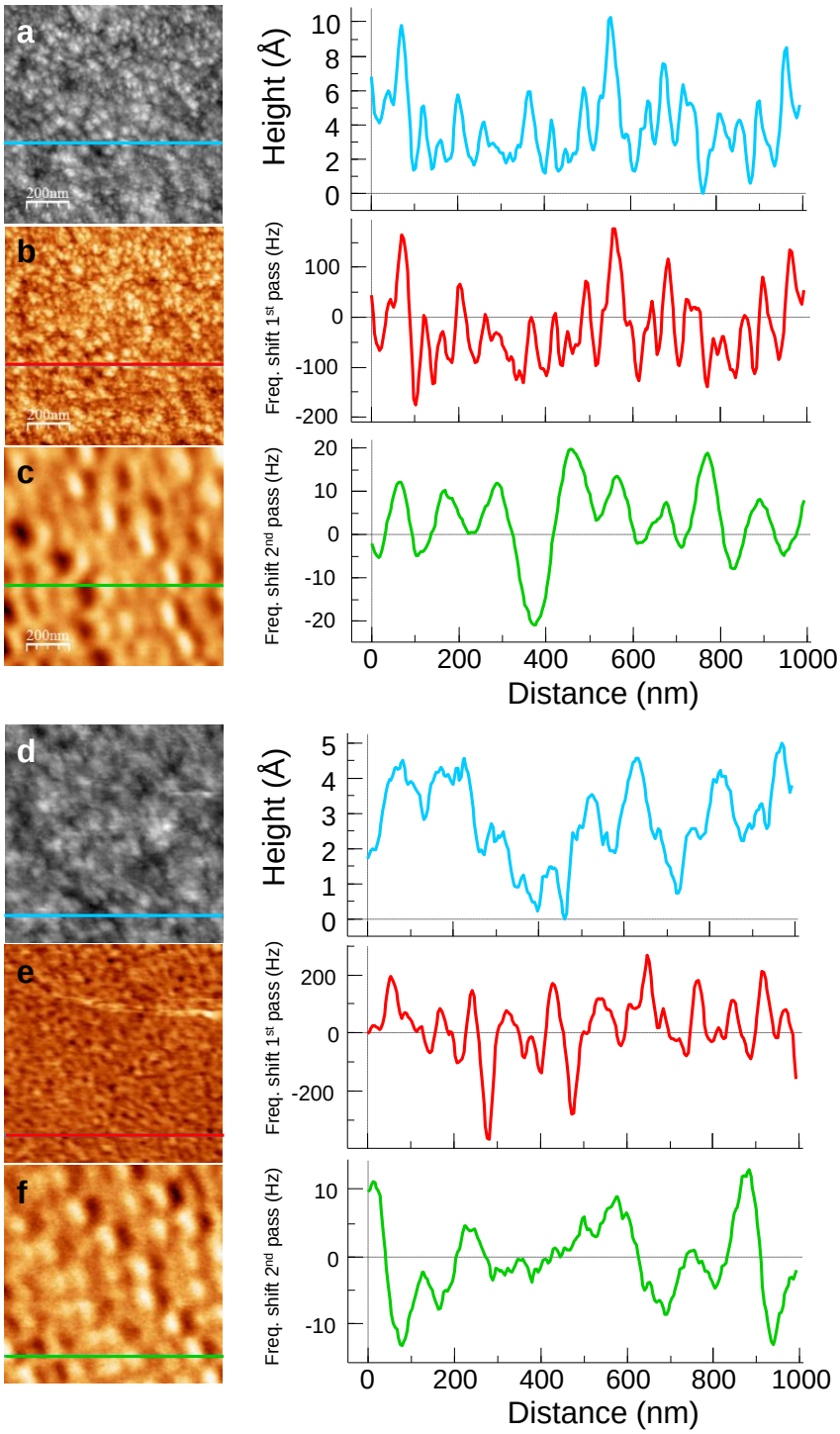

Figure 3.9 Topography (a, d) and frequency shifts in 1st (b, e) and 2nd (c, f) passes in both air (a, b, c) and liquid media (d, e, f). Frequency Shift in 1st pass highly reflects the topography of the surface, whereas the 2nd pass images mainly reflect magnetic interaction and no topography is present.

The lower magnetic signal in liquid media is a direct consequence of the low Q factor of the cantilever resonance characteristic of liquid measurements. This can be clearly seen in figure 3.10, where resonance curves of the same cantilever in different media are shown. For the high vacuum measurements, the microscope was placed in a homemade vacuum chamber with a base pressure of 10^{-6} hPa.

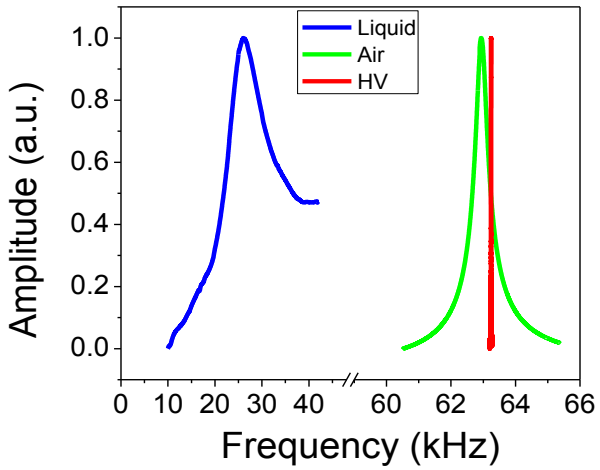

Figure 3.10 Cantilever Nanosensors PPP-MFMR resonance curves in different media: liquid (blue), ambient air (green) and High Vacuum, HV (red).

The origin of the magnetic contrast can be better understood by acquiring MFM data in a 3D Mode configuration [70, 71] (see 3D Modes in Chapter 1), monitoring the variation of the interaction with the tip-sample distance. To this end, the tip was moved along a given line in the fast scan direction (parallel to the domains transition direction, in a similar way as a magnetic reader head does), so MFM contrast from the resonance frequency shift could be readily studied at different lift heights in a fast and drift-free way. Figure 3.11 presents the results of 3D Mode experiments on a low density hard disk sample (magnetic motives of ~ 800 nm).

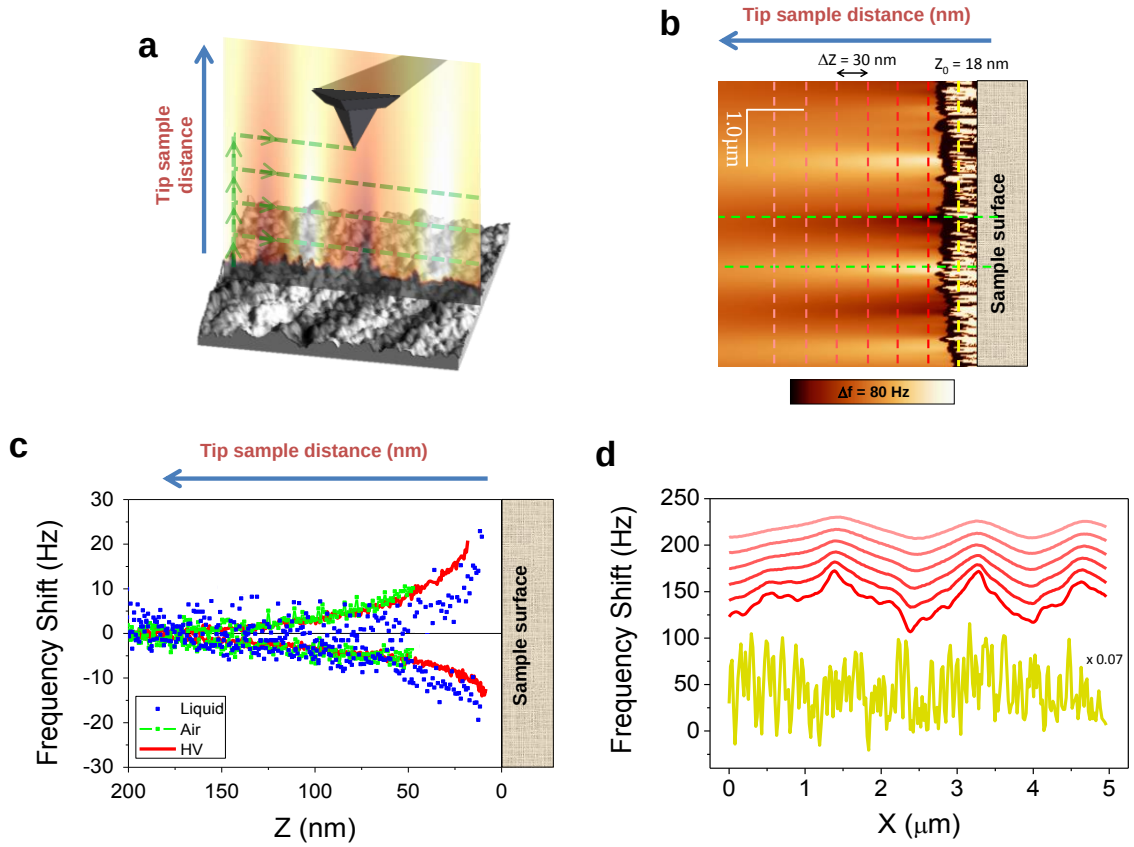

Figure 3.11 a) Scheme of 3D Mode measurements of the magnetic interaction as a function of the tip-sample distance. b) Magnetic contrast in ambient air conditions along a given scanning line as a function of the Z lift in a low density hard disk sample obtained by 3D Mode mapping $\Delta\omega$ (x, z). c) Magnetic signal from attractive and repulsive regions of the hard disk in the different media taken from 3D Mode maps similar to that shown in b). The regions chosen for each media correspond to the positions with higher attractive and repulsive contrasts, as marked by the horizontal dashed green lines in b). d) Plot of the frequency shift *vs.* X distance along the scanning line for different Z lifts according to the vertical lines in b). All lines were arbitrarily shifted for visibility and for this same reason the yellow line was divided by a factor of 15.

The frequency shift induced by the magnetic interaction at different Z lifts was recorded, showing attractive and repulsive contrast (bright and dark areas, figure 3.11b). By carrying out this same process in air and vacuum, the magnetic interaction in the different media as a function of the distance for both the attractive and repulsive areas is plotted (figure 3.11c). Figure 3.11d shows different frequency shift profiles as a function of Z lift. As the Z lift increases, it can be seen how the topographic information fades away. From this kind of plots, the optimal Z lift distance for MFM imaging with no topography cross-talk can be easily chosen.

From figure 3.11c it can be seen that the high vacuum signals are the cleanest ones, whereas the liquid signals are the noisiest, as expected from the Q factor values. But interestingly, in both vacuum and liquid, capillarity forces are not present, resulting in much lower attractive forces than in air [72], and hence it can be observed that the magnetic signal can be detected with the tip very close to the sample (tip-sample distances < 10 nm). In contrast to air conditions, where due to the presence of capillary forces the minimum distance to detect magnetic interaction with no topography cross-talk is much higher. Figure 3.12 shows a representative example to illustrate this tendency.

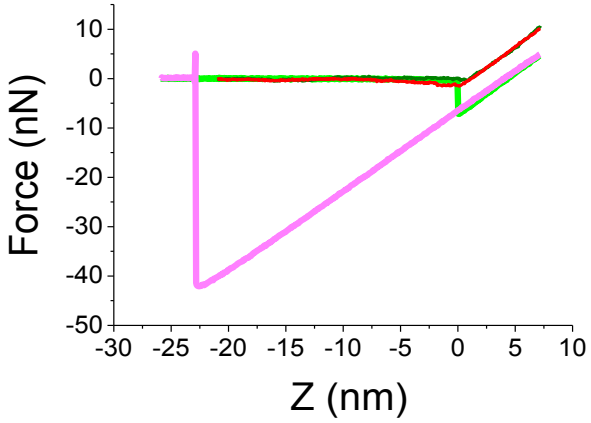

Figure 3.12 Force *vs.* Distance plot in liquid (dark green and red) and in air (light green and pink). The conditions for the above FZ plots were similar to the ones used for MFM acquisition. Attractive forces are almost negligible in liquid compared to air conditions (the adhesion force in air is ~ 30 times greater than in liquid).

To optimize the magnetic contrast in liquids, 3D Modes analysis was done for different oscillation amplitudes and different Dynamic modes, AM-AFM and DAM-AFM in both air and liquid. In terms of the acquisition of magnetic interactions, DAM-AFM is the same as FM-AFM, but since in DAM-AFM there are no frequency shift contributions to the topography, it has the advantage of no magnetic cross-talk in the first pass topography acquisition (as already mentioned in the supporting information of [24]). The MFM signal was maximized by studying the influence of the relevant measuring conditions in both AM-AFM and DAM-AFM modes. For a given operating parameter (for example the cantilever oscillation amplitude), the other relevant operating conditions (such as Setpoint, Z lift distance or Phase Lock Loop parameters) were varied to maximize the MFM signal. Figure 3.13 shows the optimization of the MFM contrast for AM-AFM and DAM-AFM modes.

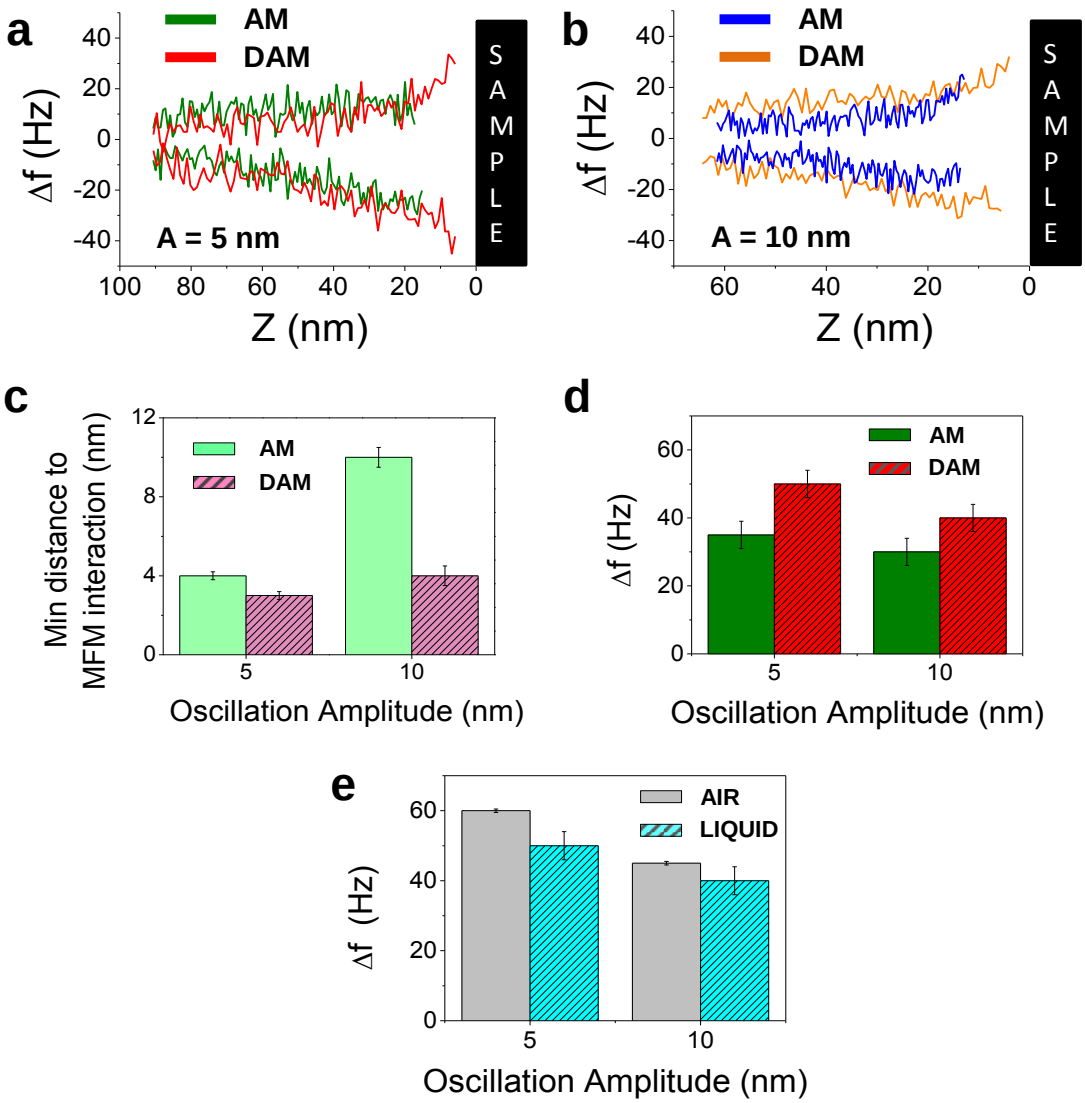

Figure 3.13 Magnetic contrast optimization for AM-AFM and DAM-AFM. a) and b) Magnetic signal as a function of the tip sample distance from attractive and repulsive regions of a hard disk in liquid, for cantilever oscillation amplitudes of 5 and 10 nm respectively. c) Minimum tip sample distance at which MFM signal could be detected in liquid with no topography cross-talk. d) Maximum magnetic signal in liquid. e) Comparison of the optimized magnetic signals detected in air and liquid.

As it can be inferred from figure 3.13, by working in DAM-AFM, the tip is able to detect the magnetic interaction closer to the sample, which translates into a higher magnetic signal. Thus, using the most appropriated oscillation amplitudes and tip-sample distances for every mode and medium, similar contrasts can be achieved in air and liquid (as shown in figure 3.8), despite a loss in sensitivity in liquid compared to air.

After the optimization of the acquisition conditions for MFM in liquids, DMSA-coated Fe_3O_4 ferrimagnetic nanoparticles, a sample of nanobiotechnology interest, were studied. These MNPs were obtained by precipitation of a $FeSO_4$ solution in a basic solution in the presence of potassium nitrate (acting as mild oxidant) under stirring and nitrogen flow. The precipitate was then placed in an oil bath at 90 ºC with mechanical stirring for 15 min and left tightly closed for 24 h without agitation [73]. Finally, the particles were coated with DMSA at pH 3 and the excess removed after two days dialysis. Magnetite particles obtained by this route present an inverse spinel structure and ferrimagnetic behavior at room temperature with very high saturation magnetization values [73]. For AFM imaging, a solution of 2.4 mg Fe/ml of MNPs was diluted in the range 1:5 in a 5 mM nickel chloride solution just before use, to ensure proper MNPs immobilization, and immediately aliquoted onto freshly cleaved mica. After 20 minutes, the mica substrates were dried in a N_2 gas flow and imaged in air conditions. For MNPs studies in liquids, distilled water was added to the mica substrates with MNPs previously imaged. Figure 3.14 shows the topography and magnetic contrast in air conditions of a typical distribution of MNPs on the substrate.

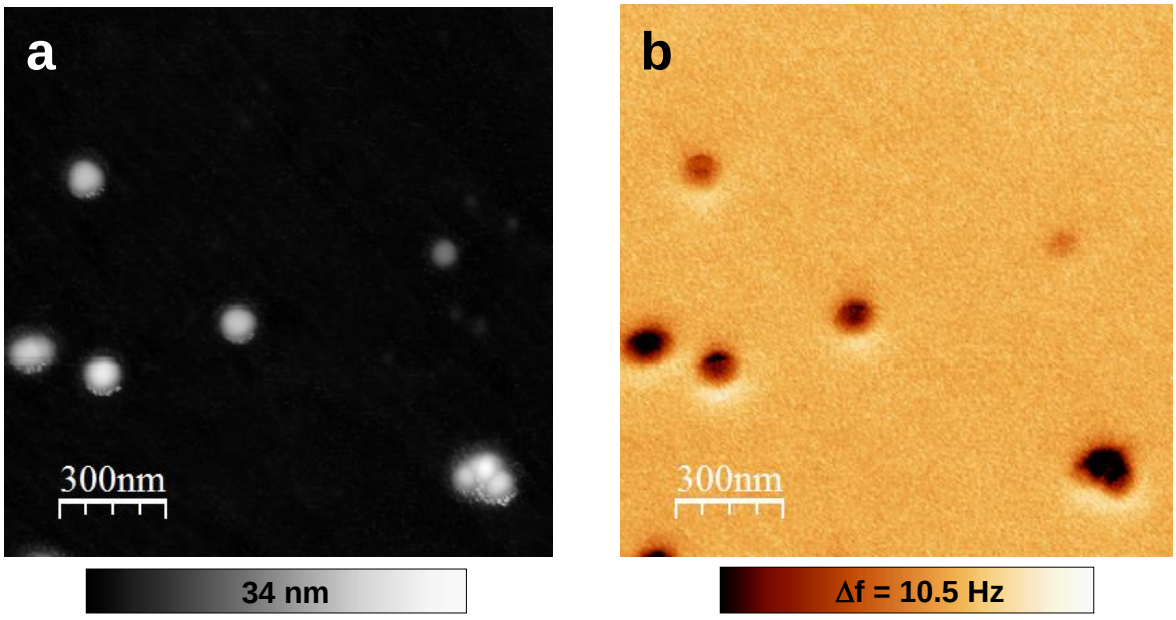

Figure 3.14 a) Topography and b) MFM images of DMSA-coated Fe_3O_4 nanoparticles acquired in ambient air conditions. Z lift = 15nm.

Figure 3.14 presents single particles and clusters comprising several particles. These nanoparticles have a cubic shape. Nevertheless, the AFM images present rounded features due to the tip-sample dilation. MNPs were magnetized in the in-plane direction by means of a permanent magnet prior to the measurements and, due the magnetocrystalline anisotropy,

the magnetization lies along one of the easy axis of the particle [74]. This was the responsible of the bright-dark contrast observed, which comes from the magnetic dipole response [47, 48]. It is important to remark that magnetic signals in the hard disks (figure 3.8) were about an order of magnitude higher than in MNPs (figure 3.14). Figure 3.15 shows topography and magnetic images of different single MNPs and clusters measured in both air and liquid. The magnetic contrast in air matches the state-of-the-art images for this kind of systems [46-48, 75].

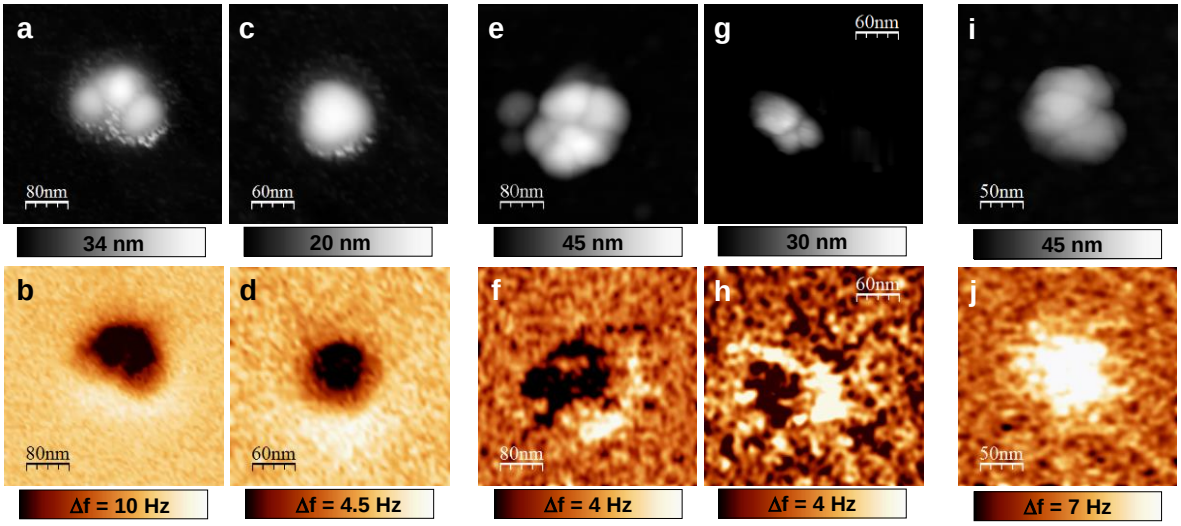

Figure 3.15 DMSA-coated Fe_3O_4 nanoparticles. a), c), e), g) and i) Topography. b), d), f), h) and j) 2nd pass frequency shift images. (a-d) Images acquired in ambient air conditions. Z lift = 15 nm. (e-j) Images acquired in liquid. Z lift = 6 nm. (a-h) were acquired using a MFM tip, whereas i) and j) were acquired using a probe with similar characteristics but without magnetic coating.

Since the dependence with tip-sample distance of both magnetic and electrostatic interactions is similar (as shown in Chapter 1), it is fundamental to demonstrate the magnetic origin of the signal measured in the nanoparticles [76, 77]. To this end, measurements in liquids using cantilevers with similar characteristics as the MFM ones, but with a metallic non-magnetic coating, were carried out in exactly the same conditions. In these cases, there is found only a bright contrast but not the dark-bright contrast associated to magnetic interactions (Figure 3.15j). It is interesting to remark that the magnetic contrast in the case of particles as low as ~ 30 nm, which is in the limit of the technique, could still be measured with negligible topography cross-talk, as shown in figure 3.16, despite of the low magnetic signal-to-noise ratio characteristic of liquids.

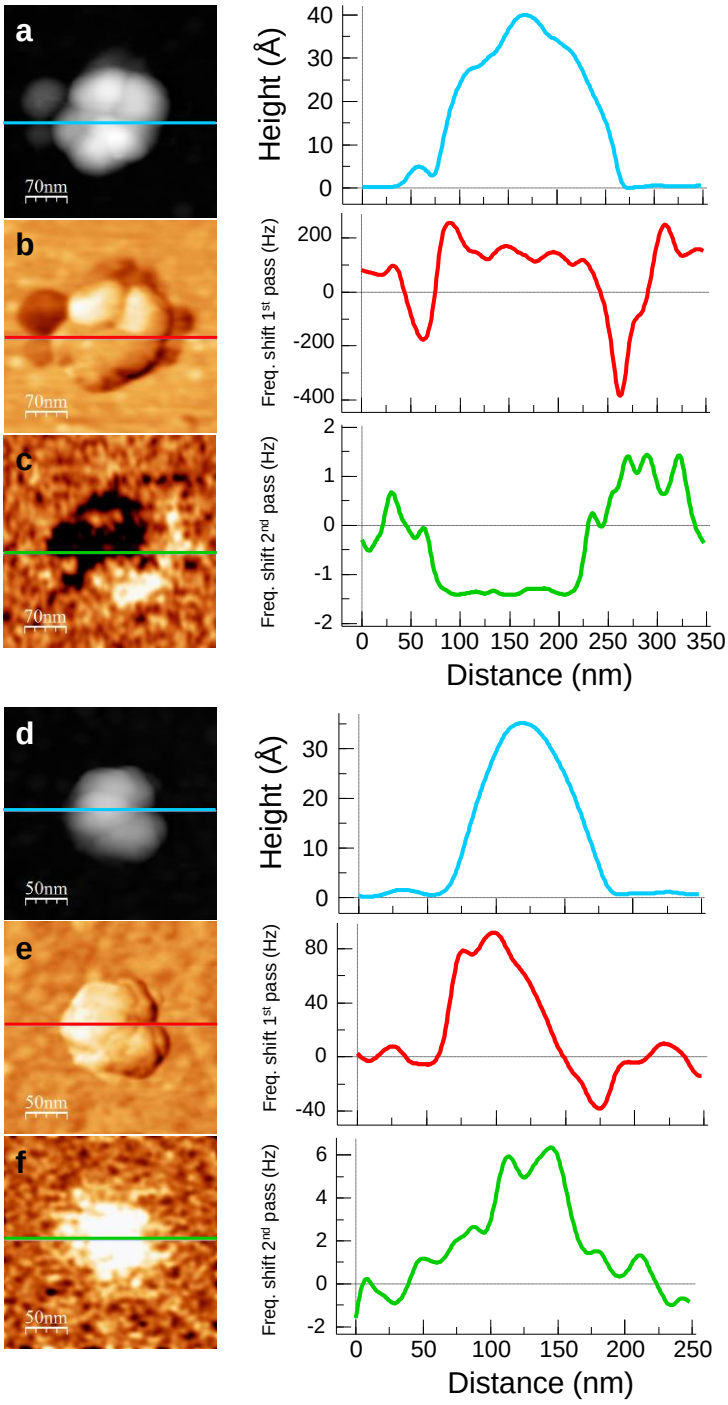

Figure 3.16 Topography (a, d) and frequency shifts in 1st (b, e) and 2nd (c, f) passes corresponding to magnetic nanoparticles in liquid media using magnetic (a-c) and non-magnetic (d-f) probes. Frequency Shift in 1st pass highly reflects the topography of the surface, whereas in the 2nd pass images no topography is present.

The magnetic signal for each of the particles and clusters observed can be compared by measuring the difference between the dark and the bright contrast. Figure 3.17 shows the comparison of the measured magnetic signal of the MNPs as a function of the volume of the MNP, this is, as a function of the magnetic material present, in both air and liquid.

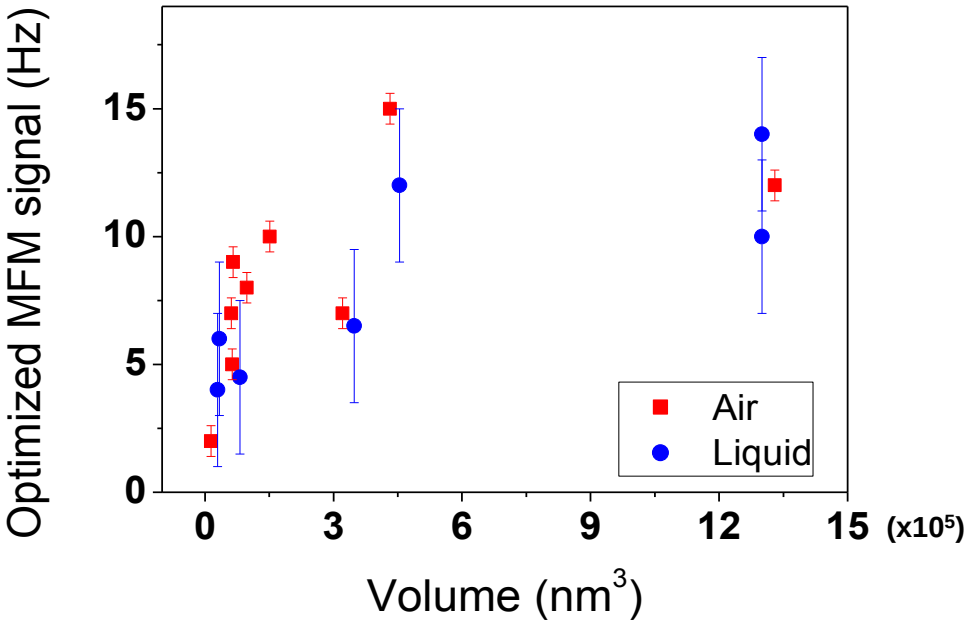

Figure 3.17 Magnetic signal as a function of the amount of magnetic material in the DMSA-coated Fe_3O_4 nanoparticles for both air and liquid measurements.

Remarkably, similar magnetic contrasts in liquid and in air could be obtained, despite the increase of the noise in the liquid measurements due to the low Q factor of the cantilever resonance.

A simple study of fundamental MFM noise shows that further improvement on the performance could be gained, through the use of specially designed cantilevers for liquid media. The frequency shift of a vibrating cantilever in the presence of a force gradient is proportional to the factor ω_0/k (equation (1.20) in the MFM section in Chapter 1). For the commercial cantilevers used in the MFM measurements in liquids, $\omega_0 = 2\pi \cdot 26000$ rad s^{-1} and $k = 2.8$ N m^{-1}, resulting in a factor in liquid $(\omega_0/k)_{MFM} \sim 5.8 \times 10^4$ rad s^{-1} N^{-1} m. There is still room for further improvement: if it would be possible to use cantilevers specifically designed for measurements in liquids, such as the ones used for the dsRNA measurements in the previous section, BL-AC40TS-C2 from Olympus [30], but customized with a magnetic coating as commercial MFM probes, then $\omega_0 \sim 2\pi \cdot 25000$ rad s^{-1} and

k ~ 0.09 N m^{-1}, resulting in a factor in liquid $(\omega_0/k)_{AC40}$ ~ 1.7 x 10^6 rad s^{-1} N^{-1} m. The ratio between these two factors leads to a ~ 29-fold improvement in the frequency shift sensitivity.

But the use of lower force constant cantilevers will result in an increase in the fundamental noise level of the measurement, worsening the frequency shift sensitivity. This noise increase is proportional to $\sqrt{1/kQ}$ [78], with k the cantilever stiffness and Q the quality factor of the resonance. For the commercial cantilevers used in the MFM measurements in liquids, k = 2.8 N m^{-1} and Q ~ 3, resulting in $\left(\sqrt{1/kQ}\right)_{MFM}$ ~ 0.35 $(N^{-1}\ m)^{1/2}$. For the BL-AC40TS-C2, k ~ 0.09 N m^{-1} and Q ~ 2, resulting in $\left(\sqrt{1/kQ}\right)_{AC40}$ ~ 2.35 $(N^{-1}\ m)^{1/2}$. The ratio between these two factors leads to a ~ 7-fold worsening in the frequency shift sensitivity. By using these cantilevers in liquids, on one side the frequency shift sensitivity would improve a factor of ~ 29 and in the other side it would worsen a factor of ~ 7, resulting in a final improvement of a factor of 29/7, roughly ~ 4.

This prediction made at the end of reference Ares, P.; Jaafar, M.; Gil, A.; Gomez-Herrero, J.; Asenjo, A. Magnetic Force Microscopy in Liquids. *Small* 2015, *11*, 4731-4736, core of this section, was now confirmed by some preliminary results with homemade magnetic BL-AC40TS-C2 cantilevers prepared by sputtering [79] by Eider Berganza (from Dr. Agustina Asenjo and Dr. Miriam Jaafar group). Figure 3.18 shows a comparison of the magnetic signal from high density hard disc domains acquired with commercial PPP-MFMR and homemade magnetic BL-AC40TS-C2 probes.

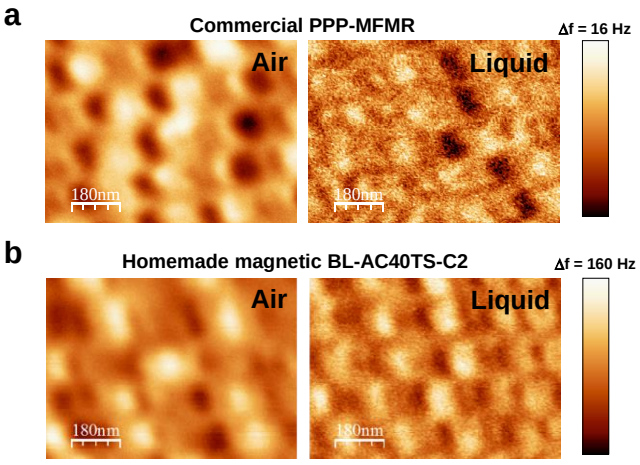

Figure 3.18 MFM images of a high density hard disk with different kind of probes. a) Commercial PPP-MFMR. b) Homemade magnetic BL-AC40TS-C2. Left panels: data acquired in air. Right panels: data acquired in liquid. The scanned areas are not the same. Acquisition parameters optimized to maximize MFM contrast for each case.

Figure 3.18 shows a remarkable increase in the magnetic signal for the homemade cantilevers (note the different values for the color tables, with an increase of a factor of 10 for the homemade probes). A comparison of data taken in liquid yields an improvement of the signal to noise ratio for the homemade probes of a factor of ~ 3, in good agreement with the estimation from studying fundamental MFM noise.

In summary, the feasibility of using the MFM technique in liquid environments has been demonstrated. MFM studies in liquids have been carried out using commercial MFM probes, being able to detect magnetic signals even from a single 30-nm Fe_3O_4 nanoparticle. This has been possible by fine tuning of the experimental setup and by imaging the surface using DAM-AFM mode. DAM-AFM has enabled optimization of the magnetic signal by allowing the AFM tip to detect it very close to the sample. Additionally, a simple study of noise in MFM acquisition in liquids has shown that, by using special magnetic cantilevers, signal to noise ratio could be further improved, as it has been confirmed experimentally by fabricating customized magnetic probes, approaching the quality of images taken in air ambient condition.

3.3 New approaches to nano-object electrical contacts

Since the continuous miniaturization of the electronic devices, nano and molecular electronics are important goals for modern science [80, 81]. Electrodes are an essential requirement for any electrical circuit and they usually provide the link between the nano- and the macro-scale [82-84]. Conventional fabrication procedures of electrodes for molecular electronics typically require a high number of steps such as metal evaporation in vacuum, lithography and sample cleaning (which involves chemical agents), thus making them complex tasks, requiring considerable time and resources that usually are not even available in many laboratories. Moreover, many candidates for conducting molecules, such as organic biomolecules [85-87] and metal-organic wires [88], are badly affected by these procedures: they are damaged when placed in vacuum, they do not withstand metal evaporation high temperatures or they are not compatible with the chemical agents used to clean the rests of lithographic masks. A paradigmatic case is that of DNA molecules, where the influence of metal evaporation on their integrity generated great debate [85, 89, 90]. The influence of the evaporated electrodes is thoroughly discussed in a recent paper on DNA conductivity [91].

In this section two different complementary approaches have been presented. First, a method to transfer exfoliated graphite flakes as soft-electrodes. These microelectrodes exhibit extremely well-defined and thin edges and can be placed on any sample location with sub-micrometer precision. Second, a method where commercial gold nanowires have been used to create nanoelectrodes taking advantage of their cold welding ability [92]. Gold nanowires can be cold welded together within seconds by mechanical contact alone and under relatively low applied pressures. Both procedures are easy, clean, inexpensive and do not require vacuum, high temperatures or chemical agents.

3.3.1 Exfoliated graphite flakes as soft-electrodes

3.3.1.1 Introduction

A technique for the transference of microelectrodes [93], in particular 2D materials [94, 95], is presented. Microelectrodes from exfoliated graphite flakes (EGFs) are fabricated in an easy, inexpensive and reliable way by taking advantage of previously described procedures [94, 96]. The microelectrodes so produced can be placed with sub-micrometer precision on any sample location. The technique presented here is already described in **Ares, P.**; Lopez-Polin, G.; Hermosa, C.; Zamora, F.; Gomez-Herrero, J.; Gomez-Navarro, C. Exfoliated graphite flakes as soft-electrodes for precisely contacting nanoobjects. *2D Materials* 2015, *2*, 035008 (see also List of Publications). It does not require vacuum or chemical agents; the whole process is based on soft-lithography procedures and it is carried out in ambient conditions. These electrodes exhibit extremely well-defined and steep edges, which facilitates measurements of very short channel lengths. As it is shown, the electrical resistances of these EGF electrodes with different conducting nanomaterials are similar to the values reported for conventional metal electrodes. The covalent-bond structure of graphite provides stable electrodes at room temperature and for long periods of time [97]. The whole EGF soft-electrode fabrication process clearly depends on the experience of the operator but after a few attempts, it should not take longer than ~ 1 - 2 hours, a much lower time compared to the days or even weeks needed with conventional lithographic techniques.

In this section first a description of the technique is provided and then four relevant examples illustrating the potential of the procedure are presented. The first two examples correspond to 1D structures (carbon nanotubes and metal-organic nanoribbons), where one of the electrodes is based on EGF and the second electrode is a conducting AFM tip (C-AFM). The last two examples deal with 2D materials. In particular, the third one is the electrical characterization of a known 2D material, reduced graphene oxide (RGO), through the use of two EGF electrodes. In the last example a broken circuit comprising graphene has been repaired by performing a controlled positioning of EGF electrodes.

The work presented here has been done in collaboration with Dr. Félix Zamora and Dr. Cristina Gómez-Navarro groups. In particular, the setup needed for the deterministic transfer of 2D materials by all-dry viscoelastic stamping [94] used in this work has been assembled by Dr. Guillermo López-Polín during his PhD, after a short stay at the Delft University of Technology (The Netherlands), where Dr. Andrés Castellanos-Gómez developed the all-dry transfer method for the assembly of 2D atomic layer heterostructures, during his postdoctoral research. In the procedure presented in this section, a contact on a selected transferred EGF is created using conductive paint to convert it into a

microelectrode. Metal-organic nanoribbons for the second example have been prepared by Dr. Cristina Hermosa (sublimation) and Dr. Pilar Amo-Ochoa (drop-casting). The third and fourth examples (RGO characterization and graphene circuit repair) have been entirely carried out by Dr. Guillermo López-Polín. They are presented in this manuscript to show the potential of the technique.

3.3.1.2 Results and discussion

The deterministic transfer of bidimensional crystals is widely used for the fabrication of heterostructures based on the artificial stacking of 2D materials [94, 95]. Figure 3.19 summarizes the key elements of the experimental setup for soft-electrode transfer and shows a photograph of it. It comprises a zoom optical microscope, a XY stage with a goniometer (which allows rotating the sample if necessary once placed on the XY stage) and a XYZ micro-manipulator. The price for the whole experimental setup is below 3000 € (in this work images taken with a high resolution optical microscope are also presented but this equipment is not essential for soft-electrode transfer). This price, compared to the cost of conventional electrode fabrication techniques such as metal evaporation or e-beam lithography, is substantially lower, making this technique affordable to many laboratories.

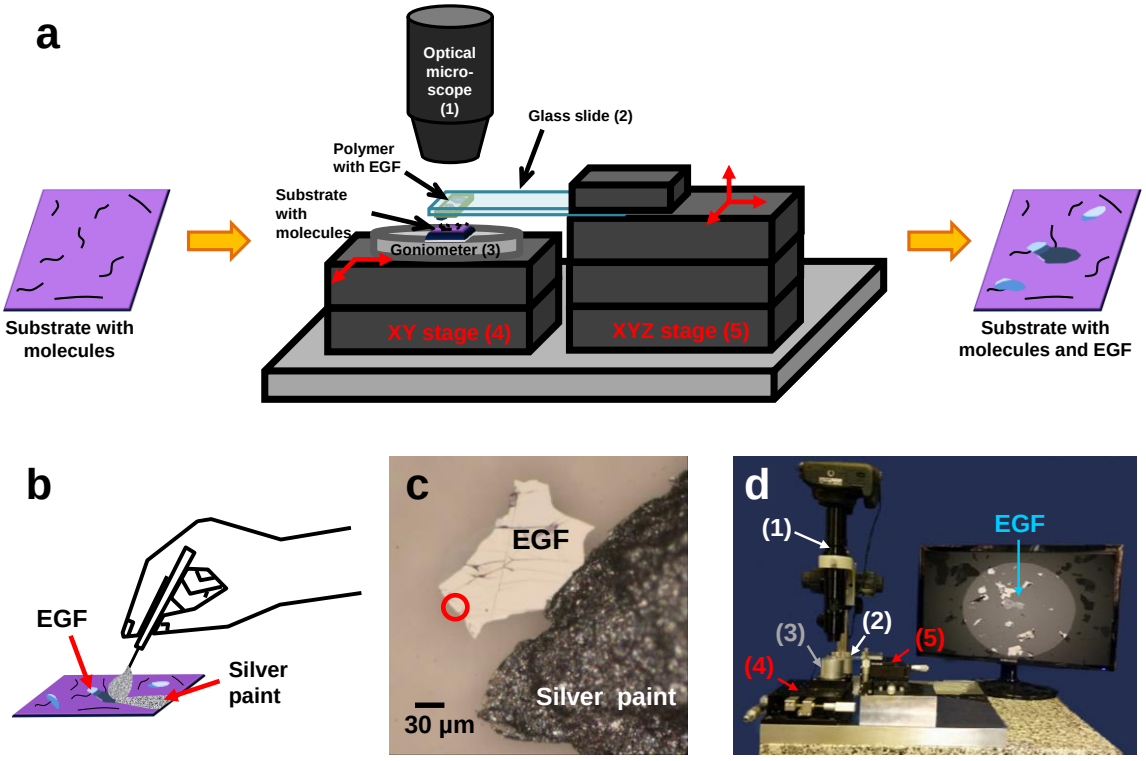

Figure 3.19 Experimental setup used for soft-electrode transfer. a) A sample with nano-objects on its surface is placed on a XY stage with a goniometer. A viscoelastic polymer is fixed underneath a glass slide held by a XYZ micro-manipulator. The viscoelastic polymer carries EGFs that are transferred to the substrate by pressing against it. b) Silver paint is used to create a contact on the selected electrode. c) Final result where an EGF microelectrode and the macroscopic silver paint contact can be readily seen. The red circle encloses an area where carbon nanotubes were previously observed by AFM. d) Photograph of the experimental setup. Numbers correspond to the different elements as indicated in a).

The procedure starts by obtaining EGFs from a graphite sample by microexfoliation through the scotch tape method. The tape containing the flakes is then pressed against a piece of transparent viscoelastic polymer (Gel-Film® from Gel-Pak® [98]) which was previously fixed to a microscope glass slide. Importantly for the procedure, the viscoelastic polymers adhesion increases with speed. The glass slide is held by the XYZ micro-manipulator. Using the optical microscope, a convenient EGF is selected. Depending on the application itself, the EGF size requirements can be different. For applications where a subsequent macroscopic contact is performed using a conductive paint, as shown in figure 3.19, at least one of the lateral dimensions of the flake has to be large enough for this handmade contact. This typically implies one of the lateral dimensions to be larger than ~ 100 µm. However, in case of small flakes, this could be accomplished by grouping several EGFs with increasing sizes if necessary. The smallest lateral dimension thus should be within optical microscopy resolution. Related to the thickness of the EGFs, they have to be thick enough to act as a continuous reservoir of electrons without discrete level structure and no gate dependence [97]. Flakes of ~ 3 to 40 nm thicknesses are typically selected to fulfil these conditions.

Then a sample with the nano-objects to be contacted is placed in the XY stage. The sample is observed from the top with the optical microscope through the glass slide with the transparent viscoelastic polymer attached to it (figure 3.19a). By displacing the sample with the XY stage it is possible to locate the desired region on the sample and then the XYZ micro-manipulator is moved to precisely align the selected EGF on top of the sample region of interest. At this point, the polymer is lowered pressing hard onto the sample and then is slowly brought back up. This is the key point of the transfer procedure: since viscoelastic polymers show a moderate adhesion at low speed, when pressing the polymer onto the sample the EGF adheres to the sample surface, but when bringing it back slowly the selected EGF detaches the polymer and remaines on the sample. Finally, with the help of the optical microscope, using a thin brush and silver paint a contact on the selected EGF is created (figures 3.19b and c). This is a distinct and important feature of the method presented here. A rather similar procedure can be carried out with a thin film of evaporated metal, as for example gold [99], but as it is shown, the flakes so fabricated cannot be so thin as the EGF ones and present much more irregular edges, that in some cases could introduce complications. Moreover, since this technique needs previous metal evaporations, it requires additional expensive evaporation equipment and is more time-consuming.

In the first two examples, AFM was used both for imaging and for electrical measurements. ElectriMulti75-G probes from BudgetSensors [100] were employed for the conductivity experiments. They have a resonant frequency of 75 kHz in air and a typical force constant of 3 N m^{-1}. The tip has a conductive Cr/Pt coating on both sides and a radius of curvature < 25 nm. The coating is characterized by a contact resistance of 300 Ω on platinum thin film surface. Samples were first imaged in AM-AFM mode, and then at a selected spot of

the nano-object a Force *vs.* Distance curve was obtained, and at the maximum tip indentation a Current *vs.* Voltage curve was acquired (see Chapter 1, conductive AFM section).
In the last two examples, probe station measurements were carried out using a home-made two-contact set up operated in ambient conditions, where the electrical probes were mounted on two independent XYZ micro-manipulators (the probe station available at that time in the laboratory, assembled by Dr. Cristina Gómez-Navarro. After the completion of this work, we assembled the variable-temperature ambient-controlled motorized probe station shown in Chapter 2). It included a Keithley 2400 sourcemeter, a Keithley 2000 multimeter and a home-made current to voltage preamplifier with selectable gains (ranging from 1 $\mu A\ V^{-1}$ to 1 $nA\ V^{-1}$).

Next the electrical characterization of different examples is presented.

- **Carbon nanotubes**

The first example of this work shows the electrical contact of carbon nanotubes. To this end, a mica substrate with nanotubes on top was prepared by drop-casting of a nanotube suspension [101]. AFM was used to visualize the nanotubes on the surface so their concentration was adjusted to be ~ 1 - 2 nanotubes every 25 μm^2. By using again AFM, regions with a good density of carbon nanotubes were first located and then, with the soft-electrode transfer method, an EGF electrode was placed in one of these regions. Figure 3.20 summarizes the procedure followed with the carbon nanotubes.

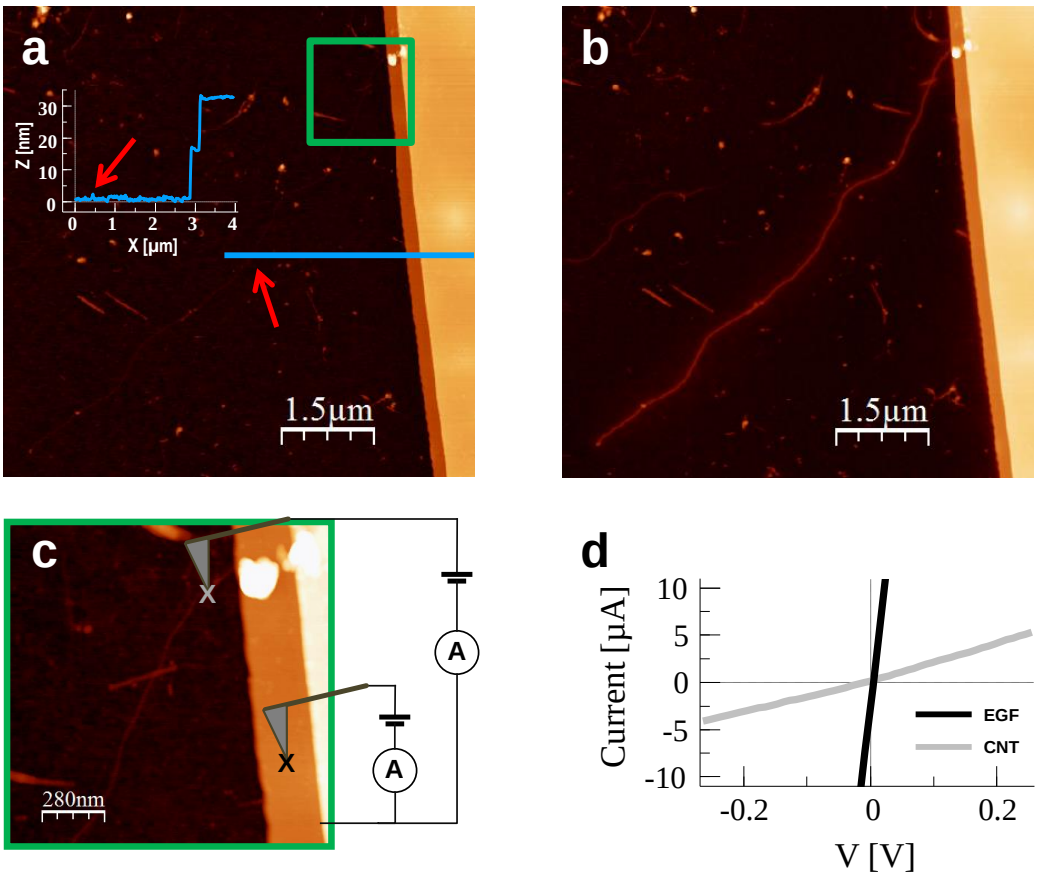

Figure 3.20 Carbon nanotubes contacts. a) AFM topographic image at zero bias voltage in the area enclosed inside the red circle in figure 3.19c. On the right, an EGF can be seen, exhibiting their characteristic sharp edge. The inset is a profile along the blue line showing the height of the EGF. The red arrows mark the position of the nanotube. b) Same as a) but with a 4 V tip-sample Bias applied in order to enhance the nanotube contrast. c) Zoom-in corresponding to the green square in a). It shows the contact positions at which the electrical characterization was carried out (gray and black crosses). Schematics of the electrical circuits at the nanotube and EGF electrode positions are also shown. d) Current *vs.* Voltage characteristics of the EGF electrode (black) and nanotube (gray).

Figure 3.20a corresponds to an AFM topographic image taken within the red circle shown in figure 3.19c. The inset shows a profile on the image, where a height of ~ 15 nm for the lower terrace of the EGF is measured. In both the image and the profile it is evident that the flake edge is extremely steep, much steeper than any contact fabricated by thermal evaporation [85]. In addition, there are no traces of contamination or degradation along it. Figure 3.20b is the same region as in figure 3.20a, but in this case a tip-sample Bias voltage of 4 V was applied to enhance the contrast of the nanotube due to the electrostatic interaction [102, 103]. Figure 3.20c corresponds to a higher magnification detail of the

green square in figure 3.20a. Figure 3.20c also shows the corresponding schemes for the associated electrical circuits of the measurements carried out. Figure 3.20d displays linear Current *vs.* Voltage characteristics measured for the EGF electrode and the nanotube (black and gray crosses in figure 3.20c respectively). Resistances of 1.7 and 47 kΩ were obtained for the flake and the nanotube respectively from the slopes of the Current *vs.* Voltage curves. Since the resistance of the EGF and the silver paint was found to be below 100 Ω, the resistance measured for the flake was a consequence of an external resistor of 1 kΩ added to the circuit (to prevent high currents on the preamplifier) and the small contact area between the AFM tip and the flake. The resistance measured for the carbon nantotube has contributions from both the contact resistance and the intrinsic resistance of the nanotube, but the obtained value allows to set an upper bound of contact resistance of ~ 46 kΩ, very similar to that measured with conventional metal electrodes [104, 105]. Previous attempts to contact carbon nanotubes with graphite flakes yielded much higher resistances [96].

- **Metal-organic MMX nanoribbons**

The next example describes the use of the procedure presented here to create electrical contacts on platinum-based MMX nanoribbons [106, 107]. Platinum-based MMX polymers are dimetallic subunits with two platinum centres connected by four bridging dithioacetate ligands and an iodine atom bridging the dimetallic units. By direct sublimation of monocrystals of $[Pt_2(dta)_4I]_n$ (*dta* = dithioacetate) on a SiO_2/Si substrate, nanoribbons are formed. Each nanoribbon is composed of thousands of parallel MMX chains of ~ 0.8 nm diameter interacting by weak van der Waals forces. These MMX polymers are perfect examples of molecule self-assembled nano-objects where it is very difficult to add contacts by conventional techniques. First, MMX nanoribbons obtained by sublimation of crystals were studied. Second, electrical properties of similar nanoribbons, but obtained by drop-casting, were able to be measured for the first time thanks to the technique presented here. In most of the cases, these drop-casted nanoribbons cannot withstand the conditions needed to evaporate conventional metal electrodes: the sudden evaporation of the solvent molecules adsorbed within the ribbons results in a large number of defects along the chains and turns them into electrical insulators [88]. Our measurements demonstrate that this technique is particularly useful in the case of molecules with limited stability under standard lithographic conditions.

As in the case of the carbon nanotubes, EGFs were transferred onto SiO_2 substrates to create electrical contacts on MMX nanoribbons previously deposited. Figure 3.21 summarizes the procedure applied to these MMX nanoribbons and the measurements for the sublimated ones.

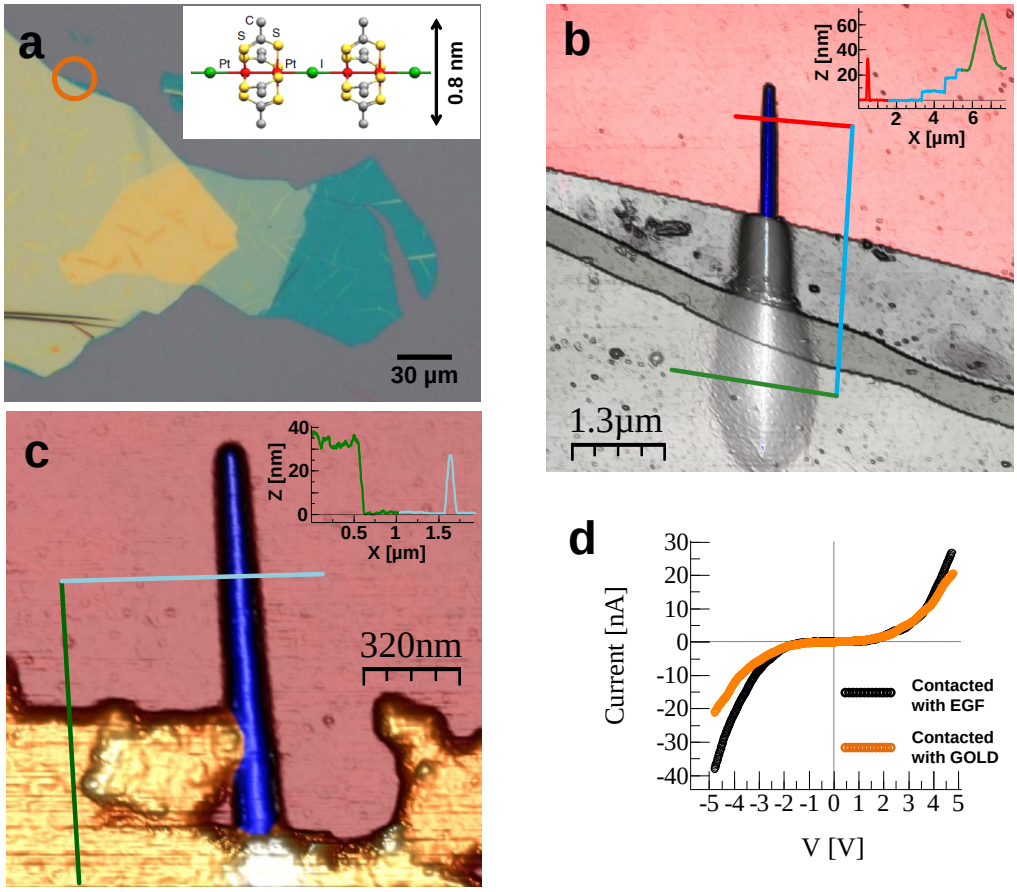

Figure 3.21 Contacts on sublimated MMX nanoribbons. a) Optical microscope image showing a transferred EGF on a silicon oxide substrate with MMX nanoribbons adsorbed on it. The inset shows the structure of an individual polymer chain. The orange circle enclosures an area with a MMX nanoribbon to be studied by AFM. b) AFM topographic image of the region within the orange circle in a) where a nanoribbon protruding from the EGF is clearly observed. c) AFM topographic image of a nanoribbon contacted with a gold flake (obtained from a piece of gold thin film transferred in a similar way to the EGF) that shows typical irregular edges at the nanometer scale. d) Current *vs.* Voltage characteristics for the nanoribbon with EGF (black) and gold (orange) contacts.

Figure 3.21a shows an optical microscope image of sublimated MMX nanoribbons where an EGF was transferred. As usual, the colors observed in the flakes reflect different thicknesses. The optical image allows seeing nanoribbons covered by the flake: the thin lines observed below the flakes are ripples caused by the nanoribbons. Figure 3.21b corresponds to an AFM topographic image showing a nanoribbon partially covered by an EGF with a very well-defined steep edge. According to the profile of the inset, the height of the lower EGF terrace is ~ 5 nm. MMX nanoribbons with these contacts were tested, as in the carbon nanotubes case, by using a conductive AFM tip as a second mobile electrode.

Figure 3.21d displays representative IV curves obtained for these nanoribbons. The conductivity obtained for them is similar to that measured previously for nanoribbons of the same kind using evaporated metal electrode contacts [107]. In the case of these MMX nanoribbons, their intrinsic resistance is much higher than that of the contacts, unlike to the case of carbon nanotubes, where it is similar to that of the electrode-nanotube contacts. As quasi-one-dimensional conductors, the electrical resistance and the shape of the IV curves of these MMX nanoribbons are mainly dictated by the density of defects in their atomic structure originated during the assembly process [106, 107] as is shown more in detail in Chapter 4.

In order to compare the electrical contact resistance from EGFs with that from soft-metal electrodes, contacts on these MMX nanoribbons using gold flakes were also created. To this end, a 30 nm thick film of gold was first evaporated on a glass substrate using a TEM grid as a stencil mask. In this way, 60 x 60 μm^2 gold squared pads separated by 25 μm were obtained. A viscoelastic polymer was pressed against the gold so evaporated, resulting in thin gold flakes adhered to the polymer. Some of them were then transferred to a substrate containing MMX nanoribbons, following the same procedure sketched in figure 3.19. Figure 3.21c depicts an AFM topographic image of a MMX nanoribbon protruding from a transferred gold flake, which shows irregular and not steep edges. C-AFM was again used to perform the electrical characterization of the MMX nanoribbons (prepared in the same conditions as the ones described above) with these gold flakes contacts, obtaining IV curves at the same tip-gold electrode distance as in the previous EFG contact, yielding a similar resistance (figure 3.21d). These measurements highlight the ability of the technique presented here to create contacts on samples with very different chemistries.

As mentioned before, up to now the electrical characterization of drop-casted MMX nanoribbons was hampered by their limited stability under standard lithographic conditions [88]. While sublimation is a suitable technique to grow different nanostructures on surfaces, is tedious and requires costly equipment and considerable time. Drop-casting is the option of choice for a more simple and powerful procedure based on wet chemistry, since it is an easy, well-known and commonly used technique to adsorb molecules on surfaces. Figure 3.22 shows characterization of drop-casted MMX nanoribbons and its comparison with previous sublimation results [107].

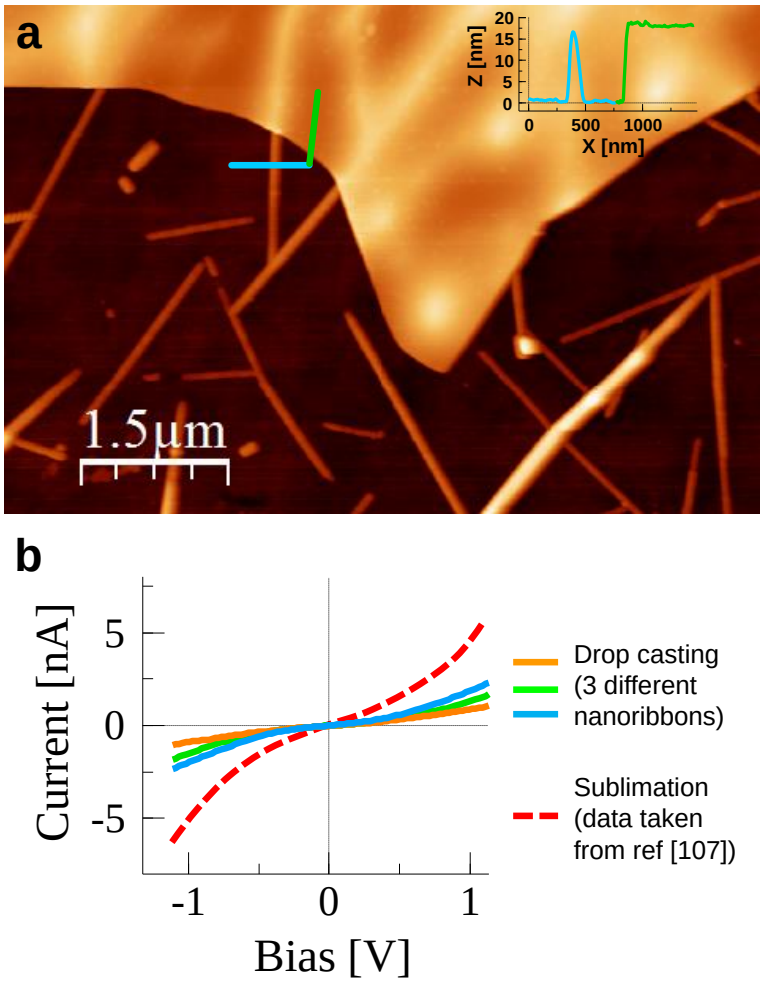

Figure 3.22 Contacts on drop-casted MMX nanoribbons. a) AFM topographic image of a region where several nanoribbons are protruding from an EGF electrode. The inset is a profile along the blue-green line showing the heights of the ribbon and the flake. b) Current *vs.* Voltage characteristics for three different drop-casted nanoribbons (solid lines) and for a typical sublimated one with similar characteristics and measured under the same conditions (dashed line, data taken from reference [107]).

Figure 3.22a corresponds to an AFM topographic image showing nanoribbons on the substrate, some of them partially covered by an EGF electrode. Figure 3.21b displays IV curves obtained for these nanoribbons using C-AFM. A direct comparison with sublimated nanoribbons of the same dimensions contacted using evaporated metal electrodes [107] is shown, remarkably resulting in very similar resistances. These measurements prove the ability of the technique presented here to create contacts on samples that can hardly stand the fabrication procedures of conventional techniques.

- **Reduced graphene electrical characterization through a double soft-electrode transfer**

The next example consists in the electrical characterization of a single layer of reduced graphene oxide by transferring two independent EGF soft-electrodes. This example illustrates the precision achievable when placing the electrodes. Figure 3.23 presents this double soft-electrode transfer application.

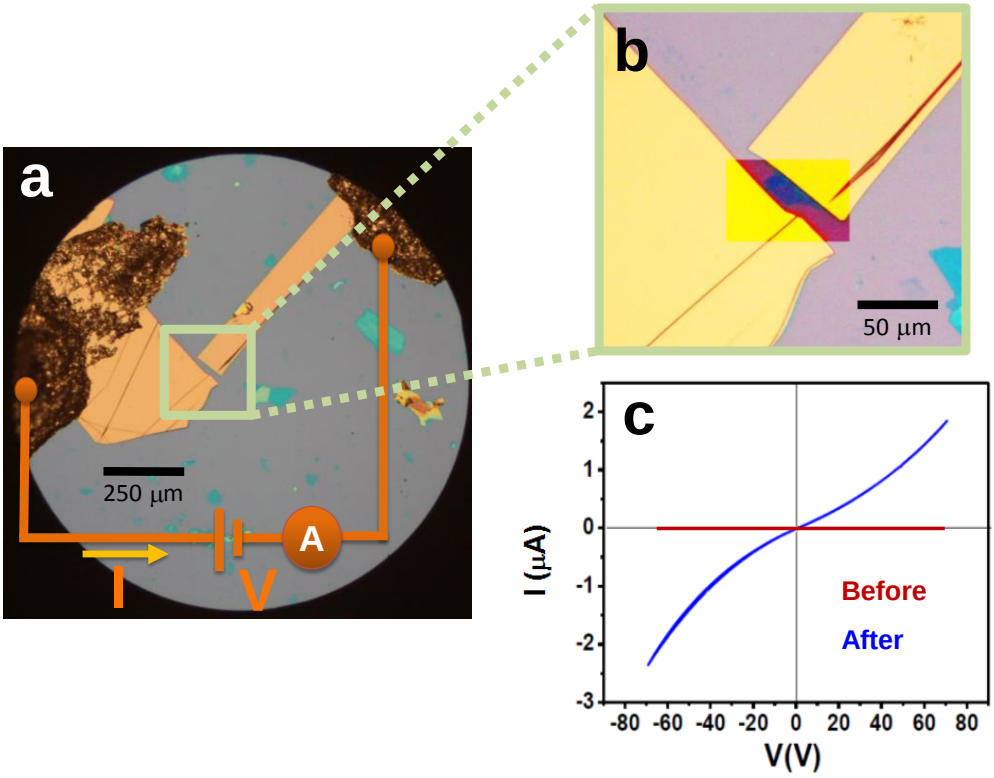

Figure 3.23 Double electrical contact in graphene oxide (GO). a) Optical microscope image showing two EGFs electrodes in contact with a single layer of graphene oxide. For the sake of clarity a schematic electrical circuit was also included. b) Magnification of the enclosed region. The contrast in the region of interest was increased to allow identification of the GO flake. c) Current *vs.* Voltage characteristics of the circuit shown in a) before and after thermal reduction. As deposited, GO is an insulator, but after reduction it behaves as a conductor.

Figures 3.23a and b show a graphene oxide (GO) flake in contact with two EGF microelectrodes. The gap between the two electrodes is ~ 10 µm. As reported in reference [108], initially the flake is an excellent insulator (figure 3.23c, IV curve "Before"). The sample was thermally reduced by annealing it overnight up to 250 ºC in a high vacuum chamber at 10^{-6} hPa [109]. Upon this thermal reduction, electrical characterization of the

sample was carried out (figure 3.23c, IV curve "After"), giving similar results to those found in the literature for reduced graphene oxide (RGO) [108, 109].

- **Damaged circuit repair**

The last example demonstrates how EGF microelectrodes can be used for repairing microcircuits. Figure 3.24 illustrates this possibility by showing the repair of two simple microcircuits.

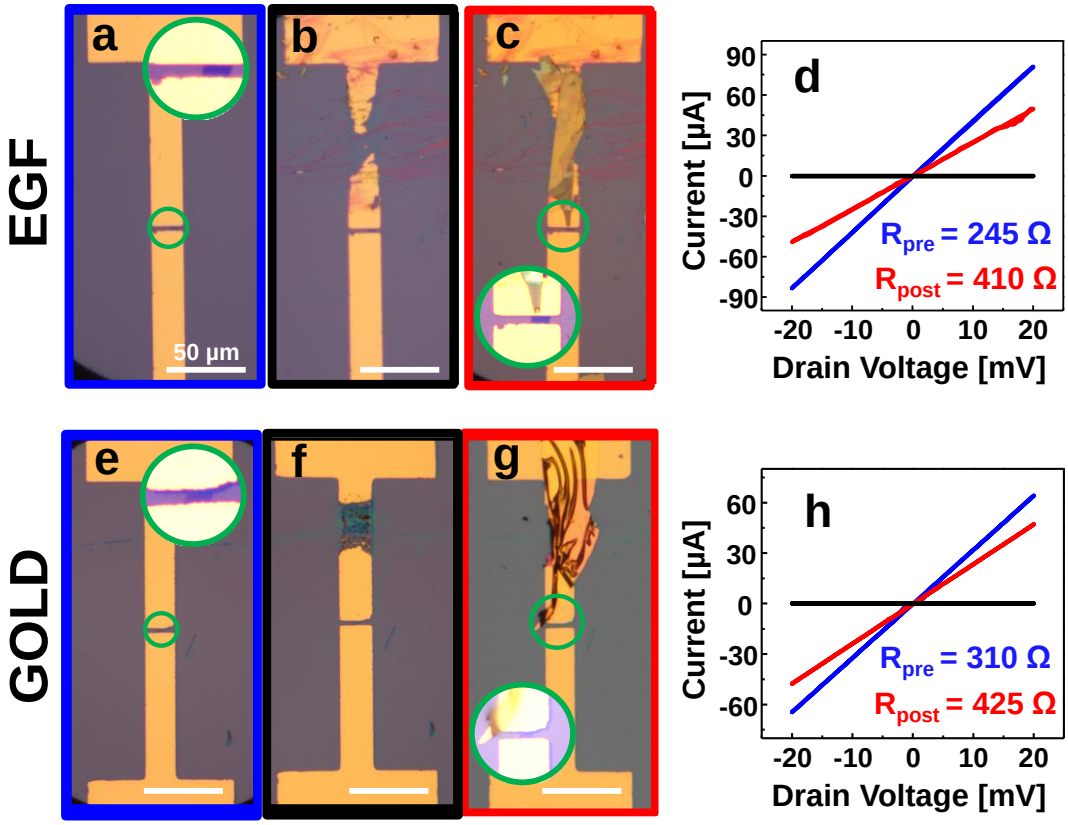

Figure 3.24 Circuit repair. a) Electrical circuit made by Au/Cr evaporation with a stencil mask. The Au/Cr electrodes are in contact with a pristine bilayer graphene flake. b) Open circuit after being scratched with a tungsten carbide tip. c) Circuit repaired using an EGF. d) Current *vs.* Voltage characteristics of the intact (blue), open (black) and repaired (red) circuit. e-h) Similar repair but this other circuit was cut using an infrared laser and repaired with a gold thin film flake. All the insets are magnifications of the central regions of the circuits where the graphene flakes are placed. Their contrasts were increased to allow better identification of the graphene flakes. Insets in panels c) and g) show the absence of short-circuits between the upper and lower Au/Cr electrodes after repairs.

Figures 3.24a-c show a pristine bilayer graphene flake in contact with two Au/Cr electrodes evaporated using a stencil mask. Figure 3.24d (blue line) shows the corresponding Current *vs.* Voltage characteristic where an electrical resistance of 245 Ω is measured. The upper electrode was scratched using a hard tungsten carbide tip, removing part of the metal (figure 3.24b) and opening the circuit, showing in this case an infinite resistance. An EGF was then transferred covering the damaged part and repairing the circuit. The electrical resistance of the repaired circuit is 410 Ω, (figure 3.24d). This increase in resistance is likely due to the contact resistance of the Au/Cr electrode and the EGF used to repair the circuit. Figure 3.24e presents a second circuit where another pristine bilayer graphene flake is in contact with other two Au/Cr electrodes, presenting an electrical resistance of 310 Ω. The upper Au/Cr electrode was in this case cut using an infrared laser (figure 3.24f). Electrical resistance measurements confirm an open circuit with no current through the damaged Au/Cr electrode. This circuit was then repaired by transferring a 30 nm thick gold film flake. Figure 3.24g shows the repaired circuit. Electrical measurements on such repaired circuit show a final resistance of 425 Ω (figure 3.24h). An increase in resistance of a few Ohms is observed in both repaired circuits. Since this resistance can be significant for the two cases described here (where a highly conducting sample such as graphene flakes is probed), the vast majority of conducting nano-objects exhibit much higher intrinsic resistances, thus making this increase in resistance negligible for their electrical characterization. Therefore, the final low resistances obtained after repair validate this methodology.

In summary, a procedure to fabricate microelectrodes based on the deterministic transfer of 2D materials by all-dry viscoelastic stamping has been introduced. This method is simple, cost-effective and it allows contacting molecules with limited stability under conventional lithographic conditions. In order to validate and illustrate the uses of this methodology, four relevant examples of its many possibilities have been provided, showing that the quality of the electrical contacts so far obtained is as good as those obtained by conventional techniques. Additionally, it has been used to contact for the first time drop-casted MMX nanoribbons, which are very difficult to contact using other approaches.

3.3.2 Probe-Assisted Nanowire (PAN) lithography: a new paradigm for nanoelectrode fabrication

3.3.2.1 Introduction

Nanowires (NWs) are proposed as ideal candidates to be the connecting elements in nanometer-scale devices [110]. Gold nanowires (Au NWs) have long been a challenging wished structure to be reached in a controlled and reproducible way and in large quantities due to their high conductance and, unlike other nanowires such as silver or copper ones, their resistance to corrosion or oxidation. While making single crystalline nanowires of other FCC metals, including silver [111, 112] and copper [113], was achieved already back in the late 90's, this was not the case with gold. Up to less than ten years ago, the synthesis of well-defined Au NWs was limited to those either very thick (> 100 nm [114]) or very thin and short (< 2 nm [115, 116] and < 10 nm [117]), thus hampering their use for technology applications. The chemical synthesis of Au NWs at room temperature in acidic solutions in 2008 by Kim *et al.* [118] allowed the fabrication of reproducible Au NWs with well-defined surfaces. Subsequent improvements in nanowire monodispersing and scaling allow nowadays finding commercially available Au NWs suitable for high technology electronics. Albeit NWs dispersed in solutions can be aligned onto substrates using different procedures (including dielectrophoretic, LangmuirBlodgett, microcontact stamping, molecular surface patterning and fluidic flow alignment techniques) [119] (and references therein), and are proposed as building blocks for self-assembling logic and memory circuits [120], a technique allowing the manipulation of single NWs is needed to fabricate nano-devices. In this sense, AFM has proven to be an ideal technique to characterize and manipulate individual nanotubes and nanowires [121-124].

In this section, a technique based on the adsorption and nanomanipulation of Au NWs to fabricate nanoelectrodes is presented. As for the case of exfoliated graphene flakes electrodes, it does not require resins or chemical agents; the process is based on the adsorption of Au NWs on the sample of interest by drop-casting them dispersed in a solution (there are commercially available NWs suspended in a number of liquids including water, ethanol…). Then, their cold welding ability (the welding of metals without heating) [92] allows creating and positioning the desired nanoelectrodes, by manipulating the adsorbed Au NWs with the aid of an AFM probe. Thus, the name chosen for this technique: Probe-Assisted Nanowire (PAN) lithography. As it is shown below, PAN lithography is a clean, cost-effective and reliable technique. Its most relevant advantages are the possibility of contacting nano-objects with dimensions down to ten nm [125] (impossible for any conventional methodology, including e-beam lithography), which will allow multiple currently intractable experiments, as for instance the connection of molecular-scale entities and nano-objects with limited stability under standard lithographic conditions (as in the

EGF soft-electrodes case). This new methodology also opens another possibility which relays on the movable character of the terminals so created, allowing the reconfiguration of their position to perform multiple electrical measurements on various entities on the same substrate and/or with different terminal geometries.

PAN lithography can be applied to create contacts almost in any electrical configuration. Figure 3.25 shows different examples that can be fabricated with PAN lithography: a single Au NWs electrode combined with C-AFM measurements; a two-terminal Au NWs electrode design; a three-terminal scheme where one of the Au NWs electrode can be used to apply a lateral gate voltage; or in a general point of view, a *n*-terminal scheme (where $n = 4$ is the most usual configuration). Any of these configurations require microelectrodes to link the PAN electrodes with the macro-scale measuring devices. For this purpose, any conventional technique to fabricate microelectrodes can be employed; in particular, metal-evaporated pads using stencil masks or the above presented EGF soft-electrode transfer can be good options. Back-gate voltages can be applied in any configuration if using an appropriate substrate (as for instance standard SiO_2/Si substrates).

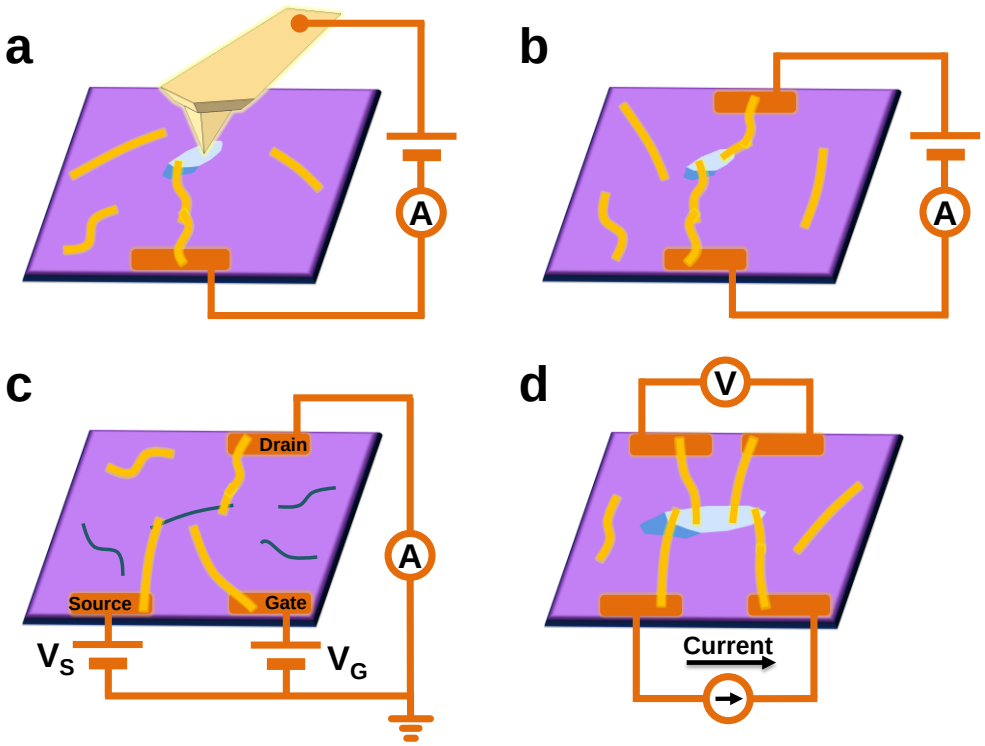

Figure 3.25 Some electrical characterization configurations that can be fabricated with PAN lithography. a) Single Au NWs electrode with a conductive AFM tip acting as a second mobile electrode. b) 2-terminal Au NWs electrodes setup. c) 3-terminal scheme where one of the Au NWs electrodes can be used to apply a lateral gate voltage. d) 4-terminal scheme. In any of the configurations, a back-gate voltage can be applied if the substrate allows it.

In this section first a description of the technique is provided and then a relevant example illustrating the procedure is presented. The potential of the technique is demonstrated by probing the electrical properties of a 150 μm long electrode formed by assembling individual NWs and by the electrical characterization of a well-known highly conducting sample: graphene flakes. A two-terminal scheme has been used, where one of them has been fabricated using PAN lithography and the other has been a conducting AFM tip (C-AFM), as in figure 3.25a. In Chapter 4, after the introduction of the isolation for the first time of antimonene (a single layer of antimony atoms), electrical characterization of few-layer antimonene flakes through PAN lithography and C-AFM has also been performed.

The work presented here is unpublished so far and it has been done in collaboration with Dr. Félix Zamora and Dr. Cristina Gómez-Navarro groups. Further work on 2- and 4-terminal Au NWs electrode configurations is now being carried out by Miriam Moreno-Moreno to demonstrate the many possibilities of PAN lithography.

3.3.2.2 Results and discussion

Figure 3.26 summarizes the key steps of the PAN lithography technique. The whole experimental setup comprises any conventional microelectrode fabrication procedure, commercial Au NWs and an AFM with lithographic capabilities. Bare Au NWs with nominal dimensions 75 nm diameter and 10 μm length, shipped in DI water in a concentration of 0.05 mg/ml with excess cetrimonium bromide (CTAB) capping agent (a surfactant to prevent the NWs from aggregating) were purchased from Nanopartz Inc. [126]. PPP-FM probes from Nanosensors^{TM} [69] were employed for the nanowire manipulation. They have a resonant frequency of 75 kHz in air and a nominal stiffness of 2.8 N m^{-1}. The tip has a radius of curvature < 10 nm.

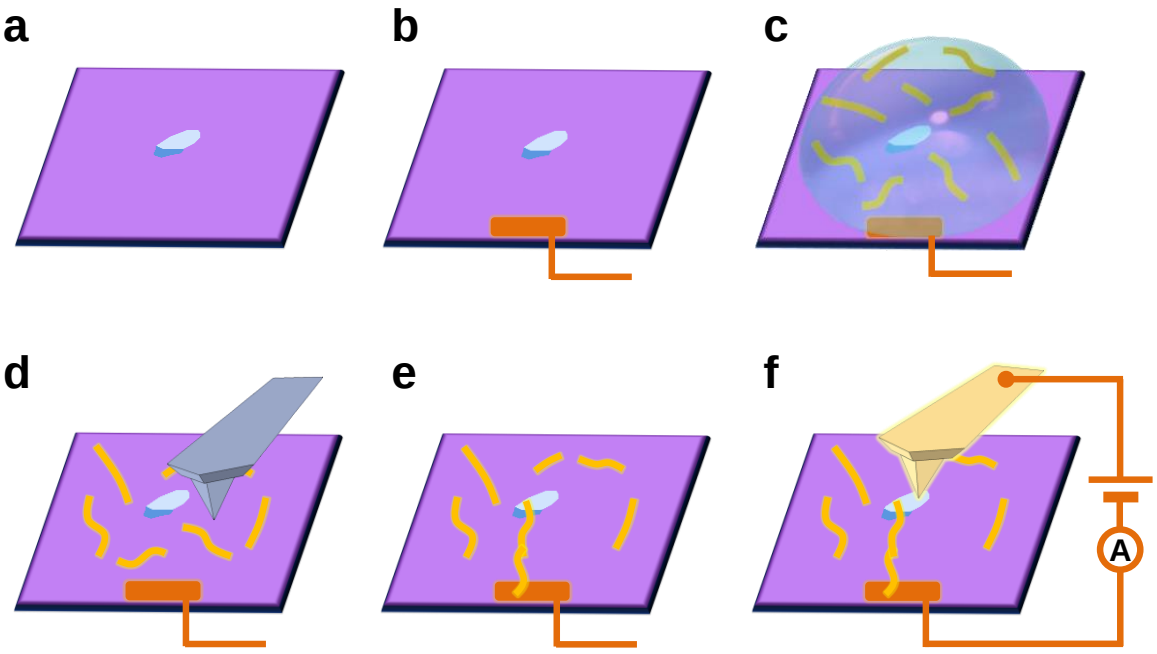

Figure 3.26 PAN lithography procedure. a) Sample under study. b) Conventional microelectrode fabrication. c) Au NWs adsorption by drop-casting. d) Au NWs manipulation with an AFM tip. e) Sample under study connected to the microelectrode through manipulated Au NWs. f) Electrical characterization of the sample.

Samples studied in this work (2D materials obtained by microexfoliation) are already located on the substrate (figure 3.26a) and the procedure starts by fabricating conventional microelectrodes. In the case of samples obtained by drop-casting, the procedure would start by first fabricating conventional microelectrodes on the bare substrate followed by deposition of the sample. In the case presented here, microelectrodes were fabricated by Au evaporation using stencil masks and connected externally using silver paint (figure 3.26b). Then, Au NWs were deposited on the substrate by drop-casting (figure 3.26c). To this end, the dispersion containing the Au NWs was first placed on vortex mixer for 1 minute and an aliquot was then sonicated in an ultrasound bath (37 kHz, 380 W) for 5 minutes at room temperature to resuspend aggregated particles. 40 µl of this aliquot were drop-casted on the substrate and left ~ 45 minutes for nanowires adsorption. After this time, substrate was washed with DI water and dried in an N_2 gas flow. A final concentration of ~ 1 NW on 5 μm^2 was used, which required repeating 4 times this drop-casting step (from the same aliquot already sonicated). The substrate was inspected using an optical microscope in a dark-field configuration to check if the concentration of Au NWs was adequate (figure 3.27).

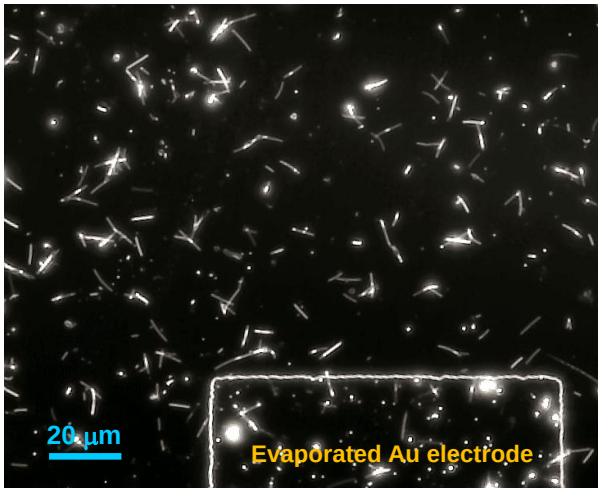

Figure 3.27 Dark-field optical microscope of a SiO_2/Si substrate with adsorbed Au NWs. The nanowires and the edge of the gold electrode shine with white light.

Once the concentration of Au NWs on the substrate was high enough, they were manipulated with an AFM tip to form a path connecting the sample and the microelectrode (figure 3.26d). Figure 3.28 depicts the steps comprising the Au NWs manipulation with an AFM probe.

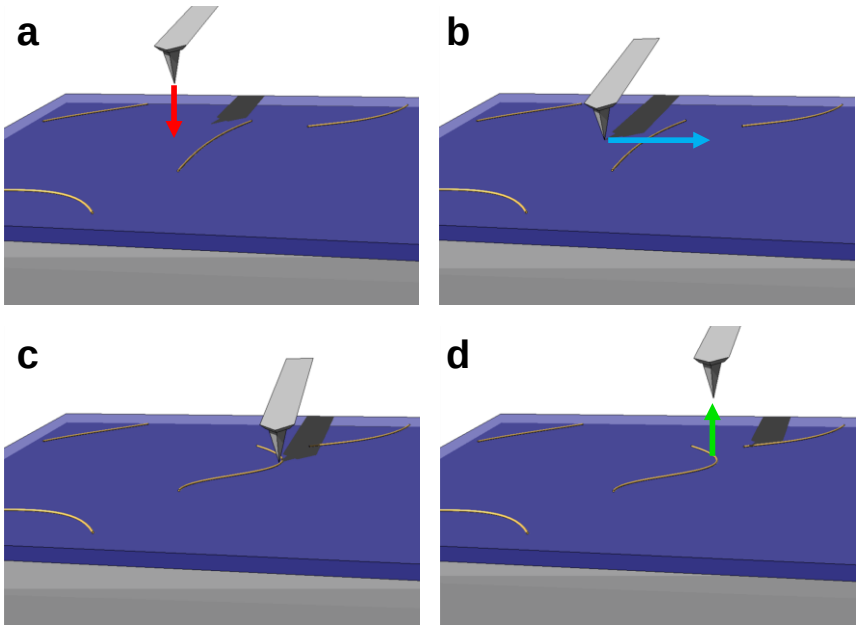

Figure 3.28 Au NWs manipulation schematics. a) After imaging Au NWs in AM-AFM mode, the tip is brought into contact. b) The tip is moved along a predefined path to manipulate the Au NW. c) The selected Au NW is moved. d) The tip is brought back to AM-AFM mode and a new image is taken.

To this end, first the sample is imaged in AM-AFM mode, with the tip far from the NWs. Then the tip is brought into contact with the substrate (figure 3.28a) and it is moved along a predefined path (figure 3.28b), manipulating/moving the Au NW (figure 3.28c). Finally, the tip is lifted back to AM-AFM mode to image the results of the manipulation. Figure 3.29 shows an example of these nanomanipulations and the corresponding script on the control software, where a remarkably simple procedure is employed.

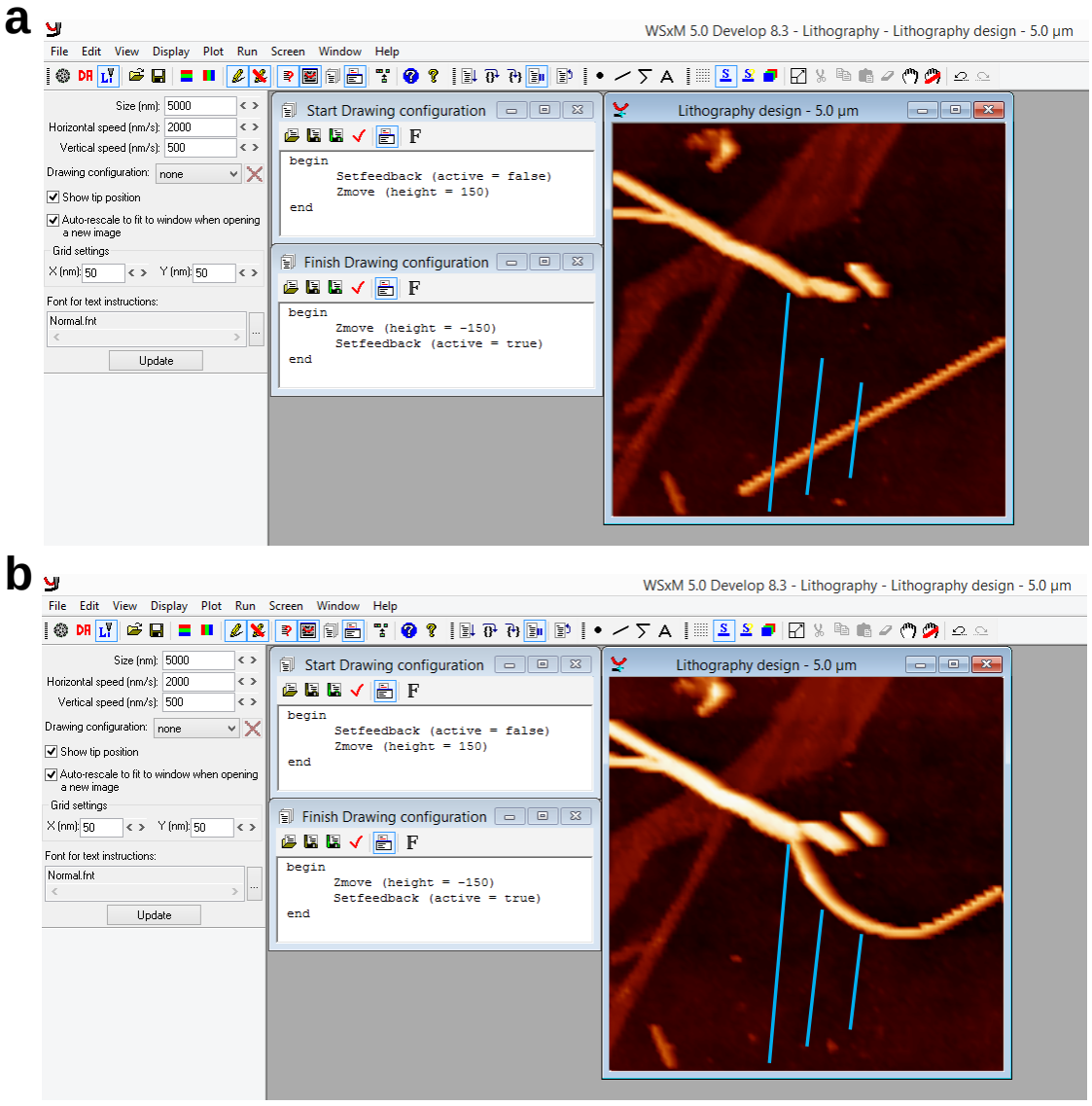

Figure 3.29 Example of Au NWs manipulation. a) WSxM Lithography frame. The design window shows some Au NWs before manipulation. Blue lines represent the tip trajectories in contact (the tip moves from the bottom to the top). b) WSxM Lithography frame after manipulation.

In order to minimize lateral forces, imaging is performed in AM-AFM mode with a cantilever oscillation of ~ 20 nm. In the WSxM Lithography frame some lines representing the tip trajectories during lithography actuation are drawn. When the lithography is selected to be performed, the tip moves to the beginning of the first line still in AM-AFM mode. Then the tip is lowered 140-190 nm (150 nm in figure 3.29), reaching the contact regime, applying forces in the range of ~ 200 - 300 nN. Then, with the topography feedback disabled, it is moved in contact along the drawn trajectory at 2 μm/s. At the end of the line, the tip is lifted back 150 nm, and the feedback is enabled restoring the AM-AFM mode. Then it is moved to the beginning of the next line, repeating the same procedure for all the drawn lines.

To obtain an optimum electrical assembly, a NW is pushed against other and they are found to cold weld just by mechanical contact [92]. Whereas for thinner Au NWs (diameters of 3 - 10 nm) almost any joining procedure is reported to be successful ("head-to-head", "side-to-side" and "head-to-side" configurations) [92], in the case of the Au NWs used here (nominal diameter or 75 nm) a "head-to-side" configuration is found to provide a better electrical joining. A one-day working time allows forming up to a ~ 40 μm long path. To check the electrical connection between Au NWs, a metallized AFM tip is used, probing the conductivity of the path by performing IV curves on top of Au NWs at different path distances from the microelectrode. If a junction failed to be connected, this same tip can be used to further push the Au NWs until a linear current response is later obtained when doing an IV curve. In this way, the sample is finally electrically connected to the microelectrode (figure 3.26e) and ready to characterize its electrical properties, either by using a metallized AFM tip as for the junction checks (figure 3.26f) or by assembling any of the measuring configurations shown in figure 3.25.

Some issues were found when performing the nanomanipulations. Some NWs broke during the manipulations, generally the longest ones, but the broken parts were also easily moved and welded, so this was not a relevant problem. Some other NWs were kind of "anchored" to the substrate, but this occurred in very few cases and, since the number of adsorbed NWs can be controlled, in the case of not having enough NWs on the substrate the deposition steps can be repeated as many times as necessary. The main issue found during the nanomanipulation process was the tendency of the tip to leave a debris particle from time to time, after having performed many manipulations. When this happened, the tip was replaced and the debris was moved away with the new tip following a similar procedure as to move the Au NWs. Then, new manipulations were performed. Metallized tips (the ones used for the conductive measurements) turned up to be more prone to leave debris, this is why they were used just for checking conductivity and, if necessary, for further pushing nanowires in a failing junction, but not for the whole nanomanipulation process. Regardless these issues, a long Au path comprising many junctions was assembled to show the potential of this technique and to better characterize the electrical properties of the

nanoelectrodes so produced. Figure 3.30 shows a ~ 150 μm long path formed by joining 93 Au NWs and statistics of their dimensions.

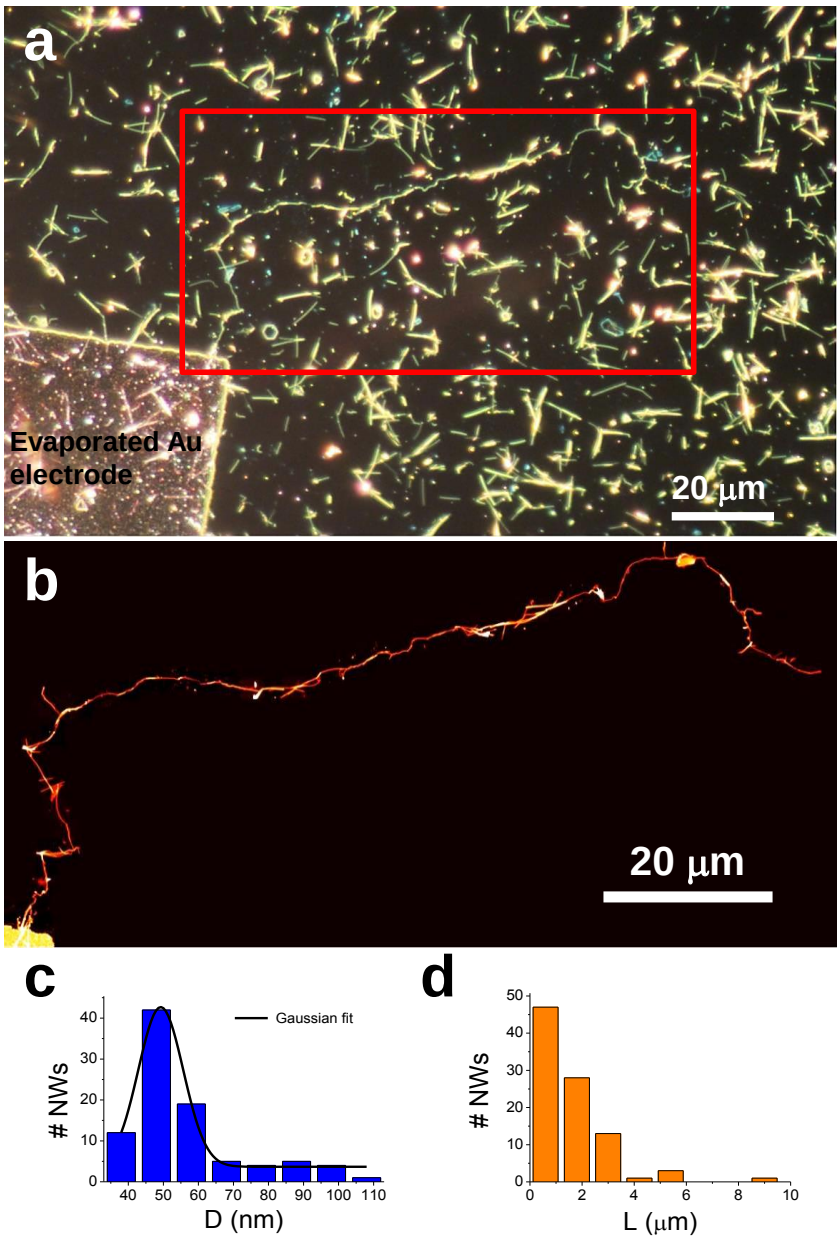

Figure 3.30 150 μm long path formed by assembling 93 Au NWs. a) Dark-field optical microscopy image. Multiple Au NWs can be observed. A continuous path of Au NWs, enclosed by a red frame, can be observed protruding from the top-right corner of the microscopic Au electrode. b) AFM topographic image corresponding to the rectangle in a). This image is a collage of AFM images of smaller areas following the Au path, hence the absence of any feature far from it. Total range of the color scale is 150 nm. c) and d) Histograms of the diameter and length respectively of the individual Au NWs forming the path, as measured from AFM. Gaussian fit in c) provides 49 ± 6 nm (mean ± SD) for the diameter of the Au NWs.

Average dimensions of the Au NWs forming the path differ from their nominal values. Whereas the manufacturer nominal diameter is 75 nm, their average value from AFM measurements is 49 ± 6 nm (mean ± SD), with almost the 80% of the NWs having a diameter lower than 60 nm. In the case of their length, it goes far from the manufacturer 10 μm nominal value, to an average length of 1.7 ± 1.3 μm, with the 95% of the NWs being shorter than 4 μm. Part of this length reduction could be due to the sonication performed to resuspend aggregated particles. Also the breakage of NWs during nanomanipulation contributed to the length reduction.

To characterize the effects of the dimensions and the presence of junctions in the conductivity of the path, IV curves were performed with a metallized AFM tip at different locations along it, measuring the current flowing from these locations to the evaporated Au electrode. As a result, a Resistance *vs.* Length (R-L) graph could be plotted. Figure 3.31 presents the experimental R-L plot. It also shows the ideal resistance values for the path, calculated considering the dimensions of each of the NWs and the Au bulk resistivity, which at room temperature is quoted to be 2.2 x 10^{-8} Ω m [127, 128].

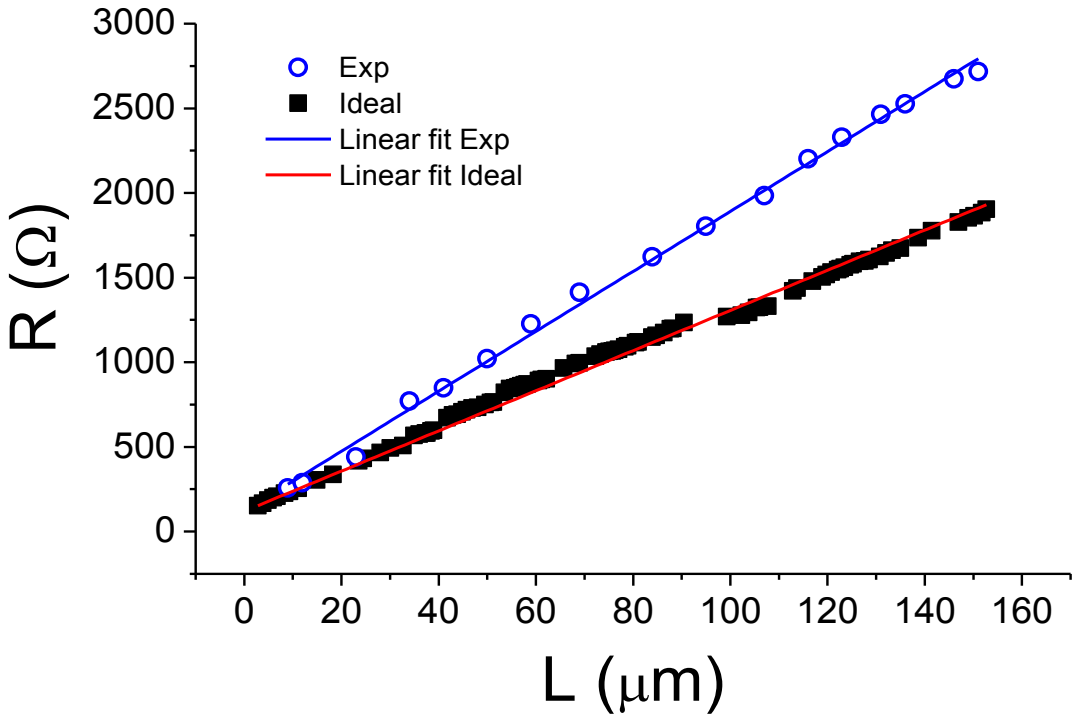

Figure 3.31 Resistance *vs.* Length for the 150 μm long Au path shown in figure 3.30. Circles correspond to the experimental data from IV measurements with a metallized AFM tip. Solid squares correspond to the ideal resistance as explained in the main text.

Au NWs of similar widths as the ones used for PAN lithography are reported to present the same or near bulk Au resistivity [119, 129]. From the data in figure 3.31, a resistivity of $(3.3 \pm 0.8)\ 10^{-8}\ \Omega$ m can be calculated, only a factor ~ 1.5 above the bulk value. Studies on the conductivity of metallic thin films and wires conclude that grain boundary reflections rather than surface scattering are the dominant contributions to the resistivity of NWs [130-132]. Taking this into account, the difference between experimental and ideal resistances at the end of the path can be attributed to grain boundaries (which would not be surprising to appear when cold welding NWs of the diameters used here). A total increase of ~ 814 Ω at the end of the path, divided into 93 junctions, yields an average resistance of ~ 8.8 Ω for each of the junctions, in very good agreement with reported values by Bietsch and Michel [130] of 4 - 10 Ω for the resistance of single grain boundaries in Au NWs. In the case of real experiments, distances around 20 μm will be much more realistic than the 150 μm of the path above studied. In such cases, an increase of only less than 100 Ω is expected, suggesting PAN lithography as a technique to create near-bulk resistivity Au nanoelectrodes.

To illustrate the power of PAN lithography in a simple case, it is applied for the electrical characterization of graphene flakes. For this purpose, few-layer graphene flakes were deposited by microexfoliation on a 300 nm SiO_2/Si surface. Then a micron-sized gold electrode was fabricated by stencil mask-assisted gold evaporation, followed by adsorption of Au NWs using the procedure described above. Figure 3.32 shows images before and after lithography manipulations of the NWs with AFM and the electrical characterization of a small few-layer graphene flake (size ~ 1 x 0.4 μm^2).

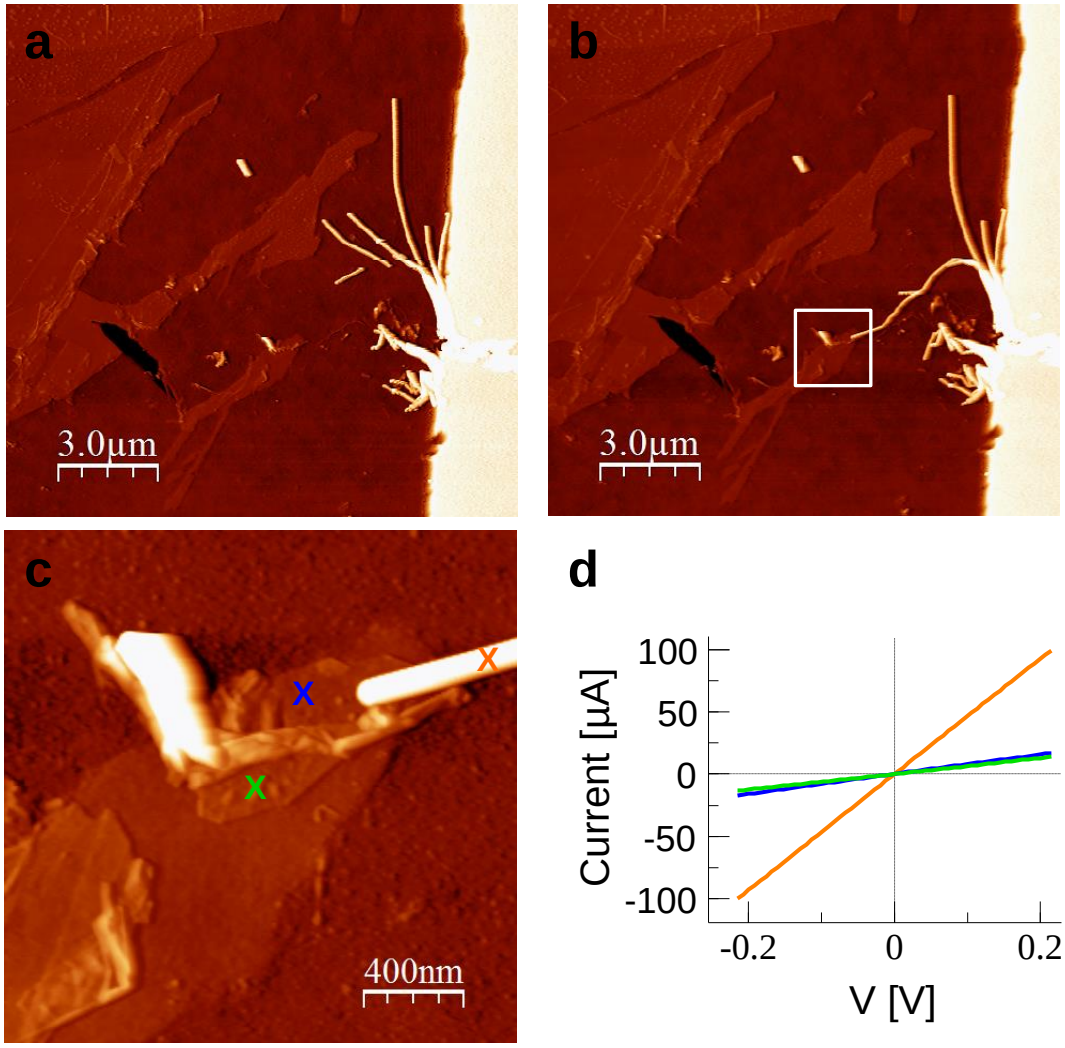

Figure 3.32 a) AFM edge-enhanced topographic image of several few-layer graphene flakes on a SiO_2/Si substrate. On the right, an evaporated Au electrode is visible. Adsorbed Au NWs, some of them protruding from the evaporated electrode, are also visible. Total color scale range is 80 nm. b) AFM topographic image of the same area after the manipulation of three NWs to create a nanoelectrode on one of the few-layer graphene flakes. c) Magnification inside the square in b). The size of the contacted flake is ~ 1 µm x 0.4 µm. d) Current *vs.* Voltage characteristics corresponding to the locations marked in c) performed with a metallized AFM tip.

Figure 3.32 demonstrates that PAN lithography was successfully applied to contact small nano-objects very difficult to access by other techniques. Figures 3.32a and b show a few-layer graphene flake before and after NWs manipulation. Figure 3.32c is a detail of the contacted flake. A small flake, delimited by sharp geometrical edges, was contacted by the Au NW. On the left there was another flake, going out of the image frame. Below them there is a debris layer. The actual size of the probed flake was ~ 0.4 μm^2. While contacting

flakes of this size is very easy with PAN lithography, it requires a great effort using other techniques such as e-beam lithography (EBL). Consulting an expert on EBL, with that technique it would take at least one week at full working time, but for these tiny flakes a successful contact would not be even guaranteed. By using PAN lithography it took less than two days to create the contact: one day for the microelectrode evaporation, external connections and NWs deposition and half a day for the NWs manipulation. Figure 3.32d presents Current *vs.* Voltage measurements on two different spots of the flake. As expected, a small decrease in current is observed with increasing distance to the NW electrode. To study this more in detail and to show the potential of PAN lithography, the NW contact was "remanipulated", to contact the upper flake in image 3.32 and perform its electrical characterization as a function of the distance to the electrode. As already mentioned, this possibility of reposition/reconformation of the nanoelectrodes is another of the main advantages of PAN lithography respect to conventional techniques. A video showing the manipulations performed in real time to reposition the NWs electrode can be found in the following link:

https://www.dropbox.com/s/ihtnq9nube3t6um/Au_NWs_manipulation.mp4?dl=0

This electrode "reallocation" was performed using a metallized AFM tip; this is why at the end of repositioning the nanolectrode a first IV characterization could be performed to ensure a proper contact. It is important to notice the total duration of the process: the whole video lasts for ~ 3.5 minutes. Figure 3.33 presents the electrical characterization of this upper flake as a function of the distance between electrodes.

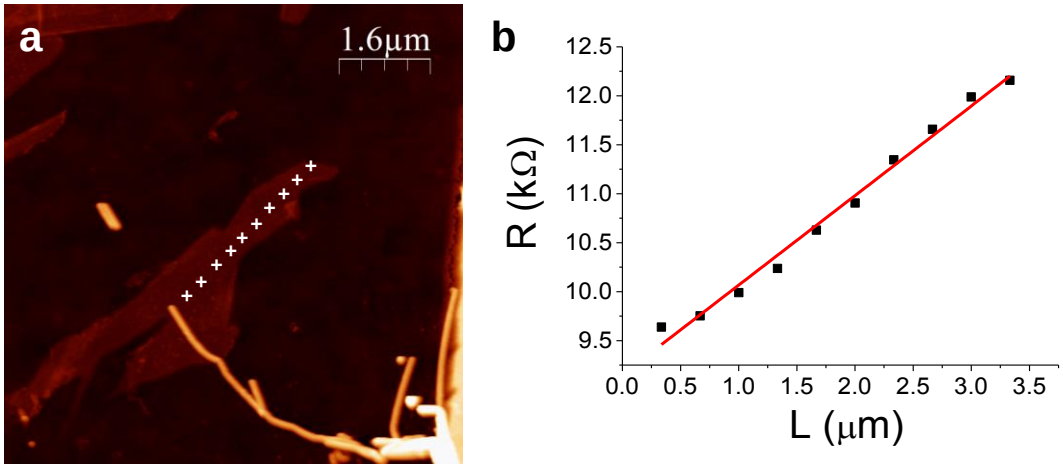

Figure 3.33 a) Few-layer graphene sheet with a nanoelectrode created through PAN lithography. White crosses indicate the positions where IV curves were acquired. b) Resistance as a function of the distance to the Au NWs electrode.

Figure 3.33a shows the flake with the Au NWs electrode after repositioning. Locations where IV curves were obtained using a metallized AFM tip are marked with white crosses. Figure 3.33b shows the resistance R of the flake as a function of the length L (distance between electrodes). The slope of the resistance or 1D resistivity, ρ_{1D} = dR/dL is fairly constant (ρ_{1D} = 0.91 ± 0.03 kΩ/μm from the slope of the linear fit). From the intersection of the fitting line for L = 0 a contact resistance R_C = 9.2 ± 0.1 kΩ is obtained, comparable to that reported in graphene nanoribbons contacted through a gold evaporated electrode and a metallized AFM tip [133] (R_C ~ 4 kΩ) or through a four-terminal approach by e-beam lithography [134] (R_C ~ 1 kΩ). While four-terminal measurements eliminate the residual contact resistance, a high contact resistance value could be an issue in conventional fabricated two-terminal configurations (where the contact resistance is not easily known). The readily repositioning of any of the nanolectrodes fabricated by PAN lithography allows performing straightforward conductivity measurements as a function of the electrodes distance in two-terminal measurements, thus quantifying and taking into account the contact resistance present in the device.

The observed linear behavior of the R-L is expected for a material with a constant sheet resistivity ρ_{2D}. The sheet resistivity can be defined as:

$$\rho_{2D} = \frac{\Delta R}{\Delta L} W \tag{3.1}$$

where ΔR is the contribution to the resistance of a portion of the flake in a length ΔL with a width W. Consequently, $\rho_{2D} = \rho_{1D}$ W. Please notice that the unit of ρ_{2D} is Ω. It is usually employed Ω/□ to express the ρ_{2D} 2-dimensional character. From equation 3.1 and taking the corresponding width from the AFM topographic image, a value for the sheet resistivity ρ_{2D} = 670 ± 60 Ω/□ is obtained. Since the flake under study cannot be considered a one dimensional object, a comparison of the obtained ρ_{2D} with reported values is more appropriate rather than comparing ρ_{1D}. The obtained ρ_{2D} value is consistent with those observed measuring few-layer graphene in a 4-terminal configuration ~ 450 Ω/□ [80], graphene nanoribbons ~ 590 Ω/□ [134] and also with that obtained for nanoribbons measured using a similar configuration as in here (a metallized AFM tip as a second mobile electrode) ~ 500 Ω/□ [133]. This result confirms PAN lithography as an alternative to conventional techniques to create nanoelectrodes.

3.4 Conclusions

In the first part of this chapter, significant AFM improvements in liquids have been presented:

First, sub-helical resolution AFM images of individual double-stranded RNA molecules have been shown. Both minor and major grooves have been resolved and the helical pitch has been quantified using three different high sensitive imaging modes: AM-AFM, DAM-AFM and JM+, resulting in 3.1 ± 0.3 nm, compatible with the A-form of dsRNA. Data obtained with the different imaging modes show similar resolution at optimized working conditions. Simulated AFM images have allowed estimating the tip radius employed for high resolution imaging, showing that radii as small as 2.5 nm are needed to discriminate both major and minor grooves. Use of slightly larger radii leads to the observation of a single periodicity in both dsDNA and dsRNA samples. It can be concluded that two aspects are critical to obtain high resolution of nucleic acids in liquid rather than the imaging mode: first, the interacting force, that can be minimized with the proper tuning of each imaging mode parameters, and second, the sharpness of the tip, which likely arises from a protrusion or a small feature located at the apex of tip of the relatively blunt commercial cantilevers.

Second, the applicability of the MFM as a means of detecting magnetic nanostructures in liquid environments has been demonstrated. The measuring conditions have been optimized by using hard disk drives and then DMSA-coated Fe_3O_4 nanoparticles have been studied. Despite the limiting factor of the low magnetic interactions, clear evidence of its performance has been presented showing that even individual 30-nm MNPs can be detected in liquid using commercial probes. It has been shown as well that by using cantilevers designed for measurements in liquids, properly magnetized, the signal-to-noise ratio can be further improved. The results presented here suggest new strategies for the characterization of magnetic nanostructures in liquids using MFM.

In the second part of this chapter, two new procedures to fabricate electrical contacts to nano-objects have been presented:

First, a technique based on the deterministic transfer of graphite flakes by all-dry viscoelastic stamping has been introduced to fabricate microelectrodes. In order to validate and illustrate the uses of this methodology some relevant examples of its many possibilities have been provided: carbon-based materials and metal-organic nanoribbons. It has been used to contact for the first time drop-casted MMX nanoribbons, which are very difficult to contact using other approaches.

Second, Probe-Assisted Nanowire (PAN) lithography has been introduced. This technique is based on the adsorption and subsequent manipulation of gold nanowires with an AFM probe. It allows creating contacts almost in any electrical configuration, contacting tiny nano-objects very difficult or even impossible to contact using conventional techniques. Another of its advantages is the possibility of repositioning any of the nanolectrodes so fabricated, which enables to readily contact multiple nano-objects in the same sample and/or to perform straightforward conductivity measurements as a function of the distance in two-terminal configurations.

Both methods are simple, clean, reliable, cost-effective and the quality of the electrical contacts obtained has been shown to be as good as those obtained by conventional techniques, making these procedures clearly powerful to create contacts with nano-objects. Although they are particularly useful in the case of molecules with limited stability and to create contacts for C-AFM, their applicability is much more general, going beyond these cases. In particular, we are convinced that PAN lithography will stablish a new paradigm for the fabrication of nanoelectrodes, that in the near future could even replace conventional techniques used in nanotechnology such as e-beam lithography. The application of PAN lithography to a number of systems is in progress.

3.5 References

[1] Watson, J. D.; Crick, F. H. C. Molecular Structure of Nucleic Acids - A Structure for Deoxyribose Nucleic Acid. *Nature* **1953,** *171*, 737-738.
[2] Nielsen, P. E.; Egholm, M.; Berg, R. H.; Buchardt, O. Sequence-Selective Recognition of Dna by Strand Displacement with a Thymine-Substituted Polyamide. *Science* **1991,** *254*, 1497-1500.
[3] Abels, J. A.; Moreno-Herrero, F.; van der Heijden, T.; Dekker, C.; Dekker, N. H. Single-molecule measurements of the persistence length of double-stranded RNA. *Biophys. J.* **2005,** *88*, 2737-2744.
[4] Herrero-Galan, E.; Fuentes-Perez, M. E.; Carrasco, C.; Valpuesta, J. M.; Carrascosa, J. L.; Moreno-Herrero, F.; Arias-Gonzalez, J. R. Mechanical identities of RNA and DNA double helices unveiled at the single-molecule level. *J. Am. Chem. Soc.* **2013,** *135*, 122-131.
[5] Lipfert, J.*, et al.* Double-stranded RNA under force and torque: similarities to and striking differences from double-stranded DNA. *Proc. Natl. Acad. Sci. U.S.A.* **2014,** *111*, 15408-15413.
[6] Mou, J.; Czajkowsky, D. M.; Zhang, Y.; Shao, Z. High-resolution atomic-force microscopy of DNA: the pitch of the double helix. *FEBS Lett.* **1995,** *371*, 279-282.
[7] Moreno-Herrero, F.; Colchero, J.; Gomez-Herrero, J.; Baro, A. M. Atomic force microscopy contact, tapping, and jumping modes for imaging biological samples in liquids. *Phy. Rev. E* **2004,** *69*, 031915.
[8] Cassina, V.; Manghi, M.; Salerno, D.; Tempestini, A.; Iadarola, V.; Nardo, L.; Brioschi, S.; Mantegazza, F. Effects of cytosine methylation on DNA morphology: An atomic force microscopy study. *BBA-GEN Subjects* **2016,** *1860*, 1-7.
[9] Lyubchenko, Y. L.; Shlyakhtenko, L. S. AFM for analysis of structure and dynamics of DNA and protein-DNA complexes. *Methods* **2009,** *47*, 206-213.
[10] Zhong, Q.; Inniss, D.; Kjoller, K.; Elings, V. B. Fractured polymer/silica fiber surface studied by tapping mode atomic force microscopy. *Surf. Sci. Lett.* **1993,** *290*, L688-692.
[11] Hansma, P. K.*, et al.* Tapping mode atomic force microscopy in liquids. *Appl. Phys. Lett.* **1994,** *64*, 1738-1740.
[12] Müller, D. J.; Fontiadis, D.; Scheuring, S.; Müller, S. A.; Engel, A. Electrostatically balanced subnanometer imaging of biological specimens by atomic force microscope. *Biophys. J.* **1999,** *76*, 1101-1111.
[13] Yamashita, H.; Voitchovsky, K.; Uchihashi, T.; Contera, S. A.; Ryan, J. F.; Ando, T. Dynamics of bacteriorhodopsin 2D crystal observed by high-speed atomic force microscopy. *J. Struct. Biol.* **2009,** *167*, 153-158.
[14] Casuso, I.; Khao, J.; Chami, M.; Paul-Gilloteaux, P.; Husain, M.; Duneau, J. P.; Stahlberg, H.; Sturgis, J. N.; Scheuring, S. Characterization of the motion of membrane proteins using high-speed atomic force microscopy. *Nat. Nanotechnol.* **2012,** *7*, 525-529.
[15] Kodera, N.; Yamamoto, D.; Ishikawa, R.; Ando, T. Video imaging of walking myosin V by high-speed atomic force microscopy. *Nature* **2010,** *468*, 72–76.
[16] Maaloum, M.; Beker, A. F.; Muller, P. Secondary structure of double-stranded DNA under stretching: elucidation of the stretched form. *Phys. Rev. E* **2011,** *83*, 031903.
[17] Kitazawa, M.*, et al.* High-Resolution Imaging of Plasmid DNA in Liquids in Dynamic Mode Atomic Force Microscopy Using a Carbon Nanofiber Tip. *Jpn. J. Appl. Phys.* **2011,** *50*, S3.
[18] Leung, C.*, et al.* Atomic force microscopy with nanoscale cantilevers resolves different structural conformations of the DNA double helix. *Nano Lett.* **2012,** *12*, 3846-3850.
[19] Pyne, A.; Thompson, R.; Leung, C.; Roy, D.; Hoogenboom, B. W. Single-molecule reconstruction of oligonucleotide secondary structure by atomic force microscopy. *Small* **2014,** *10*, 3257-3261.

[20] Marti, O.; Drake, B.; Hansma, P. K. Atomic force microscopy of liquid-covered surfaces: Atomic resolution images. *Appl. Phys. Lett.* **1987,** *51*, 484-486.
[21] Martinez-Martin, D.*, et al.* Resolving structure and mechanical properties at the nanoscale of viruses with frequency modulation atomic force microscopy. *PloS one* **2012,** *7*, e30204.
[22] Fukuma, T.; Jarvis, S. P. Development of liquid-environment frequency modulation atomic force microscope with low noise deflection sensor for cantilevers of various dimensions. *Rev. Sci. Instrum.* **2006,** *77*, 043701.
[23] Yamada, H.; Kobayashi, K.; Fukuma, T.; Hirata, Y.; T., K.; Matsushige, K. Molecular resolution imaging of protein molecules in liquid using frequency modulation atomic force microscopy. *Appl. Phys. Express* **2009,** *2*, 095007.
[24] Jaafar, M.; Martinez-Martin, D.; Cuenca, M.; Melcher, J.; Raman, A.; Gomez-Herrero, J. Drive-amplitude-modulation atomic force microscopy: From vacuum to liquids. *Beilstein J. Nanotechnol.* **2012,** *3*, 336-344.
[25] Giessibl, F. J.; Bielefeldt, H.; Hembacher, S.; Mannhart, J. Calculation of the optimal imaging parameters for frequency modulation atomic force microscopy. *Appl. Surf. Sci.* **1999,** *140*, 352-357.
[26] Melcher, J.; Martinez-Martin, D.; Jaafar, M.; Gomez-Herrero, J.; Raman, A. High-resolution dynamic atomic force microscopy in liquids with different feedback architectures. *Beilstein J. Nanotechnol.* **2013,** *4*, 153-163.
[27] Ido, S.; Kimura, K.; Oyabu, N.; Kobayashi, K.; Tsukada, M.; Matsushige, K.; Yamada, H. Beyond the helix pitch: direct visualization of native DNA in aqueous solution. *ACS Nano* **2013,** *7*, 1817-1822.
[28] Pittenger, B. B.; Erina, N.; Su, C. Application Note #128. Quantitative Mechanical Property Mapping at the Nanoscale with PeakForce QNM. *Bruker* **2012**.
[29] Ortega-Esteban, A.; Horcas, I.; Hernando-Perez, M.; Ares, P.; Perez-Berna, A. J.; San Martin, C.; Carrascosa, J. L.; de Pablo, P. J.; Gomez-Herrero, J. Minimizing tip-sample forces in jumping mode atomic force microscopy in liquid. *Ultramicroscopy* **2012,** *114*, 56-61.
[30] http://probe.olympus-global.com/en/.
[31] Sader, J. E. Frequency response of cantilever beams immersed in viscous fluids with applications to the atomic force microscope. *J. Appl. Phys.* **1998,** *84*, 64-76.
[32] Maaloum, M. A close encounter with DNA. *Eur. Biophys. J.* **2003,** *32*, 585-587.
[33] Gimeno, A.; Ares, P.; Horcas, I.; Gil, A.; Gomez-Rodriguez, J. M.; Colchero, J.; Gomez-Herrero, J. 'Flatten plus': a recent implementation in WSxM for biological research. *Bioinformatics* **2015,** *31*, 2918-2920.
[34] Moreno-Herrero, F.; Colchero, J.; Baro, A. M. DNA height in scanning force microscopy. *Ultramicroscopy* **2003,** *96*, 167-174.
[35] van Dijk, M.; Bonvin, A. M. 3D-DART: a DNA structure modelling server. *Nucleic Acids Res.* **2009,** *37*, W235-239.
[36] Pettersen, E. F.; Goddard, T. D.; Huang, C. C.; Couch, G. S.; Greenblatt, D. M.; Meng, E. C.; Ferrin, T. E. UCSF Chimera--a visualization system for exploratory research and analysis. *J. Comput. Chem.* **2004,** *25*, 1605-1612.
[37] Villarrubia, J. S. Scanned probe microscope tip characterization without calibrated characterizers. *J. Vac. Sci. Technol. B* **1996,** *14*, 1518-1521.
[38] Hernando-Perez, M.; Pascual, E.; Aznar, M.; Ionel, A.; Caston, J. R.; Luque, A.; Carrascosa, J. L.; Reguera, D.; de Pablo, P. J. The interplay between mechanics and stability of viral cages. *Nanoscale* **2014,** *6*, 2702-2709.

[39] San Paulo, A.; Garcia, R. High-resolution imaging of antibodies by tapping-mode atomic force microscopy: attractive and repulsive tip-sample interaction regimes. *Biophys. J.* **2000,** *78*, 1599-1605.
[40] Muller, D. J.; Engel, A.; Carrascosa, J. L.; Velez, M. The bacteriophage phi29 head-tail connector imaged at high resolution with the atomic force microscope in buffer solution. *EMBO J.* **1997,** *16*, 2547-2553.
[41] Rose, A., *Vision: Human and Electronic (Optical Physics and Engineering)*. Springer: **1973**.
[42] Bushberg, J. T., *The Essential Physics of Medical Imaging*. Lippincott Williams & Wilkins: **2002**.
[43] Martin, Y.; Wickramasinghe, H. K. Magnetic Imaging by Force Microscopy with 1000-A Resolution. *Appl. Phys. Lett.* **1987,** *50*, 1455-1457.
[44] L. Yue; Liou, S.-H., Magnetic Force Microscopy Studies of Magnetic Features and Nanostructures. In *Scanning Probe Microscopy in Nanoscience and Nanotechnology 2*, Bhushan, B., Ed. Springer Berlin Heidelberg: 2011; pp 287-319.
[45] Block, S.; Gloeckl, G.; Weitschies, W.; Helm, C. A. Direct Visualization and Identification of Biofunctionalized Nanoparticles using a Magnetic Atomic Force Microscope. *Nano Lett.* **2011,** *11*, 3587-3592.
[46] Neves, C. S.; Quaresma, P.; Baptista, P. V.; Carvalho, P. A.; Araujo, J. P.; Pereira, E.; Eaton, P. New insights into the use of magnetic force microscopy to discriminate between magnetic and nonmagnetic nanoparticles. *Nanotechnology* **2010,** *21*, 305706.
[47] Nocera, T. M.; Chen, J.; Murray, C. B.; Agarwal, G. Magnetic anisotropy considerations in magnetic force microscopy studies of single superparamagnetic nanoparticles. *Nanotechnology* **2012,** *23*, 270.
[48] Schreiber, S.; Savla, M.; Pelekhov, D. V.; Iscru, D. F.; Selcu, C.; Hammel, P. C.; Agarwal, G. Magnetic force microscopy of superparamagnetic nanoparticles. *Small* **2008,** *4*, 270-278.
[49] Alessandrini, A.; Facci, P. AFM: a versatile tool in biophysics. *Meas. Sci. Technol.* **2005,** *16*, R65-R92.
[50] Santos, N. C.; Castanho, M. An overview of the biophysical applications of atomic force microscopy. *Biophys. Chem.* **2004,** *107*, 133-149.
[51] Nikova, D.; Lange, T.; Oberleithner, H.; Schillers, H.; Ebner, A.; Hinterdorfer, P., Atomic force microscopy in nanomedicine. In *Applied Scanning Probe Methods III: Characterization*, Bhushan, B.; Fuchs, H., Eds. 2006; pp 1-26.
[52] Mueller, D. J.; Dufrene, Y. F. Atomic force microscopy as a multifunctional molecular toolbox in nanobiotechnology. *Nat. Nanotechnol.* **2008,** *3*, 261-269.
[53] Fotiadis, D.; Liang, Y.; Filipek, S.; Saperstein, D. A.; Engel, A.; Palczewski, K. Atomic-force microscopy: Rhodopsin dimers in native disc membranes. *Nature* **2003,** *421*, 127-128.
[54] Rief, M.; Gautel, M.; Oesterhelt, F.; Fernandez, J. M.; Gaub, H. E. Reversible unfolding of individual titin immunoglobulin domains by AFM. *Science* **1997,** *276*, 1109-1112.
[55] Pankhurst, Q. A.; Connolly, J.; Jones, S. K.; Dobson, J. Applications of magnetic nanoparticles in biomedicine. *J. Phys. D: Appl. Phys.* **2003,** *36*, R167-R181.
[56] Martinelli, A. L.; Araujo, A. B.; Franco, R. F.; Tavella, M. H.; Ramalho, L. N. Z.; Zucoloto, S.; Rodrigues, S. S.; Zago, M. A. Liver iron deposits in hepatitis B patients: Association with severity of liver disease but not with hemochromatosis gene mutations. *J. Gastroenterol. Hepatol.* **2004,** *19*, 1036-1041.
[57] Dobson, J. Nanoscale biogenic iron oxides and neurodegenerative disease. *FEBS Lett.* **2001,** *496*, 1-5.
[58] Savoiardo, M.; Girotti, F.; Strada, L.; Ciceri, E. Magnetic resonance imaging in progressive supranuclear palsy and other parkinsonian disorders. *J. Neural Transm. Suppl.* **1994,** *42*, 93-110.

[59] Yuan, X.-M.; Li, W. Iron Involvement in Multiple Signaling Pathways of Atherosclerosis: A Revisited Hypothesis. *Curr. Med. Chem.* **2008,** *15*, 2157-2172.
[60] Diebel, C. E.; Proksch, R.; Green, C. R.; Neilson, P.; Walker, M. M. Magnetite defines a vertebrate magnetoreceptor. *Nature* **2000,** *406*, 299-302.
[61] Martin, M.; Carmona, F.; Cuesta, R.; Rondon, D.; Galvez, N.; Dominguez-Vera, J. M. Artificial Magnetic Bacteria: Living Magnets at Room Temperature. *Adv. Funct. Mater.* **2014,** *24*, 3489-3493.
[62] Amemiya, Y.; Tanaka, T.; Yoza, B.; Matsunaga, T. Novel detection system for biomolecules using nano-sized bacterial magnetic particles and magnetic force microscopy. *J. Biotechnol.* **2005,** *120*, 308-314.
[63] Aljabali, A. A. A.; Sainsbury, F.; Lomonossoff, G. P.; Evans, D. J. Cowpea Mosaic Virus Unmodified Empty Viruslike Particles Loaded with Metal and Metal Oxide. *Small* **2010,** *6*, 818-821.
[64] Jaafar, M.; Aljabali, A. A. A.; Berlanga, I.; Mas-Balleste, R.; Saxena, P.; Warren, S.; Lomonossoff, G. P.; Evans, D. J.; de Pablo, P. J. Structural Insights into Magnetic Clusters Grown Inside Virus Capsids. *ACS Appl. Mater. Interfaces* **2014,** *6*, 20936-20942.
[65] Hu, S.; Guan, Y.; Wang, Y.; Han, H. Nano-magnetic catalyst KF/CaO-Fe3O4 for biodiesel production. *Appl. Energy* **2011,** *88*, 2685-2690.
[66] Giles, R.; Cleveland, J. P.; Manne, S.; Hansma, P. K.; Drake, B.; Maivald, P.; Boles, C.; Gurley, J.; Elings, V. Noncontact Force Microscopy in Liquids. *Appl. Phys. Lett.* **1993,** *63*, 617-618.
[67] Dietz, C.; Herruzo, E. T.; Lozano, J. R.; Garcia, R. Nanomechanical coupling enables detection and imaging of 5 nm superparamagnetic particles in liquid. *Nanotechnology* **2011,** *22*, 043044.
[68] Calero, M.; Gutierrez, L.; Salas, G.; Luengo, Y.; Lazaro, A.; Acedo, P.; Puerto Morales, M.; Miranda, R.; Villanueva, A. Efficient and safe internalization of magnetic iron oxide nanoparticles: Two fundamental requirements for biomedical applications. *Nanomedicine: NBM* **2014,** *10*, 733-743.
[69] http://www.nanosensors.com/.
[70] Gil, A., PhD thesis Study of the Tip-Sample Interaction at the Scanning Force Microscopy and its Application to the Visualization of Adsorption Processes on Surfaces. *Departamento de Física de la Materia Condensada. Universidad Autónoma de Madrid.* **2001**.
[71] Gomez-Navarro, C*., et al.* Scanning force microscopy three-dimensional modes applied to the study of the dielectric response of adsorbed DNA molecules. *Nanotechnology* **2002,** *13*, 314-317.
[72] Garcia, N.; Binh, V. T. Van der Waals Forces in Atomic Force Microscopy Operating in Liquids - A Spherical-Tip Model. *Phys. Rev. B* **1992,** *46*, 7946-7948.
[73] Marciello, M.; Connord, V.; Veintemillas-Verdaguer, S.; Andres Verges, M.; Carrey, J.; Respaud, M.; Serna, C. J.; Puerto Morales, M. Large scale production of biocompatible magnetite nanocrystals with high saturation magnetization values through green aqueous synthesis. *J. Mater. Chem. B* **2013,** *1*, 5995-6004.
[74] Moya, C.; Iglesias-Freire, O.; Perez, N.; Batlle, X.; Labarta, A.; Asenjo, A. Direct imaging of the magnetic polarity and reversal mechanism in individual Fe3-xO4 nanoparticles. *Nanoscale* **2015,** *7*, 8110-8114.
[75] Haeberle, T.; Haering, F.; Pfeifer, H.; Han, L.; Kuerbanjiang, B.; Wiedwald, U.; Herr, U.; Koslowski, B. Towards quantitative magnetic force microscopy: theory and experiment. *New J. Phys.* **2012,** *14*, 043044.
[76] Jaafar, M.; Iglesias-Freire, O.; Serrano-Ramon, L.; Ricardo Ibarra, M.; Maria de Teresa, J.; Asenjo, A. Distinguishing magnetic and electrostatic interactions by a Kelvin probe force microscopy-magnetic force microscopy combination. *Beilstein J. Nanotechnol.* **2011,** *2*, 552-560.

[77] Martinez-Martin, D.; Jaafar, M.; Perez, R.; Gomez-Herrero, J.; Asenjo, A. Upper Bound for the Magnetic Force Gradient in Graphite. *Phys. Rev. Lett.* **2010,** *105*, 257203.
[78] Garcia, R.; Perez, R. Dynamic atomic force microscopy methods. *Surf. Sci. Rep.* **2002,** *47*, 197-301.
[79] Iglesias-Freire, O.; Jaafar, M.; Berganza, E.; Asenjo, A. Customized MFM probes with high lateral resolution. *Beilstein J. Nanotechnol.* **2016,** *7*, 1068-1074.
[80] Novoselov, K. S.; Geim, A. K.; Morozov, S. V.; Jiang, D.; Zhang, Y.; Dubonos, S. V.; Grigorieva, I. V.; Firsov, A. A. Electric field effect in atomically thin carbon films. *Science* **2004,** *306*, 666-669.
[81] Tans, S. J.; Verschueren, A. R. M.; Dekker, C. Room-temperature transistor based on a single carbon nanotube. *Nature* **1998,** *393*, 49-52.
[82] Feldman, A. K.; Steigerwald, M. L.; Guo, X. F.; Nuckolls, C. Molecular Electronic Devices Based on Single-Walled Carbon Nanotube Electrodes. *Acc. Chem. Res.* **2008,** *41*, 1731-1741.
[83] Holmlin, R. E.; Ismagilov, R. F.; Haag, R.; Mujica, V.; Ratner, M. A.; Rampi, M. A.; Whitesides, G. M. Correlating electron transport and molecular structure in organic thin films. *Angew. Chem. Int. Ed.* **2001,** *40*, 2316.
[84] Nerngchamnong, N.; Yuan, L.; Qi, D. C.; Li, J.; Thompson, D.; Nijhuis, C. A. The role of van der Waals forces in the performance of molecular diodes. *Nat. Nanotechnol.* **2013,** *8*, 113-118.
[85] de Pablo, P. J.; Moreno-Herrero, F.; Colchero, J.; Gomez-Herrero, J.; Herrero, P.; Baro, A. M.; Ordejon, P.; Soler, J. M.; Artacho, E. Absence of dc-conductivity in lambda-DNA. *Phys. Rev. Lett.* **2000,** *85*, 4992-4995.
[86] Hsu, J. W. P. Soft lithography contacts to organics. *Mater. Today* **2005,** *8*, 42-54.
[87] Livshits, G. I.*, et al.* Long-range charge transport in single G-quadruplex DNA molecules. *Nat. Nanotechnol.* **2014,** *9*, 1040-1046.
[88] Guijarro, A.*, et al.* Conductive Nanostructures of MMX Chains. *Adv. Funct. Mater.* **2010,** *20*, 1451-1457.
[89] Cai, L. T.; Tabata, H.; Kawai, T. Self-assembled DNA networks and their electrical conductivity. *Appl. Phys. Lett.* **2000,** *77*, 3105-3106.
[90] Storm, A. J.; van Noort, J.; de Vries, S.; Dekker, C. Insulating behavior for DNA molecules between nanoelectrodes at the 100 nm length scale. *Appl. Phys. Lett.* **2001,** *79*, 3881-3883.
[91] Livshits, G. I.*, et al.* Long-range charge transport in single G-quadruplex DNA molecules. *Nat. Nanotech.* **2014,** *9*, 1040-1046.
[92] Lu, Y.; Huang, J. Y.; Wang, C.; Sun, S.; Lou, J. Cold welding of ultrathin gold nanowires. *Nat. Nanotechnol.* **2010,** *5*, 218-224.
[93] Meitl, M. A.; Zhu, Z. T.; Kumar, V.; Lee, K. J.; Feng, X.; Huang, Y. Y.; Adesida, I.; Nuzzo, R. G.; Rogers, J. A. Transfer printing by kinetic control of adhesion to an elastomeric stamp. *Nat. Mater.* **2006,** *5*, 33-38.
[94] Castellanos-Gomez, A.; Buscema, M.; van der Zant Herre, S. J.; Steele, G. A. Deterministic transfer of two-dimensional materials by all-dry viscoelastic stamping. *2D Materials* **2014,** *1*, 011002.
[95] Kang, J.; Shin, D.; Bae, S.; Hong, B. H. Graphene transfer: key for applications. *Nanoscale* **2012,** *4*, 5527-5537.
[96] Wang, W.; Niu, D. X.; Jiang, C. R.; Yang, X. J. The conductive properties of single DNA molecules studied by torsion tunneling atomic force microscopy. *Nanotechnology* **2014,** *25*, 025707.
[97] Burzurí E.; Prins F.; H., v. d. Z. Characterization of Nanometer-Spaced Few-Layer Graphene Electrodes. *Graphene* **2012,** *1*, 26-29.
[98] http://www.gelpak.com/.

[99] Tang, Q.; Tong, Y.; Li, H.; Ji, Z.; Li, L.; Hu, W.; Liu, Y.; Zhu, D. High-performance air-stable bipolar field-effect transistors of organic single-crystalline ribbons with an air-gap dielectric. *Adv. Mater.* **2008,** *20*, 1511.
[100] http://www.budgetsensors.com/.
[101] Dai, H. J.; Wong, E. W.; Lieber, C. M. Probing electrical transport in nanomaterials: Conductivity of individual carbon nanotubes. *Science* **1996,** *272*, 523-526.
[102] de Pablo, P. J.; Gomez-Navarro, C.; Gil, A.; Colchero, J.; Martinez, M. T.; Benito, A. M.; Maser, W. K.; Gomez-Herrero, J.; Baro, A. M. Visualization of single-walled carbon nanotubes electrical networks by scanning force microscopy. *Appl. Phys. Lett.* **2001,** *79*, 2979-2981.
[103] Thompson, H. T.; Barroso-Bujans, F.; Herrero, J. G.; Reifenberger, R.; Raman, A. Subsurface imaging of carbon nanotube networks in polymers with DC-biased multifrequency dynamic atomic force microscopy. *Nanotechnology* **2013,** *24*, 12.
[104] Dai, H. J. Carbon nanotubes: Synthesis, integration, and properties. *Acc. Chem. Res.* **2002,** *35*, 1035-1044.
[105] Gomez-Navarro, C.; Pablo, P. J. D.; Gomez-Herrero, J.; Biel, B.; Garcia-Vidal, F. J.; Rubio, A.; Flores, F. Tuning the conductance of single-walled carbon nanotubes by ion irradiation in the Anderson localization regime. *Nat. Mater.* **2005,** *4*, 534.
[106] Hermosa, C.; Vicente Alvarez, J.; Azani, M.-R.; Gomez-Garcia, C. J.; Fritz, M.; Soler, J. M.; Gomez-Herrero, J.; Gomez-Navarro, C.; Zamora, F. Intrinsic electrical conductivity of nanostructured metal-organic polymer chains. *Nat. Commun.* **2013,** *4*, 1709.
[107] Welte, L.; Calzolari, A.; Di Felice, R.; Zamora, F.; Gomez-Herrero, J. Highly conductive self-assembled nanoribbons of coordination polymers. *Nat. Nanotechnol.* **2010,** *5*, 110-115.
[108] Gomez-Navarro, C.; Weitz, R. T.; Bittner, A. M.; Scolari, M.; Mews, A.; Burghard, M.; Kern, K. Electronic Transport Properties of Individual Chemically Reduced Graphene Oxide Sheets. *Nano Lett.* **2007,** *7*, 3499-3503.
[109] Jung, I.; Dikin, D. A.; Piner, R. D.; Ruoff, R. S. Tunable Electrical Conductivity of Individual Graphene Oxide Sheets Reduced at "Low" Temperatures. *Nano Lett.* **2008,** *8*, 4283-4287.
[110] Han, Y. J.; Kim, J. M.; Stucky, G. D. Preparation of noble metal nanowires using hexagonal mesoporous silica SBA-15. *Chem. Mater.* **2000,** *12*, 2068-2069.
[111] Jana, N. R.; Gearheart, L.; Murphy, C. J. Wet chemical synthesis of silver nanorods and nanowires of controllable aspect ratio. *Chem. Commun.* **2001**, 617-618.
[112] Sun, Y. G.; Gates, B.; Mayers, B.; Xia, Y. N. Crystalline silver nanowires by soft solution processing. *Nano Lett.* **2002,** *2*, 165-168.
[113] Chang, Y.; Lye, M. L.; Zeng, H. C. Large-scale synthesis of high-quality ultralong copper nanowires. *Langmuir* **2005,** *21*, 3746-3748.
[114] Liu, X. G.; Wu, N. Q.; Wunsch, B. H.; Barsotti, R. J.; Stellacci, F. Shape-controlled growth of micrometer-sized gold crystals by a slow reduction method. *Small* **2006,** *2*, 1046-1050.
[115] Huo, Z. Y.; Tsung, C. K.; Huang, W. Y.; Zhang, X. F.; Yang, P. D. Sub-two nanometer single crystal Au nanowires. *Nano Lett.* **2008,** *8*, 2041-2044.
[116] Lu, X. M.; Yavuz, M. S.; Tuan, H. Y.; Korgel, B. A.; Xia, Y. N. Ultrathin gold nanowires can be obtained by reducing polymeric strands of oleylamine-AuCl complexes formed via aurophilic interaction. *J. Am. Chem. Soc.* **2008,** *130*, 8900-8901.
[117] Wang, C.; Hu, Y. J.; Lieber, C. M.; Sun, S. H. Ultrathin Au nanowires and their transport properties. *J. Am. Chem. Soc.* **2008,** *130*, 8902-8903.
[118] Kim, F.; Sohn, K.; Wu, J. S.; Huang, J. X. Chemical Synthesis of Gold Nanowires in Acidic Solutions. *J. Am. Chem. Soc.* **2008,** *130*, 14442-14443.

[119] Critchley, K.; Khanal, B. P.; Gorzny, M. L.; Vigderman, L.; Evans, S. D.; Zubarev, E. R.; Kotov, N. A. Near-Bulk Conductivity of Gold Nanowires as Nanoscale Interconnects and the Role of Atomically Smooth Interface. *Adv. Mater.* **2010,** *22*, 2338-2342.
[120] Kovtyukhova, N. I.; Mallouk, T. E. Nanowires as building blocks for self-assembling logic and memory circuits. *Chem. Eur. J.* **2002,** *8*, 4355-4363.
[121] Falvo, M. R.; Clary, G. J.; Taylor, R. M.; Chi, V.; Brooks, F. P.; Washburn, S.; Superfine, R. Bending and buckling of carbon nanotubes under large strain. *Nature* **1997,** *389*, 582-584.
[122] Kashiwase, Y.; Ikeda, T.; Oya, T.; Ogino, T. Manipulation and soldering of carbon nanotubes using atomic force microscope. *Appl. Surf. Sci.* **2008,** *254*, 7897-7900.
[123] Kim, H.-J.; Gia Hau, N.; Dinh Le Cao, K.; Da Khoa, T.; Jeon, K.-J.; Chung, K.-H. Static and kinetic friction characteristics of nanowire on different substrates. *Appl. Surf. Sci.* **2016,** *379*, 452-461.
[124] Strus, M. C.; Lahiji, R. R.; Ares, P.; Lopez, V.; Raman, A.; Reifenberger, R. Strain energy and lateral friction force distributions of carbon nanotubes manipulated into shapes by atomic force microscopy. *Nanotechnology* **2009,** *20*, 385709.
[125] Roy, S.*, et al.* Direct electrical measurements on single-molecule genomic DNA using single-walled carbon nanotubes. *Nano Lett.* **2008,** *8*, 26-30.
[126] https://www.nanopartz.com/.
[127] Munoz, R. C.*, et al.* Surface roughness and surface-induced resistivity of gold films on mica: Application of quantitative scanning tunneling microscopy. *Phys. Rev. B* **2000,** *62*, 4686-4697.
[128] Sambles, J. R.; Elsom, K. C.; Jarvis, D. J. The Electrical-Resistivity of Gold-Films. *Phil. Trans. R. Soc. A* **1982,** *304*, 365-396.
[129] Peng, Y.; Cullis, T.; Inkson, B. Accurate electrical testing of individual gold nanowires by in situ scanning electron microscope nanomanipulators. *Appl. Phys. Lett.* **2008,** *93*, 183112.
[130] Bietsch, A.; Michel, B. Size and grain-boundary effects of a gold nanowire measured by conducting atomic force microscopy. *Appl. Phys. Lett.* **2002,** *80*, 3346-3348.
[131] Steinhogl, W.; Steinlesberger, G.; Perrin, M.; Scheinbacher, G.; Schindler, G.; Traving, M.; Engelhardt, M. Tungsten interconnects in the nano-scale regime. *Microelectron. Eng.* **2005,** *82*, 266-272.
[132] Wu, W.; Brongersma, S. H.; Van Hove, M.; Maex, K. Influence of surface and grain-boundary scattering on the resistivity of copper in reduced dimensions. *Appl. Phys. Lett.* **2004,** *84*, 2838-2840.
[133] Moreno-Moreno, M.; Castellanos-Gomez, A.; Rubio-Bollinger, G.; Gomez-Herrero, J.; Agrait, N. Ultralong Natural Graphene Nanoribbons and Their Electrical Conductivity. *Small* **2009,** *5*, 924-927.
[134] Han, M. Y.; Ozyilmaz, B.; Zhang, Y. B.; Kim, P. Energy band-gap engineering of graphene nanoribbons. *Phys. Rev. Lett.* **2007,** *98*, 206805.

Chapter 4. New low-dimensional materials.

4.1 Introduction

4.2 High electrical conductivity of single metal-organic chains

4.2.1 Introduction

4.2.2 Results and discussion

4.3 Local tuning of graphene properties upon ultrahigh pressures

4.3.1 Introduction

4.3.2 Results and discussion

4.4 Isolation of highly stable antimonene

4.4.1 Introduction

4.4.2 Results and discussion

4.5 Conclusions

4.6 Appendix

4.7 References

4.1 Introduction

In this chapter the study of three different low-dimensional materials is presented. The term low-dimensional is applied to those systems where one or more spatial dimensions are small enough to allow quantum effects to take place, which can dramatically affect materials properties compared to bulk. The interest in studying low-dimensional materials comes from these new properties, not only because of the new physics and phenomena behind them, but because of the multiple applications they can be suitable for. Quantum size effects start to be relevant when going down to the nanoscale, thus AFM reveals as a very appropriate tool to study low-dimensional materials.

The first system studied in this chapter is a 1-dimensional (1D) material, metal-organic MMX chains, a long standing topic in the research line of our group, obtained here from a procedure based on wet chemistry. The structure of these MMX chains is similar as the ones studied in Chapter 3 when presenting exfoliated graphite flakes as soft-electrodes, but in this case isolation from drop-casting and electrical characterization of different polymer MMX wires have been performed, demonstrating the robustness of this technique to produce highly conductive nanofibers. Then, chains at the single-molecule level have been electrically characterized for the very first time, exhibiting significant electrical current over lengths well above 100 nm. In these chains the current is, at periodic locations, confined across an individual iodine atom, as derived from the molecule geometry. Theoretical modelling suggests that the conductance of the chains is limited by the presence of structural defects. The measured electrical transport exceeds that of molecular wires so far reported, which postulates coordination polymers as excellent candidates for forthcoming molecular electronics.

Secondly, controlled tuning of graphene electronic properties, the first of the 2-dimensional (2D) materials ever isolated, is performed. AFM diamond tips have been employed to apply ultrahigh pressures (> 10 GPa) on selected areas of graphene flakes laying on flat substrates. The high breaking strengths of both diamond and graphene have allowed achieving this pressure regime confined to microscopic regions. With this configuration, selected regions in graphene flakes have been flattened towards the substrate, giving rise to a very controlled process to modify graphene properties. As a result of this work, it is shown that this method enables the creation of doped graphene areas in a very controlled way, allowing local modification of graphene electronic properties. These modifications include the possibility of selectively modify areas to improve the electrical contact of graphene with metal electrodes, which is a very relevant issue in the field of graphene electronics. High-quality junctions between graphene and metallic contacts are crucial in the creation of high-performance graphene devices. This process has also been applied to improve the performance of graphene as sealer, reducing by a factor of ~ 3.5 gas leak rates from graphene-sealed microchambers.

The third section of this chapter is devoted to the introduction of a new 2D material, antimonene, a single layer of antimony atoms. The search for new 2D materials with relevant optoelectronics properties is a long-standing goal since the discovery of graphene. Theoretical calculations points out toward an electronic structure in antimonene with a band gap suitable for optoelectronics applications, but it had not been possible to isolate this material. In this section, micromechanical exfoliation of antimony down to the single-layer regime and experimental evidence of its stability are presented. Optimization of the optical identification of few-layer antimonene is also presented, as well as preliminary results on its electrical properties.

4.2 High electrical conductivity of single metal-organic chains

4.2.1 Introduction

Molecular wires will be essential components for nanoscale electronics, however the preparation of individual long conductive molecules or polymers is still a challenge. Molecular electronics is the event horizon for circuit miniaturization but even much more importantly, it can potentially produce circuits with very complex architectures [1]. The current state-of-the-art in silicon technology enables a resolution below 10 nm, but with relatively "simple" architectures. In contrast, many molecules, as for instance DNA [2, 3] and DNA derivatives, including origami [4], exhibit self-assembling capabilities that suggest an increase in the complexity of molecular circuits [5]. Therefore, the final goal for molecular electronics can be seen as the construction of complex circuit architectures in a test tube. Single-molecule electronics is still an incipient field and complete electronic circuits from exclusively molecular components are very far from being a reality [6]. In this context, design and synthesis of these molecular components with control on their electronic properties is a key point for the fabrication of nanoscale devices [7]. It will require the self-assemble of molecules with the capabilities of the different elements present in conventional electronic circuits such as transistors, switches, rectifiers, etc., as well as molecular wires for the interconnections. These molecular wires (molecules showing a *reasonably* low electrical resistivity) are an active target of research [8]. In particular, many organic molecules and polymers have already been studied [9-11]. However, with very few exceptions [12, 13], they show a localized mechanism of conduction with an exponential increase of the electrical resistance with the length of the molecules. At distances of only a few nanometers the resistance is already that of an insulator [10]. Figure 4.1, obtained from reference [10], illustrates this tendency.

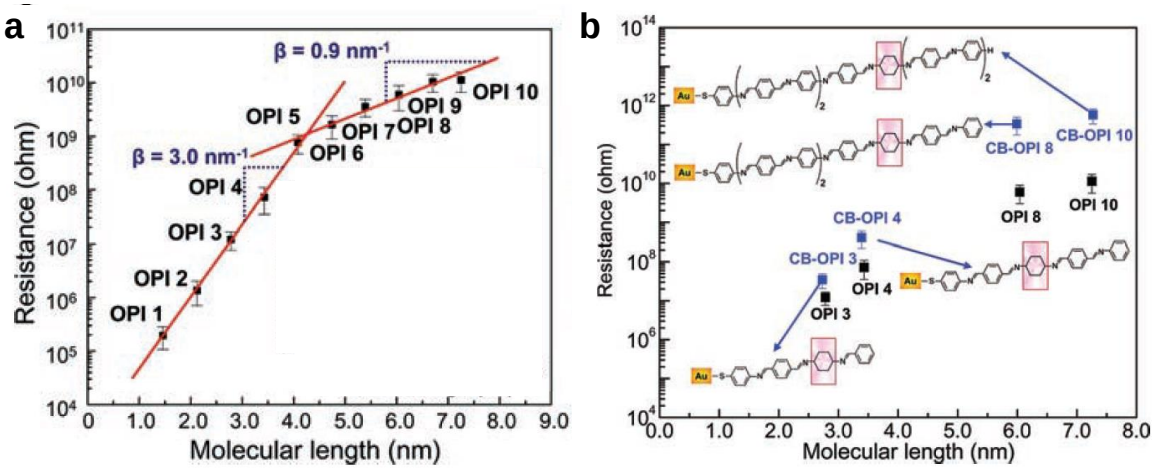

Figure 4.1 Semilog plot of Resistance *vs.* Length for molecular junctions based on conjugated oligophenyleneimine (OPI) structures. Symbols are obtained from IV curves. a) Data from OPI monolayers on gold substrates. Lines are linear fits. b) Data from OPI wires. The blue squares are the resistances of conjugation-broken (CB)-OPI wires. Pink boxes indicate the position where conjugation is broken. Image adapted from reference [10].

Actually organic polymer conductors show very low conductivity that only increases using chemical dopants in a bulk scale [14], but not isolated. As mentioned above, there are some molecular systems that are exceptions to this trend, as for instance a recent work by Slinker *et al.* reporting transport in self-assembled DNA layers with a localization length in the range of 30 nm [15], a few more works on metal-organic molecules [16-19] and polymers, one by Tuccitto *et al.* [20], based on a layer by layer assembly of metal ions with terpyridine ligands, and works by Prof. Julio Gómez-Herrero and Dr. Félix Zamora groups on MMX nanoribbons [21, 22]. Thus, the combination of metal ions with organic molecules, despite little developed, has already reported interesting results [23, 24].

MMX chains are based on the assemble of two dimetallic entities, e.g. $[Pt_2(dta)_4]$ and $[Pt_2(dta)_4I_2]$ (*dta* = ditiocarboxylate), some of them showing interesting electronic properties in bulk [25]. Unfortunately, the first attempts to synthesize nanometric forms of these polymers involved a non-conventional and tedious procedure based on sublimation from MMX crystals, which is not very appropriated for chemical synthesis [26], leading to nanoribbons formed by hundreds of individual MMX chains [21, 22]. In particular, in reference [21] it is reported that electrical transport over distances above ~ 200 nm is highly affected by the presence of structural defects and hence it is dominated by interchain electron transfer, leading to a diffusive transport regime. Recently, it has been shown that crystals of $[Pt_2(dta)_4I]_n$ dissociate in solution giving rise to solutions containing $[Pt_2(dta)_4]$ and $[Pt_2(dta)_4I_2]$, that under suitable conditions reverse to form the polymeric $[Pt_2(dta)_4I]_n$ chains [27, 28]. Based on these previous results, here it is presented first, the isolation on

surfaces and electrical characterization of fibres of three different compounds, $[Pt_2(RCS_2)_4I]_n$, with R = alkyl group; Me = CH_3; Et = CH_2CH_3; Pen = $(CH_2)_4CH_3$, demonstrating the robustness of the assembly of highly conductive MMX chains by a simple drop-casting approach. And second, isolation and electrical characterization of the $[Pt_2(EtCS_2)_4I]_n$ case down to the single chain level.

This work, currently submitted for publication, has been done in collaboration with Dr. Félix Zamora's group, Dr. Juanjo Palacios and Prof. José Soler. In particular, Dr. Pilar Amo-Ochoa synthesized the polymer chains onto flat substrates and Dr. Juanjo Palacios with Prof. José Soler carried out quantum transport calculations.

4.2.2 Results and discussion

Figure 4.2 presents crystal structure details of one of the polymers used in this work, the $[Pt_2(EtCS_2)_4I]_n$.

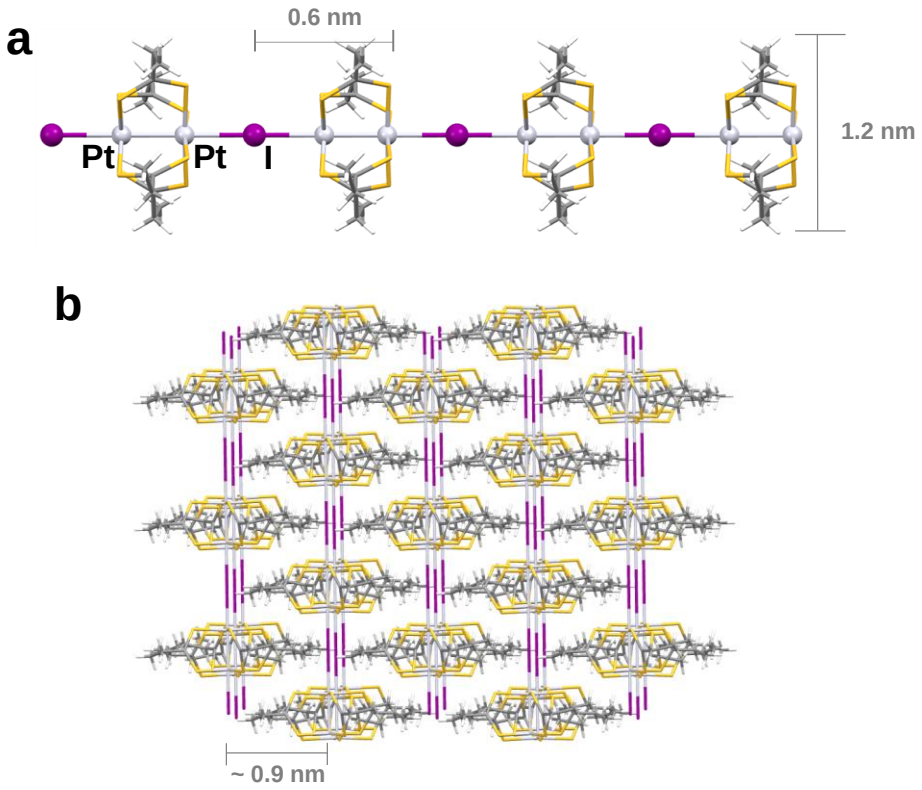

Figure 4.2 Crystal structure details of $[Pt_2(EtCS_2)_4I]_n$ (Et = CH_2CH_3). a) Schematic representation of a chain of this compound and selected distances. b) Schematic 3D representation of the crystal packing and interchain distance.

Synthesis of $[Pt_2(RCS_2)_4I]_n$ were carried out according to reference [25]. MMX chains and bundles on surfaces were prepared by dissolving crystals of $[Pt_2(RCS_2)_4I]_n$ (0.2 mg) in CH_2Cl_2 (2 mL) and then centrifuged (4000 rpm, 5 minutes) at room temperature. 30 µl were drop-casted on a 300 nm SiO_2/Si substrate exposed to an oxygen plasma pre-treatment [21] and left 40 s for adsorption. After this time substrates were dried in an argon gas flow. Samples were first imaged by high resolution optical microscopy and Atomic Force Microscopy in the AM-AFM mode. Figure 4.3 shows representative images of the structures so obtained.

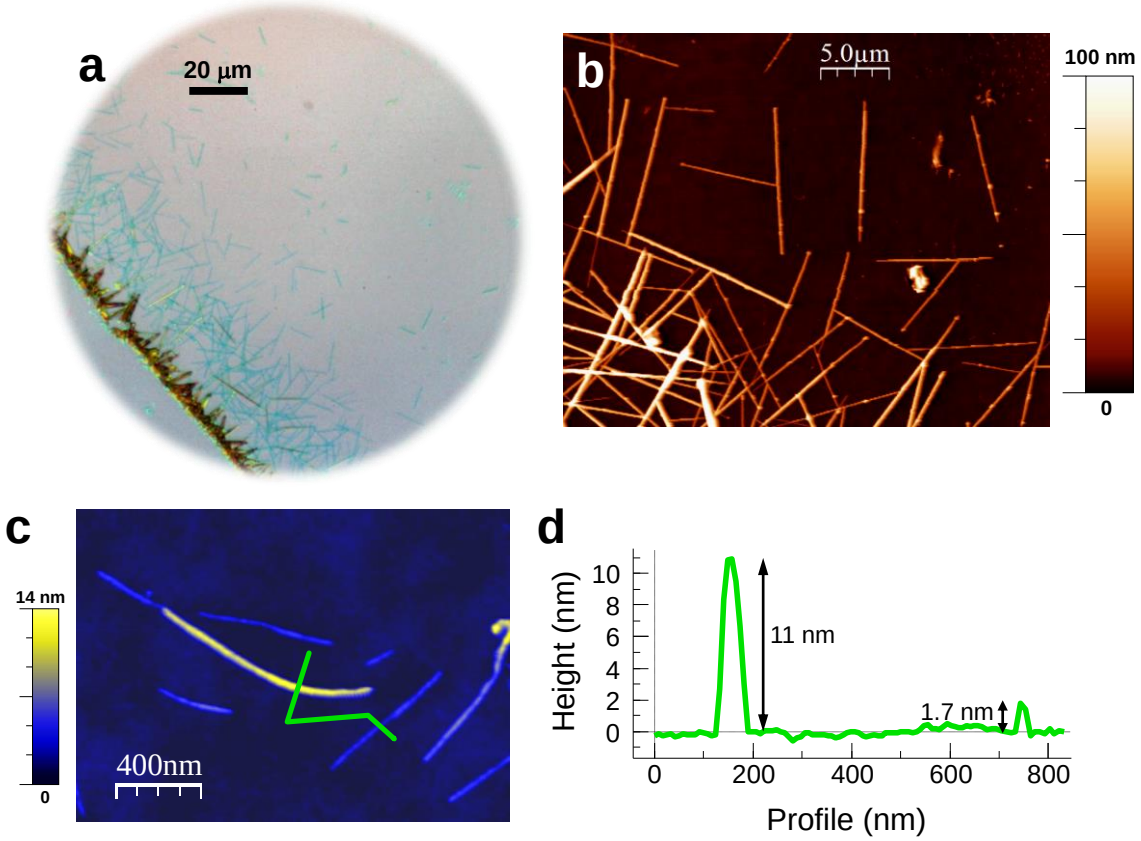

Figure 4.3 Morphological characterization of $[Pt_2(EtCS_2)_4I]_n$ fibres. a) Optical image of a drop-casted dichloromethane solution of $[Pt_2(EtCS_2)_4I]_n$ chains on a SiO_2 substrate. b) Topographic AFM image of the same substrate in a region with fibres of blue color in a) close to the border line given by large crystalline fibre-like aggregates. c) Topographic AFM image in a region far from the aggregates, where the blueish fibres in a) are almost not visible by optical microscopy. d) Height profile along the green solid line in c).

Figure 4.3a shows an optical microscope image revealing the formation of large crystalline fibre-like aggregates over micron lengths, along with a gradual decrease from this border line in both aggregation and size. Optical imaging shows a clear correspondence between color and thickness (brown from the largest to orange and yellow for medium values, and blueish colors for the thinnest). Figure 4.3b shows an AFM image taken on the region with medium density (fibres with blue color in the optical image). AFM image on this area shows that these nanostructures are over tens of microns length and present typical heights of ~ 20 - 100 nm, which are in the range of the already reported nanoribbons obtained by MMX crystal sublimation [21, 22]. Figures 4.3c and d show further AFM inspection in areas with fibres presenting blueish colors. The nanostructures located at the lower density regions exhibit lengths in the range of 100-800 nm and heights of ~ 1 - 15 nm. Since the distance between individual chains in MMX crystals is about 1 nm (figure 4.2), it is possible to identify these nanostructures as bundles of very few MMX chains. Images of representative fibres for each of the compositions $[Pt_2(RCS_2)_4I]_n$ can be found in figure A4.1 in the Appendix.

After optical and topographical AFM characterization of the bundles and chains obtained by this drop-casting method, electrical transport measurements on the fibres were carried out to assess the robustness of this methodology to isolate highly conducting polymer fibres. First, fibres with diameters ranging 10 to 20 nm diameter were studied using the EGF soft-electrode transfer method, as already shown in Chapter 3 (see figure 3.22 in the metal-organic MMX nanoribbons section). Comparison of the electrical characterization on the three different types of fibres under study, $[Pt_2(RCS_2)_4I]_n$, was carried out. Figure 4.4 shows representative Resistance *vs.* Length curves for fibres of the three different compositions.

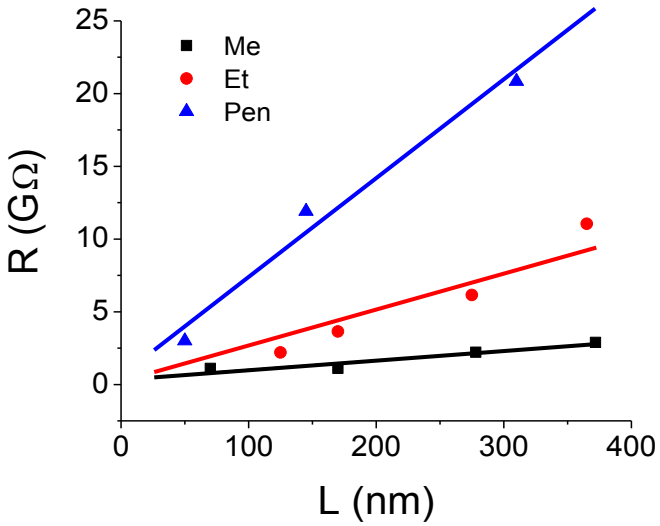

Figure 4.4 Representative Resistance *vs.* Length curves for fibres of $[Pt_2(RCS_2)_4I]_n$ with R = Me (black), Et (red) and Pen (blue) with diameters ~ 12 nm. Symbols correspond to resistance values obtained from IV curves at 1 V. Lines are linear fits. The slope of the R-L increases with the length of the alkyl group.

The conductivity σ, in S m^{-1}, can be obtained from the inverse of the slopes, α, of the linear fits in figure 4.4 and the section of the fibers, S

$$\sigma = \frac{1}{\alpha S} \tag{4.1}$$

yielding σ = 3.0, 0.3 and 0.1 (± 0.1) S m^{-1} for the Me, Et and Pen cases respectively. The results for the Me case are in good agreement with those previously reported for MMX nanoribbons of similar dimensions obtained by sublimation [22] (where conductivities of 2 - 10 S m^{-1} are reported). The decrease in conductivity observed as the length of the alkyl group increases in these fibres, composed of many chains, is compatible with the proposed conduction mechanism for sublimated nanoribbons [21]. In those cases, when the current comes to a point in the chain where it cannot go beyond, it "hops" to an adjacent chain. In the cases presented here, as the alkyl group is longer, this hopping is getting more difficult, resulting in lower conductivities.

After these encouraging results, the main goal was to probe the electrical properties of individual chains. Previous works by Guijarro *et al.* [29] were able to isolate MMX fibres by drop casting, but attempts to probe their electrical properties failed. They used evaporated gold electrodes and they observed fractures in the fibres after the electrodes fabrication. These morphological changes can be mainly due to two reasons: vacuum exposition and/or heating during gold evaporation. To gain insight on the fractures origin,

independent vacuum and heating experiments were performed here. To this end, fibres obtained by drop casting were contacted with an EFG electrode and electrically characterized. After that, they were placed into vacuum (10^{-5} hPa) for 5 hours at room temperature. Both morphological and electrical characterizations after vacuum exposition showed no changes. A different sample of the same kind was heated in air conditions from room temperature up to 50 °C. Clear morphological changes were observed, pointing heating as the source of fractures when depositing evaporated gold electrodes on drop-casted fibres. Details on these two experiments can be found in the Appendix at the end of this chapter.

To corroborate these findings, electrodes consisting on ~ 30 nm gold films were evaporated using stencil masks on previously synthesized samples, keeping them at room temperature through a cold finger while the gold deposition was performed. In this way, gold evaporated electrodes were deposited without damaging the fibres. Subsequent electrical characterization of fibres contacted in this way presented a slightly better contact resistance than with EGF electrodes. Hence, since the electrical characterization of individual MMX chains was a challenge itself, evaporated gold electrodes were chosen when hunting for the single-molecule level, in order to optimize all the possible experimental conditions. Figure 4.5 presents the geometrical characterization of a bundle of a few $[Pt_2(EtCS_2)_4I]_n$ chains protruding from a gold electrode.

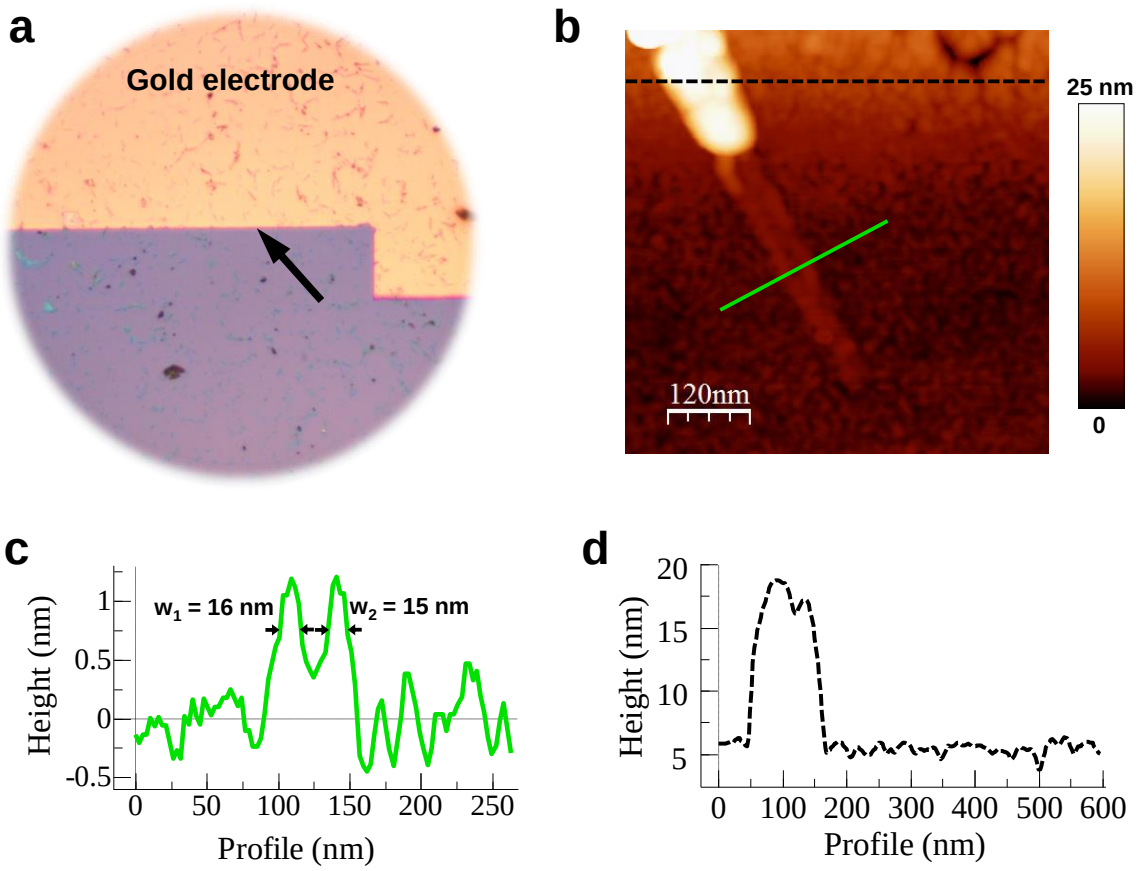

Figure 4.5 Single-molecule geometrical characterization. a) Optical microscopy image of the gold electrode edge. The black arrow points towards the region where the bundle shown in b) is located. b) Topographic AFM raw image of two single $[Pt_2(EtCS_2)_4I]_n$ chains protruding from a gold electrode. c) Height profile along the green solid line in b). Full widths at half maxima are shown. d) Height profile along the black dashed line in b).

Figure 4.5 portrays the main finding of this section. Figure 4.5a shows an optical image where a macroscopic gold electrode can be seen. The gold electrode was located on a region previously inspected by AFM showing very thin fibres. Figure 4.5b shows an AFM topographic image of a thin bundle composed of a few $[Pt_2(EtCS_2)_4I]_n$ chains acquired with a metallized tip (ElectriMulti75-G probes from BudgetSensors [30]). In particular, figure 4.5c presents the profile along the green solid line in figure 4.3b, which corresponds to a profile across the bundle, showing a height of ~ 1.2 nm, compatible with a single-molecule chain height. As explained in Chapter 1, one intrinsic artifact to the AFM technique is the well-known tip dilation. The apparent width w of a cylindrical fibre of height h when imaged with a tip of radius R can be estimated using the expression [31]:

$$w^2 = 8hR \tag{4.2}$$

Considering single molecules with height h ~ 1.2 nm and the tip radius given by the manufacturer of the cantilevers used in the experiments R = 25 nm, the apparent width of a single-molecule would be w ~ 15.5 nm, in very good agreement with the values in figure 4.5c for two individual molecules, with apparent widths of 15 and 16 nm. Figure 4.5d is the height profile along the black dashed line in figure 4.5b. An increase of ~ 12 nm in the gold electrode height indicates that the height of the fiber underneath had to be on that range, meaning that the single chains were coming from a thicker bundle. This singularity allowed a good electrical contact with the single molecules.

Figure 4.6 presents electrical transport measurements on the chains of $[Pt_2(EtCS_2)_4I]_n$ presented in figure 4.5 by using conductive AFM (C-AFM). A metallized AFM tip was used as a second mobile electrode to measure the current through the bundles as a function of their length. Images were acquired in AM-AFM mode and at selected locations the tip was brought into contact to perform I-V characteristics (see Chapter 1, conductive AFM section). During IVs acquisition it was thoroughly checked that no current was measured (within experimental noise) on the silicon oxide substrate on the vicinity of the chains.

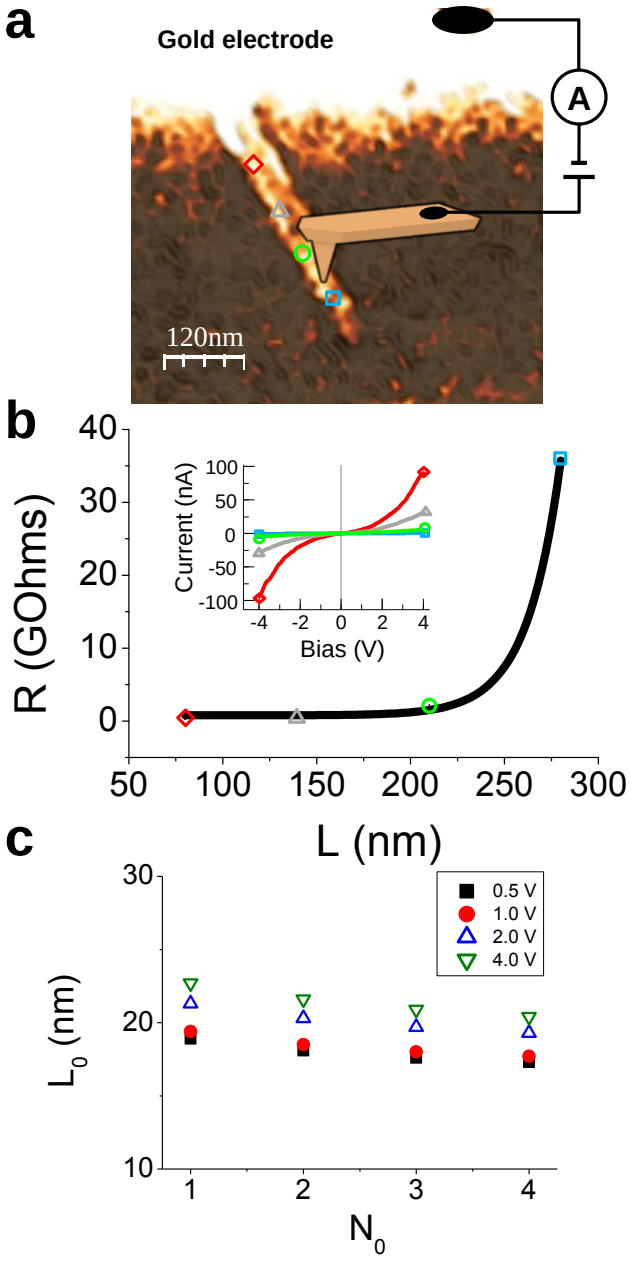

Figure 4.6 Single-molecule level electrical characterization of two $[Pt_2(EtCS_2)_4I]_n$ chains. a) Topographic AFM image of two single $[Pt_2(EtCS_2)_4I]_n$ chains protruding from the gold electrode. Color scale (3.2 nm from dark to bright) was adjusted to enhance the visibility of the chains. For clarity, the electrical circuit used in the AFM conductance experiments was added. The different symbols along the chains point the spots where IV measurements were carried out. b) Resistance *vs.* Length for the chains in a). The different symbols represent resistance measurements calculated from the IVs shown in the inset at Bias = 0.5 V, at the different distances as shown in a). The black line is a fit to equation (4.3) considering two chains. c) Localization length for resistances obtained at 0.5, 1, 2 and 4 V Bias voltages as a function of the number of chains, N_0.

Figure 4.6a is an AFM topographic image similar to figure 4.5b, but in this case the color scale was adjusted to enhance the visibility of the fibres. It also presents a schematic of the electrical circuit used for the C-AFM measurements. C-AFM enabled the control of the loading force applied by the mobile electrode to the bundles until an optimal contact resistance was reached, and then IV characteristics were measured. In this way, the maximal current was measured for an applied force of ~ 70 nN. The same force was used for all the measurements in this section. Table 4.1 shows the numerical data extracted from the IV curves used for the plots in figure 4.6.

Table 4.1 Length, current and electrical resistance for the $[Pt_2(EtCS_2)_4I]_n$ chains. Current data were extracted from IV curves at a fixed Bias voltage of 0.5 V (these resistance data are plotted in figure 4.6).

L (nm) (± 5 nm)	I (pA)	R (GΩ)
80	2000 ± 100	0.25 ± 0.02
140	750 ± 40	0.67 ± 0.04
210	230 ± 10	2.2 ± 0.1
280	14 ± 1	36 ± 3

Note: the uncertainties shown in the table account for instrumental errors in our measurements. However, we think there are other not controlled error sources that may enlarge the magnitude of uncertainty. Because of this, plots in figures 4.6 and 4.8 do not show error bars.

Figure 4.6b displays the electrical resistance R, as a function of the distance between electrodes L, obtained for the chains in figure 4.6a. A clear non-linear dependence is observed, suggesting electron-defect interactions as the main source of resistance in these chains. Previously reported electronic structure analysis performed by Density Functional Theory (DFT) calculations clearly show the metallic nature of the $[Pt_2(dta)_4I]$ polymer [32]. In fact, its band structure is characterized by a non-degenerate half-filled band that crosses the Fermi level along the Γ-A direction, which corresponds to the axis of the MMX chain. The metallicity of the chain can be tracked back to the odd number of electrons in the unit cell. Another intuitive way to justify the electrical conductivity of the MMX chains is because of the presence of a Pt^{2+} and Pt^{3+} mixed-valence state that translates in charge delocalization [25]. According to Landawer's theory, the band that crosses the Fermi level should result in a conductance of $G_0 = 2e^2/h$, which corresponds to a quantum of resistance $R_0 = 1/G_0 \approx 13$ kΩ. This value does not take into account other effects such as the electrode-chain contact resistance, electron-phonon interaction, scattering with the substrate or the presence of structural defects along the chains. A similar R-L trend as observed here

for the MMX chains is found in carbon nanotubes [33], and attributed to Anderson localization due to the interaction between electrons and structural defects. Figure 4.7, from reference [34], illustrates this behavior in the case of carbon nanotubes.

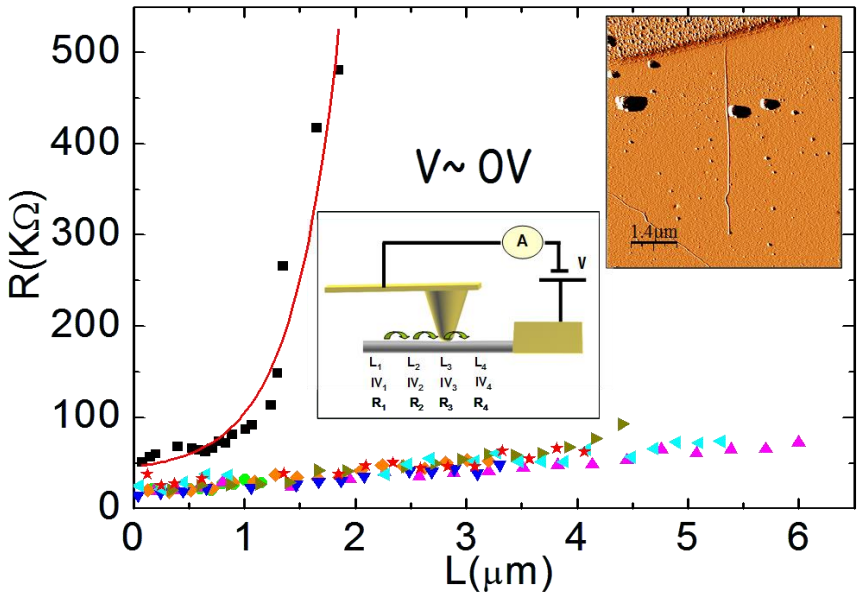

Figure 4.7 Experimental dependence of the low voltage Resistance *vs.* Length for CVD-grown single-walled carbon nanotubes (SWNTs) (triangles and stars) and HipCo SWNTs (squares). The central inset of the figure is a schematic of the procedure employed to measure the resistance as a function of the distance with a metallized AFM tip. The upper inset is an AFM image of a long nanotube partially covered with gold. The nanotubes directly grown on surface present low disorder and hence the conductance is quasiballistic; the low increment of the resistance with length is a consequence of the interaction with acoustic phonons and disorder. The HipCo SWNT presents a high density of defects resulting in an electronic transport regime governed by the Anderson localization phenomenon. Imagen taken from reference [34].

Following a similar scheme, the resistance data in our MMX chains can be fitted to an exponential expression:

$$R = R_C + \frac{R_0}{N_0} e^{L/L_0} \qquad (4.3)$$

where it can be assumed that the chains were electrically isolated one from each other. In this expression R_C accounts for the electrode-chain contact resistance, R_0 is the above mentioned quantum resistance, N_0 is the number of chains contacted by the AFM tip and L_0 is the localization length (that is related to the mean distance between defects). As it can be seen in figures 4.5b and c, in the case of the chains under study the AFM topography

suggested that N_0 can be 1 or 2. Numerical fitting of the data shown in table 4.1 to equation (4.3) with $N_0 = 2$ and Bias voltage equals 0.5 V leads to $R_C \approx 800$ MΩ and $L_0 \approx 18$ nm. According to Kelley *et al.* [35] the nonlinearity observed in the IV traces (inset figure 4.6b) is not surprising since the precise IV relationship is a function of any charge injection barriers at the tip-MMX chain junctions and hence $R_C = R_C(V)$. In order to check the robustness of the fitting, it was repeated for higher voltages, finding that L_0 ranged between ~ 17 and 23 nm (figure 4.6c). This variation is quite small taking into account the ranges taken for voltages and number of molecules and suggests that the determination of the localization length so performed is robust.

A remarkable feature of these MMX chains is that the whole current flowed through just a single iodine atom, Pt_2-I-Pt_2, thus making these chains very sensitive to punctual atom defects. Considering that Pt_2-I-Pt_2 is formed by coordination bonds, which are weaker than covalent bonds, these atomic defects can be easily generated. They might be the responsible of the observed behavior of the current through the MMX chains. The measurements at closer electrode distances (~ 80 nm) show a current density across the iodine atom ~ 10^6 A cm^{-2} (estimated at 0.5 V, considering for the iodine atom a radius I^- = 2.2 Å). This number can be put in perspective by taking into account the current density flowing through a single MMX chain J ~ 2 10^5 A cm^{-2} (considering a diameter of ~ 1.2 nm, figures 4.5b and c). Figure 4.8 shows the variation of the current density for the chains in figure 4.5 as a function of the distance between electrodes. It is remarkable the persistence of the current even for lengths as long as 280 nm.

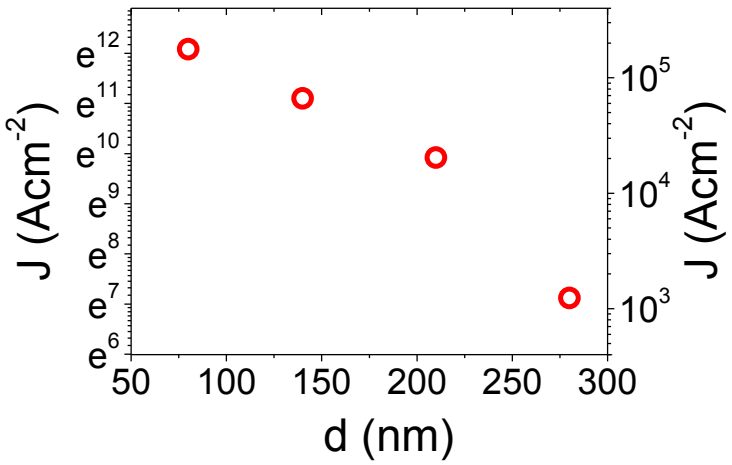

Figure 4.8 Current density along a $[Pt_2(EtCS_2)_4I]_n$ single chain as a function of the distance.

For the sake of comparison, the current density measured here is ~ 10^{10} times higher than that reported by Tuccitto *et al.* [20] for a conductive metal-based terpyridine polymer. The

value presented here takes more relevance considering that in this case the conductance is evaluated for molecule lengths of 80 nm while in reference [20] the molecule length is below 15 nm. Going further with the comparisons, β decay can be evaluated in measurements here presented. β is related to the localization length through the expression $\beta = 1/L_0$, thus lower β values correspond to higher electrical transport efficiency. It is usually expressed in $Å^{-1}$. β is commonly used in molecular electronics as an indication of the efficiency of charge transport in a given molecule. Here it is found a value of $\beta \sim 5\ 10^{-3}\ Å^{-1}$. Slinker *et al.* [15] report conductance over 34 nm in DNA layers using indirect evidence based in electron transfer rate in solution (*i.e.* they do not report IV measurements). However, DFT calculations in double stranded DNA show a band structure characteristic of an insulator and hence the electrical conductivity should be based on a different mechanism that the one accepted for MMX polymers [36]. References [20-22] also report slightly lower values for β than in here, but in configurations of large number of molecules where the probability for defects creation is usually lower.

To verify if Anderson localization induced by structural defects can be the origin of the observed exponential dependence of resistance with length (Eq. (4.3)), quantum transport calculations were carried out by Dr. Juanjo Palacios and Prof. José Soler. Since a detailed description of the calculations is out of scope of this work, only the basic concepts to follow them are provided. First, the quantum transmission for a single defect in an otherwise perfect MMX wire was computed. ANT.1D code was used [37], with DFT matrix elements computed with SIESTA [38], and the Green's function formalism for quantum transport [39, 40].

Figure 4.9 shows the three possible defects that were considered: 1) a kink; 2) an OH molecule substituting an I atom; and 3) an I vacancy.

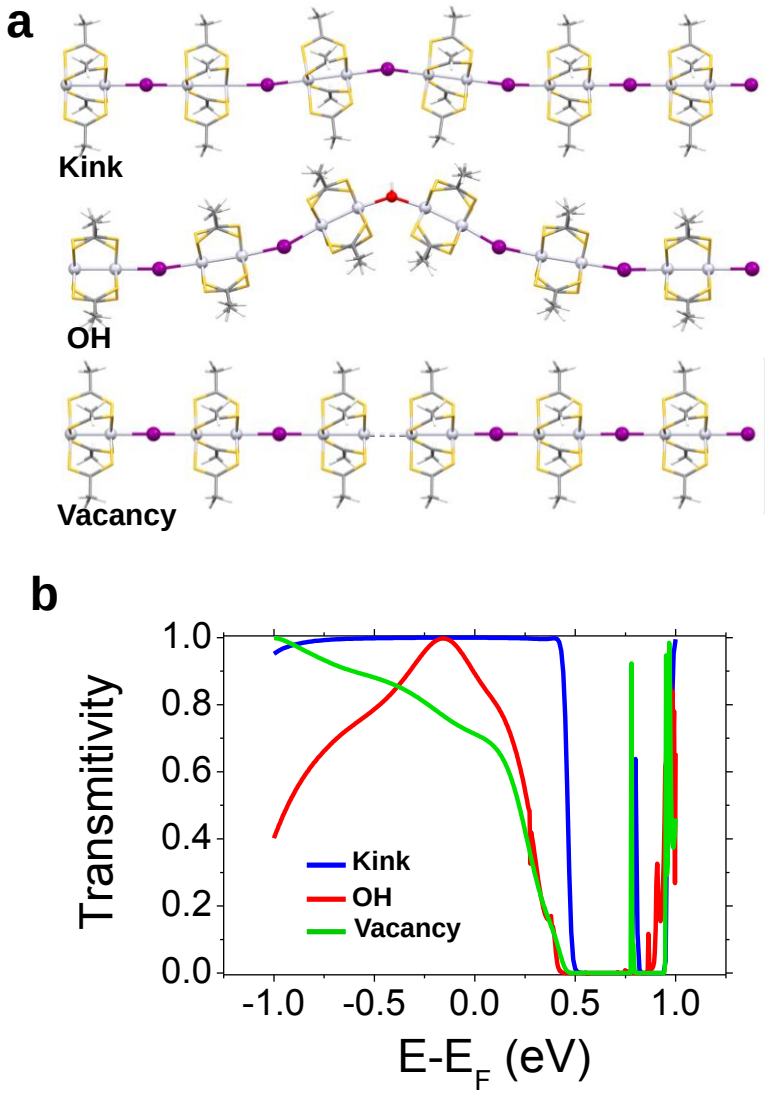

Figure 4.9 a) Schematic relaxed structures of the three types of defects considered. From top to bottom: a kink, an OH group substituting an I atom, and an I vacancy. b) Transmission as a function of energy for a single defect from the types shown in a).

Figure 4.9a shows the structures of the different defects under consideration. Figure 4.9b presents the calculated transmission for these cases. The kink, which accounts for the effects of substrate roughness, did not appreciably change the transmission at any energy within the conducting band up to $E_F \pm 0.5$ eV. OH substitution and I vacancy are a consequence of the MMX chemistry. Whereas OH substitution decreased the transmission to 0.9 near E_F, I vacancy had the largest effect on the transmission at E_F, reducing it to 0.7. Moreover, solution of MMX chains contains two dimetallic subunits, named $[Pt_2(EtCS_2)_4]$ and $[Pt_2(EtCS_2)_4I_2]$ [27, 28]. The formation of the MMX chains under study involves the

alternate assembly of these building blocks. But importantly, the assembly of two $[Pt_2(EtCS_2)_4]$ building blocks, already proved in references [41, 42], leads to I vacancies. Therefore, following calculations were focused on this type of defect. The conductance for long MMX wires with many vacancy defects was also calculated with ANT.1D, but now using a single-orbital tight-binding model [43]. This is justified because the only conductance channel in the MMX wire is made of a single band. Figure 4.10 shows results for two concentrations of defects, placed at random positions, and for segments of increasing length along three different wires. The conductance over different positions of the defects was not averaged, to mimic the actual experimental measurements with the tip moving along the same wire.

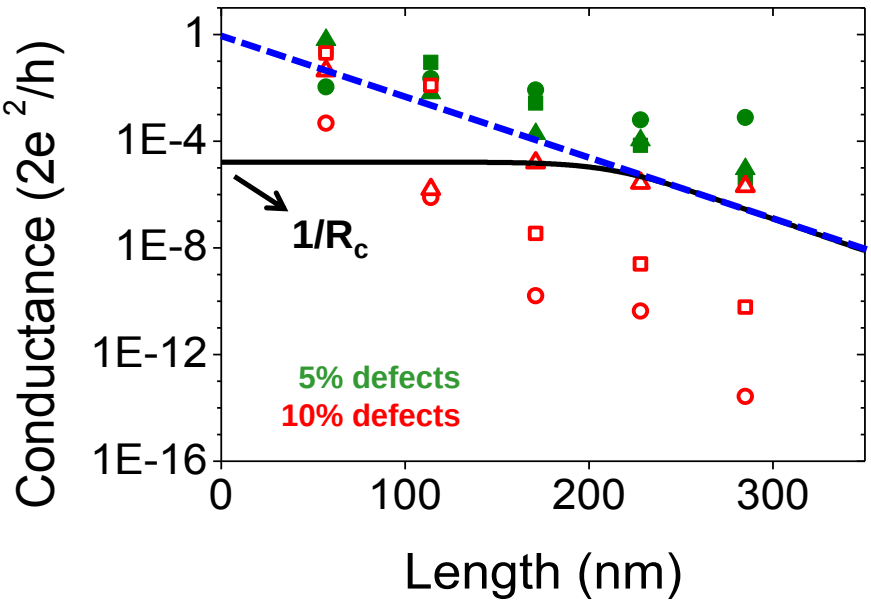

Figure 4.10 Conductance obtained for six different disorder realizations in a single-orbital tight-binding model mimicking the random presence of vacancies (green solid symbols: 5% concentration, red empty symbols: 10% concentration). Large fluctuations can be appreciated on top of an overall exponential behavior. The black line corresponds to the experimental result while the blue dashed line corresponds to an extrapolation of the measured conductance assuming absence of experimental contact resistance.

As expected in phase-coherent calculations and ignoring the inherent fluctuations, the conductance follows an exponential decay with chain length. According to these calculations, a percentage of vacancies in the range 6 - 8 % would be responsible for the observed decay length. Considering previous results on MMX nanoribbons, the content of

defects here inferred is compatible with those observed by direct sublimation of MMX microcrystals [21].

In summary, robust on surface isolation from drop-casting and electrical characterization of different polymer MMX wires have been presented, going down to the single-molecule regime. C-AFM has been employed to probe the electrical properties of individual chains, where the whole current flows through just a single iodine atom. Experimental results have been complemented with theoretical calculations which suggest that structural defects (in particular a 6-8 % of iodine vacancies) are the responsible of the observed electrical behavior. The studied MMX chains present a record electrical conductivity for long distances, confirming these polymers as excellent molecular wires.

4.3 Local tuning of graphene properties upon ultrahigh pressures

4.3.1 Introduction

Most of the knowledge acquired by the human being has been gained through studying the nature at or near one atmosphere, which is the pressure at the Earth's surface. Nevertheless, much of the matter in the Universe exists under much more pressurized conditions, as for example deep inside planets and stars. For instance, in his book "2061 - Odyssey Three", the well-known science-fiction writer Arthur C. Clarke comments the fascinating idea that, as a consequence of the extreme pressure inside giant planets, the core of the planet Jupiter would be, in fact, a diamond the size of Earth. Figure 4.11 shows a chart with the orders of magnitude for pressure found in nature.

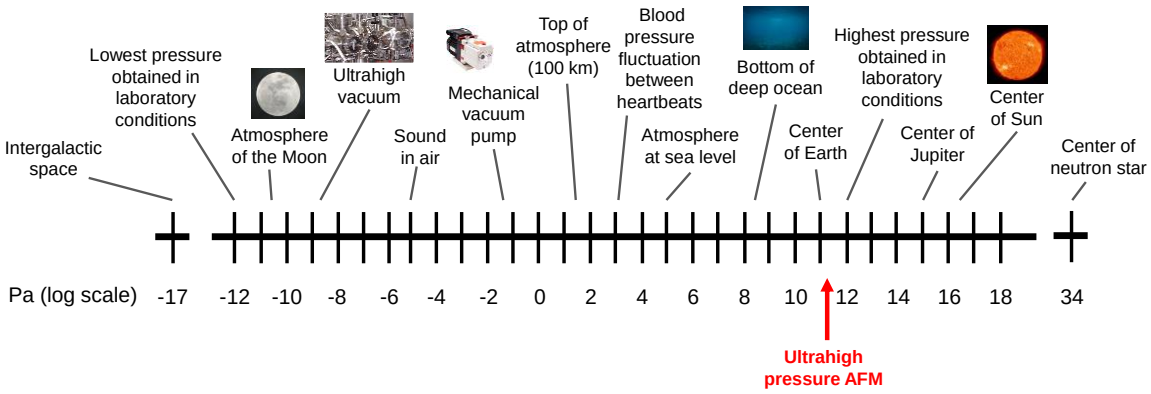

Figure 4.11 Chart of the orders of magnitude in relation to pressure expressed in pascals (logscale).

Reaching ultrahigh pressures always implies an immense experimental challenge. The most common device employed is the diamond anvil cell [44]. In brief, it consists of two opposing diamonds with a submillimeter-sized sample compressed between their polished tips. Typical tip sizes are 100 - 250 μm. Since the pressure P is the applied force F divided by the contact area A (P = F/A), a very high pressure is achieved with moderate forces. Anvils are made out of diamond due to its hardness and virtual incompressibility. Diamond anvil cells typically allow reaching pressures of 100 - 200 GPa, although values up to 750 GPa have been reported by using special cells [45]. Ultrahigh pressures in diamond anvil cells are typically used to synthesize materials and phases not observed under normal ambient conditions [46-48].

In this section, controlled local modifications of graphene, the strongest material ever measured [49, 50], have been performed by the achievement of ultrahigh pressures by using Atomic Force Microscopy with diamond tips. It can be considered as a nanotechnology

version of a diamond anvil cell. With this configuration, chemical bonding is expected to be induced between selected regions of a graphene flake and the underlying substrate where it is supported. The main goal of the work presented in this section is to locally tune the electronic properties of 2D materials, in particular graphene, in a very controlled way by applying ultrahigh pressures with the AFM. By doing so, selective doped areas are expected to be created in graphene on SiO_2/Si substrates [51], as it is shown here by Raman spectroscopy and Kelvin Probe Force Microscopy (KPM) characterizations. A direct application of this local doping has been the creation of low contact resistance areas for the fabrication of improved metal electrodes for future graphene electronics.

Another simple application of this method has been improving the performance of graphene as a sealer by applying local ultrahigh pressure. To this end graphene has been deposited on SiO_2/Si substrates with predefined microcavities, creating in this way graphene-sealed microchambers. By measuring gas leak rates before and after sealing the microchambers inside regions modified by ultrahigh pressure, it has been observed that after sealing microchamber leak rates have reduced by a factor of ~ 3.5.

These results suggest local application of ultrahigh pressures with AFM as a very powerful tool to tune 2D materials properties. Additionally, by trapping self-assembled monolayers of specific molecules between graphene layers and a substrate, AFM can provide a unique platform to carry out chemical reactions at ultrahigh pressures without the technical drawbacks characteristic of classical high-pressure procedures.

The work presented in this section is not published so far and has been performed in collaboration with Dr. Félix Zamora, Dr. Cristina Gómez-Navarro, Prof. Enrique García-Michel and Prof. Fernando Martín groups. In particular, Prof. Enrique García-Michel group is analysing X-ray Photoelectron Spectroscopy (XPS) data, comparing pristine and modified graphene regions, to gain insight on the chemical bonding between graphene and substrate induced by the AFM tip. Data have been taken at the Scanning PhotoElectron Microscope (SPEM) hosted at the ESCAmicroscopy beamline at Elettra, in Trieste (we would like to acknowledge the staff of Elettra for the professional handling of the experiments). Prof. Fernando Martín group is currently carrying out the theoretical interpretation of the experiments using state-of-the-art Density Functional Theory (DFT).

4.3.2 Results and discussion

It is very remarkable that achieving controlled local high pressures with AFM is technically very simple [52]. Typical commercial diamond AFM tip radii are in the range of 10 - 100 nm, thus, as commented above, the tip-sample contact region can be seen as a nano-anvil cell were ultrahigh pressures can be readily achieved with relatively low forces.

Figure 4.12 shows a diagram of the AFM high pressure application for the kind of samples studied here.

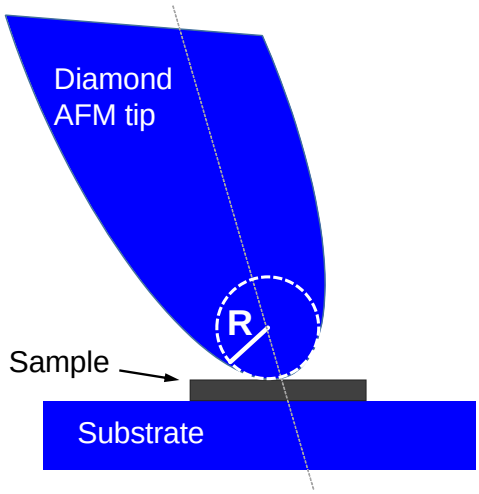

Figure 4.12 Diagram of a nano-anvil cell by using a diamond AFM tip.

A simple estimation of the pressure that can be achieved by using this configuration can be calculated following the Hertz's model [53, 54]. The contact radius ρ between a sphere and a plane is then given by:

$$\rho = \left(\frac{3FR}{4E^*}\right)^{1/3} \tag{4.4}$$

where F is the applied force, R the tip radius and E^* is the effective elastic modulus $1/E^* = 1/E_{tip} + 1/E_{sample}$. Then, the mean contact pressure P exerted on the sample by the tip can be determined as:

$$P = \frac{1}{\pi}\left(\frac{4E^*}{3}\right)^{2/3}\left(\frac{F}{R^2}\right)^{1/3} \tag{4.5}$$

Using cantilevers with stiffness k ~ 40 N m^{-1}, a conventional AFM set up can easily apply forces higher than 100 μN. Assuming E^* of ~ 1 TPa and a tip radius of ~ 50 nm, the resulting pressure is well above 100 GPa. By using sharper tips and stiffer cantilevers (as for instance commercially available R ~ 20 nm and k ~ 80 N m^{-1} [55]) this figure can reach values up to ~ 300 GPa. In the work presented here, a single crystal diamond tetrahedral pyramid SCD15/AIBS probe from MikroMasch [56] was used. The cantilever nominal length and width were 125 and 35 μm respectively. It presented a resonance frequency of 320 kHz in air and a force constant of 32 N m^{-1} (calibrated using the Sader method [57,

58]). The tip radius was calibrated by imaging carbon nanotubes and using equation (4.2). A value of R = 42 nm was obtained from nanotubes of different heights.

Graphene flakes were deposited by microexfoliation on 300 nm SiO_2/Si substrates. Single-layer areas where first located by optical microscopy and corroborated by Raman spectroscopy [59]. Raman spectroscopy is an optical technique based on inelastic scattering (or Raman scattering) of monochromatic light (usually from a laser in the visible part of the light spectrum). The laser light interacts with excitations in the system (typically molecular vibrations and/or phonons), resulting in a shift in the energy of the laser photons. This shift in energy gives information about the vibrational modes in the system. A detailed explanation of the principles of Raman spectroscopy can be found elsewhere [60]. Raman shifts are typically reported in wavenumbers, which have units of inverse length, as this value is directly related to energy. The unit commonly employed is cm^{-1} ($1\ cm^{-1} = 1.2\ 10^{-4}$ eV). The Raman spectra of all carbon systems show only a few prominent features, just a couple of very intense bands in the 1000 - 2000 cm^{-1} region of the Raman spectrum and few other second-order modulations. However, their shape, intensity and positions allow distinguishing the different carbon structures [61]. In the case of graphene, Raman spectrum clearly evolves with the number of layers. The so-called G (~ 1580 cm^{-1}) and 2D (~ 2700 cm^{-1}) Raman peaks change in shape, position and relative intensity with number of graphene layers. This allows unambiguous identification of graphene layers [59, 61]. Additionally, by monitoring the variation of both G and 2D Raman peaks in doped single-layer graphene, information about the doping level can be obtained [62]. The D Raman peak (~ 1350 cm^{-1}) gives information about the presence of defects in graphene [63]. A further refinement of the Raman technique consists on focusing the laser spot using a high numerical aperture lens. By doing so, the information of the Raman spectra is restricted to the illumination area. This method is known as micro Raman spectroscopy. Raman spectra along this PhD have been acquired using a WITEC/ALPHA 300AR Raman confocal microscope (Witec GmbH, Ulm, Germany) at ambient conditions. The laser wavelength and power were 532 nm and 1 mW respectively. It enabled micro Raman, with a laser spot diameter of ~ 300 nm, allowing the acquisition of spectra in very precise locations.

Figure 4.13 shows optical, AFM and micro Raman characterization of a pristine graphene layer before ultrahigh pressure modifications.

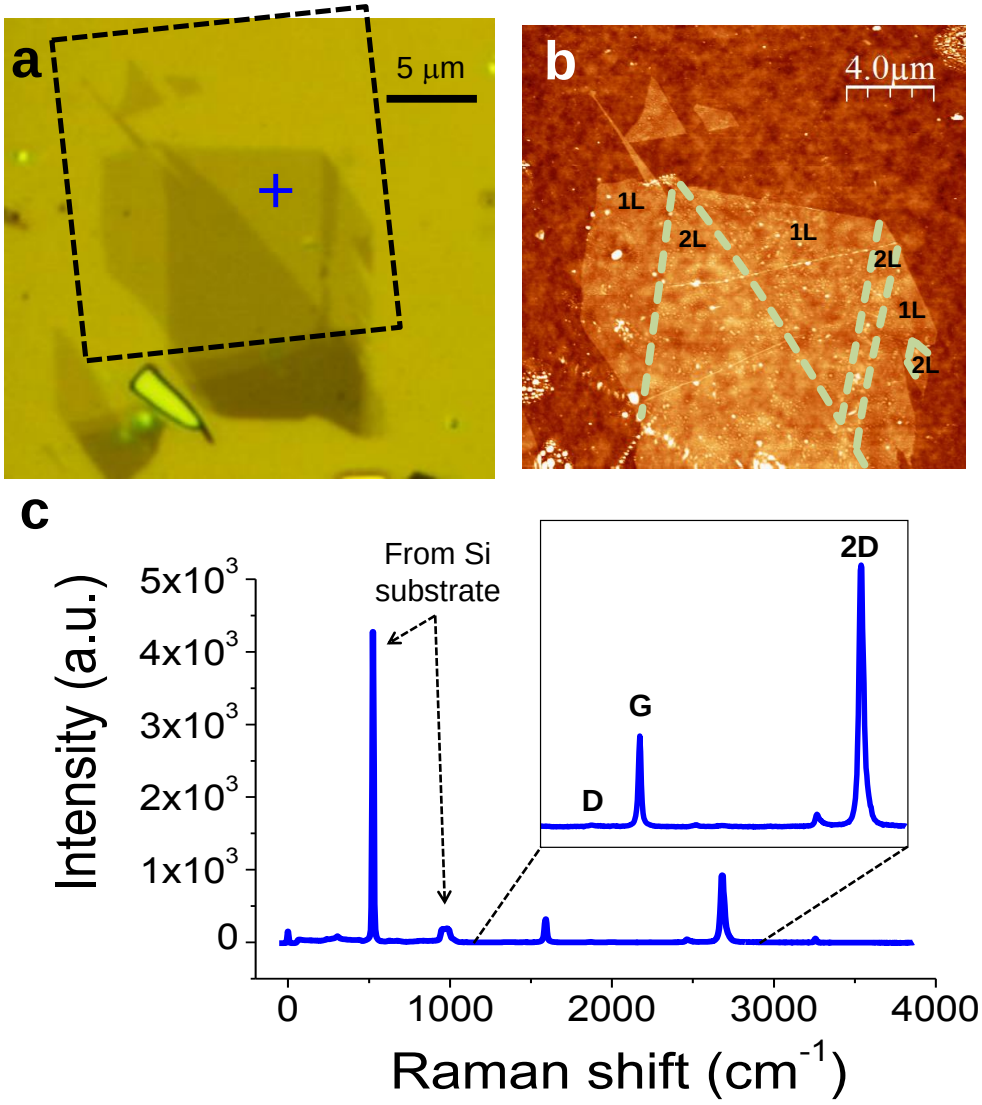

Figure 4.13 Characterization of pristine graphene on SiO_2 before modifications. a) Optical image. b) AFM topographic image of the area enclosed in the square in a). Single-layer areas are marked with 1L and bilayers with 2L. Dashed lines along the edges between 1L and 2L areas were added as a guide to the eye. c) Raman spectrum acquired in the spot marked with a cross in a). The inset corresponds to graphene characteristic peaks.

Figures 4.13 a and b show optical microscopy and AFM topographic images (AM-AFM mode) respectively of a graphene flake with several monolayer terraces. Raman spectra acquired in the different regions of the flake corroborate the thickness of each of the terraces. Figure 4.13c shows a Raman spectrum acquired in a monolayer area. The sharp 2D peak shape and the ratio intensity between G and 2D peaks clearly indicate that it

corresponds to a single-layer terrace. Additionally, the nonappearance of a D peak indicates the absence of a significant number of defects.

The procedure to modify areas under ultrahigh pressures involved the following steps: first the flake was imaged in AM-AFM mode. Then, feedback parameters were adjusted to contact mode conditions and the tip was brought into a very gentle contact in the area of interest, scanning in the fast scan axis in both forward and backward directions (also known as trace and retrace). At this point, the scanning speed was set to 2 μm/s. The precision of the pressed area can be tuned with the number of points per line, which depends of the size of the modified area: for areas below 1 μm^2, 256 points were used. Then the Setpoint was changed to the corresponding value according to the desired pressure, calculated using equation (4.5). The area was then scanned twice under these conditions: typically the area was scanned from top to bottom, and when reaching the bottom, from bottom to top. At that point, the tip was brought back to AM-AFM mode and a topography image was then acquired. Figure 4.14 shows part of the flake shown in figure 4.13, where 600 x 600 nm^2 areas were modified in monolayer terraces at different pressures, starting from 13 GPa and up to 40 GPa. The magnitude that is directly obtained from AFM is the loading force. As commented above, in order to determine the pressure, the tip radius was previously estimated by scanning a sample with carbon nanotubes. By applying equation (4.5), where the radius of the nanotube was assumed to be its height as obtained from the AFM topographic images, pressure values were obtained.

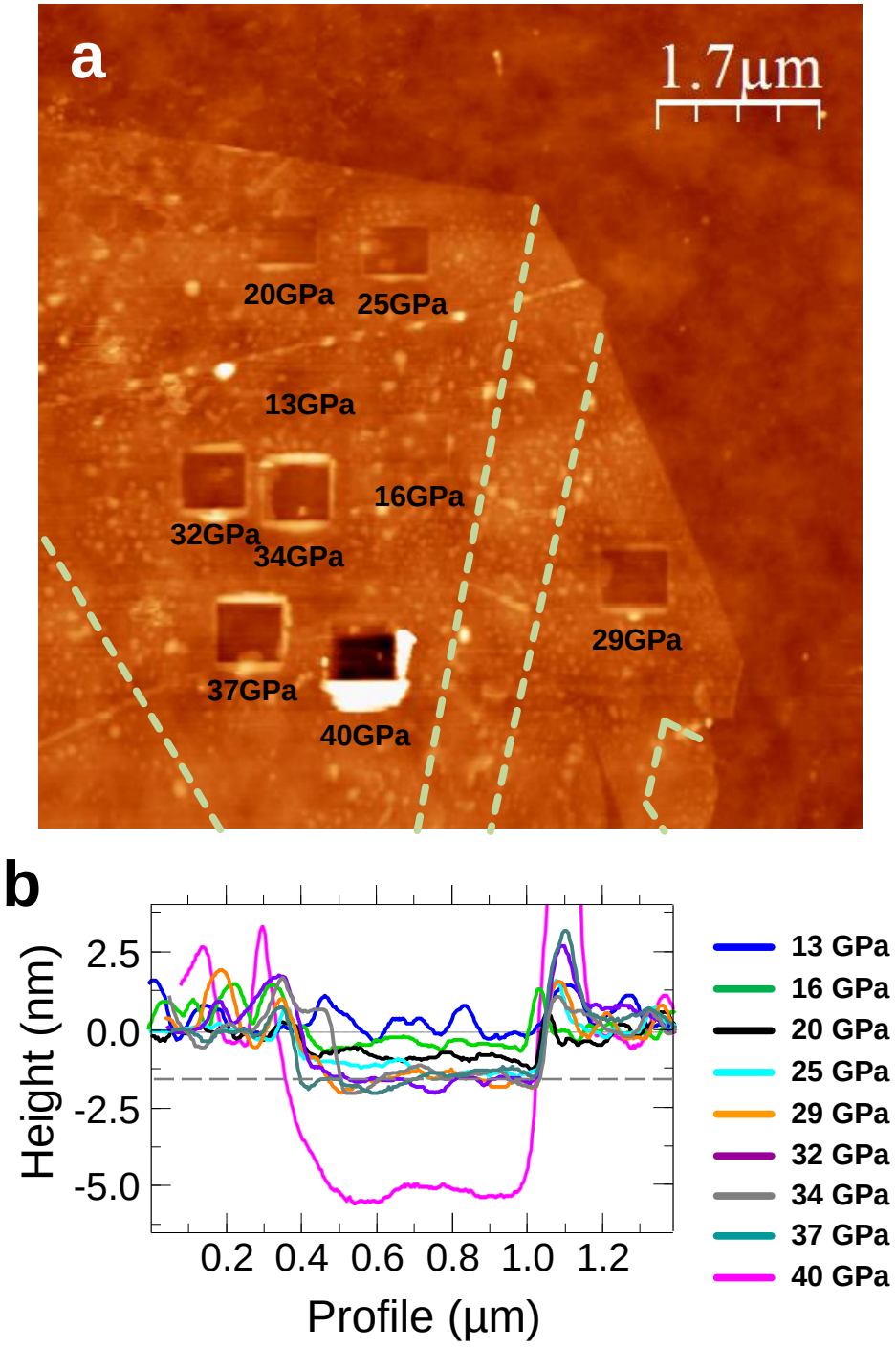

Figure 4.14 Ultrahigh pressure modifications on graphene. a) AFM topographic image showing 600 x 600 nm^2 areas modified under different pressures. b) Selected height profiles from the different modified regions. Horizontal dashed line marks the mean depth for pressures in the range 29 - 37 GPa.

Figure 4.14 shows that for pressures below 13 GPa the substrate was not modified. From 16 to 25 GPa the depth observed within the modified areas increased up to ~ 1 nm, but from 29 to 37 GPa the depth, ~ 1.3 nm, remained almost constant. Finally, for pressures of 40 GPa the graphene sheet broke and the tip induced irreversible damage in the underlying SiO_2, reaching a depth of ~ 5 nm. To better understand these observations, similar modifications were performed on the SiO_2 substrate, without graphene. Figure 4.15 shows the results of these modifications.

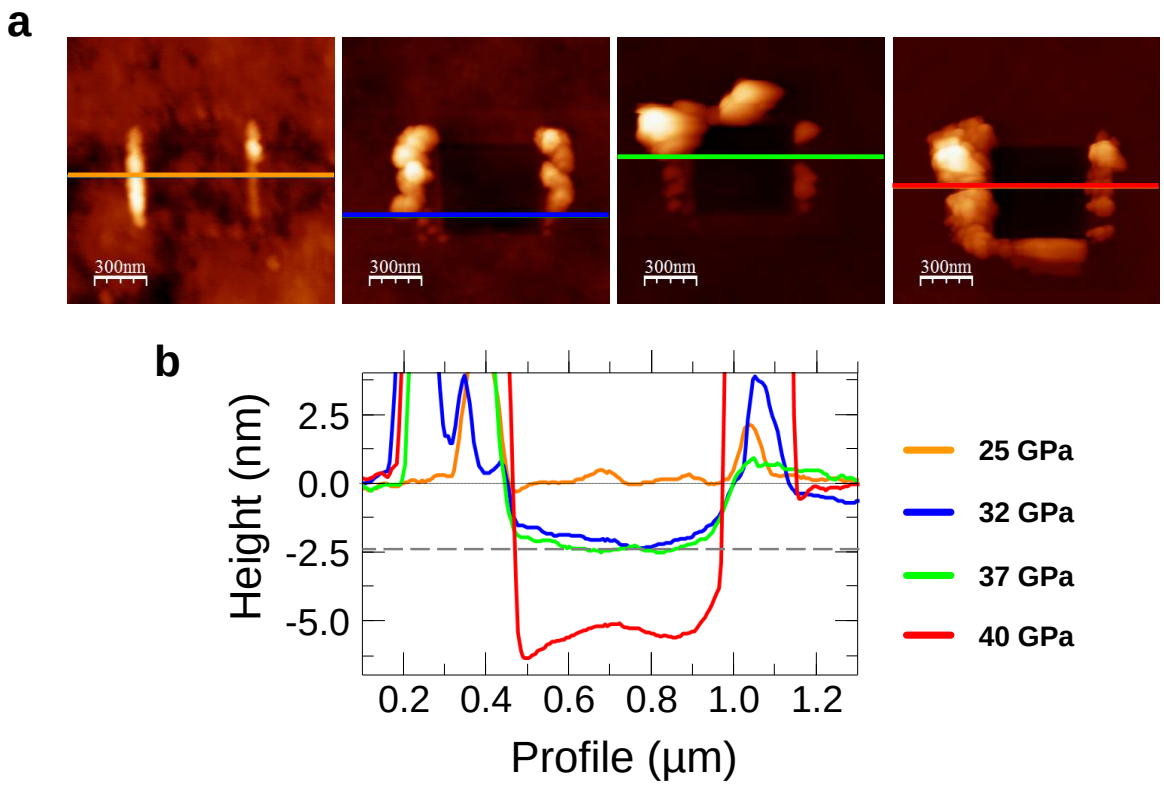

Figure 4.15 Ultrahigh pressure modifications on SiO_2. a) AFM topographic images showing 600 x 600 nm^2 areas modified under different pressures. b) Selected height profiles from the different modified regions. Horizontal dashed line marks the mean depth for pressures 32 and 37 GPa.

From the modifications on SiO_2 shown in figure 4.15, it can be observed that up to 25 GPa, the SiO_2 substrate was not modified, some debris was swept from the scanned area but its depth did not change. It is widely assumed that under ambient conditions there exists an ever-present layer of adsorbed water which remains captured between the flakes and SiO_2 [64]. This implies that the changes in depth (~ 1 nm) observed in graphene up to this pressure were related to an irreversible approach of the graphene layer towards the substrate, reaching a point where graphene is in *direct* contact with the SiO_2 substrate.

From figure 4.15 it can be observed that for higher pressures, up to 37 GPa, the SiO_2 substrate was modified, presenting a depth of ~ 2.5 nm. Comparing this value with the obtained in the graphene case, ~ 1.3 nm, since graphene was already in contact with the substrate for pressures above 25 GPa, it can be inferred that in these cases graphene was "protecting" the substrate from being modified. This result can be of great importance for applications of graphene as a protective coating. For a pressure of 40 GPa, the SiO_2 substrate sank to a depth of ~ 5 nm, similar as in the case of graphene, which for this pressure broke and exposed the AFM tip to the underlying substrate. Whereas 37 GPa were achieved by applying a 1.5 μN force with the tip, for the 40 GPa case 2 μN were necessary. This value might explain the breakage event observed in the 40 GPa case, since measured breaking forces of ~ 1.7 - 2.1 μN are reported for free standing graphene [50].

The properties of the modified areas were studied using Raman spectroscopy and Kelvin Probe Force Microscopy (KPM). Raman spectroscopy in its mapping configuration was used. The Raman laser was scanned in a kind of raster pattern, acquiring spectra at equally spaced points. Since at each of the points a whole spectrum was acquired, plots showing information at different Raman shifts can be easily created. For the KPM measurements, ElectriMulti75-G probes from BudgetSensors [30] were employed. AM+PLL AFM for the topography and FM mode with an alternate bias voltage of amplitude 3.5 V and frequency 7 kHz for the Contact Potential Difference (CPD) was employed (see Chapter 1 for details). To have a well-defined potential reference, the flake was contacted through the EGF soft-electrode procedure to provide a stable potential reference. KPM measurements were performed in an inert Ar atmosphere to avoid CPD shielding by the presence of an adsorbed water layer on the surface [65]. Figure 4.16 shows Raman and KPM analysis of the modified regions in figure 4.14.

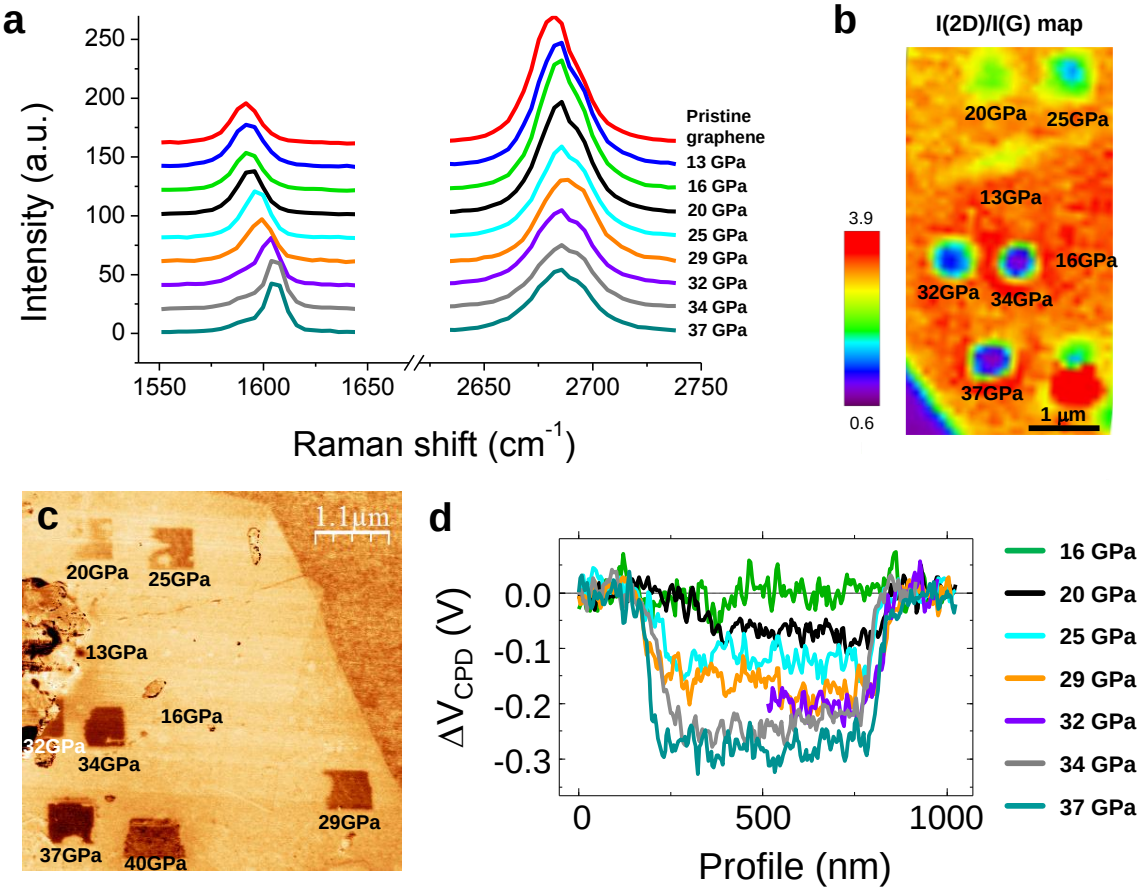

Figure 4.16 a) G and 2D peaks of the Raman spectra from the different modified regions. Raman mapping was performed as explained in the main text and the spectra for each modified region was obtained averaging all the spectra inside. b) I(2D)/I(G) map for selected modified regions. c) KPM image of the modified regions. Notice the area modified at 32 GPa is partially covered by a silver paint micro-drop deposited accidentally when placing an EGF electrode for potential reference. d) Variation of the CPD in the different regions. Curves obtained from selected profiles in c).

From the Raman mapping different images were obtained. Some examples can be found in the Appendix, where maps of the G and 2D peaks shifts and variation of their widths can be found (figure A4.4). Raman spectra centered at the D peak are also shown (figure A4.5). Interestingly, no D peak appeared, indicating that there was not a significantly creation of defects upon ultrahigh pressure modifications. In particular, following reference [66], the absence of D peaks implies that the density of defects is lower than ~ 0.01%. The observed behavior for the G and 2D peaks points towards a doping effect [67]. Figure 4.16a shows the evolution of the G and 2D peaks within the modified areas up to 37 GPa. Since for the

40 GPa case the graphene layer was broken, no further analysis on the effects of this pressure is performed. Figure 4.16b presents a map of the 2D/G height ratio, which changes significantly with doping and it is proposed as a sensitive parameter to monitor the doping in graphene [62]. The I(2D)/I(G) ratio observed here is in very good agreement with reported hole doping graphene through gated transistor configurations [62, 67]. Raman results are further analyzed later in the manuscript considering as well the results obtained with other techniques.

Figures 4.16 c and d present KPM characterization of the modified areas. A clear reduction of the CPD with increasing pressure can be observed, indicating that the Fermi level shifts down as the pressure increases, compatible with a pressure-dependent hole doping effect [68], in very good agreement with the Raman observations. Considering that the work function of the tip does not vary during KPM acquisition (which is quite a reasonable consideration, since the KPM data in figure 4.16c presents a stable CPD value for the unmodified graphene in the whole image), then the variation of the CPD can be converted to a variation in the Fermi level using the following expression (extracted from equation (1.26) in Chapter 1):

$$\Delta E_F = e\Delta V_{CPD} \tag{4.6}$$

where e is the elementary charge, 1.60210^{-19} C. And with the Fermi level shift, the variation of carrier concentration in the graphene modified areas can be estimated using the Fermi energy equation [69]:

$$\Delta n = \frac{1}{\pi}\left(\frac{\Delta E_F}{\hbar v_F}\right)^2 \tag{4.7}$$

where $\hbar$ is Planck constant, and v_F is the Fermi velocity $|v_F| = 10^6$ m/s. Figure 4.17 shows I(2D)/I(G), depth from topography data and Fermi level shift as a function of the applied pressure, and the I(2D)/I(G) variation as a function of the electron concentration.

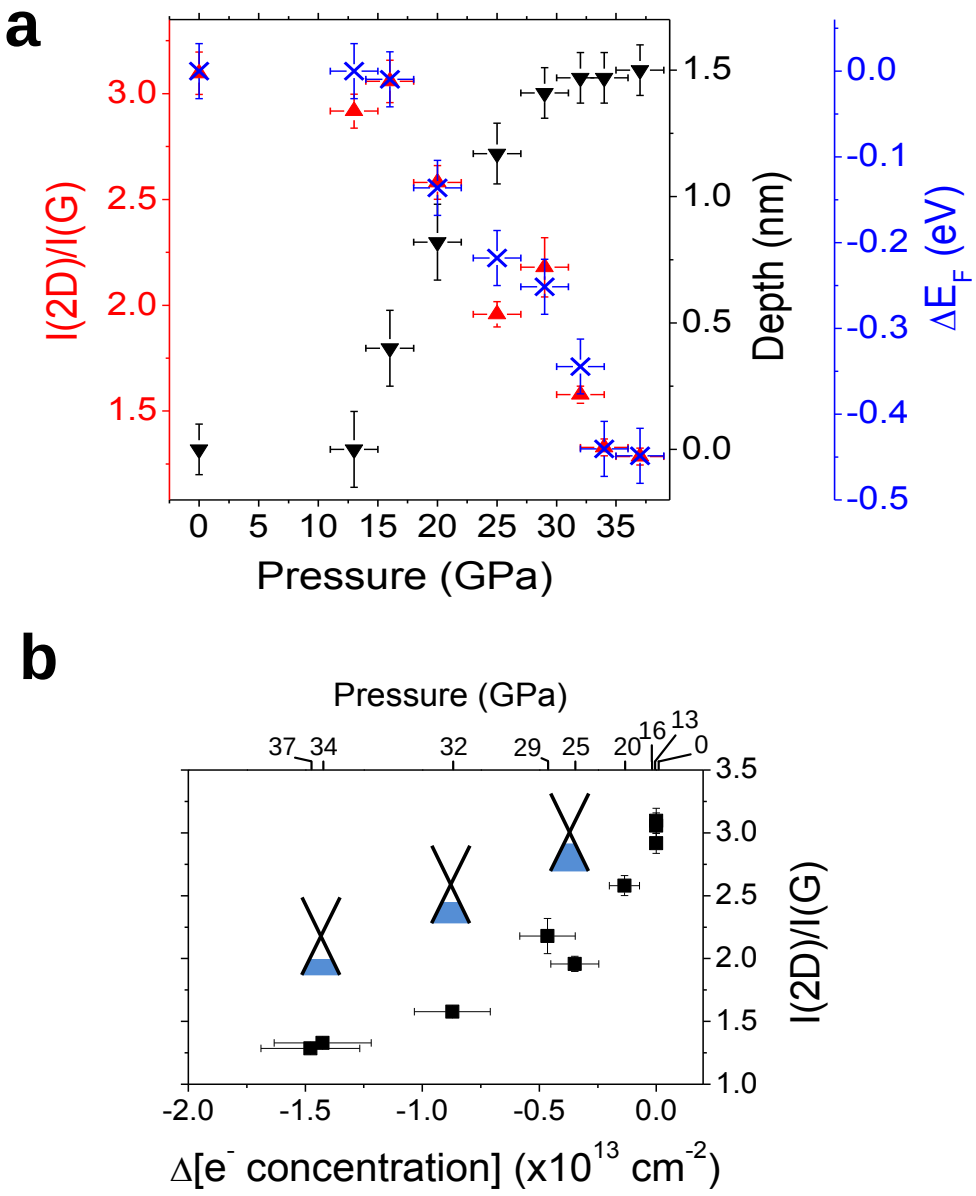

Figure 4.17 a) 2D/G intensity ratio, depth and Fermi level shift as a function of the pressure. b) 2D/G intensity ratio as a function of the electron concentration. Insets show schematic sketches of the graphene band diagram representing the increase of hole doping with applied pressure.

Figure 4.17a shows a direct correlation between the 2D/G intensity ratio and the Fermi level shift, which are both inversely proportional to the depth of the modified areas. Figure 4.17b shows the 2D/G intensity ratio as a function of the variation of the electron concentration. The obtained results are in very good agreement with graphene doping found in the literature using different techniques such as interface engineering [69], chemical

approaches [70], thermal annealing and gas flow experiments [71], electrostatic gating [62, 67, 68], or combinations, as for instance combining electrostatic gating with a Cs/O surface coating [72]. This supports the hypothesis of achieving a very controlled graphene doping through ultrahigh pressure modifications. As reported by Ryu *et al.*, the degree of graphene coupling to the substrate is an important factor controlling graphene doping [71]. In the results presented here, the pressure applied to graphene produced an increase of the coupling to the substrate and hence an increase in the doping. The effect of these pressure modifications is stable within time at ambient conditions (figure A4.6 in the Appendix shows AFM imaging of the same regions as modified and after 4 months in ambient conditions, presenting no visible changes).

To gain further insight into the properties of graphene modified upon ultrahigh pressure, samples were taken to the Scanning PhotoElectron Microscope (SPEM) hosted at the ESCAmicroscopy beamline at Elettra, in Trieste. X-ray Photoelectron Spectroscopy (XPS) data comparing pristine and modified graphene regions are currently being analysed by Prof. Enrique García-Michel group. Figure 4.18 shows AFM and the C 1s peak image from the XPS data of a graphene flake with different modified areas. A clear contrast can be observed in the XPS image between pristine and modified areas.

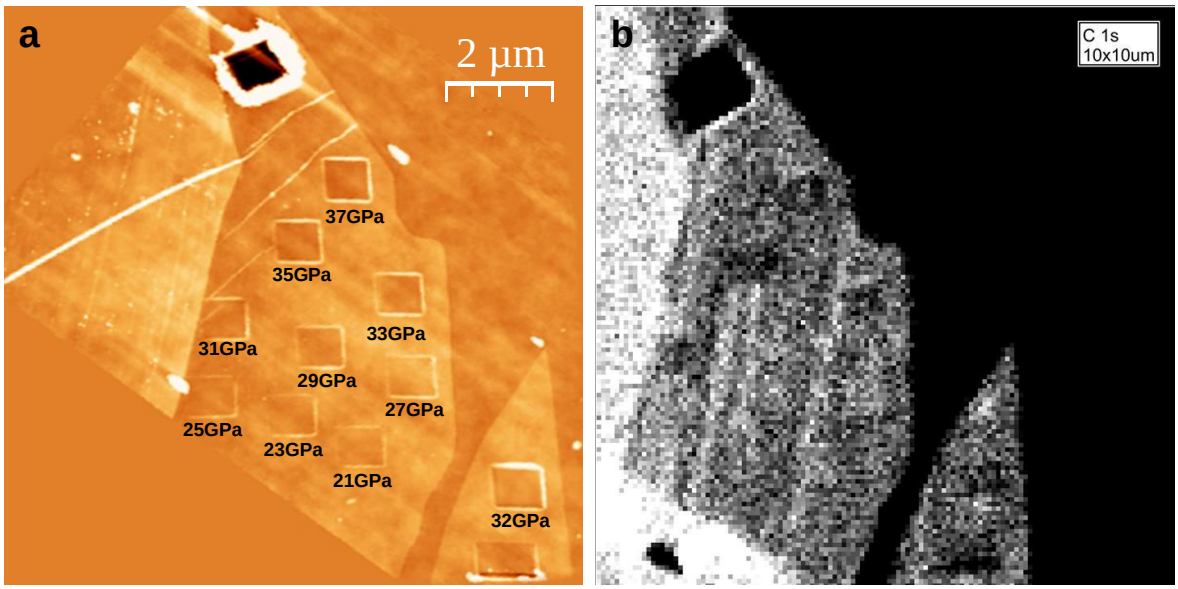

Figure 4.18 a) AFM topographic image showing 800 x 800 nm^2 areas modified under different pressures. Total Z range = 14 nm. b) C 1s peak image of the same area as in a) from XPS data.

A preliminary analysis of the C 1s peak variation upon ultrahigh pressure is shown in figure 4.19.

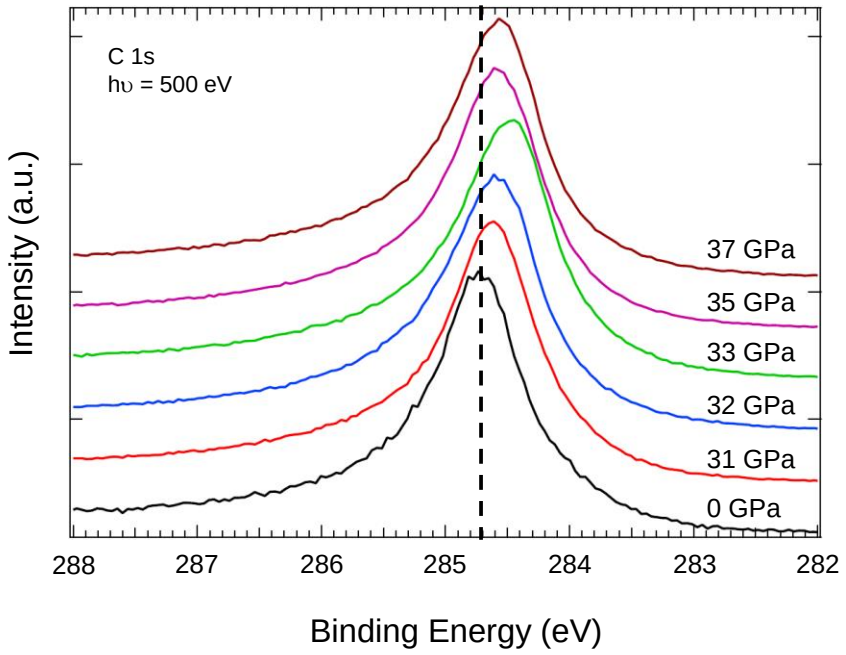

Figure 4.19 Representative C 1s peaks as a function of the applied pressure.

The position and shape of the pristine graphene (0 GPa) peak confirm the good quality of the graphene under study [73-75]. Albeit further analysis has to be performed, these preliminary results show a rigid displacement of the C 1s peak to lower binding energies, ranging from ~ 50 to 350 meV. This effect points to the Fermi level shifting towards the valence band due to a p doping effect, in good agreement with previous Raman and KPM results.

Graphene flakes with areas modified upon ultrahigh pressure were grounded to minimize beam charge effects. However, some charge effects and damage produced by the beam makes not straightforward the correlation between pressure and binding energy displacement. Nevertheless, it is observed a very robust rigid displacement of the C 1s peak always to lower binding energies in the different analyzed samples, confirming the p-doped effect. Within this preliminary analysis, no visible peak shape changes were observed, pointing to a very low amount of chemical bonds between the graphene modified areas and the substrate, in good agreement with the absence of D peak in the Raman spectra.

To understand the mechanisms that keep graphene modified areas strongly coupled to the SiO_2 substrate, Prof. Fernando Martín group is currently carrying out the theoretical interpretation of the experiments using state-of-the-art Density Functional Theory (DFT).

Albeit calculations are still running and no final results have been achieved, preliminary simulations mimicking the most probable SiO_2 configurations point that a small amount of chemical bonds between graphene and SiO_2, an amount much lower than 1%, is needed for the irreversible behavior observed in the modified areas. Simulations already performed suggest that if there is not any bond formation, graphene would not stay so close to the substrate.

Some direct applications can be inferred from the studies carried out so far. First is the possibility of local tuning the doping of graphene. Second, as a direct consequence of this ultrahigh pressure doping, is the creation of low contact resistance areas for the later fabrication of metal electrodes with improved performance in graphene devices [76-79]. As it is known from electrostatically graphene gating in a transistor configuration, when graphene is doped the drain current increases with increasing doping [68]. In the case here presented, the improvement of the conductivity upon ultrahigh pressure doping was assessed by using C-AFM. Same tips as for KPM measurements were employed (ElectriMulti75-G probes). Current maps were obtained by scanning modified areas in Contact mode with a Normal force of 150 nN and a fixed Bias voltage of 0.6 V. Figure 4.20 shows topography and the current map of a modified area under a 35 GPa pressure.

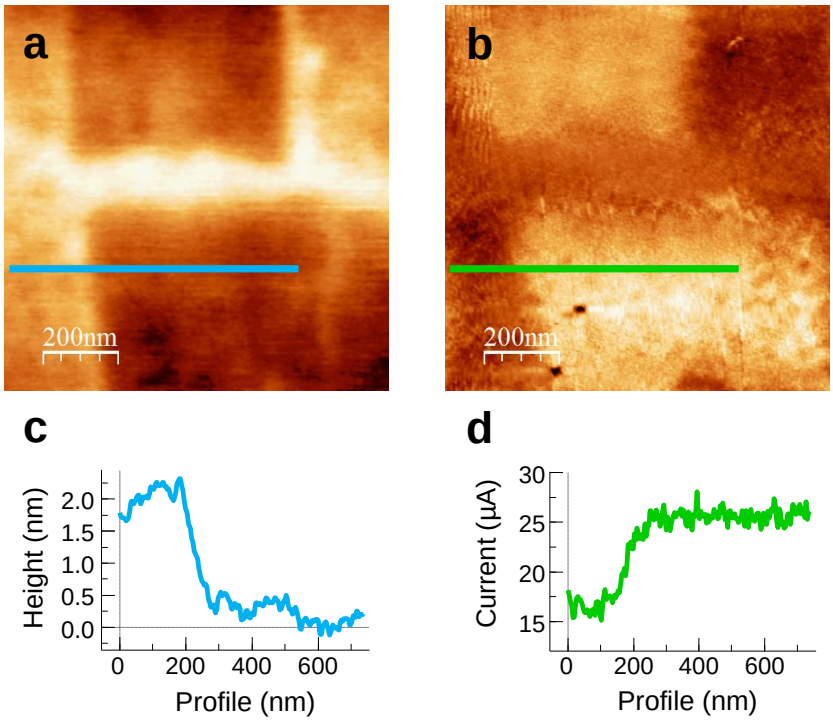

Figure 4.20 C-AFM on a 35 GPa modified region. a) Topographic image. b) Current map at a fixed Bias voltage of 0.6 V. c) and d) Profiles along the lines in a) and b) respectively.

Figure 4.20 shows a clear increase of the current measured in the modified regions, which can be attributed to a decrease of the contact resistance within these areas. From the current variation in figure 4.20d, a ~ 35% improvement for the resistance is found. Since when measuring with C-AFM there was an extra contact resistance as a consequence of the small contact area between the AFM tip and the sample, the obtained improvement can be considered as a lower bound.

Apart from the "electronic", other "mechanical" applications of the ultrahigh pressure modifications were explored. First, the suitability of graphene as a protective coating, as it was shown when comparing modifications on graphene and on the SiO_2/Si substrate. Second, the possibility of improving graphene for membrane applications. Graphene is proposed as an excellent starting point for developing size-selective membranes [80] (and references therein) by introducing pores that can allow molecules to pass through. Microchambers consisting on graphene drumheads are a very good option to study graphene membranes [50, 80-82]. Figure 4.21 shows schematics of these microchambers at different configurations in a pressure chamber.

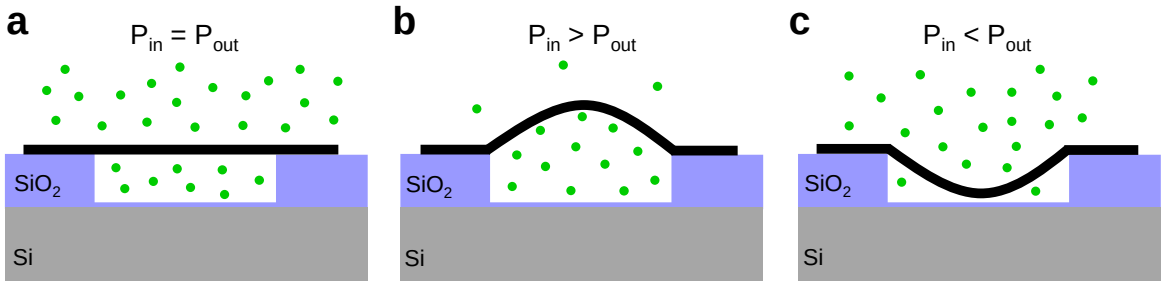

Figure 4.21 Schematics of graphene drumheads in a pressure chamber. a) $P_{in} = P_{out}$. The graphene layer is free standing. b) $P_{in} > P_{out}$. The graphene layer bulges upwards. c) $P_{in} < P_{out}$. The graphene layer deflects downwards.

Samples were fabricated by transferring micromechanically exfoliated graphene sheets over predefined microcavities. At this stage, situation was as shown in figure 4.21a. Samples were then placed in a pressure chamber and pressure differences across the graphene membrane were created either by vacuum pumping the chamber (figure 4.21b) or by using a gas to create an overpressure (figure 4.21c). In both cases shown in figures 4.21b and c, it is reported that over time the internal and external pressures equilibrate due to gas leak from/to the microchambers [81, 83]. Two leak mechanisms are proposed, either through the SiO_2 walls of the microchamber or through the graphene-SiO_2 sealed interface [81]. Estimations of gas diffusion rates lead to think that leak takes place through the slow diffusion of gas through the SiO_2 substrate [81]. To shed some light on this issue, in this work microchambers were sealed using ultrahigh pressure modifications. Leak rates before

and after sealing were measured. To this end, first vacuum up to a pressure of 10^{-6} hPa was performed (the drumhead presented an aspect as in figure 4.21b) and it was left until pressure inside was equilibrated at that value. Then, an overpressure of P_{out} = 3 atm of N_2 gas was set in the chamber; in this way a total pressure difference across the membrane of about 4 atm was obtained (at that point the drumhead presented an aspect as in figure 4.21c) [84]. Then, AFM was used to monitor the change in the membrane depth as a function of time. Measurements inside the pressure chamber were carried out in collaboration with Dr. Guillermo López-Polín. Figure 4.22 shows a microchamber before and after sealing upon AFM ultrahigh pressure.

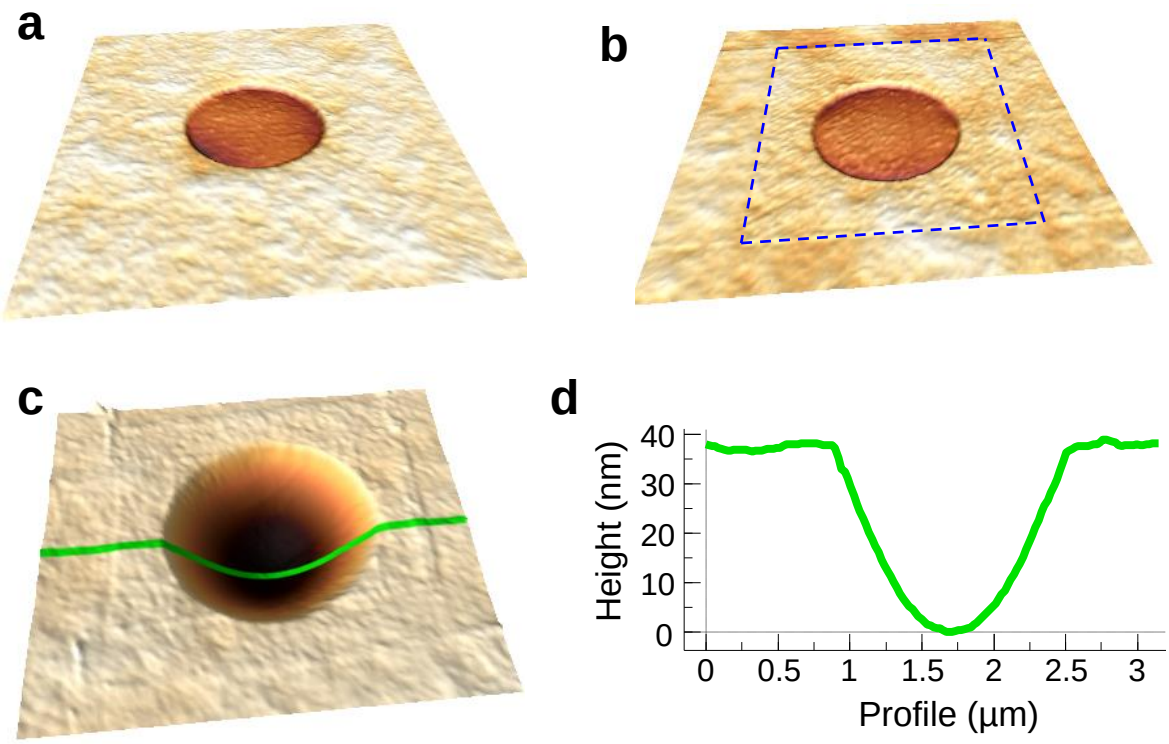

Figure 4.22 a) 3D rendered AFM topographic images of a conventional microchamber. b) Same microchamber as in a) after sealing upon local ultrahigh pressure. Dashed lines were placed along the sealing edges to guide the eye. Total Z range in a) and b) is 6.5 nm. c) Microchamber under a pressure of 4 atm, the regions modified by the diamond tip can be readily seen. d) Height profile along the line in c).

Comparison of the change in the membrane depth as a function of time was carried out for the same microchamber before and after sealing. Figure 4.23 shows the depth variation over time for both cases.

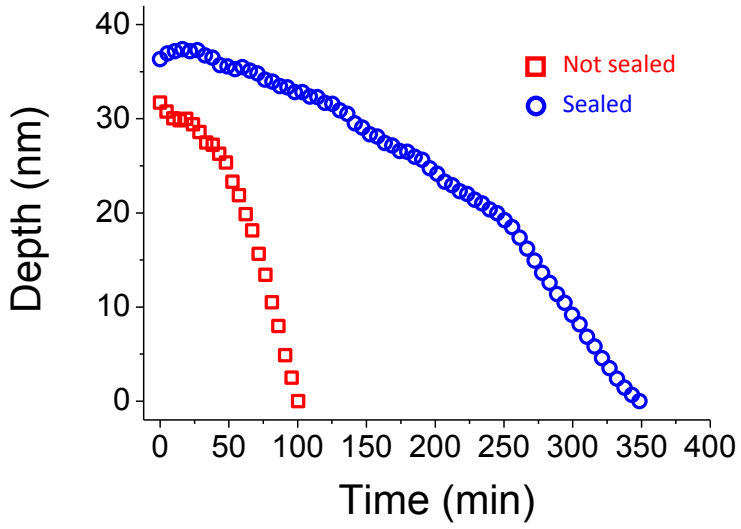

Figure 4.23 Graphene drumhead depth variation before (not sealed) and after AFM ultrahigh pressure (sealed).

From figure 4.23 it can be seen that the total time needed to equilibrate pressures inside and outside the microchamber increased in a factor of ~ 3.5 once it was sealed upon AFM ultrahigh pressure. This result suggests that the leak was mainly through the graphene-SiO_2 interface, in contrast with reported results where leak through the porous of the glass walls is proposed [80-82], and demonstrates AFM ultrahigh pressure modifications as an excellent and easy procedure to improve the performance of graphene for membrane applications.

In summary, the ability of the AFM to apply ultrahigh pressures has been employed to locally tune the electronic properties of graphene. Ultrahigh pressure with diamond tips have allowed a very precise coupling of graphene to the underlying substrate, resulting in a very controlled way of inducing p doping, as demonstrated by KPM, Raman spectroscopy and XPS. From this doping, C-AFM has demonstrated the suitability of this technique to locally improve the contact resistance when using metal electrodes, a paramount issue in the field of graphene electronics. Preliminary DFT calculations suggest that a small amount of bonds between graphene and substrate are taking place. In terms of mechanical properties, these experiments have shown the suitability of graphene as a protective coating and the possibility of improving its performance in membrane applications by providing a method to better seal graphene micro-cavities.

4.4 Isolation of highly stable antimonene

4.4.1 Introduction

The extraordinary success of graphene and its tremendous potential applications [85] paved the way for the rising of a cascade of other two dimensional materials [86, 87] presenting a variety of new properties. In the context of their electronic properties, graphene is a semimetal with zero-gap, which limits its use in the electronics technology. Transition metal dichalcogenides, which are compounds of the type MX_2, with M a transition metal atom (Mo, W, etc.) and X a chalcogen atom (S, Se, or Te), as for example MoS_2, $MoSe_2$ or $NbSe_2$, present in their 2D forms band gaps in the range of 1.5 - 2.5 eV [88] (depending on the thickness, strain level and chemical composition). These values make them inappropriate for some optoelectronics applications where band gaps in the 0.1 – 1.5 eV range are commonly preferred [89]. Black phosphorous (BP) [90] a layered allotrope of phosphorous, in its 2D form (also known as phosphorene) presents an energy gap in this range and hence it is now being intensely studied to better understand its electronic properties in the few-layer conformation.

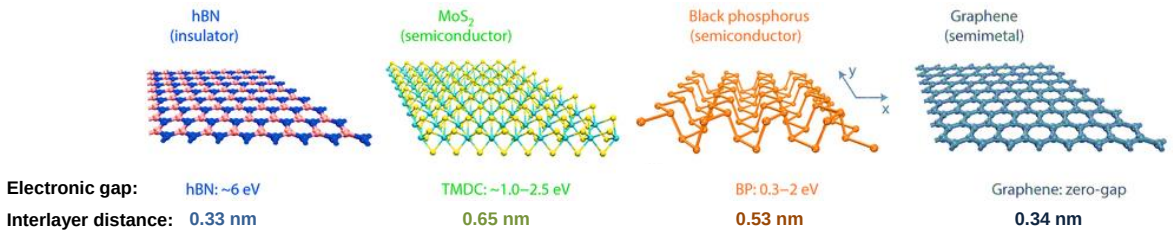

Figure 4.24 Atomic lattices of different 2D materials. Adapted from reference [91].

However, BP shows a relatively large reactivity in ambient conditions. Exfoliated flakes of BP are highly hygroscopic and tend to uptake moisture from air. The long term contact with water condensed on the surface degrades BP [92, 93], as it can be seen from measurements of flake topography over several hours, electrical performance of transistors or sheet resistance as a function of time.

Phosphorus belongs to the nitrogen group (group 15 in the periodic table of elements). In this same group, it is also found antimony, a silvery lustrous, non-hygroscopic, gray semimetal with a layered structure similar to that of BP. Theoretical calculations predict different interesting properties for this material: an electronic structure with a band gap in the ultrafast optoelectronics applications range when reaching the single-layer regime [94-96], high carrier mobilities, [96-98], topological behavior [99, 100] and optical properties [101, 102]. In this section, antimony down to the single-layer regime, known as

antimonene (albeit the name antimonene is not completely correct as there are no double bonds in its structure, it is commonly accepted in the 2D community) is presented for the first time through mechanical exfoliation, and experimental evidence of its stability is given. The experiments carried out here demonstrate that single-/few-layer antimony flakes are highly stable in ambient conditions showing mechanical stability upon origami nanomanipulation and no degradation over month periods. Density Functional Theory (DFT) simulations mimicking ambient conditions confirm the geometrical experimental findings and predict a band gap of 1.2-1.3 eV, within the range of optoelectronics applications. Optical microscopy is used to study the optical properties of few-layer antimonene flakes and quantitatively estimate their thickness in a fast and nondestructive way. Optical identification of antimonene will be useful for future nanodevices fabrication. Preliminary results on the electrical properties of few-layer antimonene are also presented, pointing to a conductivity governed by the presence of surface states, in good agreement with theoretical calculations that are currently being carried out.

The core of the work presented in this section is published in references **Ares, P.**; Aguilar-Galindo, F.; Rodríguez-San-Miguel, D.; Aldave, D. A.; Díaz-Tendero, S.; Alcamí, M.; Martín, F.; Gómez-Herrero, J.; Zamora, F. Mechanical Isolation of Highly Stable Antimonene under Ambient Conditions. *Adv. Mater.* 2016, *28*, 6332-6336 and **Ares, P.**; Zamora, F.; Gomez-Herrero, J. Optical identification of few-layer antimonene crystals. *ACS Photonics*. 2017. DOI: 10.1021/acsphotonics.6b00941 (see also List of Publications). The results presented here have been performed in collaboration with Dr. Félix Zamora, Prof. Manuel Alcamí, Prof. Fernando Martín and Dr. Juan José Palacios groups. In particular, Diego Aldave has exfoliated antimony for some samples. David Rodríguez-San-Miguel has carried out part of the characterization (electron microscopy and Raman spectroscopy). Prof. Manuel Alcamí and Prof. Fernando Martín groups have carried out DFT calculations mimicking ambient conditions. Dr. Juan José Palacios group is currently carrying out theoretical calculations on the electrical properties of few-layer antimonene. Dr. Gabino Rubio-Bollinger, Dr. Jorge Quereda and Dr. Andrés Castellanos-Gomez are acknowledged for their technical assistance in the optical identification part.

4.4.2 Results and discussion

Figure 4.25 shows relevant views and parameters of the antimony atomic lattices.

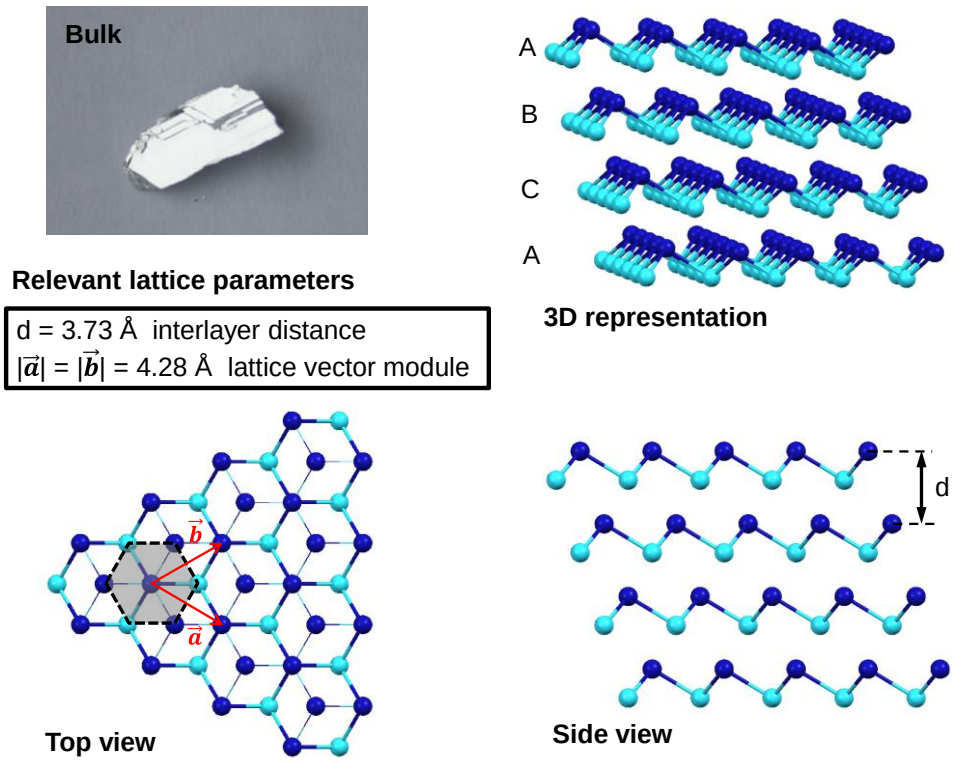

Figure 4.25 Relevant views and parameters of antimony atomic lattice.

Single- and few-layer flakes were obtained by mechanical exfoliation of a macroscopic freshly cleaved crystal of antimony. Bulk, commercially available antimony material (99.9999%, Smart Elements [103]) was used. First, submillimeter flakes were obtained by repetitive pealing using adhesive tape a freshly cleaved thin piece of bulk antimony. Albeit a initial strategy consisting of an all dry viscoelastic stamping transfer procedure [104] (using the setup showed in Chapter 3 for the EGF soft-electrode transfer) was employed, both this and the classic approaches (direct transfer from the adhesive tape) enabled to obtain thin antimony flakes with large areas. Figure 4.26 shows the mechanical exfoliation procedure together with optical and AFM characterization.

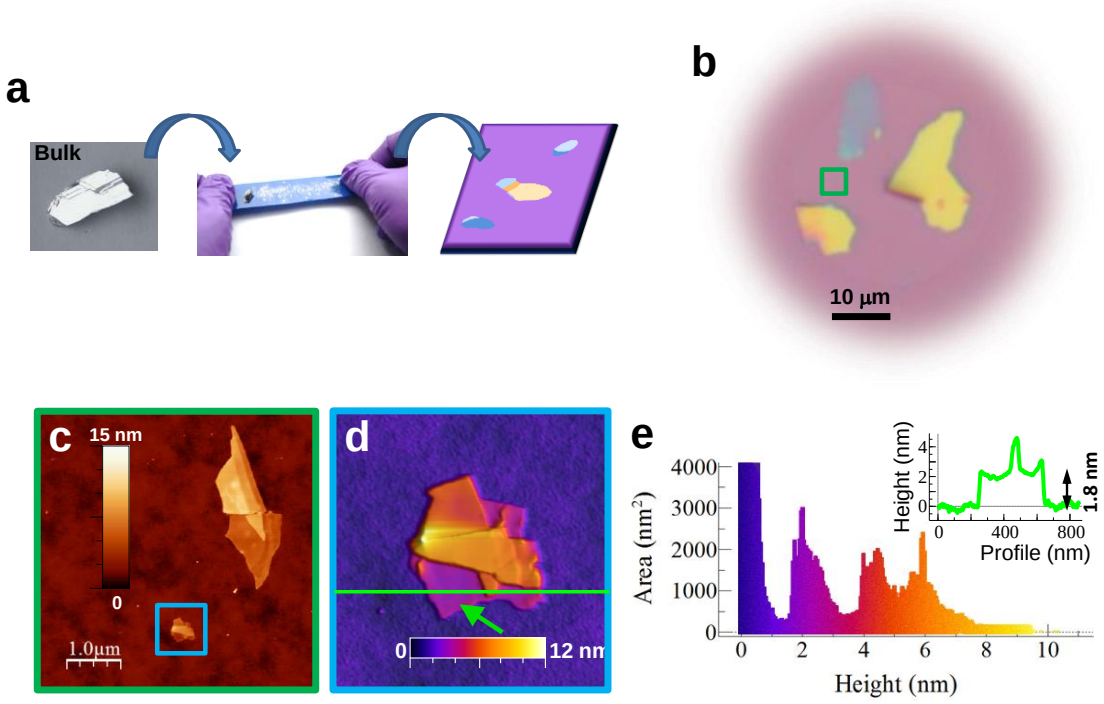

Figure 4.26 Antimonene flakes on SiO_2 substrates. a) Left, millimeter size crystals of antimony. Middle, adhesive tape with submillimeter crystals of antimony. Right, schematic of a SiO_2 substrate with single- to few-layer antimonene flakes. b) Optical microscopy image where up to 3 large flakes of antimony can be seen. Different colors reflect different thicknesses. c) AFM topographic image showing 2 flakes of antimonene located inside the green square in b). d) AFM topographic image of the ~ 0.2 μm^2 antimonene flake inside the blue square in c), showing terraces of different heights. The terrace with minimum thickness is marked with a green arrow. e) Height histogram of the image in d) where the different thicknesses of the terraces can be readily seen. For the sake of clarity, the substrate peak was cut to 4000 nm^2. The inset is a profile along the green horizontal line in d). The minimum step height is ~ 1.8 nm compatible with 2-3 layers of antimonene.

As seen in figure 4.26b, optical microscopy allowed easily finding of large flakes presenting different thicknesses. AFM revealed smaller crystals with thicknesses in the nanometer range (figures 4.26c-e). Figure 4.26d is an AFM topographic image showing a ~ 0.2 μm^2 flake with different terraces. According to the height histogram and profile (figure 4.26e) the minimum layer thickness is ~ 1.8 nm, compatible with a bilayer-trilayer of antimony. All the topographical AFM images in this section showing accurate height measurements were acquired in Contact mode to avoid possible artifacts in the flake thickness measurements [105]. OMCL-RC800PSA Olympus cantilevers [106] with a nominal spring constant of 0.39 N m^{-1} and tip radius of 15 nm were employed. Low forces

of the order of 1 nN were used for imaging to ensure that the flakes would not be deformed by the tip.

Raman spectroscopy was employed with the aim of identifying the number of layers of the flakes [59], as it is done with graphene and other 2D materials and explained in the previous section of this chapter. Figure 4.27 shows Raman measurements performed on flakes of different thicknesses at ambient conditions. The laser wavelength and power were 532 nm and 1 mW respectively. Importantly, the antimony flakes did not show any measurable Raman signal for thicknesses below ~ 100 nm.

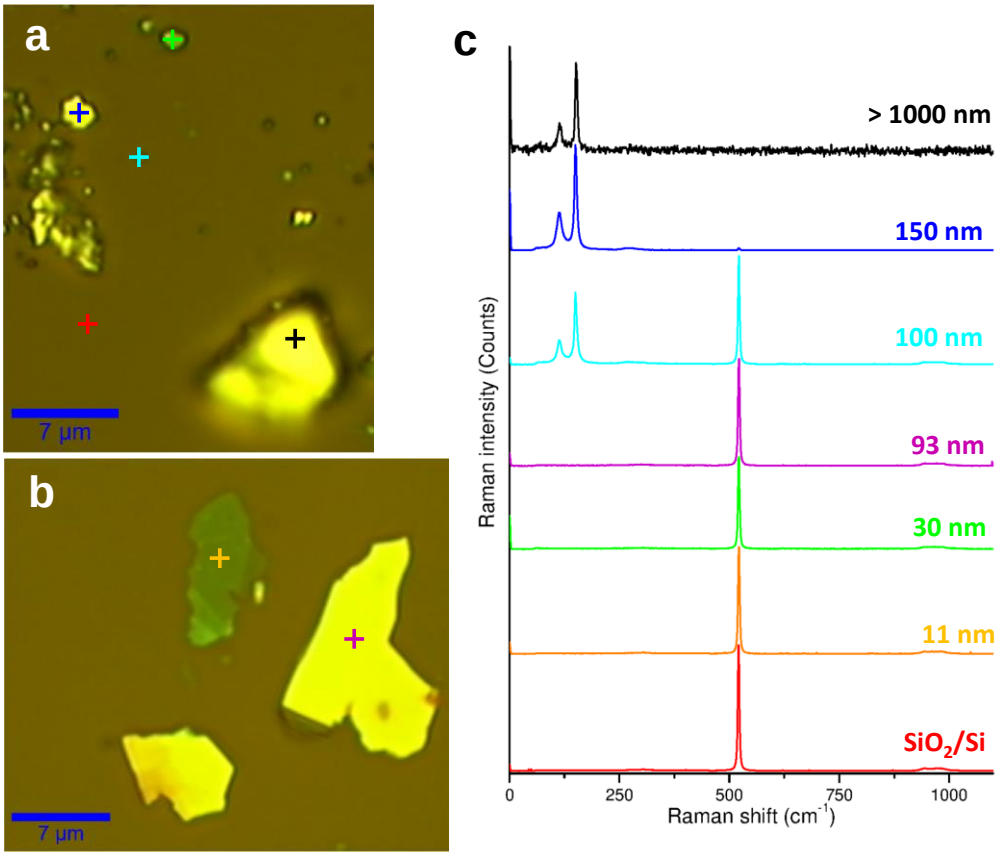

Figure 4.27 a, b) Optical microscopy images of antimony flakes with a wide range of heights. c) Raman spectra from the points indicated by crosses in a) and b). The red spectrum corresponds to the substrate; the remaining spectra correspond to antimony flakes of different thicknesses (measured by AFM). Black, h > 1000 nm (bulk antimony); dark blue, h = 150 nm; cyan, h = 100 nm; pink, h = 93 nm; green, h = 30 nm; orange, h = 11 nm; red: SiO_2/Si substrate.

Figure 4.27 depicts a Raman spectroscopy study of antimony flakes of different heights on a SiO_2/Si substrate. Figures 4.27a and b show optical microscopy images where a variety of flakes of different heights (measured by AFM) and lateral dimensions can be observed.

Figure 4.27c shows Raman spectra taken on different spots marked with crosses in a, b. It can be observed that for bulk antimony (height > 1000 nm) the spectrum matches previous results for bulk antimony [107] with almost no signal coming from the substrate (~ 520 cm^{-1}). As the thickness of the flakes decreases (h = 100 nm) the signal from the substrate is becoming dominant and for lower heights the antimony signal is lost. This behavior is related to the thickness of the flakes, not with their lateral dimensions: the h = 100 nm flake is clearly much smaller than the h = 11 and 30 nm ones, but whereas the h = 100 nm spectrum shows the characteristic peaks corresponding to antimony, the h = 11 and 30 nm spectra do not. The observed behavior is present as well in other layered materials such as mica [108], where the Raman signal is lost for thicknesses below ~ 60 nm, and has no implications upon stability. A more detailed study of the Raman characterization of antimonene can be found in reference [109].

Figure 4.28 presents a detailed study of the structure of thin antimonene flakes.

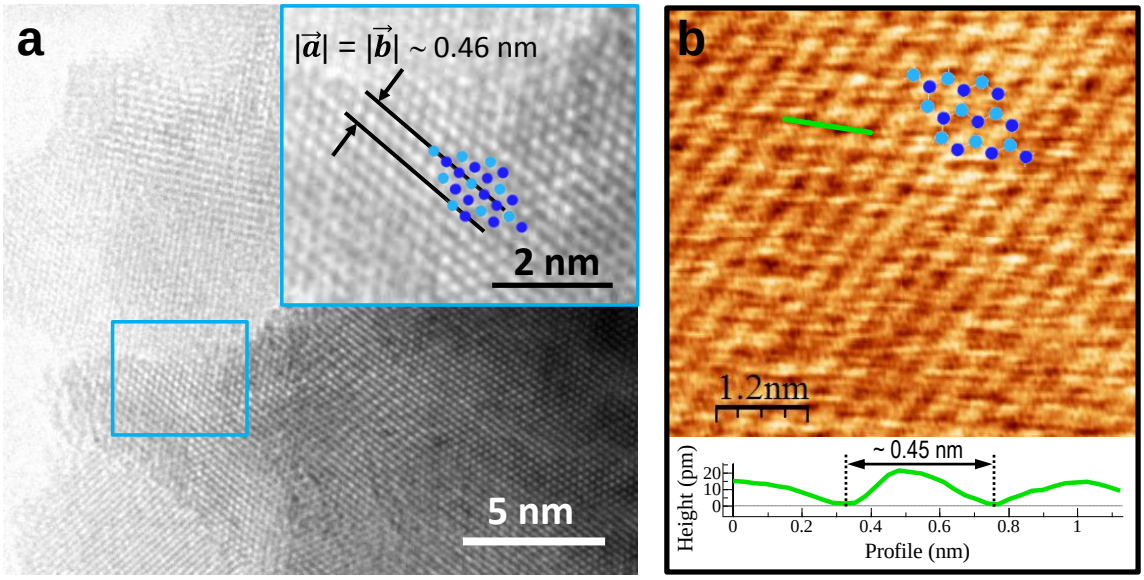

Figure 4.28 a) High resolution TEM image of a few-layer antimonene flake. The inset is a digital magnification of the area inside the blue rectangle. Bilayer antimonene structure was superimposed showing a good agreement with the hexagonal lattice. Lattice vector module is in good agreement with the crystallographic structure. b) High resolution AFM topographic image acquired on the bilayer terrace marked with a green arrow in figure 4.20d, showing atomic periodicity. The superimposed single-layer antimonene atomic lattice is compatible with the observed periodicity. Profile on the bottom was taken along the green line in the image. As in TEM, the measured distance for the lattice vector module is in good agreement with the crystallographic structure.

Figure 4.28a shows a high resolution Transmission Electron Microscopy (TEM) image of a few-layer antimonene flake. Images were obtained in a JEOL JEM 2100 FX TEM system with an accelerating voltage of 200 kV. The microscope had a multiscan charge-coupled device (CCD) camera ORIUS SC1000 and an OXFORD INCA X-Ray Energy Dispersive Spectroscopy (XEDS) microanalysis system. The image reveals very thin well-resolved terraces. The atomic structure from the different layers shows a clear hexagonal periodicity that corresponds to that expected for the β phase of few-layer antimonene. Figure 4.28b displays a high-resolution AFM topographic image taken in the lowest terrace of the isolated flake shown in figure 4.26d. The image shows an atomic periodicity again compatible with that expected for antimony. This image was acquired after exposing the flake to atmospheric conditions during more than two months.

Figure 4.29 depicts XEDS microanalysis from the TEM system.

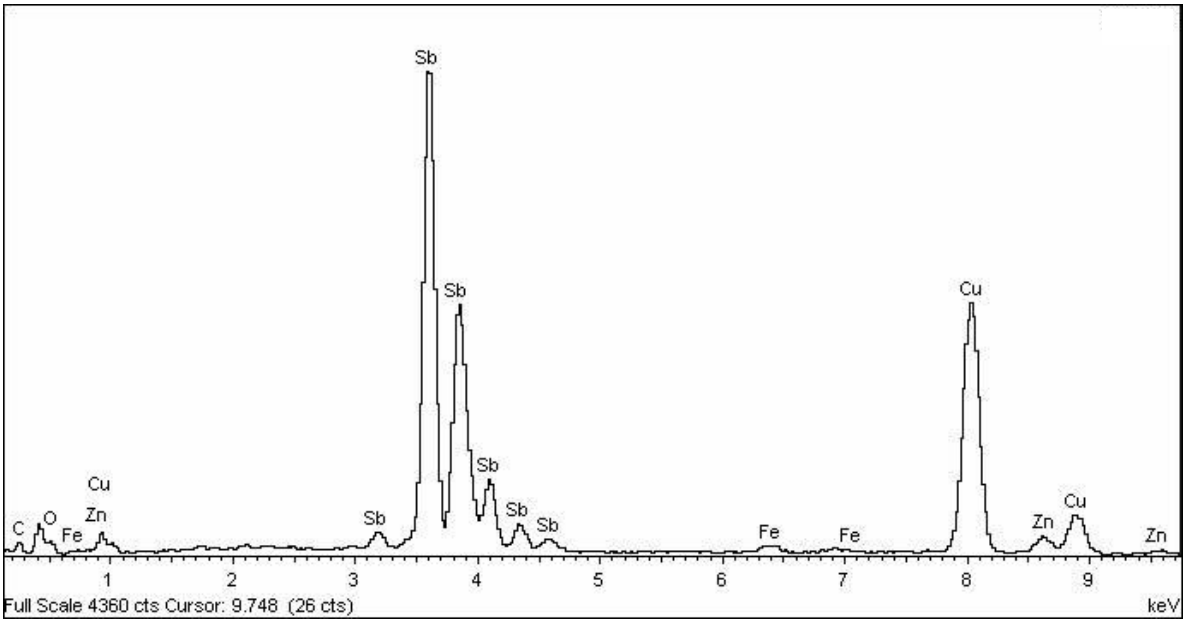

Figure 4.29 XEDS microanalysis.

XEDS microanalysis corroborates the composition of the isolated flakes. It can be observed that they are composed mainly of Sb. Copper peak on the right and its surrounding peaks correspond to the supporting grating that was made of copper. Interestingly, the oxygen peak is very low, confirming the low degree of oxidation and hence chemical stability.

DFT calculations were performed by Prof. Manuel Alcamí and Prof. Fernando Martín groups, considering one and two monolayers (ML) of antimony. As in the case of the MMX chains, a detailed description of the calculations is out of scope of this work, only the basic concepts to follow them are provided. The size of the supercell used is shown in

figure 4.30a. In order to mimic the experimental conditions, simulations were carried out at room temperature and also by including different solvent effects (water and oxygen environments). Perdew-Burke-Ernzerhof functional (PBE) [110, 111] was used for the geometry optimization and for the molecular dynamics simulations, and the Heyd-Scuseria-Ernzerhof (HSE06) functional [112] for computing the band gap. These PBE and HSE functionals were employed because they are proved to accurately predict geometries and electronic properties respectively. As a reference, simulations were first performed at 0 K in vacuum. Figure 4.30a shows the geometry obtained in the case of one and two monolayers of antimony. The simulations predicted a hexagonal order (top view) with different heights for the atoms (lateral views), in good agreement with TEM and AFM measurements (figure 4.28).

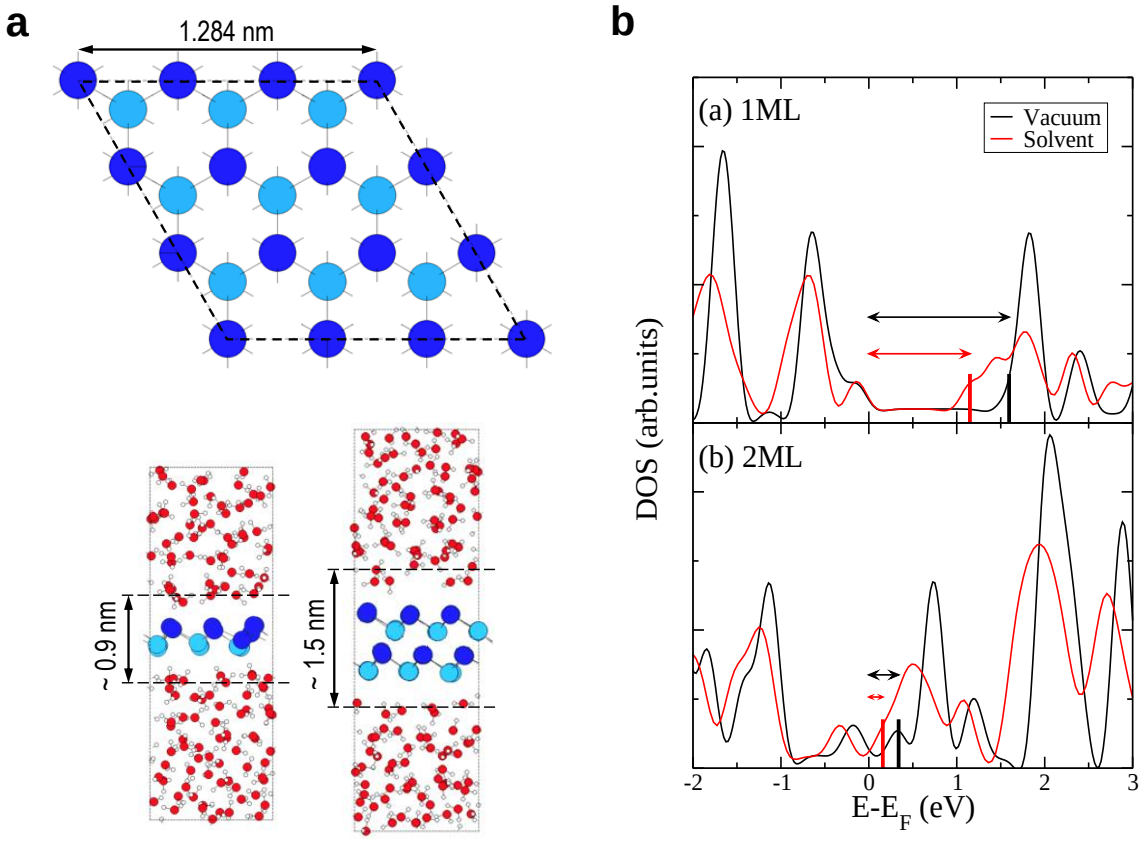

Figure 4.30 DFT simulations a) Top: top view atomic lattice of antimonene. Bottom: side view of mono- and bilayer antimonene lattices including water molecules as used for DFT calculations. b) Calculated densities of states (DOS) for 1ML and 2ML antimonene in vacuum at T = 0 K (black curves) and in the presence of a water solvent at T = 298 K (red curves) as a function of electron energy (referred to the Fermi energy, E_F).

Figure 4.30b depicts the densities of states (DOS) for the 1ML and 2ML cases in vacuum at 0 K and in water at room temperature. In simulations performed at room temperature, a slight deformation of the crystal structure (~ 5 % in Sb-Sb distances) in comparison with the case in vacuum is observed. The distance predicted between the centers of the second closest upper and lower water molecules is ~ 0.9 and ~ 1.5 nm for the monolayer and bilayer cases, respectively. Concerning the electronic structure, the calculated gap in vacuum for 1ML is 1.6 eV, which is in good agreement with previous calculations [94]. It is also observed that the band gap closes when going from 1 to 2 ML [94-96]. 3 layers up the band gap is closed and antimonene shows metallic character. Table 4.2 presents a summary of the calculated band gap values under different configurations.

Table 4.2. Band gap obtained within the HSE method using different geometries and situations.

1ML	Band gap (eV)
Vacuum – 0 K	1.59
Vacuum – 298 K	1.28
Water – 298 K	1.22
Oxygen – 298 K	1.29

As it can be seen, the effect of increasing temperature from 0 to 298 K is to reduce the band gap by approximately 0.3 eV. The effect of adding liquid water at room temperature is to reduce it a bit more (approximately 0.07 eV). Addition of oxygen did not have any observable effect. Consequently, the most likely value of the band gap at ambient conditions lies within the interval 1.2-1.3 eV.

At some points, the AFM allowed locating small flakes presenting terraces with heights compatible with single-layer antimonene. Figure 4.31 depicts a detailed characterization of a single antimonene layer. Figure 4.31a shows a few-layer antimonene flake with a well-defined monolayer terrace located at its bottom. As for graphene, rippling is caused by conformation of antimonene to the underlying SiO_2, and is not intrinsic [113]. The measured height of this terrace is ~ 0.9 nm (figure 4.31a,b) compatible with the presence of water layers as shown in figure 4.30a. It is widely assumed that under ambient conditions there exists an ever-present layer of adsorbed water (with a thickness of ~ 0.6 nm) which remains captured between the flakes and SiO_2 [64, 114].

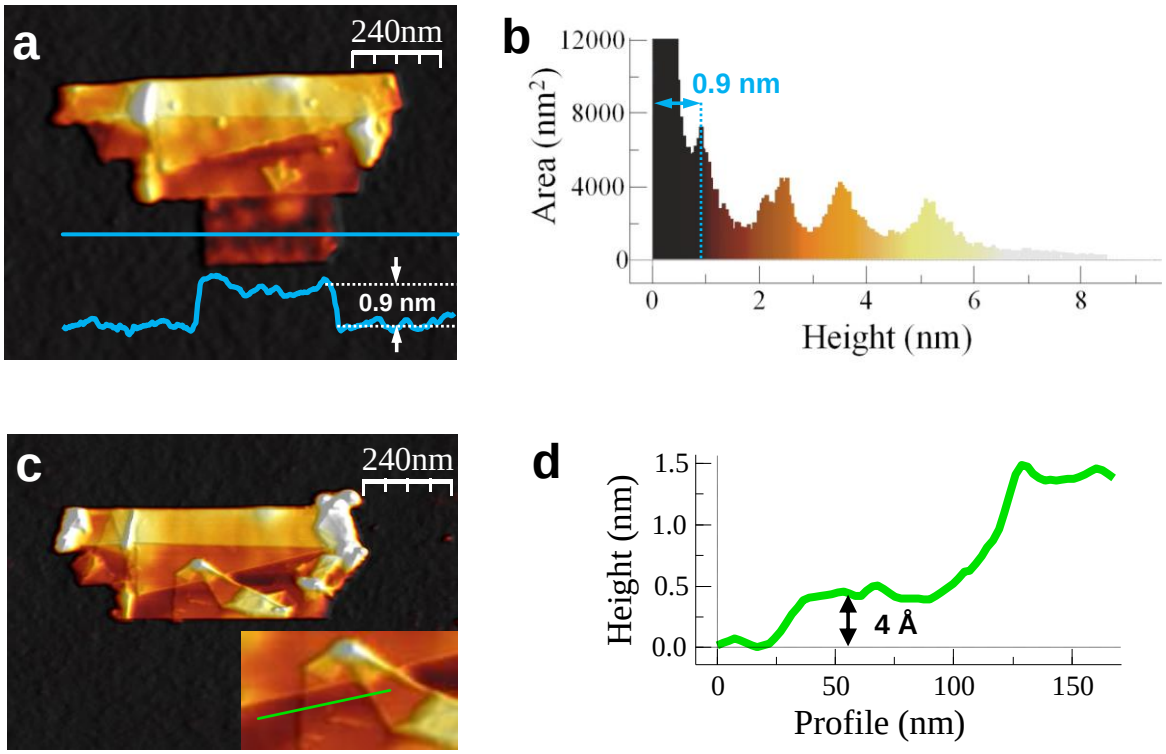

Figure 4.31 AFM topographic images of an antimonene flake with a monolayer terrace at the bottom. a) AFM topographic image showing a ~ 0.2 μm^2 antimonene flake with terraces of different heights. The profile was taken along the blue horizontal line in the image. b) Height histogram of the image in a) where the different thicknesses of the terraces can be readily seen. For the sake of clarity, the substrate peak was cut to 12000 nm^2. The minimum step height is ~ 0.9 nm compatible with a single layer of antimony adsorbed on the presence of water layers. c) Same flake as in a) but after a nanomanipulation process. The lower terrace of the flake was folded upwards with the AFM tip resulting in an origami structure with different folds. The inset corresponds to the area of the origami where the lowest step height is found. d) Profile along the green line in the inset in c). The lowest step height is ~ 4 Å corresponding to single-layer antimonene.

Since Raman spectroscopy failed to provide information on ultrathin antimonene sheets, to determine if this terrace was a monolayer nanomanipulation with AFM was performed, folding the layer into an origami structure (figure 4.31c). According to Geim and Novoselov [64] the identification of single graphene sheets can be unambiguously carried out by measuring the step height of single folds. In this case, the lowest step height is ~ 4 Å (inset in figure 4.31c and profile in figure 4.31d) that corresponds to a single layer of antimonene. Moreover, this origami nanomanipulation was performed several days after flake deposition on the substrate. The facts that the sheet folded without breaking and the

angles observed in the origami structure (mainly multiples of 60º, expected from a hexagonal atomic structure) show the mechanical stability of single antimonene sheets.

Electrical characterization on few-layer antimonene flakes using Conductive-AFM was also performed, confirming again ambient stability. This characterization is shown in some more detail at the end of this section.

To further confirm the effects of water in the flakes, AFM topographic images of the same flakes were acquired under different conditions. Figure 4.32 presents these results.

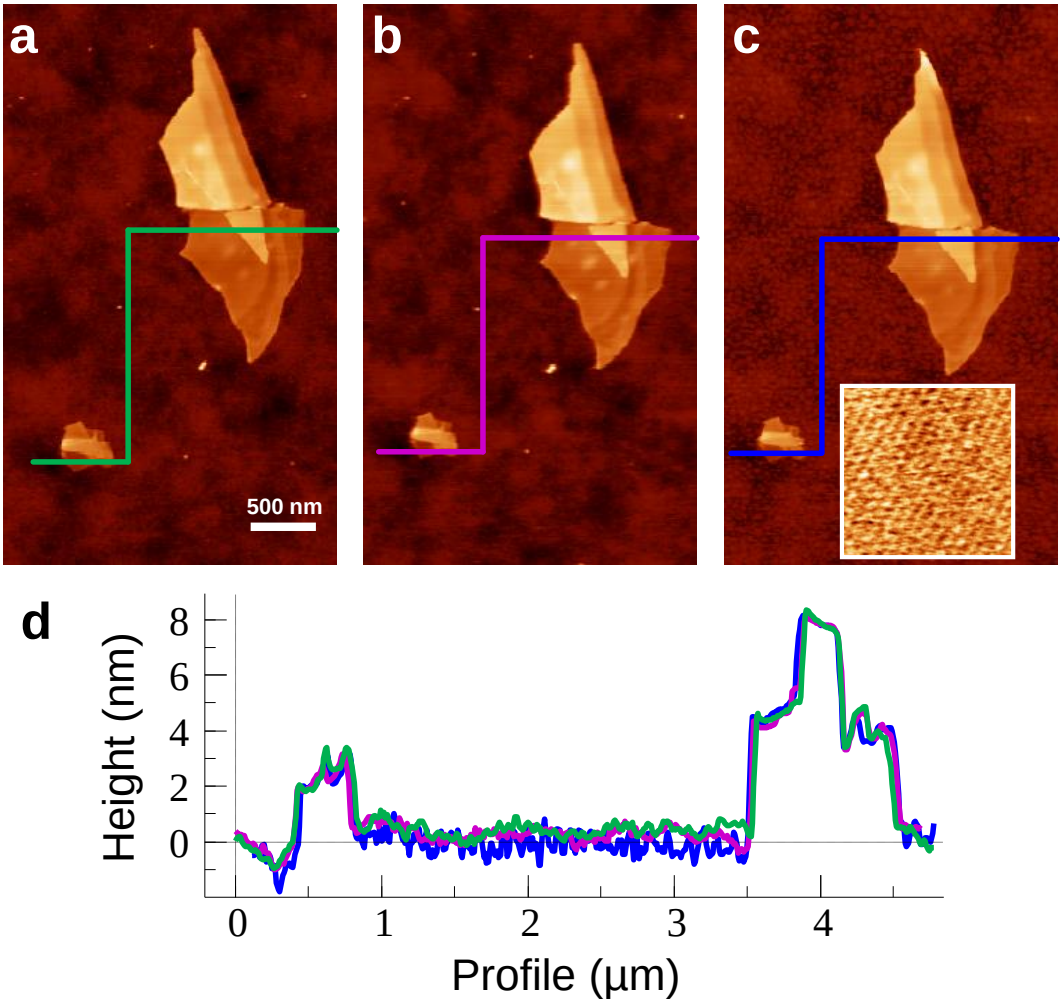

Figure 4.32 AFM topography images of antimonene flakes showing environmental stability of antimonene. a) Image taken immediately after exfoliation. b) Same as in a) but two months later. c) Image taken immediately after b) but with the sample immersed in water. The inset shows atomic periodicity compatible with antimonene atomic lattice. The selected region was the same as in figure 4.26b. d) Profiles taken along the lines in a-c.

Figure 4.32a was obtained immediately after sample preparation. Then the sample was stored under ambient conditions for two months and the image in figure 4.32b was acquired. Figure 4.32c was obtained immediately after figure 4.32b but with the sample immersed in water. The inset in figure 4.32c presents a high-resolution image in the same flake as figure 4.28b but in this case acquired while the sample was still in liquid. The atomic periodicity is again compatible with that of antimony, confirming also the low reactivity of the flakes with water. Figure 4.32d shows the profiles along the lines in a-c. The similarity of the corrugation on the antimonene flakes confirms again the absence of environmental degradation.

Nevertheless, while imaging in water a tendency of the smallest flakes to exfoliate when the AFM tip was scanned in contact with the flakes was observed. This suggested that water exfoliation assisted by ultrasounds could be a feasible way to obtain thin layer flakes of antimony, as we demonstrated in the work presented in reference [109] entitled "Few-Layer Antimonene by Liquid-Phase Exfoliation". A fast and simple method to produce highly stable isopropanol/water (4:1) suspensions of few-layer antimonene by liquid-phase exfoliation of antimony crystals is presented. The process was assisted by sonication and did not require the addition of any surfactant. Few-layer antimony flakes were characterized in a similar way as in the case of micromechanical exfoliation. Figure 4.33 presents an example of the AFM characterization. The overall lateral dimensions of the isolated flakes are greater than 1-3 μm^2, presenting well-defined structures with all heights being multiples of ~ 4 nm. This height can be compatible with the presence of one or two layer heights, since as it is well-known the apparent AFM heights of layers obtained by Liquid-Phase Exfoliation (LPE) can be overestimated because of residual solvent [115, 116], as well as contributions from effects such as capillary and adhesion forces [105].

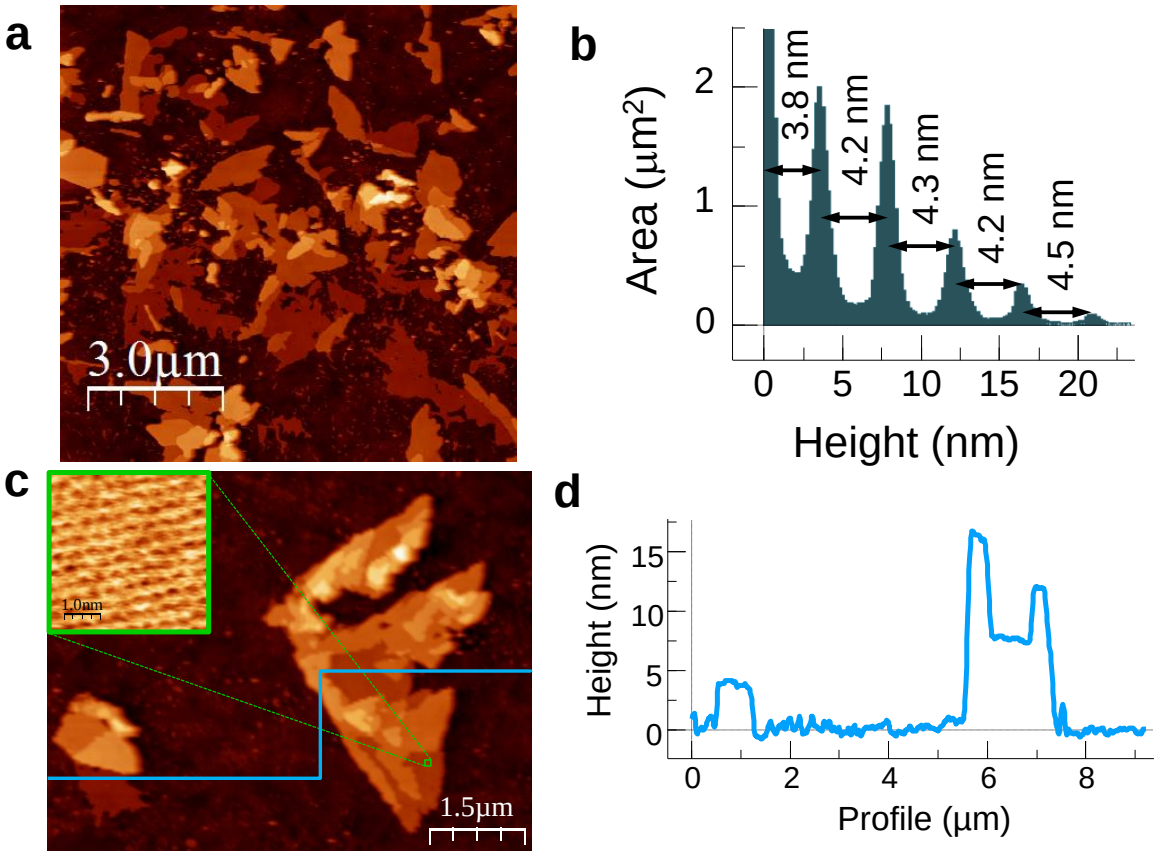

Figure 4.33 AFM characterization of liquid-phase exfoliated (LPE) few-layer antimonene flakes. a) AFM topographic image of LPE few-layer antimonene drop-casted onto SiO_2 showing flakes with micrometer lateral dimensions. b) Height histogram of the image in a) where the different thicknesses of the terraces can be readily seen. For the sake of clarity, the substrate peak was cut to 2.5 μm^2. A constant minimum thickness of about 4 nm can be easily observed. c) AFM topographic image of a different region. The inset shows atomic periodicity in good agreement with the crystallographic structure. d) Profile along the blue line in c) showing the heights of different terraces.

In reference [109] we also showed that the Raman signals were strongly thickness-dependent, which was rationalized by means of DFT calculations, explaining the observed absence of Raman signal for low height flakes.

Since Raman fails to help identification of few-layer antimonene flakes, the optical properties of the antimonene thin flakes were studied, to allow a simple and quite accurate identification of the different thicknesses based on the optical contrast. The optical contrast of micromechanically exfoliated few-layer β antimonene (FL-Sb) flakes was measured using different illumination wavelengths in the visible spectrum, and their thicknesses using AFM. From these measurements and using a simple model based on the Fresnel law,

their refractive index and absorption coefficient in the visible spectrum (wavelengths ranging from 450 to 650 nm) was obtained. Hence, the optical microscopy data can be quantitatively analyzed to determine the thickness of the flakes in a fast and nondestructive way that will be useful for future nanodevice fabrication.

Figure 4.34 shows optical and AFM characterization of FL-Sb flakes of a variety of thicknesses deposited on 300 nm SiO_2/Si substrates.

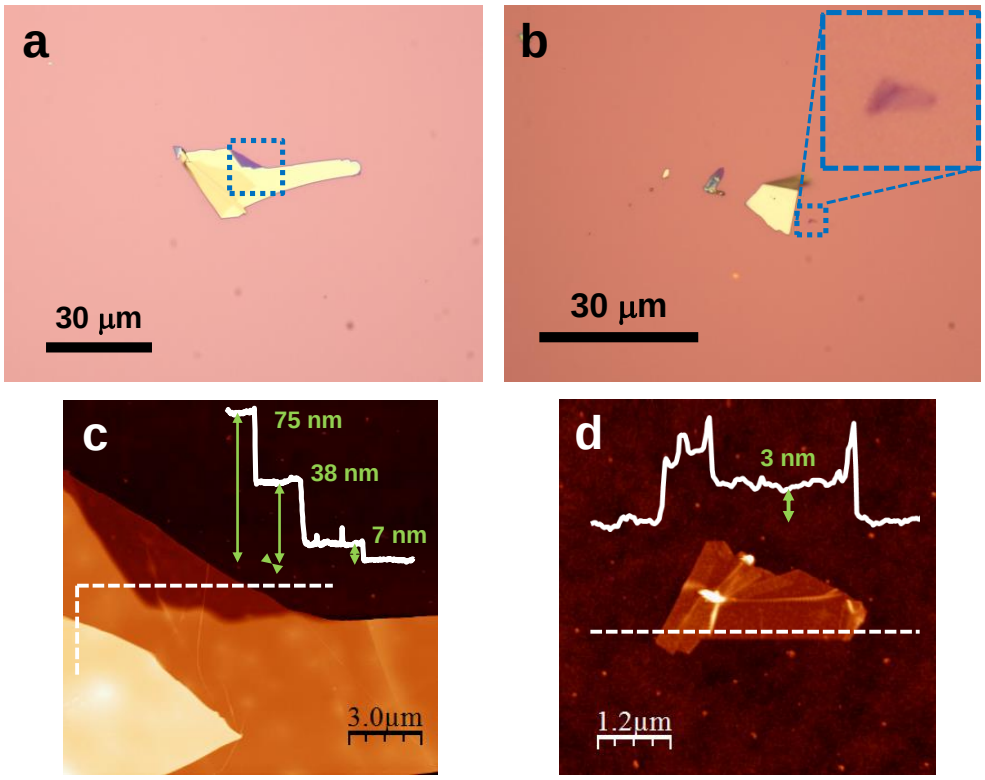

Figure 4.34 Optical and AFM characterization of FL-Sb flakes. a) and b) Optical microscopy images under white illumination of different FL-Sb flakes on a 300 nm SiO_2/Si surface. c) and d) AFM topographic images of the areas inside the dashed squares in a) and b) respectively. Inset profiles were taken along the dashed lines in the images.

It is possible to obtain an initial rough estimation of the thickness of the flakes due to a light interference effect, usually called interference color [117]. AFM allows for a more accurate measurement of the thickness of the flakes but at the price of much longer time for characterization. Hence, the optical method can be used for a fast discrimination of thicknesses that can be later fine-tuned by AFM. Different flakes with heights from tens of nm down to 2-3 nm (corresponding to ~ 4-7 layers) can be optically identified. As already shown, AFM revealed smaller crystals down to the single- and bi- layer cases in the surroundings of the larger ones but they were not large enough to be optically identified.

To study the optical contrast of these FL-Sb flakes, an approach based on the Fresnel law similar to the one developed by Blake *et al*. [118] was used. This method has been widely employed to study the optical contrast of different 2D crystals such as graphene [118-120] transition metal dichalcogenides [121-123], mica [108] or hexagonal boron nitride [124]. The optical contrast (C) depends on the flake thickness (d) and the illumination wavelength (λ):

$$C(d,\lambda) = \frac{I_{flake} - I_{substrate}}{I_{flake} + I_{substrate}} \tag{4.8}$$

where I_{flake} and $I_{substrate}$ are the reflected light intensities from the flake and the SiO_2 substrate, respectively. The reflected intensities for normal incidence of monochromatic light can be written as [118]:

$$I_{flake}(d,\lambda) = \left| \frac{r_{01}e^{i(\Phi_1+\Phi_2)} + r_{12}e^{-i(\Phi_1-\Phi_2)} + r_{23}e^{-i(\Phi_1+\Phi_2)} + r_{01}r_{12}r_{23}e^{i(\Phi_1-\Phi_2)}}{e^{i(\Phi_1+\Phi_2)} + r_{01}r_{12}e^{-i(\Phi_1-\Phi_2)} + r_{01}r_{23}e^{-i(\Phi_1+\Phi_2)} + r_{12}r_{23}e^{i(\Phi_1-\Phi_2)}} \right|^2$$

$$I_{substrate}(d,\lambda) = \left| \frac{r_{02} + r_{23}e^{-2i\Phi_2}}{1 + r_{02}r_{23}e^{-2i\Phi_2}} \right|^2 \tag{4.9}$$

where the subindexes 0, 1, 2, and 3 refer to the media: air, FL-Sb flake, SiO_2, and Si, respectively. $\tilde{n}_j(\lambda) = n_j - i\kappa_j$ is the complex refractive index of medium j, $\Phi_j = 2\pi\tilde{n}_j d_j/\lambda$ is the phase shift introduced by medium j, d_j is the thickness of medium j, and $r_{jk} = (\tilde{n}_j - \tilde{n}_k)/(\tilde{n}_j + \tilde{n}_k)$ is the amplitude of the reflected path in the interface between media j and k. $I_{substrate}$ is obtained by considering that medium 1 is air instead of a flake. The SiO_2 layer of thickness d_2 is optically characterized by a wavelength-dependent refractive index $n_2(\lambda)$ with no imaginary part [125], ranging from 1.465 at 450 nm to 1.456 at 650 nm. As the thickness of the Si layer is several orders of magnitude larger than that of the SiO_2 layer, it can be considered as a semi-infinite film. It is optically characterized by a wavelength-dependent refractive index $\tilde{n}_3(\lambda)$ [125], ranging from 4.682 – 0.1491i at 450 nm to 3.847-0.016i at 650 nm. Figure 4.35 shows a schematic diagram of the experimental setup.

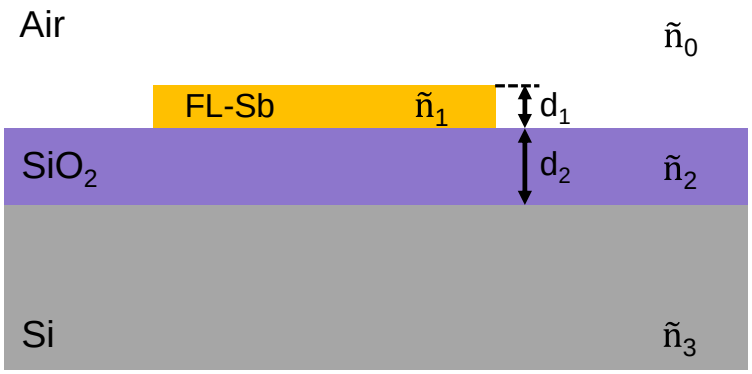

Figure 4.35 Schematic diagram of the experimental setup.

The contrast C was obtained from the optical images, the thicknesses of the different few-layer antimonene terraces were measured from AFM topography images and the wavelength of the incident light was selected by using narrow band-pass filters. Hence, in equations (4.8) and (4.9), for a given wavelength there are two unknown variables n_1 and κ_1 and a number of equations equal to the number of measured thicknesses. The solution of this system is, therefore, overdetermined and least-squares fitting was used to find $\tilde{n}_1$ (λ). Since least-squares fitting can sometimes lead to different solutions with similar convergence criteria (this is a well-known problem in fitting methods), in such cases the solutions that best match the contrast observed in the optical images were chosen. More in detail, the optical contrast of 10 antimony flakes with thicknesses ranging from $d_1 = 2$ up to $d_1 = 100$ nm (~ 4 to 270 layers) was analyzed under a well-defined illumination wavelength. For this purpose, a Nikon Eclipse LV100 optical microscope using nonpolarized illumination at normal incidence with a 50× objective (numerical aperture NA = 0.55) was used. The illumination wavelength was selected by means of eight narrow band-pass filters (10 nm full width at half maximum FWHM) with central wavelengths 450, 500, 520, 546, 568, 600, 632 and 650 nm purchased from Edmund Optics. Figure 4.36 shows optical microscopy images of several flakes using white light (Figure 4.36a) and at selected wavelengths (Figure 4.36b-e).

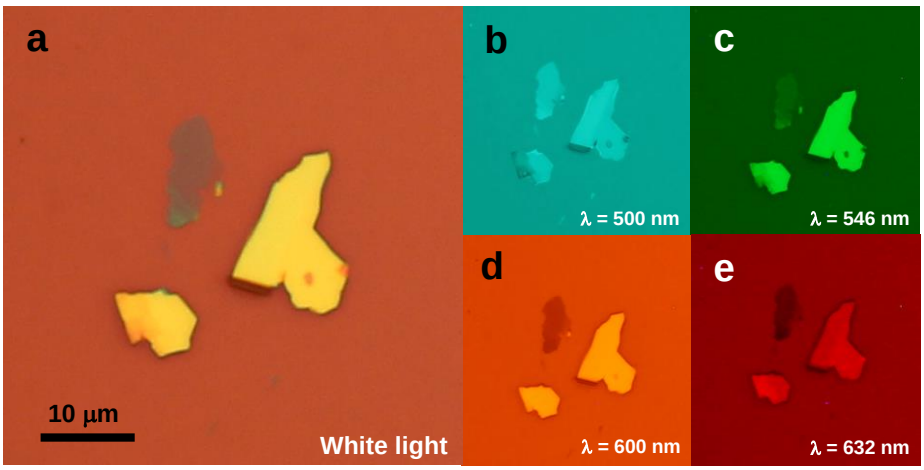

Figure 4.36 Different optical images acquired by using white light a) and by using narrow bandpass filters (b-e): 500, 546, 600 and 632 nm respectively.

The measured optical contrast *vs.* thickness for the four wavelengths in figure 4.36 is shown in figure 4.37. The optical contrast accurately follows equations (4.8) and (4.9). Solid lines correspond to fits to the Fresnel law choosing the FL-Sb complex refractive index values that best fit (within the above-mentioned criterion) the experimental data for each wavelength.

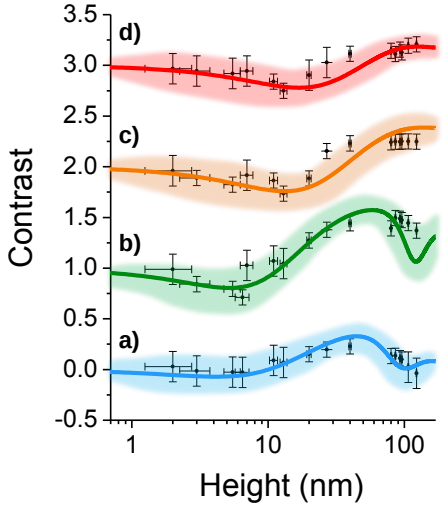

Figure 4.37 Measured optical contrast (small dot symbols) of few-layer antimonene flakes on a 300 nm SiO_2 substrate *versus* their thickness from AFM measurements at different illumination wavelengths λ (in nm): 500 a), 546 b), 600 c), and 632 d). Solid lines and shaded areas are the contrast and its uncertainty obtained from the fit to the Fresnel law. Note that b), c), and d) were vertically displaced by 1, 2, and 3 units, respectively, for the sake of clarity.

The complex refractive index for FL-Sb obtained from similar fits as in figure 4.37 at different illumination wavelengths is shown in figure 4.38.

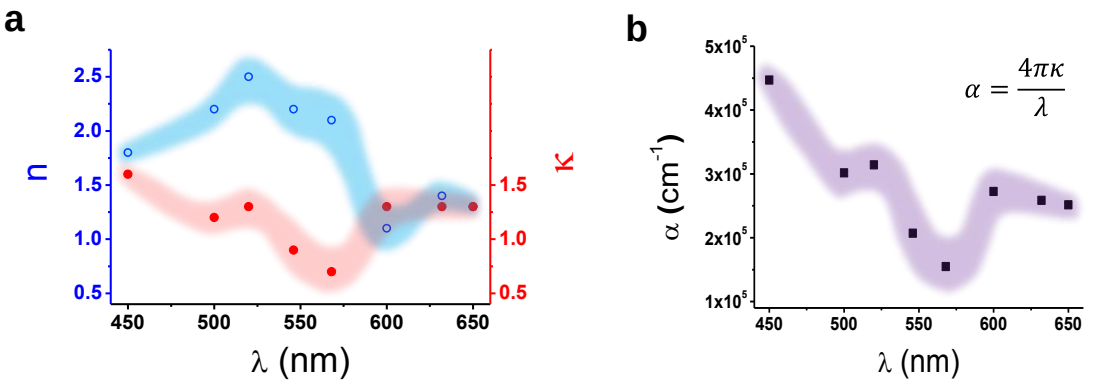

Figure 4.38 a) Determined refractive index (blue open circles, left axis) and extinction coefficient (red solid circles, right axis) of FL-Sb as functions of the incident wavelength. b) Determined absorption coefficient (black solid squares) of FL-Sb as a function of the incident wavelength. In both a) and b) the shaded areas represent the uncertainties in the data.

Figure 4.38a shows the real (n, refractive index) and imaginary (κ, extinction coefficient) parts of the FL-Sb complex refractive index in the visible spectrum. Figure 4.38b shows the absorption coefficient, which is obtained from the extinction coefficient using the relation $\alpha = 4\pi\kappa/\lambda$ [126] and is usually expressed in cm^{-1}. The absorption coefficient describes the decay in the light intensity as the light traverses through the unit distance in a medium.

The results obtained for the complex refractive index and absorption coefficient as functions of the wavelength are in good agreement with previous theoretical calculations of these magnitudes for single-layer antimonene, performed over broader spectral ranges [101, 102]: the refractive index, n, in the visible range is around 1.5 and the extinction coefficient, κ, around 1.2. Both magnitudes calculated for single-layer antimonene [101, 102] show similar dispersion relations despite lower values for the extinction coefficient. It is interesting to notice the behavior of the absorption coefficient, α, which shows an increase from the IR to the UV zone, starting more markedly from a resonance at $\lambda \sim 580$ nm. This tendency of the absorption process is predicted by the theoretical calculations, starting in the IR part of the spectrum and peaking in the UV part. To gain further insight into the physical origin of the observed behavior, a simple analytical model can be applied to describe qualitatively the dispersion relation of the obtained complex refractive index. The two-pole Sellmeier equation [127] was employed, which is commonly used to determine the dispersion of light in a medium. It takes the form:

$$n^2(\lambda) = A + \frac{B_1\lambda^2}{\lambda^2 - C_1} + \frac{B_2\lambda^2}{\lambda^2 - C_2} \quad (4.10)$$

where n is the refractive index and λ the wavelength. The first and second terms represent, respectively, the contribution to refractive indexes due to higher energy and lower energy gaps of electronic absorption. The last term accounts for the decrease in refractive indexes due to lattice absorption [127]. Figure 4.39 shows the fits of the refractive index and extinction coefficient to the two-pole Sellmeier equation.

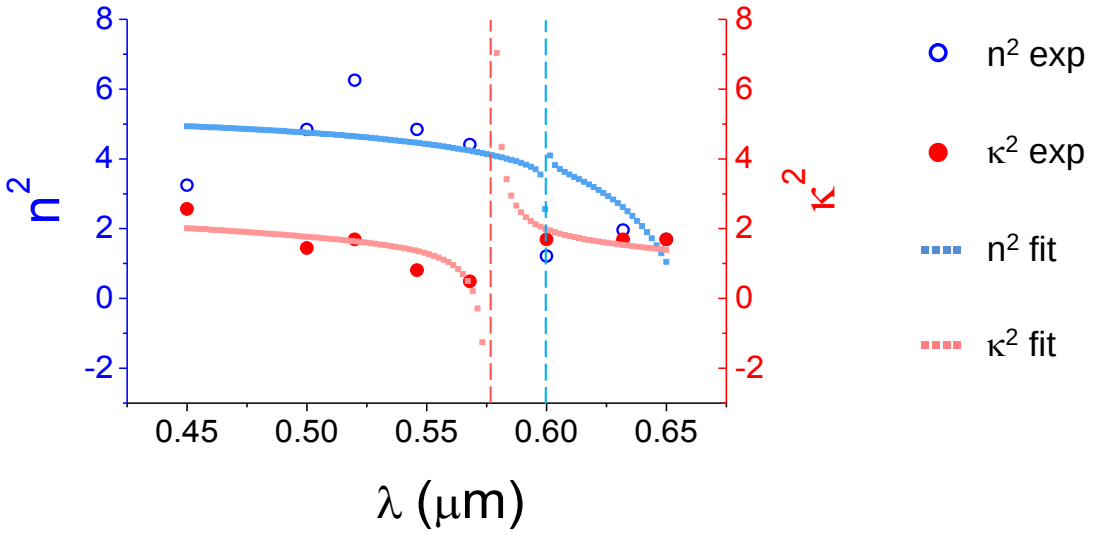

Figure 4.39 Refractive index *vs.* wavelength fits to the two-pole Sellmeier equation. Vertical dashed lines point resonances in the fitted curves.

Although fitting is not accurate, fits seem to show an absorption resonance around 575 - 600 nm (in good agreement with that observed in the absorption coefficient, α), that could be related to the presence of an electronic gap around these values.

In order to determine the optimal conditions for the optical identification of ultrathin antimonene layers, the calculated contrast as a function of incident light wavelength and SiO_2 thickness is plotted (figure 4.40). The optimal conditions for the optical identification are defined as the combination of wavelength and thickness that maximizes the absolute values of the layer contrast. To this end, the obtained complex refractive index of FL-Sb was used to calculate the optical contrast of antimonene flakes, considering a thickness of 3.73 Å for the monolayer (figure 4.25). Although quantum confinement and/or excitonic effects can affect the optical properties, the use of the obtained complex refractive index can help to find the optimal conditions to visualize single- and bilayer antimonene crystals,

as it is commonly done in the literature with other monolayer materials, where the refractive index of the bulk material is employed to study the optical properties of ultrathin crystals, including materials presenting a dependence of the band gap on the number of layers [118, 121, 128].

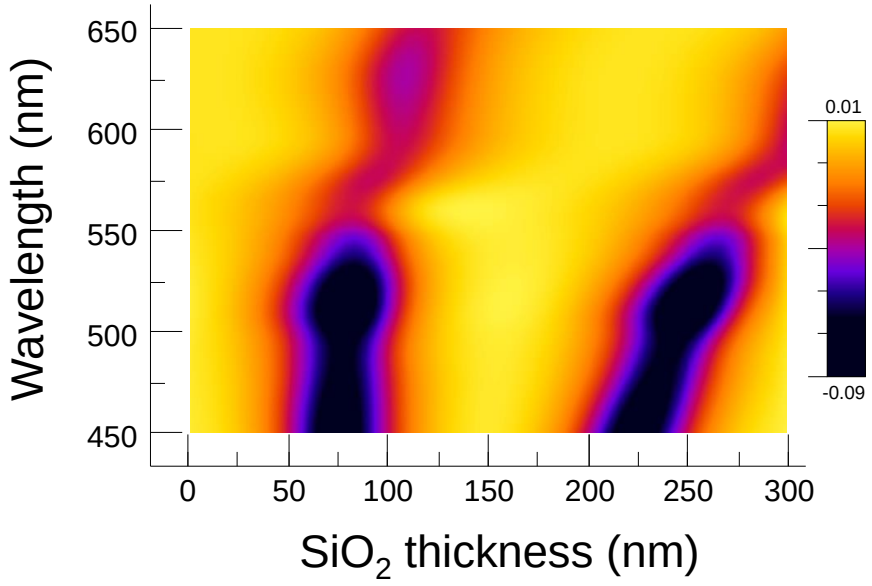

Figure 4.40 Optical contrast as a function of incident light wavelength and SiO_2 layer thickness for antimonene.

Figure 4.40 shows two characteristic negative-contrast bands centered at thicknesses of 80 and 230 nm (at 450 nm wavelength) that shift towards higher thicknesses with increasing wavelength. In particular, the highest contrasts are found for thicknesses around 80 and 220 - 250 nm at wavelengths below 550 nm. For the cases of the two most commonly used substrates, with SiO_2 thicknesses of 90 and 300 nm, whereas the wavelengths for the 90 nm substrates are very similar to those for the optimal 80 nm case, for the 300 nm thickness (the thickness used in the present study) the optimal wavelength is ~ 580 nm. This wavelength is indeed close to the one which the human eye has maximum sensitivity (~ 562 nm) [129], which might help to detect the lower terraces when using substrates with this oxide thickness. In this case, the use of light illumination at this wavelength will ease the optical identification of ultrathin antimonene layers (see figure A4.7a in the Appendix). A similar contrast plot was obtained estimating theoretical (n, κ) values for monolayer antimonene in the visible region from reference [101] (figures A4.7b and c in the Appendix). Despite a decrease in the contrast magnitude, the behavior is similar, presenting the same two characteristic negative-contrast bands as in figure 4.40, leading to similar optimal conditions for the optical identification of FL-Sb flakes.

To end this section, preliminary results on the electrical characterization of few-layer antimonene are presented. Since the size of the antimonene flakes was very small, we developed Probe-Assisted Nanowire (PAN) lithography, described in Chapter 3, to create electrical contacts on different FL-Sb flakes. C-AFM was used to probe their electrical properties at room temperature. The ~ 150 µm long Au nanowires path presented in Chapter 3 was indeed fabricated to contact three different FL-Sb flakes. Figure 4.41 shows AFM topographic images of the studied flakes, whose thicknesses varied from ~ 3.5 to 21 nm.

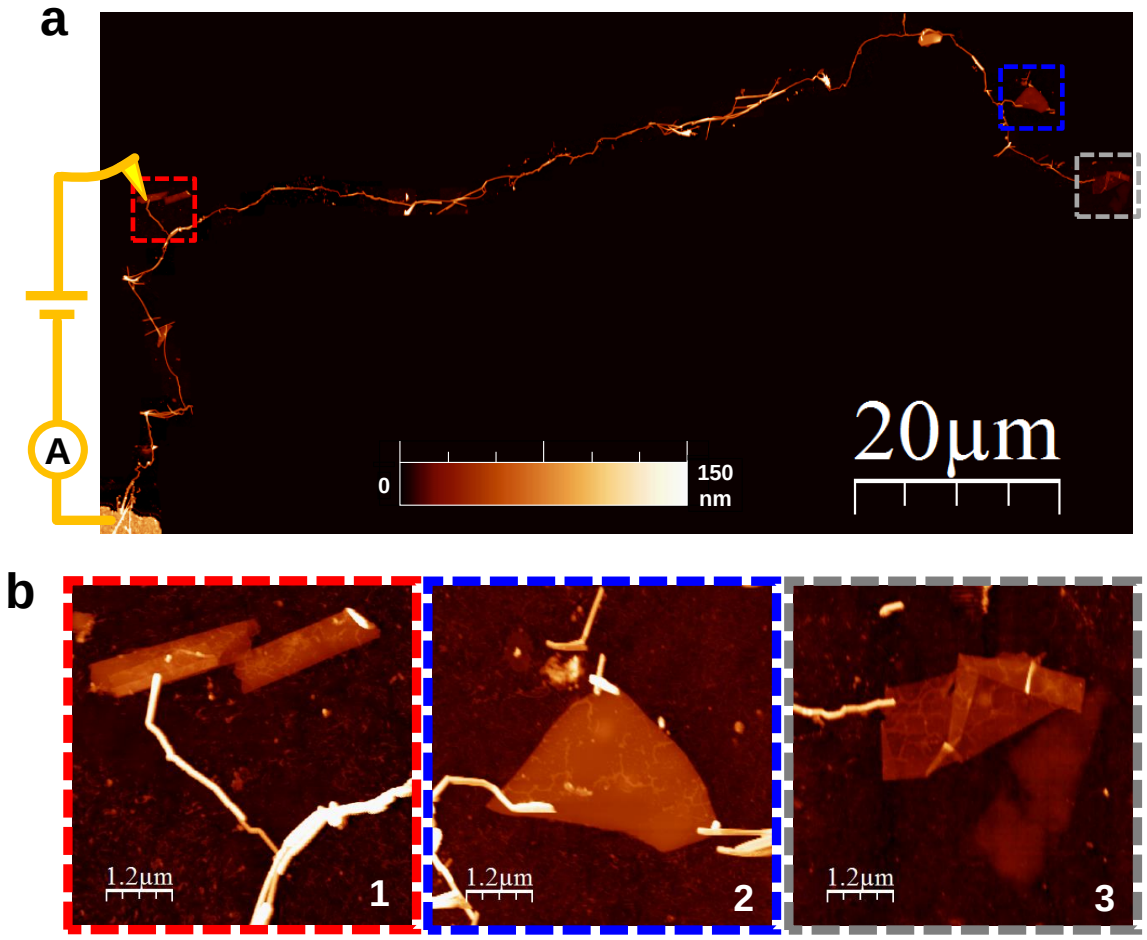

Figure 4.41 Setup for the electrical characterization of FL-Sb flakes. a) AFM topographic image of the whole area under study. This image is a collage of AFM images of smaller areas following the Au path, hence the absence of any feature far from it. A diagram of the electrical circuit for one of the flakes was included for the sake of clarity. On the bottom left corner a micrometer size gold electrode created by thermal evaporation assisted by stencil mask can be seen. b) Details of the studied FL-Sb flakes. Flakes are designated with the numbers shown in the bottom right corners: 1, 2 and 3 from left to right.

ElectriMulti75-G probes from BudgetSensors [30] were employed. C-AFM measurements were performed by using a metallized AFM tip as a second mobile electrode to measure the current in the flakes as a function of their distance to the Au nanowire electrode. As in the case of the MMX chains presented at the beginning of this chapter, images were acquired in AM-AFM mode and at selected locations the tip was brought into contact to perform IV characteristics (see Chapter 1, conductive AFM section). Figure 4.42 presents electrical characterization of the FL-Sb flakes in figure 4.41.

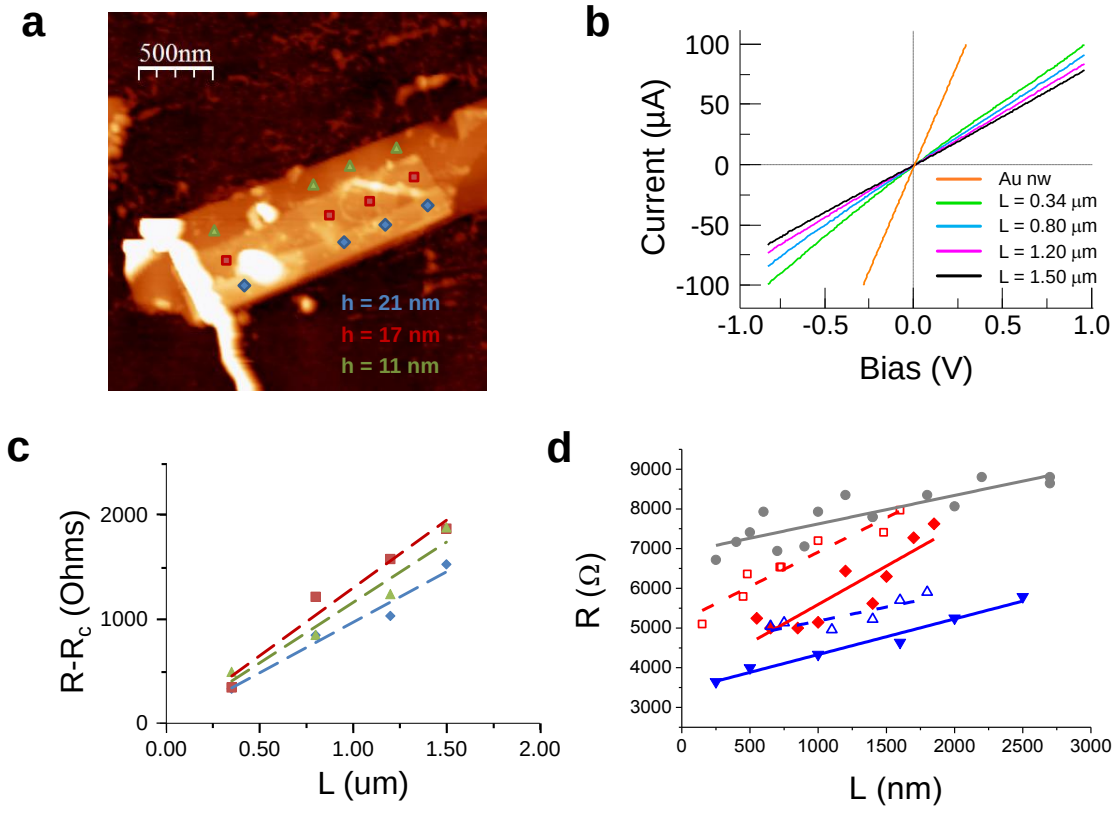

Figure 4.42 Electrical characterization of FL-Sb flakes. a) AFM topographic image of flake 1. Spots where IV curves at different tip-electrode distances were acquired are marked with different symbols. b) Representative IV curves at different tip-electrode distances for the middle terrace in flake 1. c) Resistance *vs.* Length plots obtained from IV curves in the different terraces in flake 1 as pointed by the symbols in a). Dashed lines are linear fits for data from each terrace. No significant differences in the slopes are found within error (contact resistance was subtracted in this plot for clarity). d) Resistance *vs.* Length plots from similar IV curves as in b) obtained in the different flakes using different AFM tips. Red: flake 1, blue: flake 2, gray: flake 3. Symbols are experimental values and lines are linear fits to these experimental data. Solid symbols with solid fit lines correspond to data acquired with one tip whereas empty symbols with dashed fit lines correspond to data acquired with another tip.

Figure 4.42a shows an AFM topographic image of flake 1. The locations where IV curves were acquired are marked with different symbols. Figure 4.42b shows representative IV curves acquired in flake 1 at different tip-Au electrode distances. The linear dependence of the IV curves is in good agreement with theoretical calculations for thicknesses above 3 layers, where no band gap is expected, and is another proof of the high stability of antimonene to ambient conditions. The linear shape of the curves is also indicative of good electrical contacts between both tip-sample and sample-Au electrode. Figure 4.42c presents the dependence of the resistance with the distance between electrodes for the spots marked with symbols in figure 4.42a. Neither significant differences among terraces nor correlation with the terrace height can be found. Figure 4.42d presents Resistance *vs.* Length curves for the three studied flakes using two different AFM tips. As it was done in Chapter 3 when studying graphene contacted through PAN lithography, linear fits allow extracting the 1D resistivity, $\rho_{1D} = dR/dL$, from the slopes and contact resistances, R_c, from the intersections for $L = 0$. As expected, it can be observed that, disregarding the contact resistance, the slope for each flake is independent of the tip.

Since the dimensions of the flakes are very well characterized from the AFM images, the sheet resistivity, ρ_{2D} can be calculated from the ρ_{1D}, in a same manner as it was done in Chapter 3 for graphene, using equation (3.1). For conventional 2D materials, the sheet resistance depends on thickness. Interestingly, this tendency is not observed for the measured few-layer antimonene flakes. In this case, ρ_{2D} yields an average value of $1300 \pm 400\ \Omega/\square$. This result is in good agreement with theoretical calculations that are being currently carried out by the group of Dr. Juan José Palacios, which show that few-layer antimonene band structure presents surface states that make the conductance of the flakes independent of its thickness. Figure 4.43 presents the calculated band structure of a 7-layer flake in vacuum and also including water.

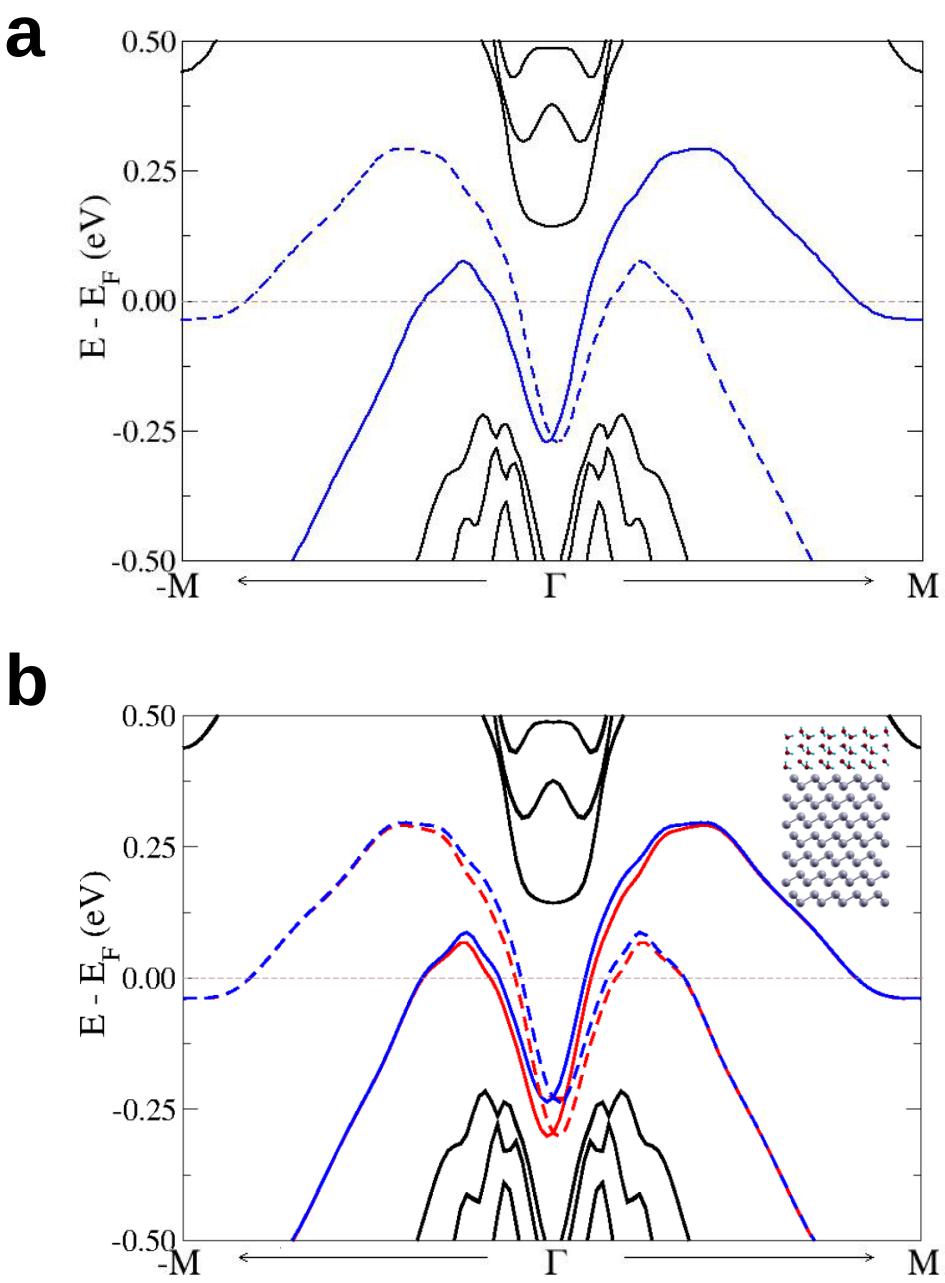

Figure 4.43 Band structure of 7-layer antimonene. Solid (dashed) lines correspond to spin up (down). Blue (red) corresponds to the layer in the top (bottom). a) Band structure from calculations in vacuum. Spin up and down are superimposed. b) Including water molecules. The inset shows a side view of the atomic configuration with the water molecules used for the calculations.

According to the calculated band structure for FL-Sb in vacuum and including water to somehow mimic ambient conditions, these surface states, which are given by the Dirac cones in the Γ point and the hole pockets nearby, are very robust and do not vanish in ambient conditions, pointing to topological protected surface states. Thus, an essential role of these surface states is expected in the electrical conduction of few-layer antimonene flakes. In particular, as commented above, these surface states originate the absence of thickness dependence on the electrical properties of FL-Sb flakes, as the experiments suggested. According to theoretical calculations, this behavior is expected at least up to approximately 100 layers (~ 40 nm) where bulk states start to be dominant [130].

A direct comparison of the ρ_{2D} values obtained in similar conditions for graphene in Chapter 3, $\rho_{2D\text{-}G}$ = 670 Ω/□, and for FL-Sb now, $\rho_{2D\text{-}FLSb}$ = 1300 Ω/□, suggests a bidimensional electrical transport, in good agreement with the theoretical calculations that are being carried out. From the band structures in figure 4.43, it can be seen that, since the two Dirac cones in FL-Sb are almost superimposed, backscattering between them is likely to occur, and then, assuming similar carrier concentrations in both graphene and FL-Sb, the resistivity in this latter case is expected to be comparable but larger than in graphene, as observed experimentally.

From the obtained ρ_{2D} value for FL-Sb, the mobility can be roughly estimated using the expression:

$$\mu = \frac{\sigma_{2D}}{e\, n_{2D}} \tag{4.11}$$

where μ is the mobility in $cm^2\ V^{-1}\ s^{-1}$, σ_{2D} the bidimensional conductivity in S, e the electron charge in C = V S s and n_{2D} the bidimensional carrier concentration in cm^{-2}. σ_{2D} can be obtained from ρ_{2D}, $\sigma_{2D} = 1/\rho_{2D}$ and n_{2D} can be calculated from the band structure, counting the number of carriers per unit area in the surface states, resulting in $n_{2D} \sim 6.10^{12}\ cm^{-2}$. This figure is in good agreement with a back-of-the-envelope calculation comparing this band structure with that of graphene. In the first Brillouin zone graphene presents 4 Dirac cones, whereas few-layer antimonene presents a central Dirac cone and 6 pockets. Therefore, assuming a similar Fermi level, in this case n_{2D} could be roughly estimated as 7/4 of the graphene carrier density, which coincides fairly well with the value from more sophisticated calculations. A mobility $\mu \sim 800\ cm^2\ V^{-1}\ s^{-1}$ is obtained, in good agreement with theoretical predictions [96-98]. This high mobility turns antimonene as a promising candidate for nanoelectronics and optoelectronics.

As mentioned at the beginning of this section, these are preliminary results and calculations are still being carried out, but initial comparison between experimental results and theory seems to agree fairly well, pointing to exciting electrical properties of few layer antimonene.

In summary, it has been demonstrated that single layers of antimony, named antimonene, can be produced by mechanical exfoliation. These flakes are not significantly contaminated upon exposure to ambient conditions and they do not react with water. Different techniques have been used to characterize its properties, showing remarkable chemical, mechanical and electrical stabilities under ambient conditions. Few-layer antimonene flakes produced by liquid phase exfoliation have been also characterized along this work. DFT calculations confirm the experimental observations and predict a band gap of 1.2-1.3 eV in ambient conditions for single-layer antimonene, which is smaller than that calculated under vacuum conditions at 0 K, and within the range of optoelectronics applications.

Since both experimentally and theoretically it has been observed that Raman spectroscopy fails to provide information on few-layer antimonene, we have demonstrated that optical microscopy can be used as a simple tool to identify ultrathin antimonene crystals and to distinguish them from thicker flakes. The dependence of the optical contrast on the flake thickness and the illumination wavelength of few-layer antimonene flakes on SiO_2/Si substrates, produced by mechanical exfoliation of bulk antimony crystals, have been studied. From the contrast *versus* thickness measurements, applying a Fresnel-law based model, the refractive index and the absorption coefficient in the visible spectrum of these ultrathin antimonene flakes has been determined. The optimal combination of wavelength and SiO_2 thickness to better identify mono or few-layer antimonene crystals has been studied. The results presented here will allow identifying and determining the thickness of the flakes in a fast and non-destructive way and will ease the integration of ultrathin antimonene crystals on future nanodevices.

Preliminary results on the electrical properties of few-layer antimonene flakes have been presented. FL (> 5 layers) antimonene flakes show metallic characteristic in good agreement with theoretical predictions. The experimental electrical properties reported herein are in good agreement with theoretical calculations still ongoing, pointing to a conduction governed by surface states in few-layer antimonene.

Altogether, this work confirms antimonene as a highly stable 2D material with appealing properties and promising relevant applications in optoelectronics.

4.5 Conclusions

In this chapter three different studies on low dimensional materials have been presented. In all of them, AFM has proven to be an essential tool for their characterization as well as for their manipulation.

In the first section, the reversibility of the MMX crystal-to-solution has allowed to isolate on surface few to single MMX chains by adjustment of simple experimental parameters (solvent and concentration). AFM imaging of individual bundles and chains has allowed carrying out electrical transport characterization along the MMX chains, demonstrating their high electrical conductivity and confirming these polymers as excellent molecular wires with a very low β decay factor.

In the second section, the application of very controlled local ultrahigh pressures with AFM diamond tips to tune graphene properties has been presented. Evidences of the possibilities that this procedure offers in graphene, including local tuning of doping, enhancement of contact resistance, suitability as a protective coating and improvement in sealing actuation have been demonstrated. Preliminary DFT calculations point to the presence of a small degree of chemical bonding between graphene and SiO_2 within the modified areas. These results confirm AFM ultrahigh pressure as an easy and powerful procedure to locally tune 2D materials properties, opening new possibilities, such as locally modifying the optoelectronic behavior of other 2D materials or the study of chemical reactions at ultrahigh pressures by trapping molecules between graphene and substrate.

In the third section, the isolation and characterization of a novel 2D material, antimonene, has been presented. Theoretical calculations predict a variety of very interesting properties, including the aperture of a gap for the monolayer case suitable for optoelectronics applications and bidimensional electrical conductivity. High stability under ambient conditions has been demonstrated, together with relevant optical and exciting electrical properties overcoming some of the drawbacks observed in black phosphorus. The results presented here are probably just the tip of an iceberg and we are sure there will be a blossoming of relevant studies on this topic in the near future.

4.6 Appendix

MMX fibers of different structures

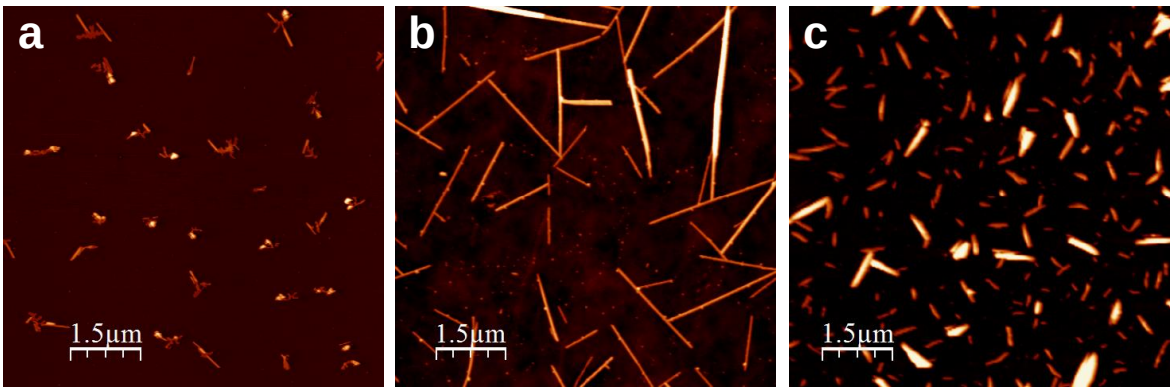

Figure A4.1 AFM topographic images of $[Pt_2(RCS_2)_4I]_n$ (R = Me (a), Et (b) and Pen (c)). Total Z range = 30 nm.

Vacuum effect on drop casted MMX fibres

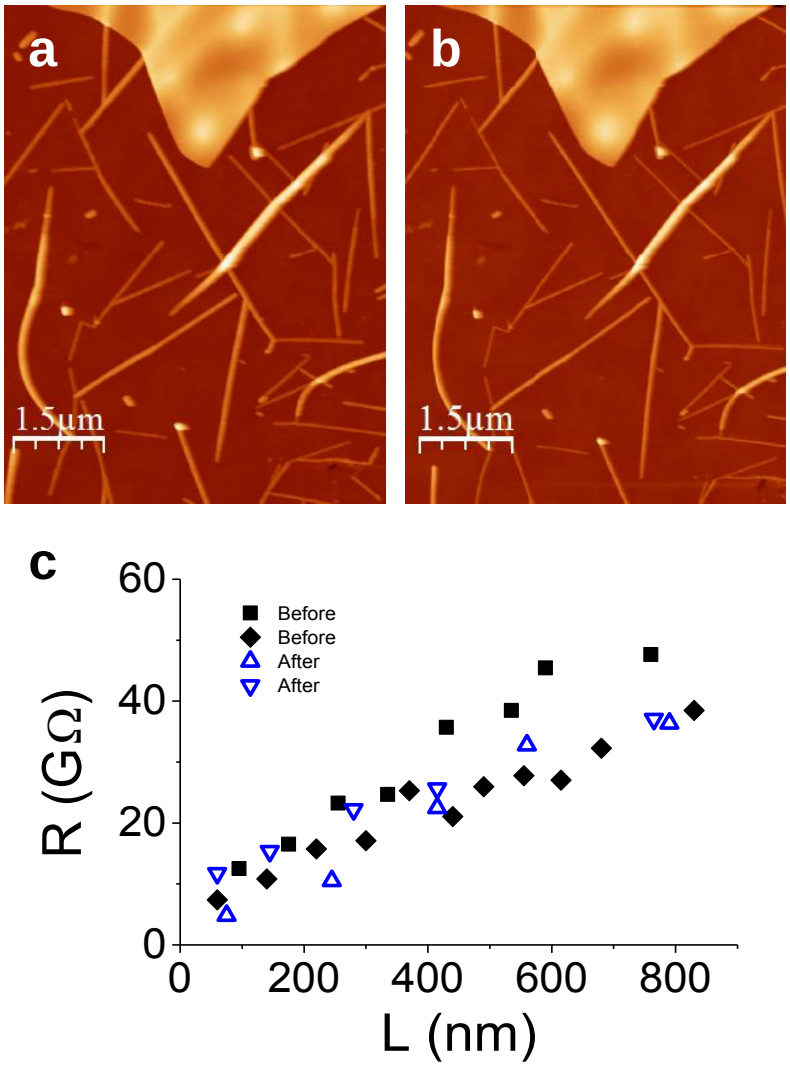

Figure A4.2 Effect of vacuum on drop-casted MMX fibres. a) Topographic AFM image of initial sample with and EGF electrode. b) Same as a) after 5 h at 10^{-5} hPa. Total Z range = 60 nm in both AFM images. c) Electrical characterization of representative fibres of similar dimensions before and after vacuum. Resistance values obtained at 2 V Bias voltage. No morphological or electrical changes can be appreciated.

Temperature effect on drop casted MMX fibres

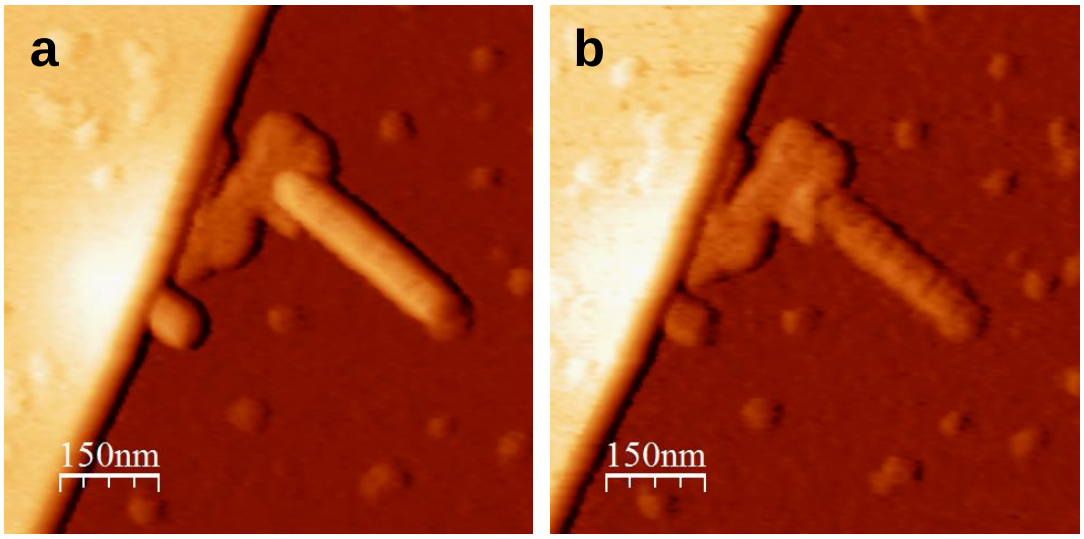

Figure A4.3 Effect of temperature on drop-casted MMX fibres. a) Edge-enhanced topographic AFM image at room temperature. b) Same as in a) at 50°C. Loss of material and fractures on the fibre are clearly visible.

Raman mapping of graphene upon ultrahigh pressure modifications

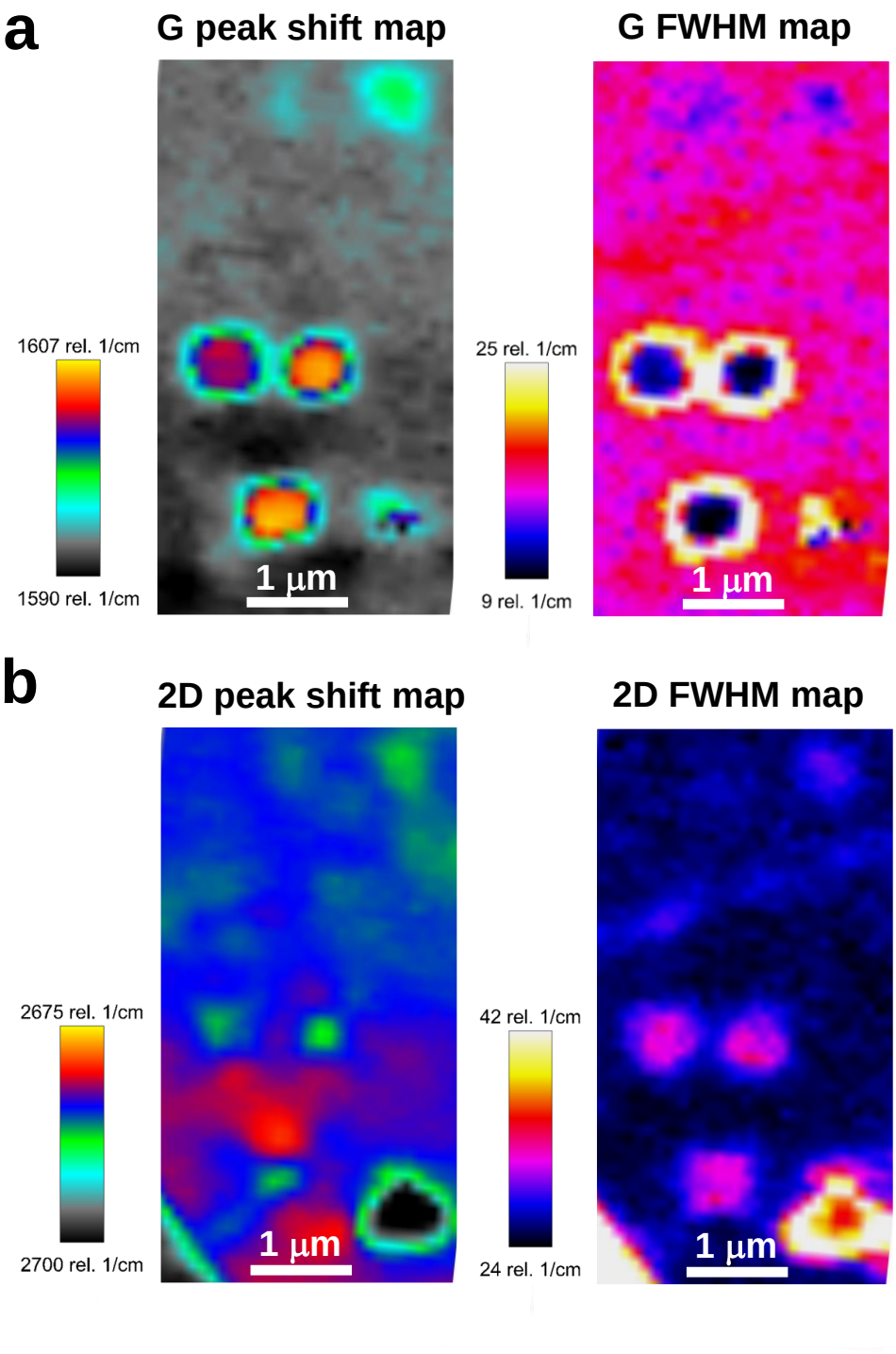

Figure A4.4 Raman mapping of different magnitudes of ultrahigh pressure modified areas. a) G peak. b) 2D peak. Left panels: peak position shift. Right panels: full width at half-maximum (fwhm) variations.

Absence of Raman D peak on graphene upon ultrahigh pressure modifications

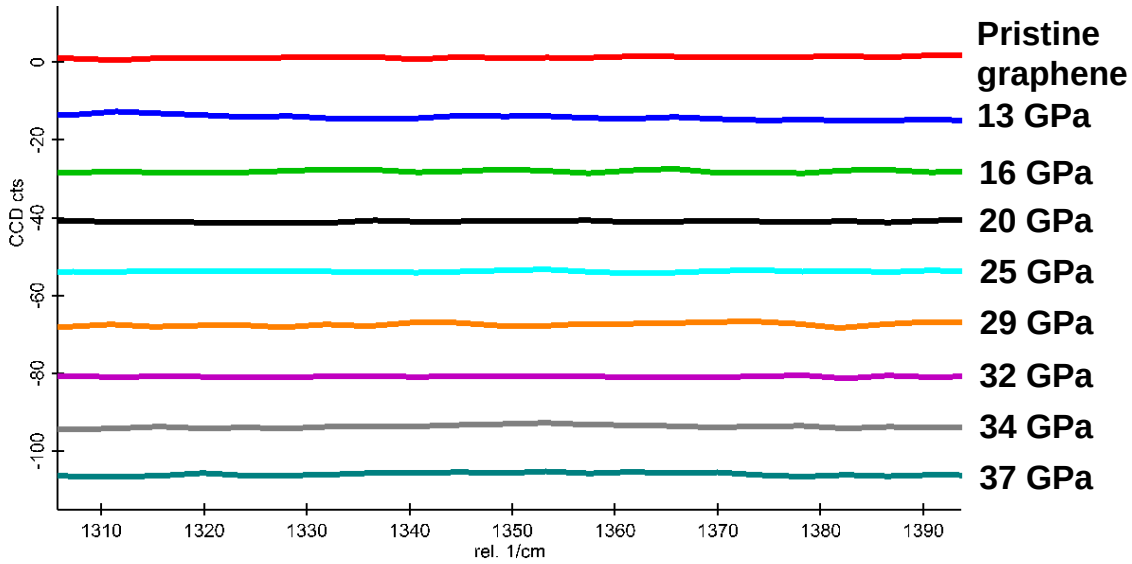

Figure A4.5 Raman spectra around 1350 cm^{-1}. No D peak is observed at any pressure.

Ultrahigh pressure graphene modifications stability

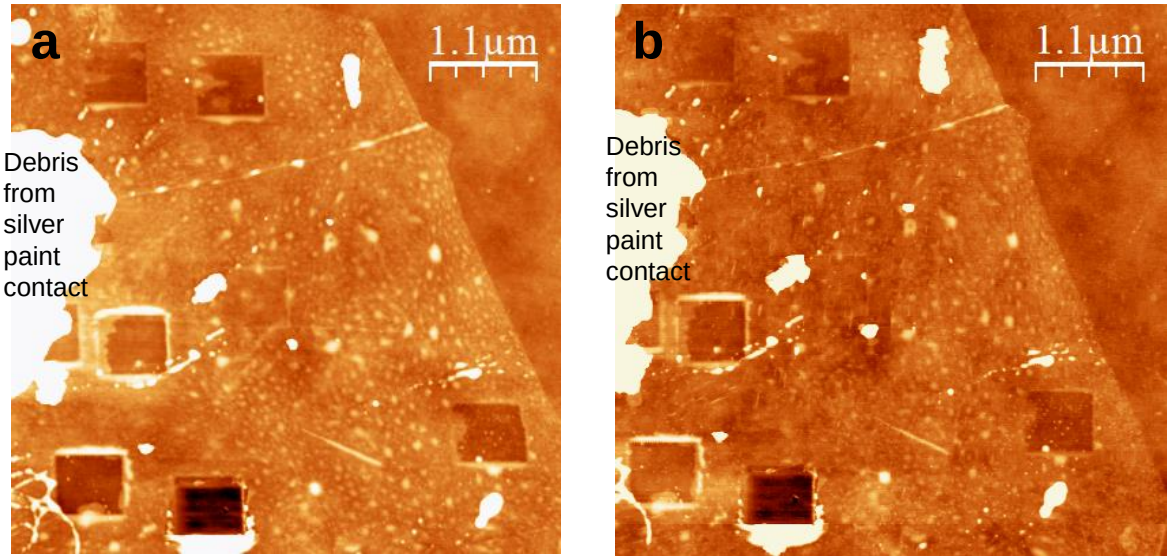

Figure A4.6 AFM topographic images of modified regions. a) After EGF soft electrode contact for KPM measurements. b) Four months after a). Total Z range = 9 nm. The modified regions did not change, presenting the same depths.

Optical contrast as a function of incident light wavelength and SiO_2 layer thickness for monolayer antimonene

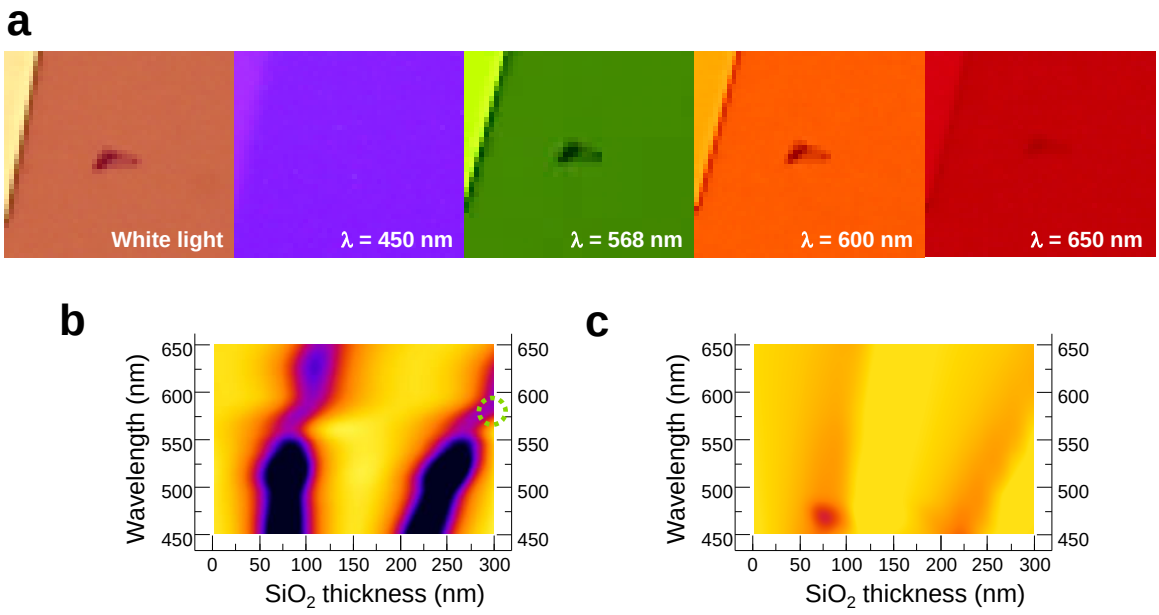

Figure A4.7 a) Optical images at white light and different wavelengths of one of the thinnest flakes deposited on 300 nm thickness SiO_2/Si substrates. The best identification can be performed at 568 and 600 nm wavelengths, in good agreement with the optimal value obtained from the contrast plots (which corresponds to the wavelength inside the dotted green circle in b), ~ 580 nm). b) Optical contrast as a function of incident light wavelength and SiO_2 layer thickness for monolayer antimonene from the obtained complex refractive index. c) Same as in b), but in this case complex refractive index was estimated from calculations of Singh, *et al.* [101]. The behavior of the contrast is similar in both cases, presenting the same two characteristic negative-contrast bands. Contrast ranges from -0.09 to 0.01 in both plots.

4.7 References

[1] Waldrop, M. M. The chips are down for Moore's law. *Nature* **2016,** *530*, 144-147.
[2] Livshits, G. I.*, et al.* Long-range charge transport in single G-quadruplex DNA molecules. *Nat. Nanotech.* **2014,** *9*, 1040-1046.
[3] Porath, D.; Cuniberti, G.; Di Felice, R. Charge transport in DNA-based devices. *Top. Curr. Chem.* **2004,** *237*, 183-227.
[4] Rothemund, P. W. K. Folding DNA to create nanoscale shapes and patterns. *Nature* **2006,** *440*, 297-302.
[5] Seeman, N. C. DNA in a material world. *Nature* **2003,** *421*, 427-431.
[6] Sun, L.; Diaz-Fernandez, Y. A.; Gschneidtner, T. A.; Westerlund, F.; Lara-Avila, S.; Moth-Poulsen, K. Single-molecule electronics: from chemical design to functional devices. *Chem. Soc. Rev.* **2014,** *43*, 7378-7411.
[7] Yuan, L.; Nerngchamnong, N.; Cao, L.; Hamoudi, H.; del Barco, E.; Roemer, M.; Sriramula, R. K.; Thompson, D.; Nijhuis, C. A. Controlling the direction of rectification in a molecular diode. *Nat. Commun.* **2015,** *6*, 6324.
[8] Aviram, A.; Ratner, M. A. Molecular Rectifiers. *Chem. Phys. Lett.* **1974,** *29*, 277-283.
[9] Lafferentz, L.; Ample, F.; Yu, H.; Hecht, S.; Joachim, C.; Grill, L. Conductance of a Single Conjugated Polymer as a Continuous Function of Its Length. *Science* **2009,** *323*, 1193-1197.
[10] Choi, S. H.; Kim, B.; Frisbie, C. D. Electrical resistance of long conjugated molecular wires. *Science* **2008,** *320*, 1482-1486.
[11] Song, F.*, et al.* Direct measurement of electrical conductance through a self-assembled molecular layer. *Nat. Nanotech.* **2009,** *4*, 373-376.
[12] Faramarzi, V.; Niess, F.; Moulin, E.; Maaloum, M.; Dayen, J. F.; Beaufrand, J. B.; Zanettini, S.; Doudin, B.; Giuseppone, N. Light-triggered self-construction of supramolecular organic nanowires as metallic interconnects. *Nat. Chem.* **2012,** *4*, 485-490.
[13] Lloveras, V.; Vidal-Gancedo, J.; Figueira-Duarte, T. M.; Nierengarten, J. F.; Novoa, J. J.; Mota, F.; Ventosa, N.; Rovira, C.; Veciana, J. Tunneling versus Hopping in Mixed-Valence Oligo-p-phenylenevinylene Polychlorinated Bis(triphenylmethyl) Radical Anions. *J. Am. Chem. Soc.* **2011,** *133*, 5818-5833.
[14] Shirakawa, H.; Louis, E. J.; Macdiarmid, A. G.; Chiang, C. K.; Heeger, A. J. Electrically Conducting Organic Polymers - Halogen Derivatives of Polyacetylene, (Ch)X. *J. Chem. Soc., Chem. Commun.* **1977**, 578-580.
[15] Slinker, J. D.; Muren, N. B.; Renfrew, S. E.; Barton, J. K. DNA charge transport over 34 nm. *Nat. Chem.* **2011,** *3*, 228-233.
[16] Aragones, A. C.; Darwish, N.; Saletra, W. J.; Perez-Garcia, L.; Sanz, F.; Puigmarti-Luis, J.; Amabilino, D. B.; Diez-Perez, I. Highly Conductive Single-Molecule Wires with Controlled Orientation by Coordination of Metalloporphyrins. *Nano Lett.* **2014,** *14*, 4751-4756.
[17] Park, J.*, et al.* Coulomb blockade and the Kondo effect in single-atom transistors. *Nature* **2002,** *417*, 722-725.
[18] Ponce, J.; Arroyo, C. R.; Tatay, S.; Frisenda, R.; Gavina, P.; Aravena, D.; Ruiz, E.; van der Zant, H. S. J.; Coronado, E. Effect of Metal Complexation on the Conductance of Single-Molecular Wires Measured at Room Temperature. *J. Am. Chem. Soc.* **2014,** *136*, 8314-8322.
[19] Ruben, M.; Landa, A.; Loertscher, E.; Riel, H.; Mayor, M.; Goerls, H.; Weber, H. B.; Arnold, A.; Evers, F. Charge Transport Through a Cardan-Joint Molecule. *Small* **2008,** *4*, 2229-2235.
[20] Tuccitto, N.; Ferri, V.; Cavazzini, M.; Quici, S.; Zhavnerko, G.; Licciardello, A.; Rampi, M. A. Highly conductive similar to 40-nm-long molecular wires assembled by stepwise incorporation of metal centres. *Nat. Mater.* **2009,** *8*, 41-46.

[21] Hermosa, C.; Vicente Alvarez, J.; Azani, M.-R.; Gomez-Garcia, C. J.; Fritz, M.; Soler, J. M.; Gomez-Herrero, J.; Gomez-Navarro, C.; Zamora, F. Intrinsic electrical conductivity of nanostructured metal-organic polymer chains. *Nat. Commun.* **2013,** *4*, 1709.
[22] Welte, L.; Calzolari, A.; Di Felice, R.; Zamora, F.; Gomez-Herrero, J. Highly conductive self-assembled nanoribbons of coordination polymers. *Nat. Nanotech.* **2010,** *5*, 110-115.
[23] Mas-Balleste, R.; Castillo, O.; Sanz Miguel, P. J.; Olea, D.; Gomez-Herrero, J.; Zamora, F. Towards Molecular Wires Based on Metal-Organic Frameworks. *Eur. J. Inorg. Chem.* **2009**, 2885-2896.
[24] Mas-Balleste, R.; Gomez-Herrero, J.; Zamora, F. One-dimensional coordination polymers on surfaces: towards single molecule devices. *Chem. Soc. Rev.* **2010,** *39*, 4220-4233.
[25] Mitsumi, M.; Murase, T.; Kishida, H.; Yoshinari, T.; Ozawa, Y.; Toriumi, K.; Sonoyama, T.; Kitagawa, H.; Mitani, T. Metallic behavior and periodical valence ordering in a MMX chain compound, Pt-2(EtCS2)(4)I. *J. Am. Chem. Soc.* **2001,** *123*, 11179-11192.
[26] Welte, L*., et al.* Organization of Coordination Polymers on Surfaces by Direct Sublimation. *Adv. Mater.* **2009,** *21*, 2025-2028.
[27] Azani, M.-R.; Perez Paz, A.; Hermosa, C.; Givaja, G.; Gomez-Herrero, J.; Mas-Balleste, R.; Zamora, F.; Rubio, A. The Isolation of Single MMX Chains from Solution: Unravelling the Assembly-Disassembly Process. *Chem. Eur. J.* **2013,** *19*, 15518-15529.
[28] Gentili, D*., et al.* Patterned conductive nanostructures from reversible self-assembly of 1D coordination polymer. *Chem. Sci.* **2012,** *3*, 2047-2051.
[29] Guijarro, A*., et al.* Conductive Nanostructures of MMX Chains. *Adv. Funct. Mater.* **2010,** *20*, 1451-1457.
[30] http://www.budgetsensors.com/.
[31] Markiewicz, P.; Goh, M. C. Atomic-Force Microscopy Probe Tip Visualization and Improvement of Images Using a Simple Deconvolution Procedure. *Langmuir* **1994,** *10*, 5-7.
[32] Calzolari, A.; Alexandre, S. S.; Zamora, F.; Di Felice, R. Metallicity in individual MMX chains. *J. Am. Chem. Soc.* **2008,** *130*, 5552-5562.
[33] Gomez-Navarro, C.; Pablo, P. J. D.; Gomez-Herrero, J.; Biel, B.; Garcia-Vidal, F. J.; Rubio, A.; Flores, F. Tuning the conductance of single-walled carbon nanotubes by ion irradiation in the Anderson localization regime. *Nat. Mater.* **2005,** *4*, 534.
[34] Sundqvist, P.; Garcia-Vidal, F. J.; Flores, F.; Moreno-Moreno, M.; Gomez-Navarro, C.; Bunch, J. S.; Gomez-Herrero, J. Voltage and length-dependent phase diagram of the electronic transport in carbon nanotubes. *Nano Lett.* **2007,** *7*, 2568-2573.
[35] Kelley, T. W.; Granstrom, E. L.; Frisbie, C. D. Conducting probe atomic force microscopy: A characterization tool for molecular electronics. *Adv. Mater.* **1999,** *11*, 261–264.
[36] de Pablo, P. J.; Moreno-Herrero, F.; Colchero, J.; Gomez-Herrero, J.; Herrero, P.; Baro, A. M.; Ordejon, P.; Soler, J. M.; Artacho, E. Absence of dc-conductivity in lambda-DNA. *Phys. Rev. Lett.* **2000,** *85*, 4992-4995.
[37] Jacob, D.; Palacios, J. J. Critical comparison of electrode models in density functional theory based quantum transport calculations. *J. Chem. Phys.* **2011,** *134*, 044118.
[38] Soler, J. M.; Artacho, E.; Gale, J. D.; Garcia, A.; Junquera, J.; Ordejon, P.; Sanchez-Portal, D. The SIESTA method for ab initio order-N materials simulation. *J. Phys. Condens. Matter* **2002,** *14*, 2745-2779.
[39] Palacios, J. J.; Perez-Jimenez, A. J.; Louis, E.; Verges, J. A. Fullerene-based molecular nanobridges: A first-principles study. *Phys. Rev. B* **2001,** *64*, 115411.
[40] Palacios, J. J.; Pérez-Jiménez, A. J.; Louis, E. J.; Vergés, J. A. Electronic transport through C 60 molecules. *Nanotechnology* **2001,** *12*, 160.

[41] Guijarro, A.; Castillo, O.; Calzolari, A.; Miguel, P. J. S.; Gomez-Garcia, C. J.; di Felice, R.; Zamora, F. Electrical Conductivity in Platinum-Dimer Columns. *Inorg. Chem.* **2008,** *47*, 9736-9738.
[42] Mas-Balleste, R.; Gonzalez-Prieto, R.; Guijarro, A.; Fernandez-Vindel, M. A.; Zamora, F. Nanofibers generated by self-assembly on surfaces of bimetallic building blocks. *Dalton Trans.* **2009**, 7341-7343.
[43] Harrison, W. A., *Electronic Structure and the Properties of Solids*. Dover: New York, **1989**.
[44] Jayaraman, A. Diamond Anvil Cell and High-Pressure Physical Investigations. *Rev. Mod. Phys.* **1983,** *55*, 65-108.
[45] Dubrovinsky, L*., et al.* The most incompressible metal osmium at static pressures above 750 gigapascals. *Nature* **2015,** *525*, 226-229.
[46] Caldwell, W. A.; Nguyen, J. H.; Pfrommer, B. G.; Mauri, F.; Louie, S. G.; Jeanloz, R. Structure, bonding, and geochemistry of xenon at high pressures. *Science* **1997,** *277*, 930-933.
[47] Eremets, M. L.; Hemley, R. J.; Mao, H.; Gregoryanz, E. Semiconducting non-molecular nitrogen up to 240 GPa and its low-pressure stability. *Nature* **2001,** *411*, 170-174.
[48] Goncharov, A. F.; Struzhkin, V. V.; Somayazulu, M. S.; Hemley, R. J.; Mao, H. K. Compression of ice to 210 gigapascals: Infrared evidence for a symmetric hydrogen-bonded phase. *Science* **1996,** *273*, 218-220.
[49] Lee, C.; Wei, X. D.; Kysar, J. W.; Hone, J. Measurement of the elastic properties and intrinsic strength of monolayer graphene. *Science* **2008,** *321*, 385-388.
[50] Lopez-Polin, G.; Gomez-Navarro, C.; Parente, V.; Guinea, F.; Katsnelson, M. I.; Perez-Murano, F.; Gomez-Herrero, J. Increasing the elastic modulus of graphene by controlled defect creation. *Nat. Phys.* **2015,** *11*, 26-31.
[51] Nicolle, J.; Machon, D.; Poncharal, P.; Pierre-Louis, O.; San-Miguel, A. Pressure-Mediated Doping in Graphene. *Nano Lett.* **2011,** *11*, 3564-3568.
[52] Domingo, N*., et al.* Giant reversible nanoscale piezoresistance at room temperature in Sr2IrO4 thin films. *Nanoscale* **2015,** *7*, 3453-3459.
[53] Hertz, H. Über den kontakt elastischer körper. *J. Reine Angew. Mathematik* **1881,** *92*, 156.
[54] Johnson, K. L., *Contact Mechanics*. Cambridge University Press: Cambridge, **1985**.
[55] http://www.nanosensors.com/.
[56] https://www.spmtips.com/.
[57] Sader, J. E. Frequency response of cantilever beams immersed in viscous fluids with applications to the atomic force microscope. *J. Appl. Phys.* **1998,** *84*, 64-76.
[58] Sader, J. E.; Chon, J. W. M.; Mulvaney, P. Calibration of rectangular atomic force microscope cantilevers. *Rev. Sci. Instrum.* **1999,** *70*, 3967-3969.
[59] Ferrari, A. C*., et al.* Raman spectrum of graphene and graphene layers. *Phys. Rev. Lett.* **2006,** *97*, 187401.
[60] Long, D. A., *Raman spectroscopy*. McGraw-Hill International Book Company: **1977**.
[61] Ferrari, A. C. Raman spectroscopy of graphene and graphite: Disorder, electron-phonon coupling, doping and nonadiabatic effects. *Solid State Commun.* **2007,** *143*, 47-57.
[62] Das, A*., et al.* Monitoring dopants by Raman scattering in an electrochemically top-gated graphene transistor. *Nat. Nanotech.* **2008,** *3*, 210-215.
[63] Cancado, L. G*., et al.* Quantifying Defects in Graphene via Raman Spectroscopy at Different Excitation Energies. *Nano Lett.* **2011,** *11*, 3190-3196.
[64] Novoselov, K. S.; Geim, A. K.; Morozov, S. V.; Jiang, D.; Zhang, Y.; Dubonos, S. V.; Grigorieva, I. V.; Firsov, A. A. Electric field effect in atomically thin carbon films. *Science* **2004,** *306*, 666-669.
[65] Jaafar, M.; Lopez-Polin, G.; Gomez-Navarro, C.; Gomez-Herrero, J. Step like surface potential on few layered graphene oxide. *Appl. Phys. Lett.* **2012,** *101*, 263109.

[66] Eckman, A.; Felten, A.; Mishchneko, A.; Britnell, L.; Krupke, R.; Novoselov, K. S.; Casiraghi, C. Probing the nature of defects in graphene by raman spectroscopy. *Nano Lett.* **2012,** *12*, 3925-3930.
[67] Pisana, S.; Lazzeri, M.; Casiraghi, C.; Novoselov, K. S.; Geim, A. K.; Ferrari, A. C.; Mauri, F. Breakdown of the adiabatic Born-Oppenheimer approximation in graphene. *Nat. Mater.* **2007,** *6*, 198-201.
[68] Yu, Y. J.; Zhao, Y.; Ryu, S.; Brus, L. E.; Kim, K. S.; Kim, P. Tuning the Graphene Work Function by Electric Field Effect. *Nano Lett.* **2009,** *9*, 3430-3434.
[69] Wang, R.; Wang, S. N.; Zhang, D. D.; Li, Z. J.; Fang, Y.; Qiu, X. H. Control of Carrier Type and Density in Exfoliated Graphene by Interface Engineering. *ACS Nano* **2011,** *5*, 408-412.
[70] Kim, Y. J.; Kim, Y.; Novoselov, K.; Hong, B. H. Engineering electrical properties of graphene: chemical approaches. *2D Materials* **2015,** *2*, 042001.
[71] Ryu, S.; Liu, L.; Berciaud, S.; Yu, Y. J.; Liu, H. T.; Kim, P.; Flynn, G. W.; Brus, L. E. Atmospheric Oxygen Binding and Hole Doping in Deformed Graphene on a SiO2 Substrate. *Nano Lett.* **2010,** *10*, 4944-4951.
[72] Yuan, H. Y.*, et al.* Engineering Ultra-Low Work Function of Graphene. *Nano Lett.* **2015,** *15*, 6475-6480.
[73] Emery, J. D.; Detlefs, B.; Karmel, H. J.; Nyakiti, L. O.; Gaskill, D. K.; Hersam, M. C.; Zegenhagen, J.; Bedzyk, M. J. Chemically Resolved Interface Structure of Epitaxial Graphene on SiC(0001). *Phys. Rev. Lett.* **2013,** *111*, 215501.
[74] Ferrah, D.; Penuelas, J.; Bottela, C.; Grenet, G.; Ouerghi, A. X-ray photoelectron spectroscopy (XPS) and diffraction (XPD) study of a few layers of graphene on 6H-SiC(0001). *Surf. Sci.* **2013,** *615*, 47-56.
[75] Zhang, R.*, et al.* Direct graphene synthesis on SiO2/Si substrate by ion implantation. *Appl. Phys. Lett.* **2013,** *102*, 193102.
[76] Moon, J. S.*, et al.* Ultra-low resistance ohmic contacts in graphene field effect transistors. *Appl. Phys. Lett.* **2012,** *100*, 203512.
[77] Smith, J. T.; Franklin, A. D.; Farmer, D. B.; Dimitrakopoulos, C. D. Reducing Contact Resistance in Graphene Devices through Contact Area Patterning. *ACS Nano* **2013,** *7*, 3661-3667.
[78] Xia, F. N.; Perebeinos, V.; Lin, Y. M.; Wu, Y. Q.; Avouris, P. The origins and limits of metal-graphene junction resistance. *Nat. Nanotech.* **2011,** *6*, 179-184.
[79] Zhong, H.; Zhang, Z. Y.; Chen, B. Y.; Xu, H. T.; Yu, D. M.; Huang, L.; Peng, L. M. Realization of low contact resistance close to theoretical limit in graphene transistors. *Nano Res.* **2015,** *8*, 1669-1679.
[80] Koenig, S. P.; Wang, L. D.; Pellegrino, J.; Bunch, J. S. Selective molecular sieving through porous graphene. *Nat. Nanotech.* **2012,** *7*, 728-732.
[81] Bunch, J. S.; Verbridge, S. S.; Alden, J. S.; van der Zande, A. M.; Parpia, J. M.; Craighead, H. G.; McEuen, P. L. Impermeable atomic membranes from graphene sheets. *Nano Lett.* **2008,** *8*, 2458-2462.
[82] Koenig, S. P.; G., B. N.; Dunn, L. M.; Bunch, J. S. Ultrastrong adhesion of graphene membranes. *Nat. Nanotech.* **2011,** *6*, 543-546.
[83] López-Polín, G.; Jaafar, M.; Guinea, F.; Roldán, R.; Gómez-Navarro, C.; Gómez-Herrero, J. Strain dependent elastic modulus of graphene. *arXiv:1504.05521* **2015**.
[84] López-Polín, G.; Jaafar, M.; Guinea, F.; Roldán, R.; Gómez-Navarro, C.; Gómez-Herrero, J. Strain dependent elastic modulus of graphene. *arXiv:1504.05521* **2016**.
[85] Geim, A. K.; Novoselov, K. S. The rise of graphene. *Nat. Mater.* **2007,** *6*, 183-191.
[86] Mas-Balleste, R.; Gomez-Navarro, C.; Gomez-Herrero, J.; Zamora, F. 2D materials: to graphene and beyond. *Nanoscale* **2011,** *3*, 20-30.

[87] Tang, Q.; Zhou, Z. Graphene-analogous low-dimensional materials. *Prog. Mater Sci.* **2013,** *58*, 1244-1315.
[88] Wang, Q. H.; Kalantar-Zadeh, K.; Kis, A.; Coleman, J. N.; Strano, M. S. Electronics and optoelectronics of two-dimensional transition metal dichalcogenides. *Nat. Nanotech.* **2012,** *7*, 699-712.
[89] Tan, C. L.; Zhang, H. Two-dimensional transition metal dichalcogenide nanosheet-based composites. *Chem. Soc. Rev.* **2015,** *44*, 2713-2731.
[90] Castellanos-Gomez, A. Black Phosphorus: Narrow Gap, Wide Applications. *J. Phys. Chem. Lett.* **2015,** *6*, 4280-4291.
[91] Xia, F. N.; Wang, H.; Xiao, D.; Dubey, M.; Ramasubramaniam, A. Two-dimensional material nanophotonics. *Nature Photonics* **2014,** *8*, 899-907.
[92] Island, J. O.; Steele, G. A.; van der Zant, H. S. J.; Castellanos-Gomez, A. Environmental instability of few-layer black phosphorus. *2D Materials* **2015,** *2*, 011002.
[93] Moreno-Moreno, M.; Lopez-Polin, G.; Castellanos-Gomez, A.; Gomez-Navarro, C.; Gomez-Herrero, J. Environmental effects in mechanical properties of few-layer black phosphorus. *2D Materials* **2016,** *3*, 031007.
[94] Akturk, O. U.; Ozcelik, V. O.; Ciraci, S. Single-layer crystalline phases of antimony: Antimonenes. *Phys. Rev. B* **2015,** *91*, 235446.
[95] Zhang, S.; Yan, Z.; Li, Y.; Chen, Z.; Zeng, H. Atomically Thin Arsenene and Antimonene: Semimetal-Semiconductor and Indirect-Direct Band-Gap Transitions. *Angew. Chem. Int. Ed.* **2015,** *54*, 3112-3115.
[96] Zhang, S. L.; Xie, M. Q.; Li, F. Y.; Yan, Z.; Li, Y. F.; Kan, E. J.; Liu, W.; Chen, Z. F.; Zeng, H. B. Semiconducting Group 15 Monolayers: A Broad Range of Band Gaps and High Carrier Mobilities. *Angew. Chem. Int. Ed.* **2016,** *55*, 1666-1669.
[97] Pizzi, G.; Gibertini, M.; Dib, E.; Marzari, N.; Iannaccone, G.; Fiori, G. Performance of arsenene and antimonene double-gate MOSFETs from first principles. *Nat. Commun.* **2016,** *7*, 12585-12585.
[98] Wang, Y.; Ding, Y. Electronic Structure and Carrier Mobilities of Arsenene and Antimonene Nanoribbons: A First-Principle Study. *Nanoscale Res. Lett.* **2015,** *10*, 1-10.
[99] Yao, G.; Luo, Z.; Pan, F.; Xu, W.; Feng, Y. P.; Wang, X.-s. Evolution of Topological Surface States in Antimony Ultra-Thin Films. *Sci. Rep.* **2013,** *3*, 2010.
[100] Zhao, M.; Zhang, X.; Li, L. Strain-driven band inversion and topological aspects in Antimonene. *Sci. Rep.* **2015,** *5*, 16108.
[101] Singh, D.; Gupta, S. K.; Sonvane, Y.; Lukacevic, I. Antimonene: a monolayer material for ultraviolet optical nanodevices. *J. Mater. Chem. C* **2016,** *4*, 6386-6390.
[102] Xu, Y.; Peng, B.; Zhang, H.; Shao, H.; Zhang, R.; Lu, H.; Zhang, D. W.; Zhu, H. First-principle calculations of phononic, electronic and optical properties of monolayer arsenene and antimonene allotropes. *arXiv:1604.03422* **2016**.
[103] http://www.smart-elements.com/.
[104] Castellanos-Gomez, A.; Buscema, M.; van der Zant Herre, S. J.; Steele, G. A. Deterministic transfer of two-dimensional materials by all-dry viscoelastic stamping. *2D Materials* **2014,** *1*, 011002.
[105] Nemes-Incze, P.; Osvath, Z.; Kamaras, K.; Biro, L. P. Anomalies in thickness measurements of graphene and few layer graphite crystals by tapping mode atomic force microscopy. *Carbon* **2008,** *46*, 1435-1442.
[106] http://probe.olympus-global.com/en/.
[107] Wang, X.; Kunc, K.; Loa, I.; Schwarz, U.; Syassen, K. Effect of pressure on the Raman modes of antimony. *Phys. Rev. B* **2006,** *74*, 134305.

[108] Castellanos-Gomez, A.; Wojtaszek, M.; Tombros, N.; Agrait, N.; van Wees, B. J.; Rubio-Bollinger, G. Atomically Thin Mica Flakes and Their Application as Ultrathin Insulating Substrates for Graphene. *Small* **2011,** *7*, 2491-2497.
[109] Gibaja, C*., et al.* Few-Layer Antimonene by Liquid-Phase Exfoliation. *Angew. Chem. Int. Ed.* **2016,** *55*, 14345-14349.
[110] Perdew, J. P.; Burke, K.; Ernzerhof, M. Generalized gradient approximation made simple. *Phys. Rev. Lett.* **1996,** *77*, 3865-3868.
[111] Perdew, J. P.; Burke, K.; Ernzerhof, M. Errata: Generalized gradient approximation made simple. *Phys. Rev. Lett.* **1997,** *78*, 1396.
[112] Krukau, A. V.; Vydrov, O. A.; Izmaylov, A. F.; Scuseria, G. E. Influence of the exchange screening parameter on the performance of screened hybrid functionals. *J. Chem. Phys.* **2006,** *125*, 224106.
[113] Ishigami, M.; Chen, J. H.; Cullen, W. G.; Fuhrer, M. S.; Williams, E. D. Atomic structure of graphene on SiO2. *Nano Lett.* **2007,** *7*, 1643-1648.
[114] Isrraelachvili, J. Intermolecular and Surface Forces. *Academic Press, London* **1991**.
[115] Hanlon, D*., et al.* Liquid exfoliation of solvent-stabilized few-layer black phosphorus for applications beyond electronics. *Nat. Commun.* **2015,** *6*, 8563.
[116] Paton, K. R*., et al.* Scalable production of large quantities of defect-free few-layer graphene by shear exfoliation in liquids. *Nat. Mater.* **2014,** *13*, 624-630.
[117] Kvavle, J.; Bell, C.; Henrie, J.; Schultz, S.; Hawkins, A. Improvement to reflective dielectric film color pictures. *Opt. Express* **2004,** *12*, 5789-5794.
[118] Blake, P.; Hill, E. W.; Castro Neto, A. H.; Novoselov, K. S.; Jiang, D.; Yang, R.; Booth, T. J.; Geim, A. K. Making graphene visible. *Appl. Phys. Lett.* **2007,** *91*, 063124.
[119] Jung, I.; Pelton, M.; Piner, R.; Dikin, D. A.; Stankovich, S.; Watcharotone, S.; Hausner, M.; Ruoff, R. S. Simple approach for high-contrast optical imaging and characterization of graphene-based sheets. *Nano Lett.* **2007,** *7*, 3569-3575.
[120] Roddaro, S.; Pingue, P.; Piazza, V.; Pellegrini, V.; Beltram, F. The optical visibility of graphene: Interference colors of ultrathin graphite on SiO2. *Nano Lett.* **2007,** *7*, 2707-2710.
[121] Benameur, M. M.; Radisavljevic, B.; Heron, J. S.; Sahoo, S.; Berger, H.; Kis, A. Visibility of dichalcogenide nanolayers. *Nanotechnology* **2011,** *22*, 125706.
[122] Castellanos-Gomez, A.; Agrait, N.; Rubio-Bollinger, G. Optical identification of atomically thin dichalcogenide crystals. *Appl. Phys. Lett.* **2010,** *96*, 213116.
[123] Castellanos-Gomez, A*., et al.* Fast and reliable identification of atomically thin layers of TaSe2 crystals. *Nano Res.* **2013,** *6*, 191-199.
[124] Gorbachev, R. V*., et al.* Hunting for Monolayer Boron Nitride: Optical and Raman Signatures. *Small* **2011,** *7*, 465-468.
[125] Palik, E. D., *Handbook of Optical Constants of solids*. San Diego, **1998**.
[126] Hecht, E., *Optics*. Addison-Wesley: Boston, **2001**.
[127] Ghosh, G.; Endo, M.; Iwasaki, T. Temperature-Dependent Sellmeier Coefficients and Chromatic Dispersions for Some Optical Fiber Classes. *J. Lightwave Technol.* **1994,** *12*, 1338-1342.
[128] Brotons-Gisbert, M.; Sanchez-Royo, J. F.; Martinez-Pastor, J. P. Thickness identification of atomically thin InSe nanoflakes on SiO2/Si substrates by optical contrast analysis. *Appl. Surf. Sci.* **2015,** *354*, 453-458.
[129] Wald, G. Human Vision and the Spectrum. *Science* **1945,** *101*, 653-658.
[130] Hsieh, D*., et al.* Observation of Unconventional Quantum Spin Textures in Topological Insulators. *Science* **2009,** *323*, 919-922.

Chapter 5. Summary.

5.1 Conclusions and prospects

5.2 References

Conclusiones

5.1 Conclusions and prospects

The great potential of Atomic Force Microscopy (AFM) to study low-dimensional systems has been highlighted along this manuscript. The versatility of this instrument has allowed studying the behavior of a variety of relevant systems in different configurations. Experiments in this PhD started aiming at electrical characterization of individual chains of MMX polymers from a drop-casting approach and studying different properties of 2D materials. The lack of adequate techniques to create electrical contacts on the MMX chains and/or nanometer-sized objects led us to develop new approaches to electrically contact them. While optimizing these procedures, our interest in the AFM technique itself drove us to its improvement when applied in liquid media, optimizing its performance in different acquisition modes for high resolution of nucleic acids and developing the MFM technique in liquids. In the last part of this PhD, we have focused on the study of the electronic and optical properties of 2D materials, in particular graphene and antimonene. This last one was indeed isolated along this PhD for the very first time. Characterizations of these systems with other complementary techniques, as for instance Raman spectroscopy, Electron Microscopies or X-ray Photoelectron Spectroscopy (XPS), as well as comparison with theoretical calculations, have allowed gaining insight of their multiple properties. The main achievements of this PhD are summarized here. Open questions and prospects arising from the research and instrumental development carried out are also presented.

❖ Two major instrumental developments have been presented:

An experimental setup to allow simultaneous AFM and Total Internal Reflection Fluorescence Microscopy (TIRFM) has been designed, assembled and tested. It enables a variety of measuring modes and user configurable options, through the use of WSxM as control software. It exhibits high stability, being able to image virus like particles with resolutions comparable to the state of the art high resolution images found in the literature.

Albeit this system has shown a promising performance, it still needs more testing. Updates and improvements will show up while the system is being used. For example, a precise temperature control of the sample will be a very interesting option, as well as the possibility to change the sample buffer *in operando*. The combination of a fast Z piezo actuator located in the probe holder for operation in liquid environments will allow faster scanning, including a faster Jumping mode performance. Or the use of the 100 x 100 μm^2 version of the piezo scanner (which is already commercially available) will extend the system capabilities to higher entities, as for example cells.

A probe station setup for the electrical characterization of micro- and nano- materials and devices at temperatures ranging from 80 to 400 K, in a controlled atmosphere, has been designed, assembled and tested. Preliminary results on a novel 2D coordination polymer

have been presented, demonstrating the probe station ready for the measurements it is intended for.

A natural update of the probe station is the assembly of another two X, Y, Z motorized stages for a 4-terminal setup. Further development in the system is currently in progress to allow reaching lower temperatures, ideally down to liquid helium (LHe) temperature (~ 4 K). For this purpose, a continuous flux LHe cryostat has been designed and it is now under construction in SEGAINVEX. Figure 5.1 shows a schematic of this new cryostat.

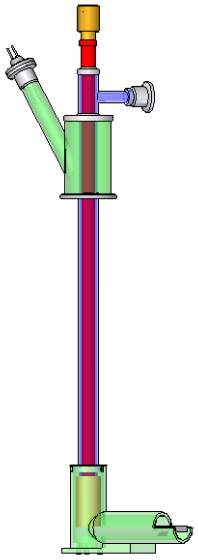

Figure 5.1 Schematic of the liquid helium cryostat designed for the probe station. The cryostat will be inserted in the same vacuum chamber used for the current probe station set up.

The two developments presented here have been carried out on a cross-cutting basis, originated by investigations related to the results presented along this PhD, and thanks to the group long-standing tradition in developing instrumentation and my previous experience in instrumental development. These two instruments will allow experiments that were inaccessible in the group. They will open new lines of research and collaborations with other groups, enabling the advance of different research fields. For example, in the case of the AFM/TIRFM combination a collaboration with Prof. Trevor Douglas (Indiana University) will study the disassembly of P22 virus like particles internally functionalized with green fluorescence protein (GFP). An in the case of the probe station, the study of electrical properties of the so-called smart materials, in particular coordination polymers, is already ongoing. After assembling and initial testing, the two developments have been inherited by new members of the group that are carrying out these experiments.

❖ Double-stranded RNA (dsRNA) has been imaged under near-physiological conditions at high resolution, resolving its A-form sub-helical pitch periodicity. Different high-sensitive force-detection methods have been employed, obtaining images with similar spatial resolution. A combination of experimental results and tip dilation simulations have shown that the limiting factors for high-resolution AFM imaging of soft materials in liquids are the force between tip and sample and the sharpness of the tip apex, rather than the imaging mode.

Further work on this topic can be focused on better understanding the mechanisms that govern high resolution conditions in liquid media. For example, it has been observed experimentally that some tips, unable to provide high resolution in topography images, show double helix features on any of the auxiliary channels, as presented in figure 5.2. To understand this behavior, experimental results combined with much more realistic simulations, at an atomic level, in a fashion as simulations typically carried out by Prof. Rubén Pérez's group in other systems, could shed some light. As already commented, a proper understanding beyond the rough model used in Chapter 3 will require sophisticated simulations.

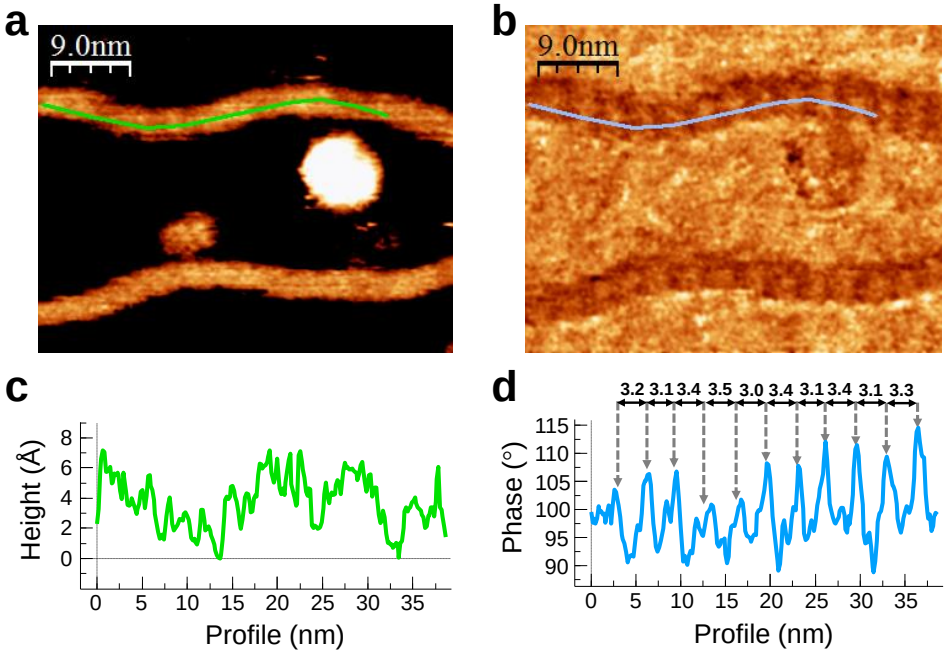

Figure 5.2 AFM images of dsRNA molecules in buffer conditions acquired in AM-AFM mode. a) Topography. b) Phase. Color scales (from dark to bright) were adjusted to enhance the corrugation observed along the dsRNA (1.4 nm and 50° total ranges). c) and d) Profiles along the lines in a) and b) respectively. Whereas the topography image does not present high-resolution, the phase image clearly resolves the double helix pitch.

❖ Magnetic Force Microscopy (MFM) in liquid environments has been presented. A fine tuning of the experimental conditions together with the use of DAM-AFM have allowed imaging magnetic nanostructures in liquids with a resolution close to ambient conditions. It has been applied to the study of Fe_3O_4 nanoparticles, detecting magnetic signals even from a single 30-nm size particle. Preliminary results with customized MFM probes point to an enhanced magnetic signal that will allow studying "bio-nano-magnetic" samples in physiological conditions, opening new possibilities in fields such as nanomedicine, nanobiotechnology or catalysis. Further work on optimizing these customized probes is still needed and is currently being carried out.

In the context of "bio-nano-magnetic" samples, two collaborations have already started. First one is focused on studying magnetic bacteria, which are interesting entities for applications involving magnetic markers for biosensing. The second collaboration intends to study virus-like particles filled with a magnetic cargo, which are promising candidates as nano-containers for applications such as magnetic hyperthermia treatments.

❖ Exfoliated graphite flakes (EGF) as soft-electrodes for the electrical contact of nano-objects have been introduced. This procedure takes advantage of all-dry viscoelastic stamping transfer methods to create microelectrodes, avoiding the harsh conditions of standard lithographic techniques. Multiple possibilities of EGF soft-electrodes have been presented, including electrical characterization of carbon nanotubes, MMX fibers, and graphene-based materials, as well as circuit repairing. Among the advantages of EGF soft-electrodes, two of them can be highlighted. First, it is a very cost-effective solution for creating microelectrodes with very well-defined edges and sub-micrometer positioning resolution. And second, and more important, it allows contacting molecules with limited stability under standard lithographic conditions.

Up to now we have connected the EGF soft-electrodes to the macro-world by using hand-deposited silver paint contacts. Improvements on the technique could go through the use of a more reproducible way of connection to external devices. On this sense, a simple example could be the use of conductive pens, which are pens loaded with conductive inks, as for instance silver [1] or nickel [2] based solutions. By coupling this kind of pens to the XYZ micromanipulator used for the EGF transfer, a much more controlled creation of the final macro-contact could be achieved. Figure 5.3 shows photographs of these conductive pens.

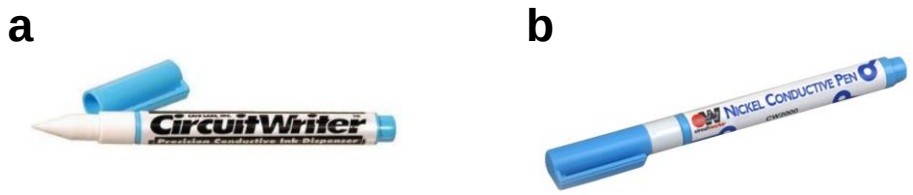

Figure 5.3 Conductive pens. a) Silver based. b) Nickel based. Images taken from http://www.mcmelectronics.com and https://www.chemtronics.com respectively.

❖ Probe-Assisted Nanowire (PAN) lithography has been presented. This technique is based on the adsorption of Au nanowires on the sample of interest and subsequent manipulation with an AFM probe to create nanoelectrodes, thanks to their cold welding ability. Albeit in this thesis two-terminal configurations have been used, employing a metallized AFM probe as a second mobile electrode, any electrical configuration can be created (two-terminal plus a gate voltage, four-terminal, etc.). PAN lithography presents a series of advantages that make us think it can revolutionize the way nanoelectrodes are fabricated so far. As in the case of the EGF soft-electrodes, Au nanoelectrodes created with PAN lithography avoid the harsh conditions of standard lithographic techniques. Electrode locations can be easily reconfigured, hence allowing multiple measurements in different features and/or configurations on the same sample. It allows probing the electrical properties of very small nano-objects, otherwise impossible to contact using conventional procedures. In this context, combination with thinner Au nanowires or nanorods (also commercially available), as depicted in figure 5.3, could enable electrical characterizations with nanometer-sized gaps in a very controlled way.

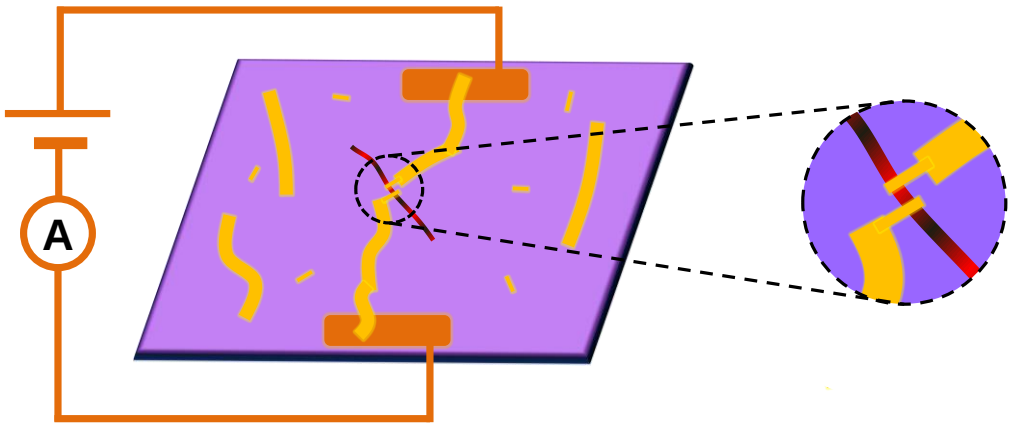

Figure 5.3 Schematics of PAN lithography applied to measurements with nanometer-sized gaps. Au nanorods could be cold welded at the end of the nanowires to achieve even smaller gaps.

Albeit the operation principle of PAN lithography has been successfully demonstrated, a lot of work needs still to be done. Measurements in different terminal configurations and with different samples are being carried out to demonstrate all the potential of the technique. Longer Au nanowires would be desirable in order to facilitate the creation of nanoelectrodes assemblies minimizing the number of manipulations. In this sense, other metal nanowires should be explored, such as for instance silver nanowires, which are commercially available in lengths much longer than for gold, for example 50 nm diameter and 50 μm long (http://novarials.com). Their dimensions and also their active role in the conduction properties of some materials (as for instance in the $[Cu_{2.6}I_{2.6}(TAA)]_n$ nano-films, presented at the end of Chapter 2) make them good candidates to explore for application in PAN lithography. A full development of this method is a potential topic for an ambitious research project.

❖ Electrical properties of MMX chains obtained from a wet chemistry approach have been presented, going down to the single molecule level. The robustness of the assembly of highly conductive MMX chains by a simple drop-casting approach has been assessed by initially studying fibers of three different compounds, $[Pt_2(RCS_2)_4I]_n$, with R = alkyl group: Me, Et and Pen. Additionally, electrical characterization of the $[Pt_2(EtCS_2)_4I]_n$ case down to individual chains has been performed, presenting a record electrical conductivity for long distances on the single molecule level, confirming MMX chains from a wet chemistry approach as very good candidates for molecular wires.

The measurements performed here demonstrate the potential of MMX chains obtained from drop-casting. However, further characterization will shed light on their transport mechanisms. For example, electrical characterization of MMX fibres at different temperatures and/or in a Field-Effect Transistor (FET) configuration would be interesting to gain insight of the effect of disorder and doping on these structures.

For the use of these MMX chains in real applications further improvements are required. A more controlled geometry of the resulting fibers would be desirable. This could be enhanced by a fine tuning of the deposition conditions. Additionally, by adjusting the chemistry of the self-assembling process, individual chains with a lower amount of defects could be created, increasing their already high conductivity.

❖ Controlled tuning of graphene electronic properties upon ultrahigh pressure AFM (> 10 GPa) has been presented. This process enables the creation of different hole-doped graphene areas, as corroborated by Kelvin Probe Force Microscopy (KPM), Raman spectroscopy and X-ray Photoelectron Spectroscopy (XPS), allowing a very controlled and stable tuning of graphene doping level. One direct application of this doping is the

improvement of the contact resistance of selected areas when using metal electrodes, a very relevant issue in the field of graphene electronics. Ultrahigh pressure modifications in graphene have provided as well evidence of its suitability as a protective coating and an easy way to improve sealing actuation, important for membrane applications.

It remains still as a challenge the identification of the mechanism that keeps graphene so well coupled to the substrate. Preliminary DFT calculations suggest that a small degree of chemical bonding between graphene and SiO_2 is needed for the irreversible coupling observed in the modified areas. The low bending rigidity of graphene, ~ 0.6 eV [3], allows it to easily accommodate to the substrate surface roughness. Thus, a very small amount of bonds are expected to be necessary, below the sensitivity of the instruments. A possible option to detect these bonds experimentally could be the use of atomically flat substrates, such as mica or sapphire single crystals, where a higher number of bonds would be expected.

Results here presented open a lot of new possibilities. The controlled doping achieved here could be combined with other doping techniques (such as electrostatic gating, interface engineering, chemical approaches, thermal annealing or gas flow experiments), possibly resulting in unprecedented levels of controlled graphene doping.

The application of similar procedures on the different elements and compounds of the 2D family could enable the local tuning of their electronic properties. This can be particularly relevant in those materials presenting band gaps, since it would allow controlled local modifications of the band gap values. As in the case of graphene, it could provide as well an easy way to create areas with improved resistance for the positioning of metal electrodes, which will enhance their performance when incorporated to electronic devices.

Our results could be also applied to heterostructures of 2D materials, which are isolated atomic planes of different species assembled into layer-by-layer structures in a precisely chosen sequence. The properties of different heterostructures, such as for example graphene/boron nitride, graphene/molybdenum disulfide, etc. and combinations of them could be locally tuned upon ultrahigh pressure modifications.

In the membranes context, it is reported that graphene is “ultrastrongly” adhered to SiO_2 substrates by van der Waals forces [4]. Our results suggest that graphene adhesion can be locally increased, resulting in a “giant ultrastrong” adhesion, with relevance in membrane applications. An interesting measurement would be to quantify the adhesion energy in graphene modified upon ultrahigh pressure, as done by Koenig and coworkers in reference [4].

Another novel and appealing application would be the local study of chemical reactions upon ultrahigh pressures. Molecules could be trapped between a supporting substrate and a

graphene layer. Then, ultrahigh pressure could be applied to the system to induce chemical reactions otherwise very difficult to produce.

All these possibilities will be explored in a new project that has been recently approved to study the properties of 2D materials at ultrahigh local pressures.

❖ A new 2D material has been presented, antimonene, isolated along this thesis for the very first time. Theoretical calculations predict different interesting properties for this material, including a band gap opening when reaching the single layer regime, interesting for optoelectronic applications. It can be somehow compared to Black Phosphorus (BP), but without the high hygroscopicity (tendency to absorb water) in ambient conditions exhibited by BP. We have isolated single to few-layer antimonene on SiO_2/Si substrates and given evidence of its high mechanical, electrical and chemical stability under ambient conditions and even immersed in water. Optical identification of few-layer antimonene has been performed, providing the optimal combination of illumination conditions and SiO_2 substrate thickness to ease its visualization. Preliminary results on the electrical properties of few-layer antimonene have been also presented, pointing to an exciting conductive behavior governed by topologically protected surface states.

The isolation for the first time of antimonene has triggered the study of the many interesting properties that are predicted by theory, opening an exciting field to explore. Among one of the most relevant questions which is still elusive, we can find the experimental measurement of the band gap of single to few-layer antimonene. Theoretical calculations predict a band gap opening, ranging from ~ 1.6 to 2.3 eV depending on the authors [5, 6]. PAN lithography on micromechanically exfoliated flakes could be an option, but the low yield of single-layer terraces has hampered this measurement. A recent work producing single layer antimonene films by molecular beam epitaxy (MBE) on $PdTe_2$ substrates [7] could possibly help on this achievement.

Many research groups have started experimental studies on antimonene encouraged by our results. Further fabrication methods, characterization and applications derived of its exciting properties are expected in the near future.

5.2 References

[1] http://www.mcmelectronics.com/product/CAIG-LABORATORIES-CW100P-/200-175.
[2] https://www.chemtronics.com/p-705-circuitworks-nickel-conductive-pen.aspx.
[3] Anemone, G.; Climent-Pascual, E.; Yu, H. K.; Al Taleb, A.; Jimenez-Villacorta, F.; Prieto, C.; Wodtke, A. M.; De Andres, A.; Farias, D. Quality of graphene on sapphire: long-range order from helium diffraction versus lattice defects from Raman spectroscopy. *RSC Adv.* **2016,** *6*, 21235-21245.
[4] Koenig, S. P.; G., B. N.; Dunn, L. M.; Bunch, J. S. Ultrastrong adhesion of graphene membranes. *Nat. Nanotech.* **2011,** *6*, 543-546.
[5] Akturk, O. U.; Ozcelik, V. O.; Ciraci, S. Single-layer crystalline phases of antimony: Antimonenes. *Phys. Rev. B* **2015,** *91*, 235446.
[6] Zhang, S.; Yan, Z.; Li, Y.; Chen, Z.; Zeng, H. Atomically Thin Arsenene and Antimonene: Semimetal-Semiconductor and Indirect-Direct Band-Gap Transitions. *Angew. Chem. Int. Ed.* **2015,** *54*, 3112-3115.
[7] Wu, X.*, et al.* Epitaxial Growth and Air-Stability of Monolayer Antimonene on PdTe2. *Adv. Mater.* **2016**, 1605407.

Conclusiones.

A lo largo de esta memoria se ha mostrado el gran potencial de la microscopía de fuerzas atómicas (AFM por sus siglas en inglés) para el estudio de sistemas de baja dimensionalidad. La versatilidad de este instrumento ha permitido estudiar el comportamiento de diversos sistemas de interés, en diferentes configuraciones. La investigación llevada a cabo en esta tesis inicialmente estaba enfocada en dos aspectos. En primer lugar, al estudio de las propiedades eléctricas de cadenas individuales de polímeros MMX obtenidos por autoensamblaje en fase líquida. En segundo lugar, al estudio de diferentes propiedades de materiales bidimensionales (2D). La falta de técnicas adecuadas para contactar eléctricamente estas cadenas o nanoobjetos de dimensiones muy reducidas, nos llevó a desarrollar nuevos métodos para la fabricación de micro- y nanocontactos. A la vez que optimizábamos estos procedimientos, nuestro interés en la técnica del AFM por sí misma nos condujo a su mejora aplicada a medidas en medio líquido. Por una parte, optimizamos el funcionamiento de distintos modos de medida aplicada a la alta resolución de ácidos nucleicos. Y por otra, desarrollamos la técnica de microscopía de fuerzas magnéticas (MFM por sus siglas en inglés) aplicada a líquidos. En la parte final de la tesis, nos hemos centrado en el estudio de las propiedades electrónicas y ópticas de materiales 2D, en particular de grafeno y antimoneno. De hecho, este último, hasta ahora solamente predicho teóricamente, ha sido por primera vez aislado en el desarrollo de esta tesis. La caracterización de estos sistemas con técnicas complementarias, como pueden ser espectroscopía Raman, microscopías electrónicas o espectroscopía de fotoelectrones emitidos por rayos X (XPS por sus siglas en inglés), junto con cálculos teóricos, han permitido obtener información de sus múltiples propiedades. A continuación se resumen los principales logros de esta tesis.

- Se han presentado dos desarrollos instrumentales:

Se ha diseñado, construido y probado un nuevo sistema de AFM que permite medidas simultáneas de AFM y microscopía de fluorescencia por reflexión total interna (TIRFM por sus siglas en inglés). La elección de WSxM como programa de control le permite una gran variedad de modos de medida y opciones configurables por el usuario. Presenta una alta estabilidad, siendo capaz de tomar imágenes de partículas víricas, obteniendo resoluciones comparables a las imágenes punteras en el campo presentes en la literatura.

Se ha diseñado, construido y probado una estación de puntas para la caracterización eléctrica de materiales en la micro- y nanoescala, en un rango de temperaturas entre 80 y 400 K y con un ambiente controlado. Resultados preliminares en un novedoso polímero de

coordinación bidimensional han demostrado que la estación está lista para el tipo de medidas para las que fue diseñada.

Estos dos desarrollos han sido realizados de forma transversal en el trascurso de esta tesis, originados por investigaciones relacionadas con los resultados que se han presentado en esta memoria. Se han llevado a cabo gracias a la larga tradición del grupo en desarrollo instrumental y a mi experiencia previa en instrumentación.

❖ Se han obtenido imágenes de alta resolución de ácido ribonucleico de cadena doble (dsRNA por sus siglas en inglés) en condiciones próximas a las fisiológicas, resolviendo su estructura tipo A con resolución por debajo del paso helicoidal. Para ello, se han empleado diferentes modos de medida de alta sensibilidad para la detección de fuerzas, obteniendo imágenes con una resolución espacial similar independiente del modo de medida. Se ha llevado a cabo una combinación de resultados experimentales y simulaciones de efectos de dilatación de la punta del AFM. Dicha combinación muestra que, para la obtención con AFM de alta resolución en materiales blandos en medio líquido, los factores limitantes son, no tanto la elección de uno u otro modo de medida, si no la fuerza entre punta y muestra y el afilado de la terminación de la punta.

❖ Se ha presentado la microscopía de fuerzas magnéticas (MFM) en líquidos. Un ajuste fino de las condiciones experimentales y el uso del modo de adquisición por modulación de la amplitud de excitación (*Drive Amplitude Modulation*, DAM-AFM en inglés) ha permitido visualizar nanoestructuras magnéticas en medio líquido con una resolución cercana a la obtenida en condiciones ambiente. La técnica de MFM se ha aplicado al estudio de nanopartículas de Fe_3O_4, detectando señales magnéticas incluso de partículas individuales de tamaño 30 nm. Estudios preliminares usando puntas magnéticas personalizadas, apuntan a la obtención de aumentos significativos en la medida de señales magnéticas. Dichas puntas, todavía en desarrollo, permitirán el estudio de muestras "bio-nano-magnéticas" en condiciones fisiológicas, abriendo nuevas posibilidades en campos como la nanomedicina, la nanobiotecnología o la nanocatálisis.

❖ Se han presentado láminas de grafito exfoliado (*exfoliated graphite flakes*, EGF en inglés) como electrodos suaves para el contacto eléctrico de nanoobjetos. Este procedimiento aprovecha los métodos secos de transferencia mediante un sello viscoelástico para fabricar microelectrodos, evitando así las condiciones agresivas de las técnicas litográficas habituales. Se han mostrado ejemplos de las múltiples posibilidades que ofrece esta técnica: caracterización de nanotubos de carbono, fibras MMX obtenidas

por autoensamblaje en fase líquida y materiales basados en carbono, como grafeno exfoliado y grafeno reducido a partir de óxido de grafeno. De igual manera se ha mostrado su potencial para reparar microcircuitos. De entre las ventajas que ofrece esta técnica, podemos resaltar dos. En primer lugar, ofrece una solución muy económica para la fabricación de microcontactos, los cuales tienen bordes muy bien definidos y se pueden posicionar con resolución submicrométrica. En segundo lugar, y más importante, permite contactar eléctricamente moléculas con estabilidad limitada a las condiciones de las litografías estándar.

❖ Se ha presentado la litografía de nanohilos asistida por sonda local (*Probe-Assisted Nanowire* (PAN) *lithography* en inglés). Esta técnica se basa en la adsorción de nanohilos de oro en la muestra de interés, combinado con su manipulación utilizando la punta de un AFM, para la fabricación de nanoelectrodos, aprovechando su habilidad para soldar a temperatura ambiente. Si bien en esta memoria se ha utilizado una configuración de dos terminales de medida, donde uno de ellos es una punta metálica de AFM que se utiliza como segundo electrodo móvil, esta técnica permite la fabricación de nanoelectrodos en cualquier configuración (dos terminales con voltaje *gate*, cuatro terminales, etc.). La litografía PAN presenta una serie de ventajas que nos hacen pensar que en un futuro podría revolucionar la fabricación de nanolectrodos. Como en el caso de los electrodos de grafito exfoliado, los nanoelectrodos fabricados con litografía PAN evitan las duras condiciones de las técnicas litográficas estándar. Además, las posiciones de los electrodos pueden ser fácilmente reconfiguradas, permitiendo así múltiples medidas en distintos nanobjetos y/o en distintas configuraciones dentro de una misma muestra. También permite la caracterización eléctrica de nanoobjetos de dimensiones muy reducidas, imposibles de contactar con los procedimientos habituales, y medidas con distancias entre electrodos de unos pocos nanómetros.

❖ Se han obtenido y caracterizado eléctricamente fibras y cadenas de polímeros MMX obtenidas a partir de autoensamblaje en fase líquida, llegando hasta la obtención y caracterización de cadenas a nivel de molécula individual. La robustez del autoensamblado de estas cadenas altamente conductoras se ha verificado estudiando fibras de tres compuestos diferentes, $[Pt_2(RCS_2)_4I]_n$ (R = grupo alquilo: Me - metilo; Et - etilo; Pen - pentilo). Además, en el caso del etilo, se han llegado a visualizar y caracterizar eléctricamente cadenas individuales, las cuales presentan el record de conductividad a largas distancias a nivel de molécula individual. Estos resultados confirman las cadenas de polímeros MMX obtenidas desde fase líquida como muy buenas candidatas a cables moleculares con aplicaciones en nanoelectrónica.

❖ Se ha presentado la modificación controlada de las propiedades electrónicas de grafeno mediante la aplicación de presiones ultra altas (> 10 GPa). Este procedimiento ha permitido la fabricación de diferentes áreas de grafeno dopadas con huecos, tal y como han confirmado medidas de microscopía local de sonda Kelvin (KPM por sus siglas en inglés), espectroscopía Raman y XPS. Esto ha dado lugar a una forma muy controlada y estable de modificar el nivel de dopaje del grafeno. Una aplicación directa de este dopaje es la mejora de la resistencia de contacto de áreas seleccionadas, para la posterior colocación en ellas de electrodos metálicos. Este hecho es muy relevante en el campo de la electrónica basada en grafeno. Las modificaciones en grafeno a través de la aplicación de presiones ultra altas, han permitido mostrar evidencias de su aplicabilidad como recubrimiento protector de superficies. De igual manera, se ha demostrado que es una forma sencilla de mejorar su comportamiento en el sellado de microcavidades, hecho relevante para aplicaciones de grafeno como membrana.

❖ Se ha presentado un nuevo material 2D, el antimoneno, hasta ahora sólo predicho teóricamente y aislado por primera vez en el desarrollo de esta tesis. Cálculos teóricos predicen muchas y muy interesantes propiedades para este material, incluyendo la apertura de un *gap* electrónico al llegar a la monocapa, con un valor muy atractivo para aplicaciones optoelectrónicas. De alguna manera se puede comparar al fósforo negro en su forma bidimensional, pero sin la relativamente alta reactividad de éste en condiciones ambiente. En esta tesis se ha aislado antimonene desde una única monocapa a unas pocas capas en sustratos de SiO_2/Si. Se han dado evidencias de su estabilidad mecánica, eléctrica y química en condiciones ambiente, e incluso sumergido en agua. Se ha estudiado el comportamiento óptico de antimoneno de pocas capas, proporcionando la combinación óptima de iluminación y espesor del SiO_2 del sustrato para facilitar su identificación óptica. También se han presentado resultados preliminares de las propiedades electrónicas de antimoneno de pocas capas, los cuales apuntan a un fascinante comportamiento de conducción gobernado por estados superficiales protegidos topológicamente.
Muchos grupos de investigación han comenzado estudios en antimoneno alentados por estos resultados. Estamos convencidos de que en un futuro próximo aparecerán nuevos métodos para su fabricación, así como aplicaciones basadas en sus fascinantes propiedades.

Agradecimientos.

Una vez mostrado el trabajo desarrollado a lo largo de esta tesis, es el momento de dar las gracias a todos los que, de una u otra forma, habéis contribuido a que se haya podido llevar a buen término. Quede de antemano dicho que, si tuviese que mencionar una por una a todas las personas que me habéis ayudado, esto se convertiría en una lista interminable. Es por ello que, si no aparece tu nombre aquí de forma explícita, no por ello quiere decir que no te lo agradezca. De hecho, si te encuentras leyendo estas páginas, gracias por tu interés en el trabajo y esfuerzo que ha supuesto el poder llegar a escribir esta tesis.

Una vez dicho esto, en primer lugar es un placer para mí agradecer a mis directores de tesis, Julio y Adriana. Por su confianza, la ilusión que han puesto en todo momento y su paciencia para guiarme por el buen camino, en las ocasiones en que me pude apartar de él. Ciertamente, ha sido una gran combinación de directores de tesis, complementándose a la perfección, no sólo para abarcar, si no para mejorar todos los aspectos necesarios en la buena dirección de una tesis. Entre todas vuestras cualidades, en Julio quiero resaltar tu ilusión por la ciencia, tu fuente inagotable de ideas, todas ellas de gran valor, que sin lugar a dudas han modelado lo que es esta tesis. Gracias por tu tiempo, siempre dispuesto a estar conmigo en el laboratorio a pesar de tus muchas obligaciones. Gracias también todas las veces que me has acercado en coche hasta Madrid, momentos a última hora de la tarde que, en muchas ocasiones, servían para resumir lo que había sido el día o ir preparando lo que íbamos a hacer al día siguiente. Adriana, en ti me gustaría resaltar tu grado de sensatez a la hora no sólo de afrontar nuevos retos, sino también a la hora de analizar lo que íbamos obteniendo, aportando en todo momento un punto de vista reflexivo y un rigor indispensables en cualquier investigación. Quiero agradecerte también tu compromiso y tu tiempo, sé que no ha sido fácil compaginar la dirección de esta tesis con el resto de tus obligaciones.

A continuación, a Félix por todo el apoyo que me ha proporcionado en las numerosas colaboraciones que hemos llevado a cabo. Has estado siempre ahí para discutir sobre cualquier tema, aportando un punto de vista diferente desde tu formación química al que podíamos aportar nosotros. El tándem que hacéis Julio y tú me parece excepcional, os agradezco que confiarais en mí para incorporarme a proyectos complicados en los que llevabais largo tiempo trabajando.

Paso ahora a agradecer a los que fueron mis compañeros en Nanotec a lo largo de los años que estuve allí. En particular, a Rafa Fernández, director general en el momento en que empezó a gestarse la idea de que yo pudiese hacer una tesis. En aquel momento, junto con Adriana, directora científica, me permitieron compaginar mi trabajo allí con el máster de Física de la Materia Condensada y Nanotecnología, paso previo y necesario para poder comenzar a continuación el doctorado. Si bien éste finalmente se ha desarrollado prácticamente en su totalidad ya una vez cerrado Nanotec, toda la experiencia previa acumulada allí ha sido fundamental para el desarrollo de esta tesis. Así mismo, al resto de compañeros su apoyo y comprensión en todo lo que me pudo hacer falta durante ese período. Aquí he de hacer una mención especial a Nacho, Alejandro y Belén, siempre dispuestos a implementar dentro de lo posible mis comentarios, sugerencias y necesidades en el WSxM. En particular a Nacho, con el que he coincido también en el laboratorio, por tu disposición a echarme una mano en lo que hiciese falta, aportando tu siempre valioso y razonado punto de vista a cualquier problema que pudiese tener. A Luis, gran conocedor de todos los aspectos de la técnica del AFM, te agradezco gran parte de lo que sé sobre ella. A Miriam Moreno, con la que he coincidido también después en el laboratorio, por toda la ayuda que me has prestado, tanto en la etapa de Nanotec como en la posterior en el laboratorio. Siempre has estado ahí con una buena cara cuando he necesitado algo, como por ejemplo cuando te preguntaba por enésima vez alguna cosa sobre la evaporadora. A Edu y a Jaime por vuestro apoyo y confianza en mi persona. A todos vosotros quiero agradeceros finalmente también vuestra amistad, que ha trascendido más allá del ámbito profesional. Finalmente, en el contexto de Nanotec, quiero hacer una especial mención a todos los que fuisteis clientes y usuarios. Fueron en gran parte vuestras preguntas y necesidades las que me permitieron ir profundizando cada vez más en la técnica del AFM.

En el ámbito científico, quiero agradecer a todos los integrantes del grupo con los que he coincidido a lo largo de los años vuestra disponibilidad y ayuda siempre que la he necesitado. Soy consciente de que, sobre todo durante mi etapa en Nanotec, cuando venía al laboratorio en los momentos que tenía disponibles, podía ser un incordio que os distraía de vuestras tareas cuando necesitaba ayuda. Gracias por prestármela desinteresadamente y por poner siempre una buena cara. Mención especial para la parte de AFM, Cristina, Willy y Miriam Jaafar (junto con Miriam Moreno, como ya he mencionado anteriormente), con los que he tenido el placer de colaborar más estrechamente, y con los que he compartido más tiempo. Lo he dicho ya alguna vez, pero quiero repetirlo aquí, es difícil pensar en mejores compañeros de laboratorio, siempre ahí para lo que hiciese falta. Gracias también a los "exfoliadores" con los que he coincidido, Raúl y Diego.

Del laboratorio de virus, Merche, Álvaro, Aida, y más recientemente Marina, Natalia, Manu y Paco, siempre amables a la hora de echarme una mano para preparar alguna muestra o cualquier cosa que necesitase. Pedro, muchas gracias por tu entusiasmo y tu

vitalidad. Ha sido un gusto trabajar contigo, siempre mostrando un apasionamiento contagioso por lo que haces.
De la gente de UHV, Antonio, Bruno, Héctor y Ana, y más recientemente Alba, Mariano, Eva y Diego. Ha sido un placer compartir este tiempo con vosotros, gracias por vuestros puntos de vista distintos a los de la gente que trabajamos con cosas que dirías "enormes" y "sucias". Chema e Iván, gracias por vuestros consejos y puntos de vista críticos. Me parecen fundamentales en la formación de un buen científico.
En este contexto, hacer mención a todos los docentes que he tenido a lo largo de mi vida, tanto a los buenos como a los no tan buenos, ya que de todos he aprendido algo.
Para terminar con el ámbito científico, quiero agradecer a mis colaboradores su tiempo y confianza en los proyectos conjuntos llevados a cabo. Agus y Eider del ICMM; Fernando, Maru y Alejandro del CNB; Pilar, David, Miguel Ángel y Carlos del grupo de Félix; y finalmente Pilar Segovia y Enrique García Michel, gracias por ilustrarme en el mundo de los sincrotrones. Y a los grupos teóricos de Juanjo Palacios, José Soler y Fernando Martín, gracias por vuestro tiempo para explicarme vuestros cálculos e intentar ayudarme a entender mejor las cosas.

Special thanks to Ron Reifenberger and Arvin Raman. Our initial collaboration manipulating carbon nanotubes into shapes with the AFM triggered somehow this PhD. I want to acknowledge your time for discussion along these years and your valuable advice.

En un ámbito más técnico, gracias a Santiago, José María y a todo el personal del SEGAINVEX, por vuestra inestimable ayuda para la fabricación y montaje de los distintos instrumentos que hemos construido durante la tesis. Gracias no sólo por hacer bien vuestro trabajo, sino también por aportar vuestra experiencia y saber hacer, poniéndonos los pies en el suelo cuando era necesario, lo cual en la mayoría de las ocasiones nos aportaba soluciones mejores a las que se nos habían ocurrido. A Eloy, por su paciencia para probar las cosas. Y a Adolfo, del Raman, por su dedicación y buen hacer. Gracias a Elsa, Luisa y más recientemente Ángeles por vuestro buen hacer en el siempre complicado tema de papeleos.

Para terminar los agradecimientos del ámbito más profesional, mi reconocimiento a todos los que, de alguna manera, habéis revisado parte o la totalidad de esta memoria.

En el ámbito personal, quiero agradecer en primer lugar a mi familia. A mis padres, Santiago y Ángela, que sólo desean lo mejor para mí y se alegran por los frutos del trabajo de estos años. Nunca podré estar suficientemente agradecido por todos los esfuerzos que habéis hecho a lo largo de vuestra vida, y que ahora en mi caso se ven reflejados en esta tesis. A mi hermano Saúl, faro que en cierta medida sirve de referencia a mi carrera científica, y a Sanna, por hacerlo feliz. Quiero agradecer también a mis otros padres, Arturo y Leonor, vuestro apoyo incondicional e interés en mis investigaciones. A Grego e Ignacio, junto con mis sobrinas Marta y Sara, por vuestros ánimos.

A mis amigos tanto de El Bierzo como de Madrid, dispersados ahora por todo el mundo (y más allá), quiero agradeceros vuestra ayuda y compañía en aspectos más cotidianos de la vida, tan necesarias para no acabar desquiciado a veces del ámbito científico.

Y en último lugar, pero no por ello menos importante, sino todo lo contrario, quiero agradecer a mi mujer, Cristina. Ella es la que me aguanta todos los días y me sirve de inspiración y apoyo. Si alguna vez alguien ha podido pensar que soy una persona trabajadora y eficiente, es porque no te conocen. Gracias por tu vitalidad y tu entusiasmo. Por estar siempre ahí y por todo lo que haces por mí. Por todas las cosas que me dices, y también por las que no me dices. Por tu apoyo incondicional a mi carrera científica, a sabiendas de que no es un camino fácil. Gracias por compartir tu vida conmigo y de esta forma hacerme feliz. GRACIAS.

Pablo Ares García

Madrid, abril de 2017

Este trabajo ha sido en parte posible gracias a la financiación de los proyectos “Tecnología de Microscopía de Fuerza para Aplicaciones de Nanomecánica y Nanomedicina”, ref. CSD2010-00024, dirigido por Julio Gómez Herrero y “Caracterización de la estabilidad de contenedores proteicos funcionales” ref. FIS2014-59562-R, dirigido por Pedro J. de Pablo.

List of Publications.

Publications during my PhD

1. **Few-layer antimonene electrical properties**
   In preparation.

2. **Probe Assisted Nanowire (PAN) lithography**
   In preparation.

3. **Invited chapter on high resolution imaging of nucleic acids for an edition on Nanoscale Imaging**
   In preparation.

4. **Invited review article on antimonene for Adv. Mater.**
   In preparation.

5. **Noncovalent functionalization and charge transfer in antimonene**
   To be submitted.

6. **High electrical conductivity of single metal-organic chains**
   Ares P., Amo-Ochoa P., Soler J., Palacios J. J., Gomez-Herrero J., and Zamora F., *Submitted*.

7. **Optical identification of few-layer antimonene crystals**
   Ares P., Zamora F., and Gomez-Herrero J., *ACS Photonics*. **2017** DOI: 10.1021/acsphotonics.6b00941

8. **Few-Layer Antimonene by Liquid-Phase Exfoliation**
   Gibaja C., Rodriguez-San-Miguel D., Ares P., Gomez-Herrero J., Varela M., Gillen R., Maultzsch J., Hauke F., Hirsch A., Abellan G., and Zamora F., *Angew. Chem. Int. Ed.* **2016**, *55*, 14345-14349. Hot paper. Cover.

9. **Mechanical Isolation of Highly Stable Antimonene under Ambient Conditions**
   Ares P., Aguilar-Galindo F., Rodriguez-San-Miguel D., Aldave D. A., Díaz-Tendero S., Alcamí M., Martín F., Gomez-Herrero J., and Zamora F., *Adv. Mater.* **2016**, *28*, 6332-6336. VIP paper. Cover.

10. **High resolution atomic force microscopy of double-stranded RNA**
    Ares P., Fuentes-Perez M. E., Herrero-Galán E., Valpuesta J. M., Gil A., Gomez-Herrero J., and Moreno-Herrero F., *Nanoscale* **2016**, *8*, 11818. Cover.

11. **Magnetic Force Microscopy in Liquids**
    Ares P., Jaafar M., Gil A., Gomez-Herrero J., and Asenjo A., *Small* **2015**, *11*, 4731-4736.

12. **Exfoliated graphite flakes as soft-electrodes for precisely contacting nanoobjects**
    Ares P., Lopez-Polin G., Hermosa C., Zamora F., Gomez-Herrero J., and Gomez-Navarro C., *2D Materials* **2015**, *2*, 035008.

13. **'Flatten plus': a recent implementation in WSxM for biological research**
    Gimeno A., Ares P., Horcas I., Gil A., Gomez-Rodriguez J. M., Colchero J., Gomez-Herrero J., *Bioinformatics* **2015**, *31*, 2918-2920.

Patents:

Procedimiento de obtención de microcontactos, microcontacto obtenible y uso del mismo
López-Polín G., Ares P., Zamora F. & Gómez-Herrero J., ES2557507B1. **2014**.

Oher publications (before PhD)

1. **Interplay between the mechanics of bacteriophage fibers and the strength of virus-host links**
   Ares P., Garcia-Doval C., Llauro A., Gomez-Herrero J., van Raaij M. J., and de Pablo P. J., *Phys. Rev. E* **2014**, *89*, 052710.

2. **Minimizing tip–sample forces in jumping mode atomic force microscopy in liquid**
   Ortega-Esteban A., Horcas I., Hernando-Perez M., Ares P., Perez-Berna A. J., San Martin C., Carrascosa J. L., de Pablo P. J., and Gomez-Herrero J., *Ultramicroscopy* **2012**, *114*, 56-61.

3. **Tailored graphene materials by chemical reduction of graphene oxides of different atomic structure**
   Botas C., Alvarez P., Blanco C., Gutierrez M. D., Ares P., Zamani R., Arbiol J., Morante J. R., and Menendez R., *RSC Adv.* **2012**, *2*, 9643-9650.

4. **Neck-size distributions of through-pores in polymer membranes**
   Agarwal C., Pandey A. K., Das S., Sharma M. K., Pattyn D., Ares P., and Goswami A., *J. Membrane Sci.* **2012** *415-416*, 608-615.

5. **The effect of the parent graphite on the structure of graphene oxide**
   Botas C., Alvarez P., Blanco C., Santamaria R., Granda M., Ares P., Rodriguez-Reinoso F., and Menendez R., *Carbon* **2012**, *50*, 275-282.

6. **Strain energy and lateral friction force distributions of carbon nanotubes manipulated into shapes by atomic force microscopy**
   Strus M. C., Lahiji R. R., Ares P., Lopez V., Raman A., and Reifenberger R., *Nanotechnology* **2009**, *20*, 385709.

7. **Variable-field magnetic force microscopy**
   Jaafar M., Gomez-Herrero J., Gil A., Ares P., Vazquez M., and Asenjo A., *Ultramicroscopy* **2009**, *109*, 693-699. Cover.

8. **Cutting down the forest of peaks in acoustic dynamic atomic force microscopy in liquid**
   Carrasco C., Ares P., de Pablo P. J., and Gomez-Herrero J., *Rev. Sci. Instrum.* **2008**, *79*, 126106.

Covers

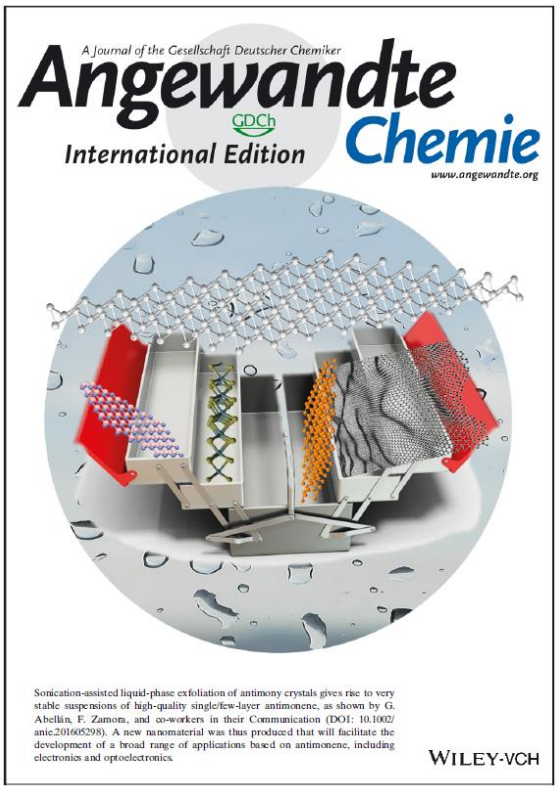

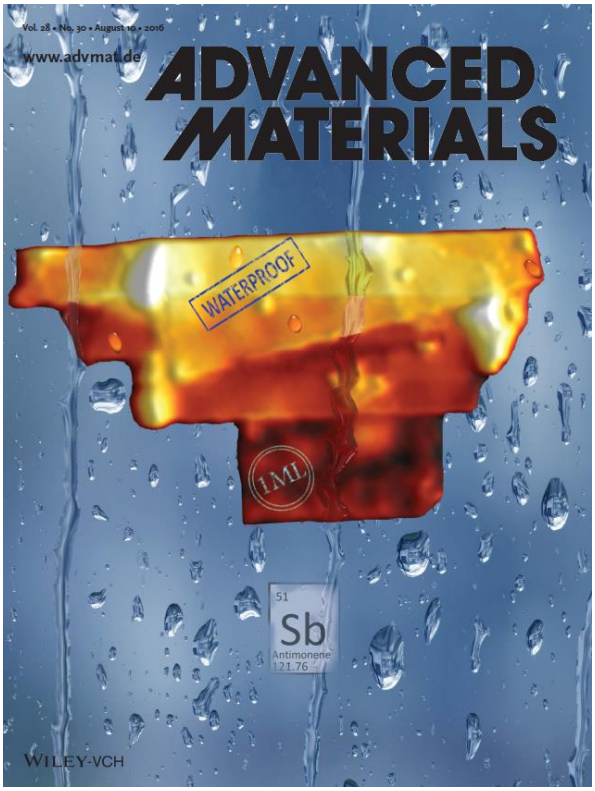

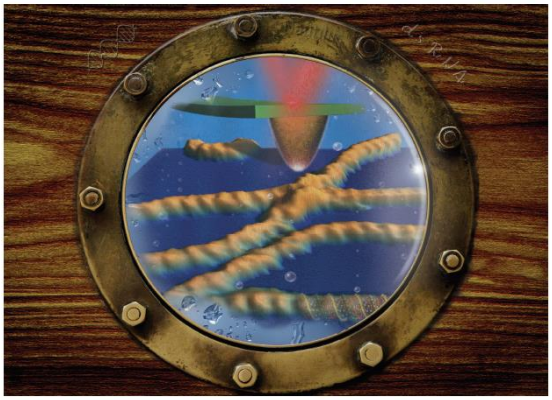

Showcasing research from the Department of Condensed Matter Physics, Universidad Autónoma de Madrid, and the Department of Macromolecular Structures, National Centre of Biotechnology, CSIC, Madrid, Spain.

High resolution atomic force microscopy of double-stranded RNA

Imaging of the pitch periodicity of double-stranded RNA under liquid using high-resolution Atomic Force Microscopy (AFM). High-resolution images were reproduced with different high-sensitivity AFM imaging modes. The experiments highlighted the two critical aspects to obtain such a resolution. Firstly, the interacting force, that can be minimized with the appropriate tuning of each imaging mode parameters, and secondly, the sharpness of the tip.

As featured in:

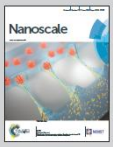

See Julio Gomez-Herrero, Fernando Moreno-Herrero *et al.* *Nanoscale*, 2016, **8**, 11818.

ROYAL SOCIETY OF CHEMISTRY

www.rsc.org/nanoscale

Registered charity number: 207890